Non-linear modelling and estimation for diesel engines

Zweiri, Yahya Hashem

Nonlinear Modelling and Estimation for Diesel Engines

By: Yahya H. Zweiri

KING'S College LONDON
Founded 1829

Department of Mechanical Engineering, King's College London,

Strand, London WC2R 2LS, UK.

This thesis is submitted to the School of Physical Science and Engineering, Division of Engineering, King's College London, University of London, for the degree of Doctor of Philosophy.

Declaration

I declare that the work presented in this thesis is my own.

Signature 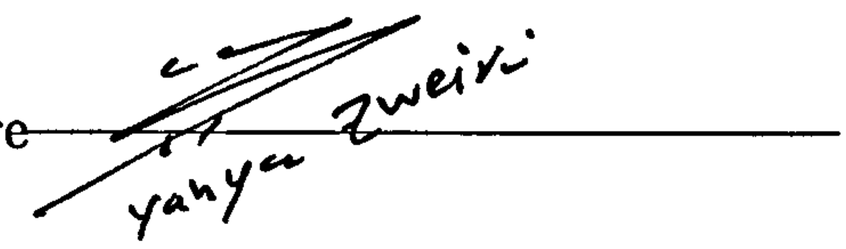

Abstract

Diesel engines have many advantages, such as high life span, reliability and efficiency, making them the most frequently used power source in vehicles. However, environmental concerns mean that there is a need to reduce engine emissions; improvements to engine estimation and control can help achieve this. The main aim of the work presented in this thesis is to develop modelling and estimation strategies to estimate Diesel engine parameters and engine indicated torque using only low cost/easily accessible sensors.

The main contributions of this thesis are as follows. First, a detailed model of the non-linear dynamics of a generic four-stroke direct injection single-cylinder Diesel engine is developed; the model is validated against experimental data showing very good agreement. Second, a novel numerical technique to invert the dynamic model of a single-cylinder Diesel engine, for estimating engine parameters, is developed. The method can be employed as a design tool to estimate engine parameters required to achieve a given performance characteristic and for tuning parameters that play an important role in dynamic modelling accuracy. Third, two estimation strategies are developed and used for predicting variables that are not easily measured and need expensive sensors, such as cylinder indicated torque and load torque. The two strategies use sliding mode observers and artificial neural networks respectively, and are based on the developed engine model. A new backpropagation algorithm is proposed in order to speed-up the weight adjusting process and to create conditions to guarantee the learning stability.

Contents

List of Tables

List of Figures

Notation

The following is a list of the main symbols used in this thesis, together with a brief description of their significance.

a_i: reduction factors for the piston rings

c: compression ratio

d: cylinder bore diameter [m]

c_r: radial clearance [m]

d_i: wire diameter of the intake or exhaust valve spring [m]

d_o: mean coil diameter of the intake or exhaust valve spring [m]

d_r: piston ring diameter [m]

f: fuel air ratio

f_s: stoichiometric fuel air ratio

g: acceleration of the gravity [m/s^2]

g_c: gap closure of the piston ring [m]

h: total oil film thickness [m]

h_f: forced heat transfer convective coefficient

h_{for}: enthalpy of formation of the hydrocarbon

h_l: maximum oil film thickness [m]

h_m: minimum oil film thickness [m]

h_n: natural heat transfer convective coefficient

h_o: stagnation enthalpy

$\hbar$: ratio length

ii: subscript to identify different entries to the control volume

i: subscript to identify each piston ring

j: subscript to identify surfaces with different rates of heat transfer

m_a: air mass [kg]

m_c: crankshaft mass [kg]

m_f: mass of fuel [kg]

m_p: piston mass [kg]

m_r: connecting rod mass [kg]

$\acute{m}$: mass flow rate (w.r.t crankangle)

$\acute{m}_f$: fuel rate (w.r.t crankangle)

$\acute{m}_{fb}$: burned fuel mass rate (w.r.t crankangle)

$\acute{m}_{fburn}$:fuel mass burning rate (w.r.t crankangle)

n_c: number of cylinders

n_{iv}: number of intake valves per cylinder

p_{atm}: atmospheric pressure(101 kPa)

p_I: indicated pressure [Pa]

p_o: oil pressure [Pa]

r: crank radius [m]

r_b: bearing radius [m]

t: time [s]

u: specific internal energy

y: piston displacement [m]

z: hydrodynamic friction coefficient [m]

A: heat transfer area [m^2]

A_m: exhaust manifold area [m^2]

A_p: piston area [m^2]

A_v: valve area [m^2]

B_i: the width of the ring in the direction of motion (slider width) [m]

C_d: discharge coefficient

C_p: specific heat

D: damping coefficient [Nm/(rad/s)]

D_i: inner exhaust manifold diameter [m]

D_{iv}: intake valve diameter [m]

D_o: outer exhaust manifold diameter [m]

E_i: nominal modulus of elasticity of piston ring [N/m^2]

F: equivalence ratio

F_f: friction force [N]

G_v: nominal modulus of rigidity of valve train spring [N/m^2]

$G(\theta_1)$:geometric function

ID: ignition delay

J_c: moment of inertia of crankshaft [kgm^2]

J_R: moment of inertia of connecting rod [kgm^2]

J_1: moment of inertia of crankshaft, flywheel, main gear and rotating part of connecting rod [kgm^2]

J_2: moment of inertia of dynamometer rotating parts [kgm^2]

K: thermal conductivity

L: connecting rod length [m]

L_b: bearing length [m]

L_{eq}: total equivalent length [m]

L_s: skirt length [m]

M: piston, rings, pin and small end of connecting rod mass [kg]

N_t: number of active coils in the intake or exhaust spring

N_v: number of intake and exhaust valves

O_c: oil clearance [m]

P: control volume pressure [Pa]

P_d: down stream pressure [Pa]

P_u: up stream pressure [Pa]

Q_{ht}: heat transfer

R: gas constant

R_{eq}: total equivalent radius [m]

S: coupling stiffness [Nm/rad]

T: temperature [K]

T_D: damping torque [Nm]

T_{f1}: piston-ring assembly friction torque [Nm]

T_{f2}: crankshaft bearing friction torque [Nm]

T_{f3}: valve train friction torque [Nm]

T_{f4}: pumping losses torque [Nm]

T_{f5}: pumps friction torque [Nm]

T_I: indicated torque [Nm]

T_{Lj}: engine load torque [Nm]

T_m: exhaust manifold temperature [K]

T_o: oil temperature [K]

T_r: reciprocating inertia torque [Nm]

T_{rad}: apparent radiant temperature [K]

T_S: torsional stiffness torque [Nm]

T_w: cylinder wall temperature [K]

U: velocity of the slider [m/s]

V_d: displacement volume [m^3]

V_l: valve lift [m]

α: curvature index

β: connecting rod angle [rad]

γ_s: specific heat ratio

δ: piston pin offset [m]

ϵ: bearing eccentricity [m]

ϵ: apparent grey-body emissivity

η_{bm}: mixed friction coefficient

θ_{ign}: crank angle ignition begins

θ_{inj}: crank angle injection begins

θ_1: crankshaft angular position [rad]

θ_2: dynamometer angular position [rad]

$\lambda(\theta_1)$: geometric function

μ: the dynamic viscosity of the oil [Ns/m^2]

μ_g: the dynamic viscosity of the exhaust gas [Ns/m^2]

ν: oil kinematic viscosity [m^2/s]

ν_g: exhaust gas kinematic viscosity [m^2/s]

ξ: inclination angle of the ring profile

ϖ: average exhaust flow rate

ρ: oil density [kg/m^3]

ς: volumetric coeffficient

τ: moment of inertia of crankshaft assembly and the reciprocating parts [kgm^2]

ϕ: connecting rod angle when piston is at TDC [rad]

$\omega_1, \dot{\theta}_1$: engine speed [rad/s]

$\omega_2, \dot{\theta}_2$: coupling speed [rad/s]

$(')$: derivative with respect to crank angle

$(\dot{})$: derivative with respect to time

To my parents

my wife Nadia
my children Feras, Mohammed and Lina.

Acknowledgments

I am indebted to many people without whose help and support I could never have reached a successful conclusion to this project. First and foremost, I would like to thank Dr. James Whidborne for his patient and liberal supervision. Although he never intervened in my work, he would always make sure I was progressing in a meaningful direction. His talent to envision solutions that go beyond current trends is remarkable. I am also thankful to him for his guidance through the early years of chaos and confusion. My sincerest thanks also go to Prof. Lakmal Seneviratne, who readily agreed to co-supervise this project and whose advice, remarks and financial support considerably helped me to consolidate my project. I would like also to thank Dr. K. Althoefer for his help and for many useful discussions and comments.

I had the pleasure of being supported by Mu'tah University, Jordan. Their support makes research like this possible. The scholarship which was awarded to me for the period 1997–2002, was crucial to the successful completion of this project. I am most grateful to Professor E. Dahiyat (President of Mu'tah University) and my uncle Mahmood Zweiri for their encouragement and help.

Of course, I am grateful to my parents. My mother (Hassana) keeps giving me love and real motherhood. My father (Hashem) is a military man and a mathematician. He taught me mathematics when I was at school, some topics for instance (analytical geometry, sets, algebra,...) were presented to me when my age was less than twelve years. I learned from him to work very hard and to be successful in all aspects of my life. Last, but not least, I am indebted to Nadia and the kids for their love and understanding during the past years. Nadia bore the brunt of my self-absorbed immersion in work, with very little to offer in return from my side. Nadia, thanks for being the wonderful wife. I hope, we will be able

to climb many more new heights together in the future. Many kisses to my kids for their patience and love, without them this work would never have come into existence.

Finally, I wish to thank the following: Prof. Khalid Tawarah, Prof. Bassam Jubran, Prof. M. Yianneskis and Prof. Mohammed Obaidat for their encouragement and help; Dr. Biniam Bekit, Dr. Bruno Lara, Dr. Suparerk, Mongkorn Klingajay, Olga Duran and Fauzi Ben Hussien for their friendship and for all the good and bad times we had together; my brothers and sisters, Nabil Abd-Al-hady, Farida Bedwany, Mohammed Tawarah and Dr. Asem Hiari for their help.

Chapter 1

Introduction

1.1 Motivation

Diesel engines are one of the most efficient internal combustion engines and are able to reach efficiencies of over 40%. Consequently, Diesel engines are the most common power plant for heavy vehicles and machines. Furthermore, Diesel powered cars are becoming increasingly popular, both in the UK and world wide. However, for this trend to continue, and to meet modern requirements for clean and efficient engines, further progress in Diesel engine control and diagnostics is necessary. A main focus of the thesis research is to develop models and modelling techniques which will enable engine simulations to predict accurately the engine state variables. With the recent rapid advance of microprocessor technology, it is feasible to use these models for real-time applications, such as state estimation, control and fault diagnostics. Such models can be used in a number of ways [WM95, GA98, NKM+00, JJK00]:

- for engine design and performance prediction
- for controller design
- as a real-time model for use in simulation and tests
- as an embedded model for state estimation for control or diagnostics.

1.2 Aims and objectives

This thesis deals with research into generic four-stroke direct injection single-cylinder Diesel engines. The main aim of this thesis is to investigate non-linear modelling and estimation strategies for single-cylinder Diesel engines to estimate system parameters and indicated torque using only low cost/easily accessible angular velocity and displacement signals.

The main objectives of the research are:

(a) To develop analytical nonlinear models for a single-cylinder Diesel engine.

(b) To use the models to develop an engine parameter estimation methodology.

(c) To use the models to develop estimation strategies for indicated torque.

1.3 Summary of past work

Detailed literature surveys on Diesel engine modelling and estimation are given in main chapters 2-7, and a brief summary is given below.

1.3.1 Analytical modelling

Early studies into Diesel engine modelling relied on the use of empirical data to develop linear dynamic models [LW71, WT81, BCHW73] to predict engine performance. These models link steady-state experimental data representing engine thermodynamics and gas flow, with simple dynamic models of the mechanical components. Such quasi-linear models are heavily reliant on experimental data. Furthermore, they poorly represent the transient response of the engine. More recently, nonlinear engine simulation models using the Filling and Emptying Method, and the Method of Characteristics have been developed [WJ82, Hey88, AAB+97, RG97] for the purpose of engine design and performance predictions. Some researchers have developed steady-state nonlinear models, for example [Riz89, RZ94, LAK90],

to simulate spark ignition engines in order to estimate engine torque and cylinder pressure.

A number of models have been developed for the purpose of Diesel engine control. In [JKS+91], a mean value model was used. The model consists of several empirical algebraic and first order differential equations in order to reduce the computational complexity and to achieve real-time implementations. Diesel engine models for electronic control were developed in [Wat84, GRH89], where the in-cylinder combustion process was included by using a single zone model, and a filling and emptying modelling technique. In [Wat84], several modifications to the model are proposed to reduce the computational time. These models do not predict in-cycle crankshaft angular speed variations. In [KM95], hybrids of two engine models, a mean torque production model and a simplified cylinder-by-cylinder model, are investigated in order to provide control engineers with tools for developing control and diagnostic algorithms.

Engine friction and lubrication is a factor that affects the performance of the internal combustion engines. A review of the literature from various companies and institutes suggested various ways to reduce engine friction [TC99, Ric00]

1.3.2 Estimation strategies

One important application of engine estimation is fault diagnosis. Fault diagnosis on Diesel engines is a difficult problem due to the complex structure of the engine. Indicated torque estimators based on sliding mode observers are given in [KM94, CM97, SM95]. All these estimators are implemented in the time domain. In [RDW95, WKR97], the estimator was implemented in crank angle domain but nonlinear inertia variation is not included, which could give false estimation at high engine speeds. Also the load estimation is not explored. Various diagnosis methods have been proposed for Diesel engine condition monitoring that are mainly statistical, based on known engine operating curves. These systems provide general information only and do not reveal the actual cause of an engine fault or low performance. A method based on the processing of measured engine data

using a simulation model and providing the current engine condition and its tuning is presented in [HK99]. Rough Sets theory [LFLY00] is used to diagnose the valve fault for a multi-cylinder Diesel engine. The analysis in [LFLY00] shows that Rough Sets theory is an effective method for valve fault diagnosis. Self-organising map (SOM) networks for condition monitoring of Diesel engines using acoustic signals is presented in [LPCG02].

The application of artificial neural networks for fault detection in Diesel engines has recently started to emerge. In [Mes01], a neural network is trained to classify and consequently recognize faulty and healthy behaviour of a 6-cylinder turbocharged Diesel engine for a wide range of operating conditions. Also advanced engine control systems require accurate dynamic models of the combustion process, and these are highly nonlinear. This creates the potential for the application of fast and efficient neural network models for Diesel engine estimation and control design purposes. The neuro-models can then be integrated into an upper-level emission optimization tool which calculates a cost function for exhaust versus consumption/torque and determines optimal engine settings [LDCL01]. Neural networks are widely applied to various Diesel engine research areas, including modelling, control and diagnosis [HSNI00, BDV+99, Mes01, IH01, PKG00].

1.4 Overview of the thesis

- **Chapters 2 - Engine Dynamic Model.**

  The nonlinear dynamic equations of a single-cylinder Diesel engine, describing the relationship between the net engine torque and the angular speed of the crankshaft are introduced. Mean frictional loss components are evaluated. Inertia of the dynamometer, and the stiffness and damping of the coupling are included. In addition, the piston pin offset is taken into consideration during the analysis.

- **Chapter 3 - Instantaneous Friction Components Model.**

  The equations of the friction components are based on theoretical considerations, namely Reynolds equation and dynamic analysis. New equations for the friction components of ring assembly, bearing mixed lubrication and valve train are introduced. The calculation of engine friction during starting depends on the oil viscosity, and is modelled by including the effect of temperature variations on oil viscosity.

- **Chapter 4 - Engine Model Including Dynamic and Thermodynamic Effects.**

  A combined dynamic, instantaneous friction and thermodynamic engine model is developed in the crank angle domain and used to predict the in-cycle variations of the engine states. The inertia variations of the crankshaft assembly are included. Equations of the thermodynamic model presented are derived from the filling and emptying method. Three thermodynamic control volumes are considered; cylinder, inlet manifold and exhaust manifold. Equations for the conservation of mass and energy, gas property relations and perfect gas laws are solved in the crank-angle domain. A single zone combustion model is used for simulating the theoretical fuel burning rate. The cylinder is treated as one control volume with homogeneous temperature and pressure.

- **Chapter 5 - Parameter Estimation Based on a Numerical Inversion Technique.**

  A numerical inversion of the dynamic model of a single-cylinder Diesel engine is presented. From data of crankshaft velocity, indicated torque, dynamometer angular velocity and applied load, a set of nonlinear algebraic equations are formulated. These equations are solved using a generalized Newton-Raphson method in order to estimate engine parameters.

- **Chapter 6 - Indicated and Load Torque Estimation Using Sliding Mode.**

  A nonlinear sliding mode observer is developed. The observer can be used to estimate both the engine indicated torque and load torque using low cost measurements of more accessible variables, such as the instantaneous angular velocities and instantaneous angular displacements of the engine crank shaft and the dynamometer coupling. The estimation is based on a sliding mode observer system, where the control is switched from one value to another in finite time. Switching usually causes a chattering effect. Moreover, in order to avoid the chattering, the sliding gain of the indicated torque estimator is designed as a nonlinear function of the engine crank angle. The stability of the observers are analyzed using Lyapunov theory.

- **Chapter 7 - Indicated Torque Estimation Based on Neural Networks.**

  A technique for Diesel engine indicated torque estimation using an artificial neural network (ANN) trained by a novel three term backpropagation algorithm is presented. The technique is applied to the problem of estimating indicated torque from measurements of crankshaft angular velocity and displacement in internal combustion engines. Efficient training algorithms for the ANN are essential in practical applications. To improve training efficiency, a new three-term backpropagation algorithm is developed; a third term is added in addition to the usual learning rate and momentum factor terms of the standard backpropagation algorithm, this being a proportional factor (PF). This new three-term algorithm can be viewed as being analogous to the common three-term PID algorithm used in feedback control. Local stability properties around an equilibrium point are examined using small signal analysis. Efficient backpropagation algorithm learning using simultaneously optimized learning rate (LR), momentum factor (MF) and proportional factor (PF) terms is presented. A set of recursive formulae is

used for calculating the derivatives of the optimization target with respect to LR, MF and PF.

- **Chapter 8 - Conclusions and Future Research.**

  The main conclusions of the thesis with a number of possible future research topics are presented.

1.5 Achievements

i) A detailed dynamic model for a four-stroke direct injection single-cylinder Diesel engine is presented. The new features in this model are

  - The model includes the piston pin offset and the inertia of the dynamometer as well as the stiffness and the damping of the coupling, which enables a variety of engine tests to be carried out.
  - A novel combination of equations for the friction of ring assembly, bearing mixed lubrication and valve train are presented. The friction model can simulate instantaneous engine friction behaviour under transient and cold-start operating conditions by simulation the temperature-viscosity changes.

- The proposed dynamic model with instantaneous friction components was tested with experimental data and is shown that the model has a prediction accuracy of 97%. This compares to accuracy of 88% for the model using mean friction components.
- A combined dynamic and thermodynamic engine model is developed in the crank angle domain and used to predict in-cycle variations of the engine states. The inertia variations of the crank shaft assembly effects are included. The model was validated on a single cylinder Diesel engine during cold conditions. Predicted profiles of the cylinder gas pressure and the instantaneous crankshaft angular velocity through the transient and steady-state cycles are in good agreement with measurements.

ii) A novel numerical inversion method for parameters estimation of a single cylinder Diesel engine is proposed. The numerical inversion technique can be used for estimating the system parameters which play an important role in dynamic modelling prediction accuracy.

iii) Novel estimation strategies for engine indicated torque are presented. The new aspects are:

- A new sliding mode observer is developed to estimate both the engine indicated and load torque. The estimation accuracy of the indicated torque is improved since estimation of the engine load is considered. The sliding gain of the indicated torque estimator is designed as a nonlinear function of the engine crank angle to reduce the chattering effect.
- A new estimation approach utilizing artificial neural networks is presented. Such an approach has the potential for real-time implementation and gives opportunity for on-board diagnostics. An efficient algorithm, the three-term backpropagation (BP) algorithm, is developed to train the neural network. The three-term BP algorithm allows the system to escape from stalls whilst maintaining the simplicity of standard BP algorithms. Test results indicate that the new algorithm offers much higher speeds of convergence than the standard BP algorithm. The necessary and sufficient conditions for the convergence and stability behaviour of the three-term backpropagation algorithm are established. The algorithm is implemented in an estimation scheme to estimate the indicated torque in Diesel engines.

The work presented in this thesis has resulted in 6 peer reviewed journal papers. In addition 10 refereed conference papers have been presented. A further 2 journal papers are to be submitted shortly. A full list of publications based on the thesis is given in Appendix A.

Chapter 2

Engine Dynamic Model

2.1 Introduction

Many engineering systems include nonlinear parts (subsystems) which might affect the dynamic behaviour of the system. In some products like Diesel engines, the nonlinearities of the piston assembly, bearings and fuel elements can introduce undesirable effects [JS00, Bla99]. Direct-injection (DI) four-stroke Diesel engine models have long been established as effective tools for studying engine performance and aiding design. Most of the work done in this area has concentrated on steady-state models for the purpose of modifying engine design parameters in order to minimize emissions and maximize power and fuel economy of the engine. However, recent regulations have imposed stringent emission and fuel economy standards that cannot be addressed by a steady-state analysis of the engine. Simulation of transient engine response is needed to predict performance and fuel economy of Diesel engines that frequently experience rapid changes of speed and load. Hence, to contribute towards solving this problem, the current research work is conducted with the aim of developing a non-linear dynamic model for DI, four-stroke, single-cylinder, Diesel engines which can simulate the engine performance under transient and steady-state operating conditions.

Previous efforts in the area of engine dynamic modelling can be grouped into

two major categories, non-linear steady-state, and transient dynamic non-linear models. Examples of steady-state non-linear models can be found in [Riz89, RZ94, LAK90], which simulate spark ignition engines in order to estimate engine torque and cylinder pressure. The engine is treated as a system with input given by cylinder pressure and the outputs corresponding to crankshaft angular acceleration and crankshaft torque. In the models, cylinder pressure is deterministically related to net engine torque through the geometry and dynamics of the reciprocating assembly. In [ZR93], the relationship between net engine torque and crankshaft angular acceleration is simplified as a linear second-order system.

Some examples of transient non-linear dynamic models can be found in [AAB+97] where a model composed of thermodynamic and dynamic constitutive elements for a transient, multi-cylinder Diesel engine simulation is developed. This model utilizes a quasi-steady thermodynamic process. A comparison of predicted and measured pressure traces during the transient response was satisfactory overall, but also indicated some limitations of the quasi-steady process sub-models. So the authors [FA97] have extended the steady-state Diesel engine simulation to include the prediction of instantaneous engine speed and torque during transients.

An important aspect of engine dynamic operation is the instantaneous torque, and the cyclic nature of the gas pressure force and the slider-crank kinematics. Therefore, the objective of this chapter is to develop a non-linear single-cylinder Diesel engine model with transient capability explaining the relationship between the net engine torque and the angular speed of the crankshaft. Another aspect that plays an important role in engine transient modelling is the evaluation of frictional losses, especially piston assembly friction because it is a factor which strongly affects the economy, performance and durability of reciprocating internal combustion engines. In this chapter, a simplified friction torque model is assumed. The model is extended and developed in Chapter 3 to include instantaneous engine friction behaviour, oil viscosity variation and additional detailed effects of engine friction components. The proposed model takes the inertia of the dynamometer and the stiffness and damping of the coupling into consideration. In addition, the

piston pin offset is taken into consideration during the analysis. The dynamic engine operation is illustrated by simulation results, and the predicted engine response is validated through comparison with measured data from two different engines.

The chapter is arranged as follows. In Section 2.2, the engine and dynamometer model, composed of the engine dynamic model and the inertia of the dynamometer and stiffness and damping of the coupling model, the instantaneous single-cylinder engine torque model and the mean friction torque model, is developed. In Section 2.3, description of the implementation is presented, followed by some simulation results to show the model behaviour and validation. Finally, there is a discussion and some conclusions are drawn.

2.2 Engine modelling

2.2.1 Engine dynamic model

Figure 2.1 shows a model of the engine coupled to a dynamometer. The following two equations describe the dynamic system:

$$T_I - \sum_{k=1}^{5} T_{fk} - T_r = J_1\ddot{\theta}_1 + T_S + T_D, \tag{2.1}$$

$$T_D + T_S = J_2\ddot{\theta}_2 + T_L. \tag{2.2}$$

Equations (2.1) and (2.2) simply state Newton's second law for a rotational body. The variables used for these and all the other equations are defined in the Notation.

The indicated engine torque, T_I, is generated by the conversion of chemical to thermal to mechanical energy during the combustion process. The reciprocating torque, T_r, is produced due to the motion of piston assembly and small end of the connecting rod. The reciprocating torque and the friction torque terms, $\sum_{k=1}^{5} T_{fk}$, are subtracted from the instantaneous indicated torque value to produce the brake torque at the shaft. The resistance torque, T_L, which is the result of external loading imposed on the engine by the dynamometer, is in addition to the dynamometer

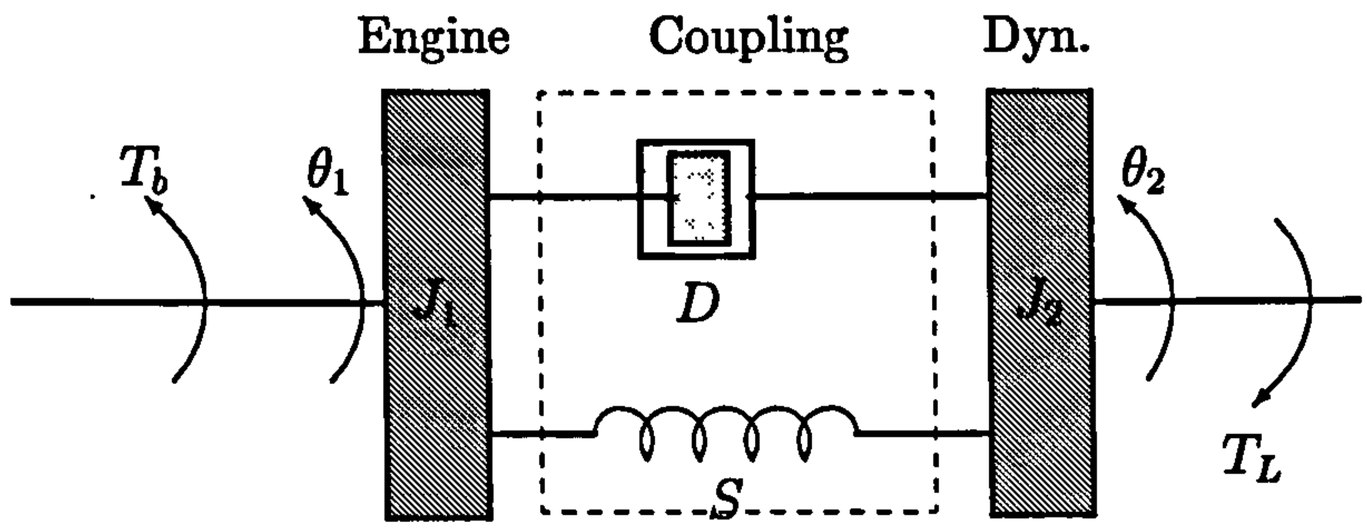

Figure 2.1: Engine and dynamometer model

inertia. Due to rapid changes in the cylinder pressure and consequent changes in the forces acting on the crank during a cycle, the instantaneous rotational speed of the crankshaft varies during any engine cycle, even if the mean speed is constant. The torsional stiffness torque, T_S, and damping torque, T_D, which depend on the stiffness and damping in the coupling between the engine and dynamometer are given by the linear relationships

$$T_S = S(\theta_1 - \theta_2), \tag{2.3}$$

and

$$T_D = D(\dot{\theta}_1 - \dot{\theta}_2). \tag{2.4}$$

2.2.2 Instantaneous engine torque model

Figure 2.2 shows the piston-crank mechanism with approximate kinetically equivalent point masses replacing the connecting rod. The model includes piston

pin offset for the piston acceleration. Important geometrical parameters are the crankshaft angular position, θ_1, measured from where the crankshaft and the connecting rod are in a straight line; the angle of connecting rod, β; the crank radius, r, which is equal to half of the stroke; the connecting rod length, L; the piston pin offset, δ and the connecting rod angle when piston is at top dead centre, ϕ. The piston pin is slightly offset in order to reduce engine noise and wear during the change of the direction of normal force on the piston at the end of compression.

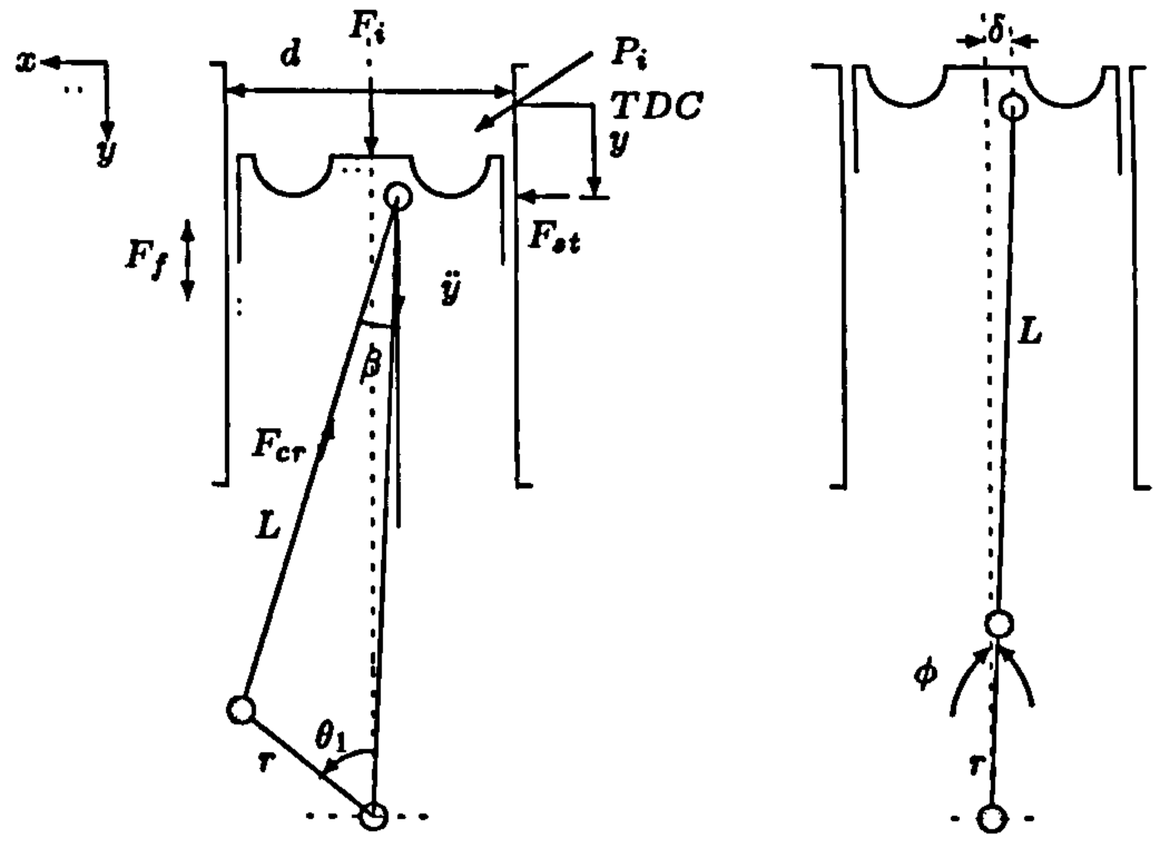

Figure 2.2: Forces and acceleration of the piston-crank mechanism

The relationship between the indicated gas pressure, p_I, and the indicated torque, T_I, is deterministic and is a function of engine geometry. This relationship is expressed as

$$T_I = (p_I - p_{atm}) A_p r G(\theta_1), \tag{2.5}$$

where

$$G(\theta_1) = \frac{\sin(\theta_1 + \beta)}{\cos\beta} = \sin\theta_1 + \sqrt{\frac{1 - \lambda(\theta_1)}{\lambda(\theta_1)}}\cos\theta_1, \tag{2.6}$$

and $\lambda(\theta_1)$ is a geometric function given by

$$\lambda(\theta_1) = 1 - \left(\frac{\delta + r\sin(\theta_1 - \phi)}{L}\right)^2. \tag{2.7}$$

From the piston-crank geometry, the piston displacement, y, is given by

$$y = \sqrt{(r+L)^2 - \delta^2} - [L\cos\beta + r\cos(\theta_1 - \phi)], \tag{2.8}$$

where angles ϕ and β can be expressed as

$$\phi = \sin^{-1}\frac{\delta}{r+L} \text{ and } \beta = \sin^{-1}\frac{\delta + r\sin(\theta_1 - \phi)}{L}. \tag{2.9}$$

The reciprocating torque, T_r.

This term is the torque produced due to the motion of the engine reciprocating components and is given as:

$$T_r = MrG(\theta_1)\ddot{y} = MrG(\theta_1)[G_1(\theta_1)\dot{\theta_1}^2 + G_2(\theta_1)\ddot{\theta}_1], \tag{2.10}$$

where geometrical functions $G_1(\theta_1)$ and $G_2(\theta_1)$ are

$$G_1(\theta_1) = r\left[\cos(\theta_1 - \phi)\left[1 + \frac{(\frac{r}{L})\cos(\theta_1 - \phi)}{\lambda(\theta_1)^{\frac{3}{2}}}\right] - \sqrt{\frac{1-\lambda(\theta_1)}{\lambda(\theta_1)}}\sin(\theta_1 - \phi)\right], \tag{2.11}$$

$$G_2(\theta_1) = r\left[\sin(\theta_1 - \phi) + \sqrt{\frac{1-\lambda(\theta_1)}{\lambda(\theta_1)}}\cos(\theta_1 - \phi)\right], \tag{2.12}$$

where M is the mass of piston, rings, pin and the small end of the connecting rod, and $\ddot{y}$ is the acceleration of the reciprocating components. The connecting rod is treated as an equivalent mass system, the first concentric mass is assumed to be connected to the crank-pin as a big end while the second concentric mass is attached to the piston assembly as a small end [LCH97]. Thus there are no transverse components of the force between the ends of the rod to bend or shear the link, and therefore the member is in axial tension or compression. The forces acting on the connecting rod, the inertia forces and the bearing forces, act at the ends of the rod.

2.2.3 Friction torque model

Piston-ring assembly friction torque, T_{f1}.

The literature [UP83, Mcg78, KP88] suggests that the piston-ring assembly may be responsible for 50-75% of the entire engine friction. The components that contribute to friction are: compression rings, oil control ring, piston skirt and piston pin. The forces acting on the piston assembly include static ring tension, the gas pressure force and the inertia force. The piston assembly friction is dominated by the ring friction components [FTT81]. This model takes into account only the hydrodynamic lubrication, since the friction torque is identically zero at the top and the bottom dead centre positions. The piston-assembly friction torque is expressed as:

$$T_{f1} = F_{f1} r G(\theta_1), \tag{2.13}$$

where

$$F_{f1} = \text{sgn}(\dot{y}) \left[\sum F_{f Ring_i} + F_{f Skirt} \right], \tag{2.14}$$

where $\text{sgn}(\dot{y})$ is the signum function (i.e. the sign of the friction force is the same as the sign of the piston velocity) defined as

$$\text{sgn}(\dot{y}) = \begin{cases} 1 & \dot{y} > 0, \\ 0 & \dot{y} = 0, \\ -1 & \dot{y} < 0. \end{cases} \tag{2.15}$$

This approach is based on calculating the piston-assembly friction using a simplified model [MP97, Mil87], based on hydrodynamic lubrication. The lubrication is considered to be one-dimensional as both ring and bore are assumed perfectly circular with the same centre. Then clearance in the circumferential direction is constant. When the oil film thickness h is much less than the ring width B, the Navier-Stokes equation for the liquid film motion reduces to a Reynolds equation of the form (as given in [MP97]):

$$\frac{\partial}{\partial x}\left(\frac{h^3}{\mu}\frac{\partial p}{\partial x}\right) = -6U\frac{\partial h}{\partial x} + 12\frac{\partial h}{\partial t}, \tag{2.16}$$

where x is a Cartesian coordinate in the direction of the ring motion. The load on the slider (ring width) is given in [MP97] by the following equation

$$W = \int_0^B p dx. \tag{2.17}$$

The total friction force in the x direction is expressed as [MP97]

$$F_f = \int_0^B \left[-\frac{h}{2}\frac{\partial p}{\partial x} + \frac{\mu U}{h}\right] dx. \tag{2.18}$$

By integrating the Reynolds equation twice with boundary conditions at $x = 0$, $p = p_1(t)$ and $x = B$, $p = p_2(t)$, the oil film pressure is expressed as [MP97]

$$p = \frac{6\left(U - \frac{2(h_l - h_m)}{\tan\xi(\Delta t)}\right)\mu B}{h_m^2 K}\left[\frac{1}{h_2} - \frac{K+1}{h_2^2(K+2)} - \frac{1}{K+2}\right] + p_1 + (p_1 - p_2)\frac{(K+1)^2(h_2^2-1)}{((K+1)^2-1)h_2^2} \tag{2.19}$$

where

$$h_2 = h/h_m \text{ and } K = \frac{B\tan\xi}{h_m} \tag{2.20}$$

and h_2 is a non-dimensional oil film thickness, h is a total oil film thickness and h_m is a minimum oil film thickness. Finally from (2.18) the friction force per circumferential length of the ring l is

$$\frac{F_f}{l} = \frac{h_m}{2}[p_1 - p_2(K+1)] + \frac{1}{2}\left[\frac{W}{l}\right]\tan\xi + \frac{\mu U B}{h_m K}\ln(K+1) \tag{2.21}$$

where W is obtained from (2.17).

Bearings friction torque, T_{f2}.

Bearings friction contributions come from the journal bearings and their associated seals. Journal bearings are usually designed to provide a minimum film thickness

of about 2μm. The journal bearings operate under hydrodynamic lubrication, this means a large load can be carried by the journal bearing with low energy losses under normal operating conditions. Following work done by Reseka and Heinen [RH84], the friction torque, T_{f2}, in the bearing is expressed as

$$T_{f2} = \frac{r_b}{2} A_p (p_I - p_{atm}) \frac{|\cos\theta_1|}{\sqrt{\dot{\theta}_1}}. \tag{2.22}$$

Valve train friction torque, T_{f3}.

The valve train carries high loads over the entire speed range of the engine. Loads acting on the valve train at lower speeds are due primarily to the spring forces, while at higher speeds the inertia forces of the component masses dominate. Following work of [Bis65], the friction torque, T_{f3}, in the valve train is expressed as

$$T_{f3} = 169.8 \left[\frac{[1 - 0.00127\dot{\theta}_1] n_{iv} D_{iv}^{1.75} V_d}{d^2 (2r)} \right]. \tag{2.23}$$

Pumping losses torque, T_{f4}.

The pumping work is the integral of the product of the pressure and the volume over inlet and exhaust strokes. The work measures two effects. The first effect is the restrictions outside the cylinder, in the inlet and exhaust systems; air filter and intake manifold (on the inlet side); exhaust manifold, muffler and tail pipe (on the exhaust side). The second effect is the valve flow, corresponding mainly to pressure losses in the inlet and exhaust valves. The pumping losses torque is the summation of the two effects. From [Bis65], it is expressed as

$$T_4 = 1.06 \left[\frac{V_d^{2.28}}{(n_{iv} n_c D_{iv}^2)^{1.28}} \right] \dot{\theta}_1^{1.7}. \tag{2.24}$$

Pump friction torque, T_{f5}.

The pumps are employed to circulate the oil, water and fuel. Following work done by [Bis65], the pumps friction torque is expressed as

$$T_5 = 6.79 \times 10^{-6} \left[\rho V_d (2r)^{2.5} \sqrt{\frac{d}{\nu}} \right] \dot{\theta}_1^{2.5}. \tag{2.25}$$

The friction Equations (2.23)-(2.25) are transformed from friction mean effective pressure (f_{mep}) to torque as follows:

$$f_{mep} = \frac{4\pi T_f}{V_d} \tag{2.26}$$

Note that the constant terms in (2.23)-(2.25) differ from [Bis65] because there has been a change of dimensions, i.e., the length to be in metres, the pressure in Pascal and the rotational speed in (rad/s).

The formulation, obtained by the model presented in this chapter leads to a set of nonlinear differential equations given by Equations (2.1) and (2.2). These can be numerically integrated to obtain the engine performance.

2.3 Model implementation

The model is implemented and simulated using Matlab/SIMULINK [Mat97, SIM97]. Figure 2.3 shows the block-diagram of the single-cylinder Diesel engine model. In Figure 2.3, $T_I(\theta_1)$ is the input measured indicated torque, T_L is the load torque and $\dot{\theta}_1$ is the output engine rotational speed. The Friction Model block composes of the mean friction components, Equations (2.13)-(2.25). The Reciprocating Torque block represents the torque produced due to the motion of the engine reciprocating components, Equation(2.10). The Coupling Model block is developed from Equations (2.3) and (2.4).

The main advantages of SIMULINK are its capability for representing the entire engine model by an assembly of interconnected blocks. Also it has eight variable-step solvers and six fixed-step solvers for the integration of differential

equations, and hence the most suitable integration method can be chosen. Input design parameters are passed on to the blocks from an input file, but all of the operating parameters come from the block (functions) for the other components of the system.

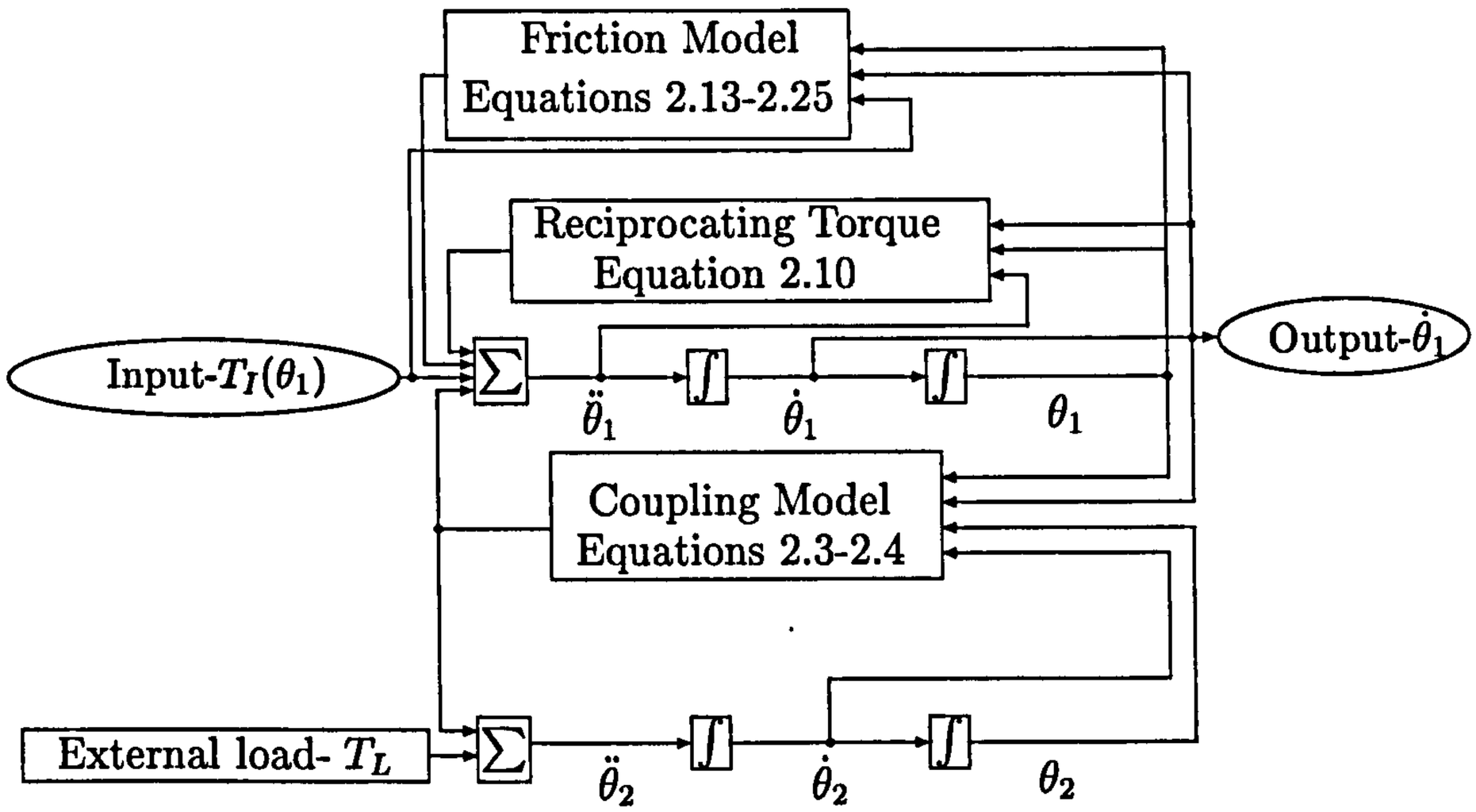

Figure 2.3: Dynamic Diesel engine model block diagram

2.4 Model behaviour and validation

In order to validate the behaviour of the engine dynamic model with experimental results under warm-up conditions, simulations have been performed for two single cylinder Diesel engines, a DDC DI four-stroke Diesel engine and a Caterpillar 8201 DI four-stroke Diesel engine, labeled A and B respectively.

The geometrical specifications for Engine A are shown in Table G.1 in Appendix G. A comparison between predicted and measured values of the crankshaft instantaneous angular velocity during engine transient behaviour is illustrated in Figure 2.4. The measured values of the engine speed and indicated pressure as well as engine parameters are taken from [FA97] and directly from the authors [Fil98].

Almost no external load is imposed by the dynamometer for the first two seconds, so the engine accelerates from low idle speed and passes through the entire speed range until it is at high engine speed. The acceleration during the transient is shown in Figure 2.5, where the engine accelerates because the net torque value is positive. As shown in Figure 2.4, between 2.4 and 3 seconds, the dynamometer increases the external load in order to avoid engine overrunning, hence acting as a cut-off of the fuel pump. Finally, the external load is increased significantly after 3 seconds in order to reduce the engine speed while indicated torque remains at the same value. The resulting net torque value is negative, so the engine decelerates as shown in Figures 2.4 and 2.6.

The overall agreement between the measured and predicted crankshaft angular velocity traces is good as shown in Figure 2.4, the maximum relative error during transient response (950-2100 rpm) is about 12%. The discrepancies maybe due to inaccuracies in the values of the engine model parameters, changes in friction and oil viscosity during transient process, inertia variations effects and from the fact that the engine angular velocity fluctuations are subject to the effect of not only engine torque but also of the reactive forces from the engine and dynamometer mounting in a sharp transient operation.

The instantaneous torque produced by the engine at low idle speed over one engine cycle (two revolutions) is shown in Figure 2.7. The maximum torque value corresponds to the maximum pressure in the cylinder during the combustion stroke. As a consequence of the huge fluctuations in engine torque during the cycle, the variations of the instantaneous crankshaft rotational speed are obvious between t1 and t2 in Figure 2.8; the sudden drop of the speed and its subsequent increase can be linked with the negative and positive peaks of the engine torque. The amplitudes of the cyclic speed fluctuations tend to increase as the mean engine speed decreases due to the fact that at low engine speed the cycle time is long and the engine deceleration at the end of compression stroke is dominant and vice versa, as shown in Figures 2.8 and 2.9. This is a very important criterion in making compromises between the flywheel size, the engine speed of response and

the engine low idle speed limit. Due to the harmonic motion of the reciprocating assembly, the relation between the phase of indicated torque and the instantaneous engine acceleration is virtually identical, as shown in Figures 2.10 and 2.5.

To test the dynamic model behaviour under steady-state with an exerted external load, a simulation has been performed for a medium speed single cylinder Diesel engine, the geometrical specifications for Engine B are shown in Table G.2 in Appendix G. The measured values of speed and indicated pressure as well as system parameters are provided by King Abdullah Design and Development Bureau, Jordan [Kah98].

Figure 2.11 shows the predicted instantaneous angular velocity from start till steady-state angular velocity at rated torque. The starter-off speed was about 382 rpm. After the starter torque is turned off, the angular velocity is accelerated by increasing input torque to achieve rated indicated torque. The external load torque (from the dynamometer) was increased between 4 and 9 seconds in three steps until it reached the rated load torque (maximum engine output torque), and the steady-state angular engine speed was achieved. To validate the model during steady-state, Figure 2.12 shows the comparison between predicted and measured angular engine velocity at rated torque for Engine B and there is good agreement.

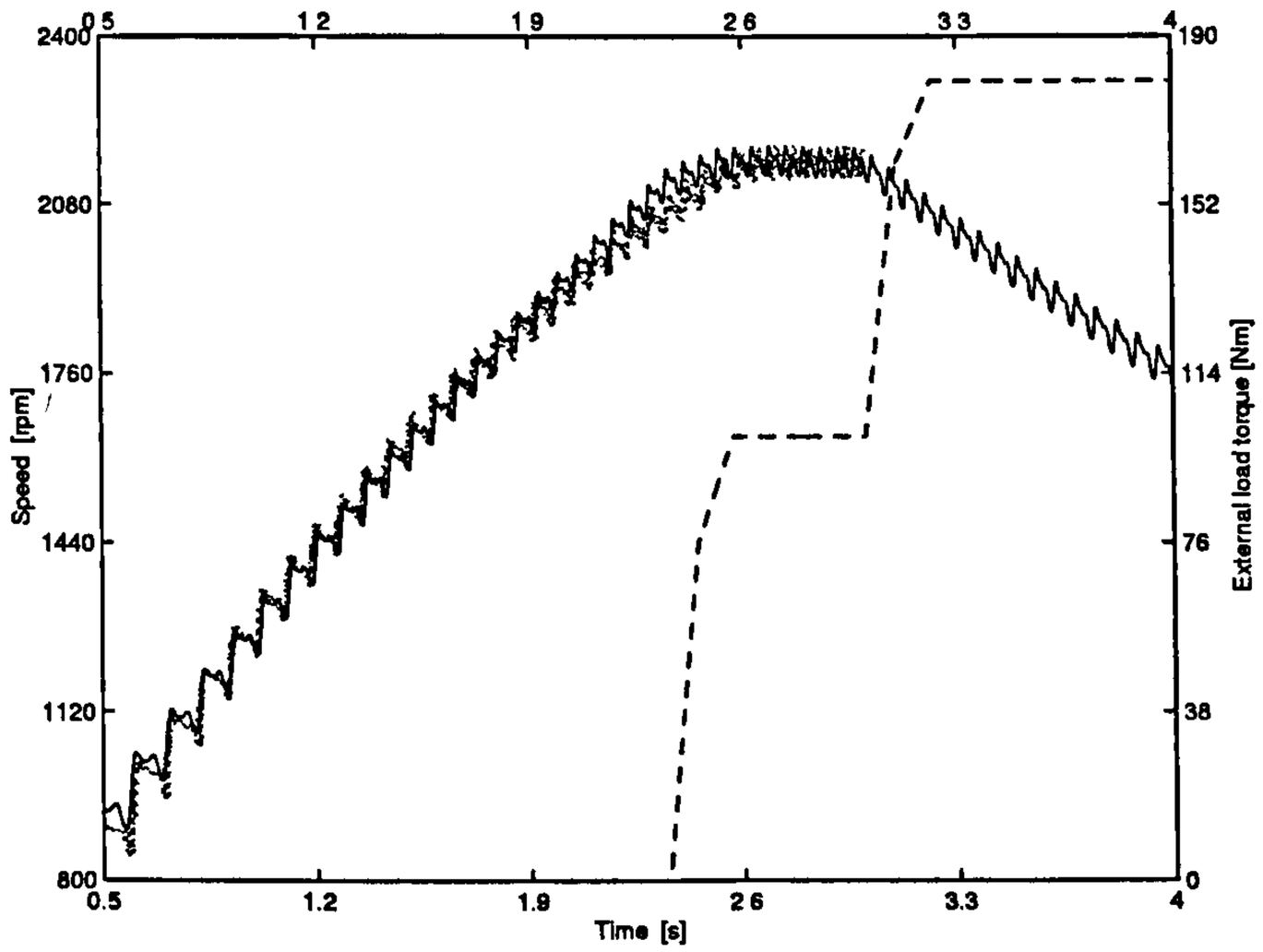

Figure 2.4: Comparison between the predicted (——) and measured [FA97] (· · ·) instantaneous speed of Engine A with dynamometer load (- - -)

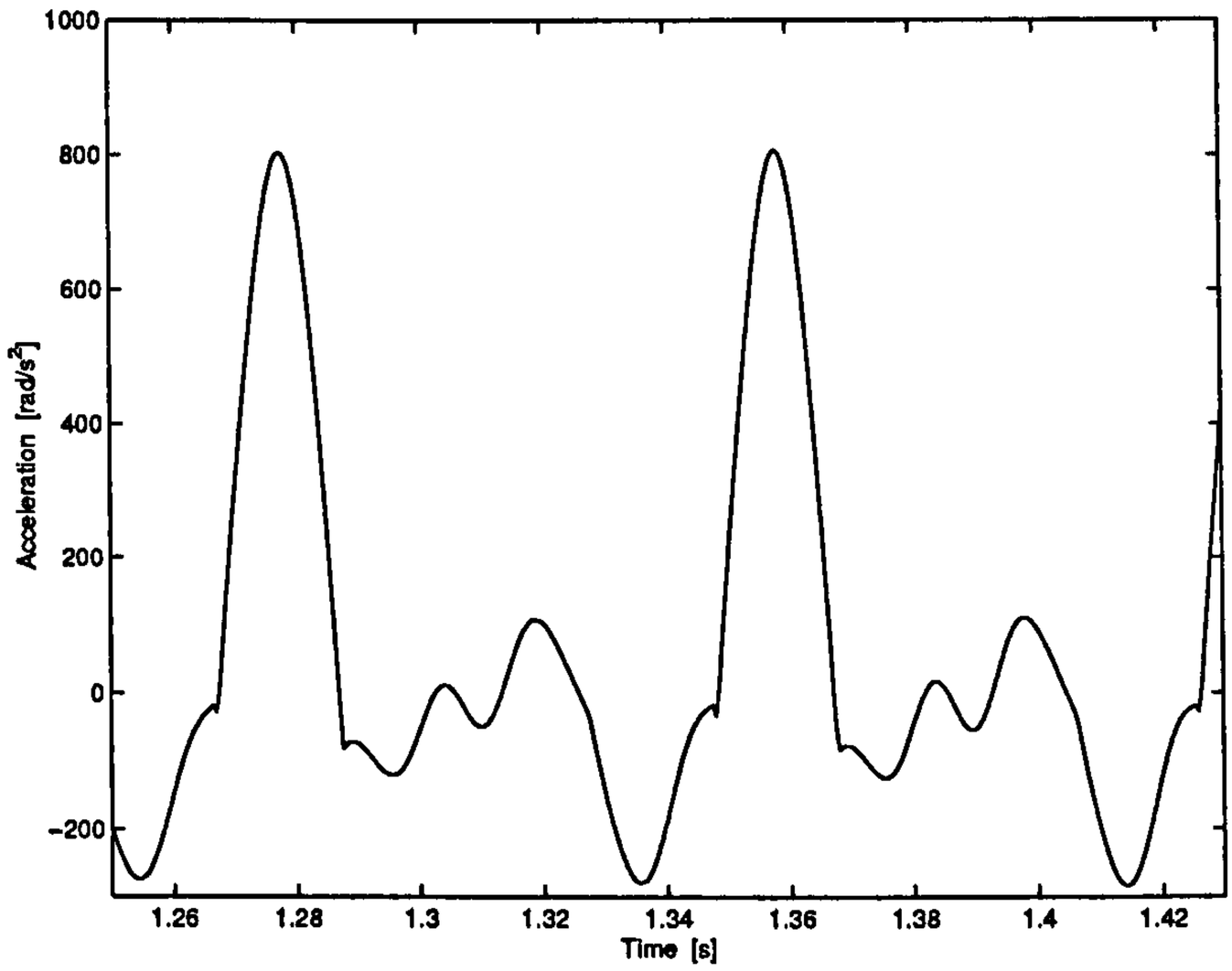

Figure 2.5: Predicted fluctuation of the crankshaft angular acceleration of Engine A during transient response

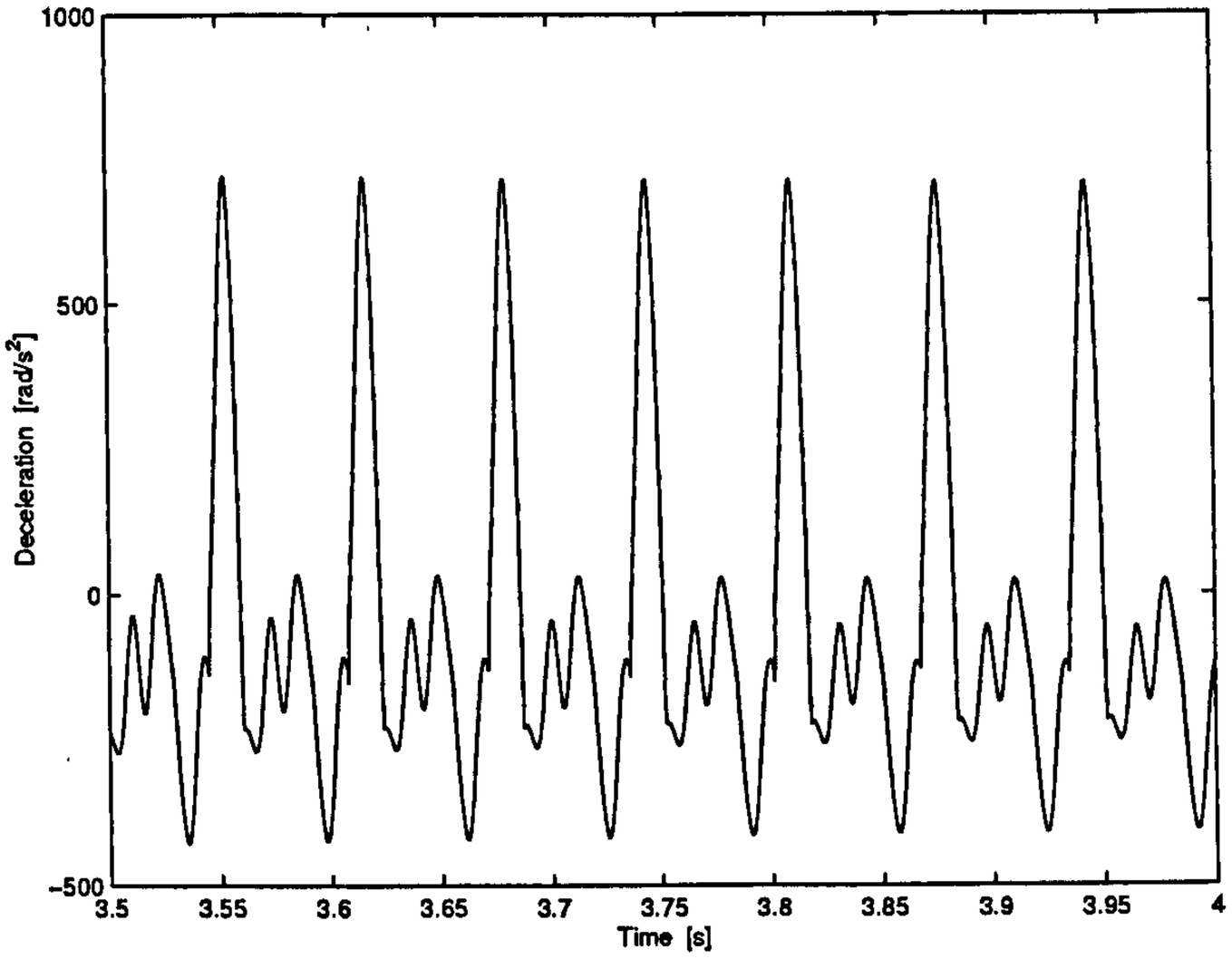

Figure 2.6: Predicted fluctuation of the crankshaft angular deceleration of Engine A during applied external loads

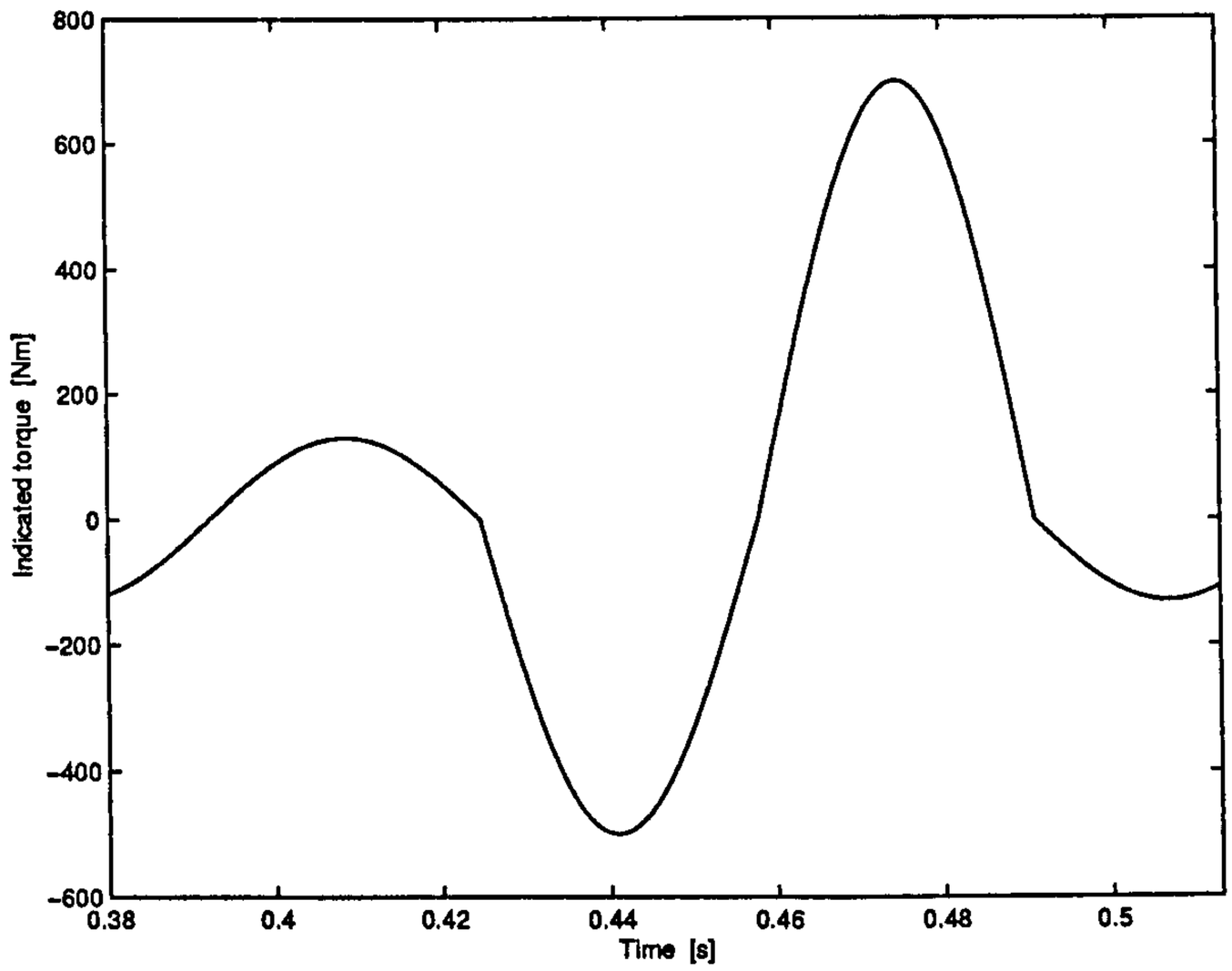

Figure 2.7: Measured fluctuations of the indicated torque on the crankshaft of Engine A during steady state low idle speed over one engine cycle, [FA97]

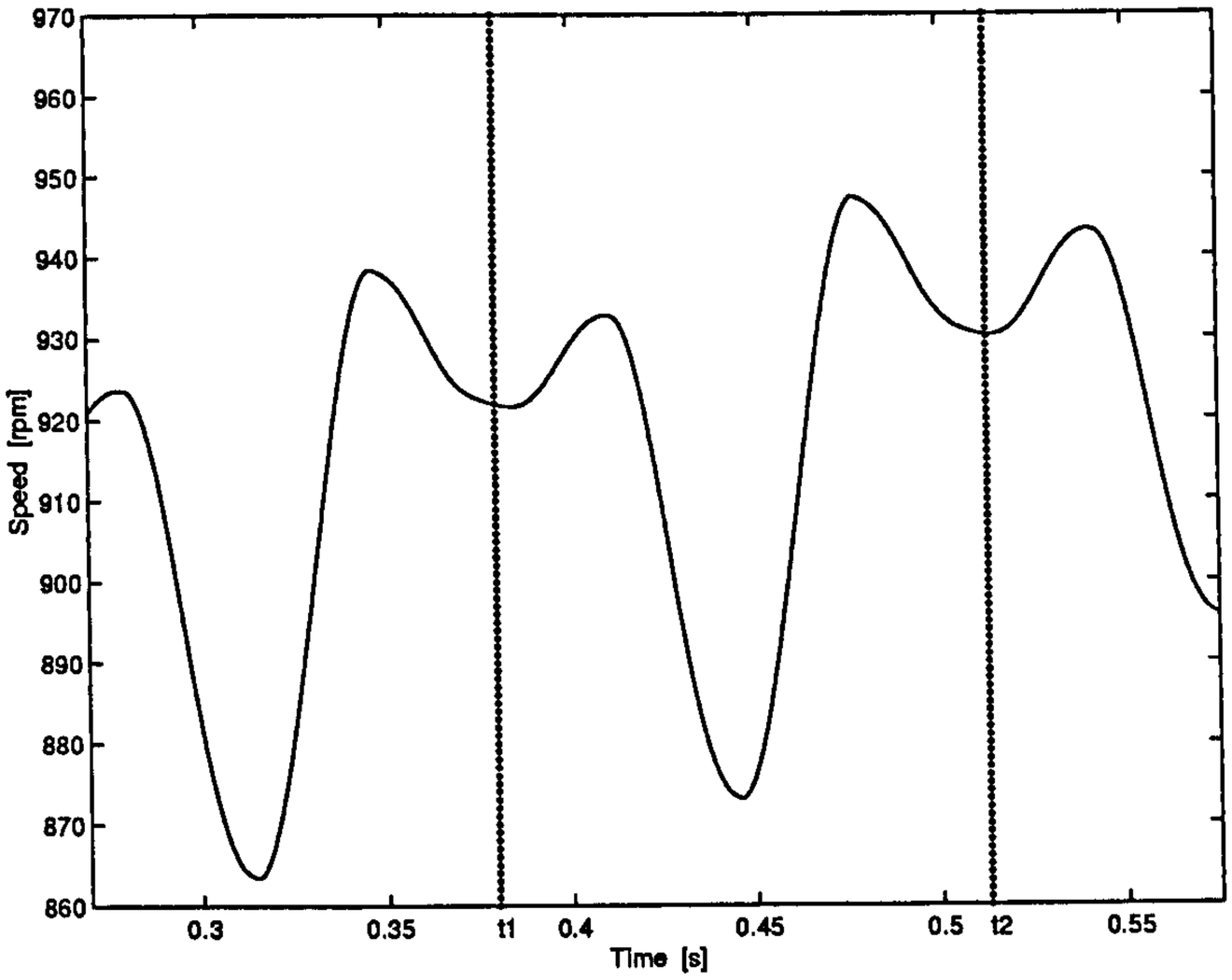

Figure 2.8: Predicted fluctuations of the instantaneous crankshaft angular speed of Engine A during steady state low idle speed (from t1 to t2 represents one engine cycle)

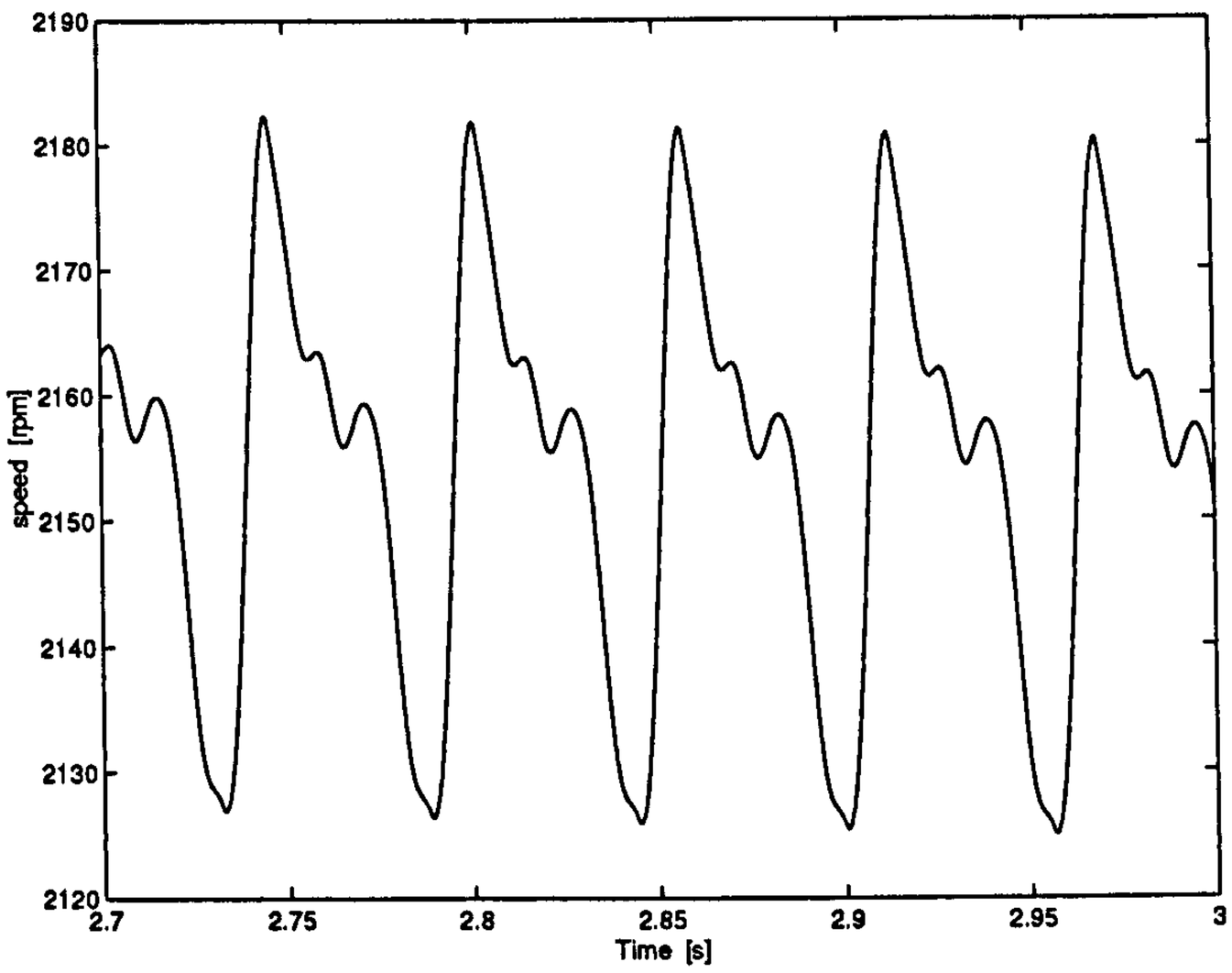

Figure 2.9: Predicted steady state high crankshaft speed of Engine A

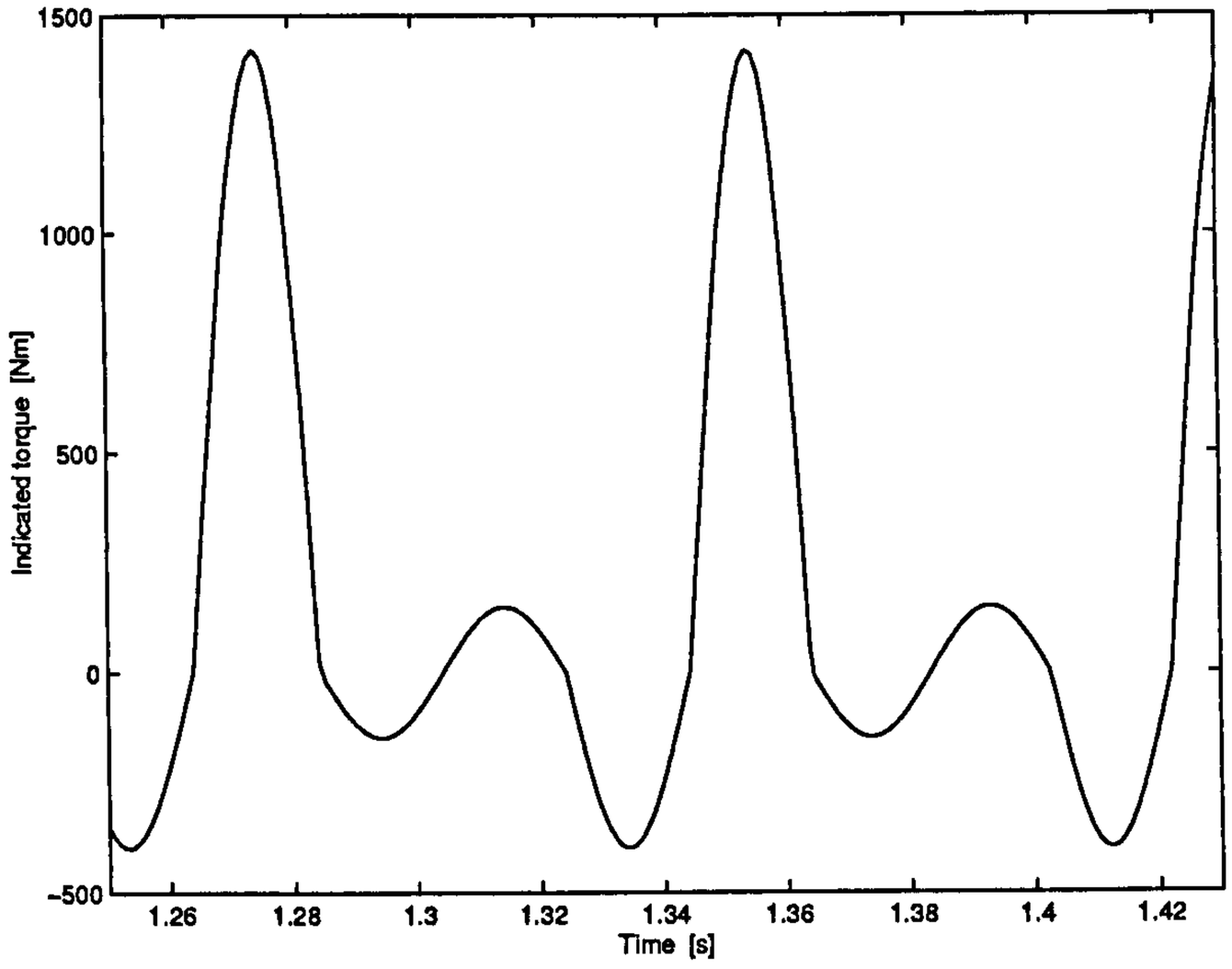

Figure 2.10: Measured fluctuation of the indicated torque on the crankshaft of Engine A during transient response, [FA97]

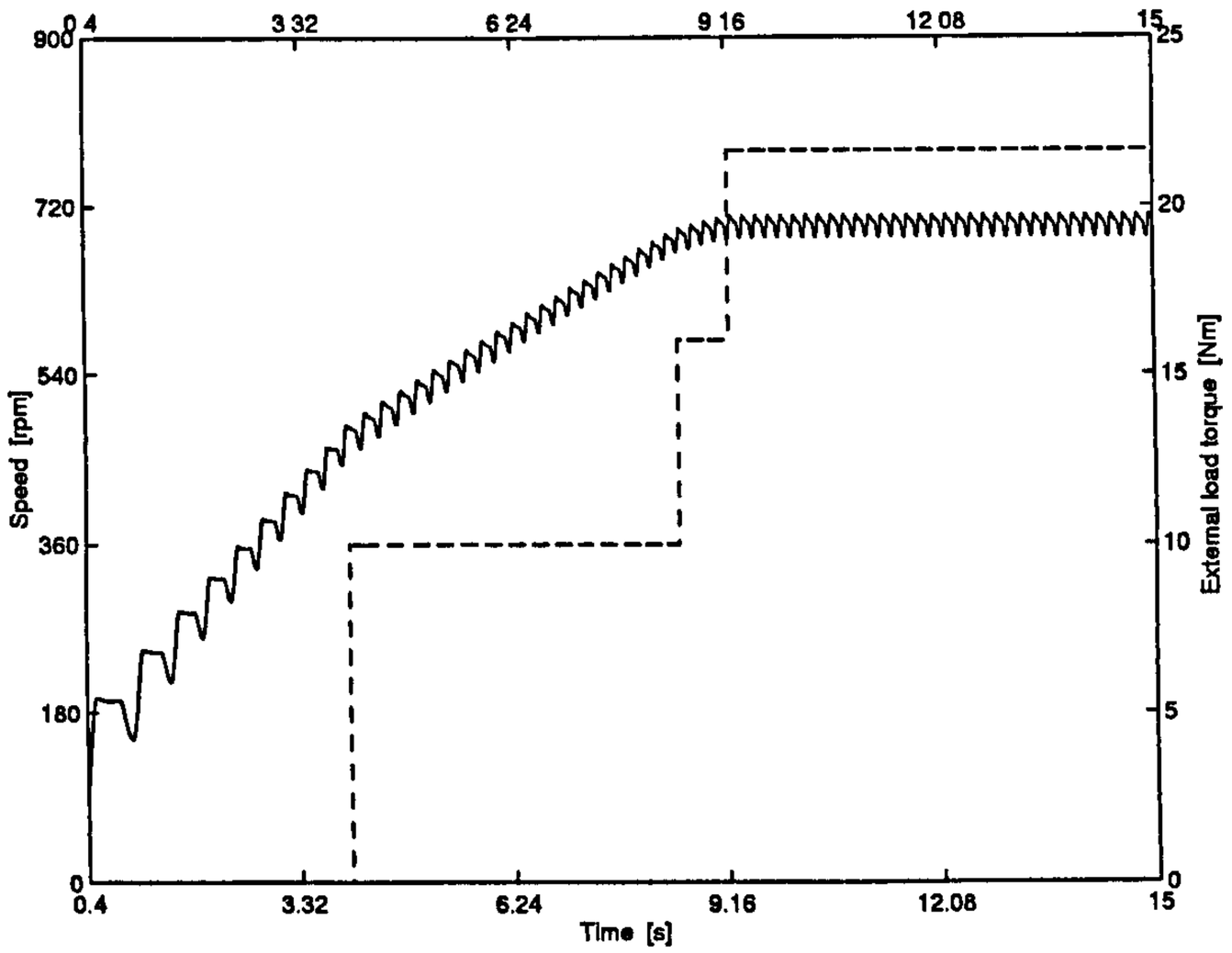

Figure 2.11: Predicted instantaneous speed of Engine B from starting (——) with dynamometer load (- - -)

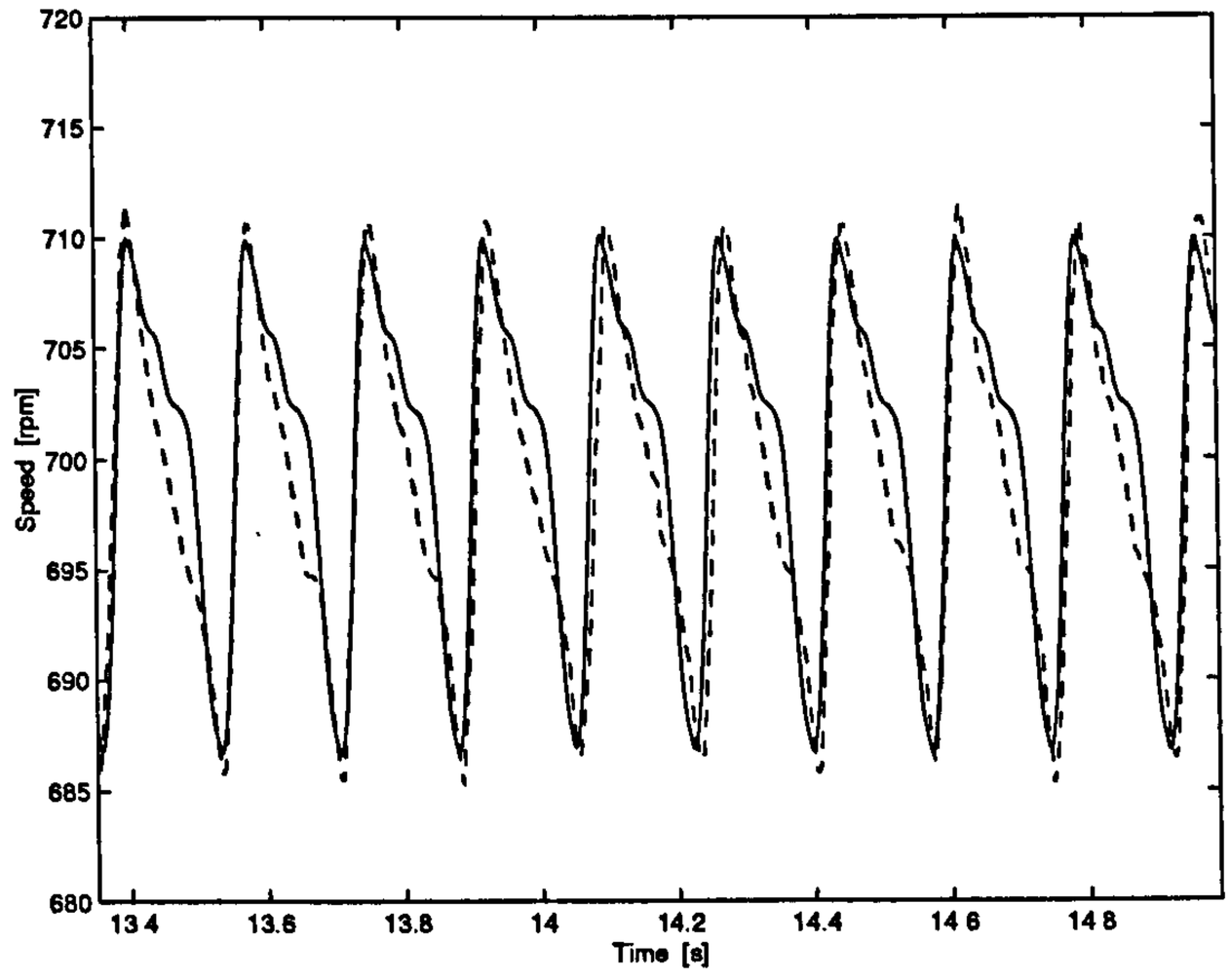

Figure 2.12: Comparison between predicted (——) and measured [Kah98](- - -) steady state fluctuation speed of Engine B at rated torque

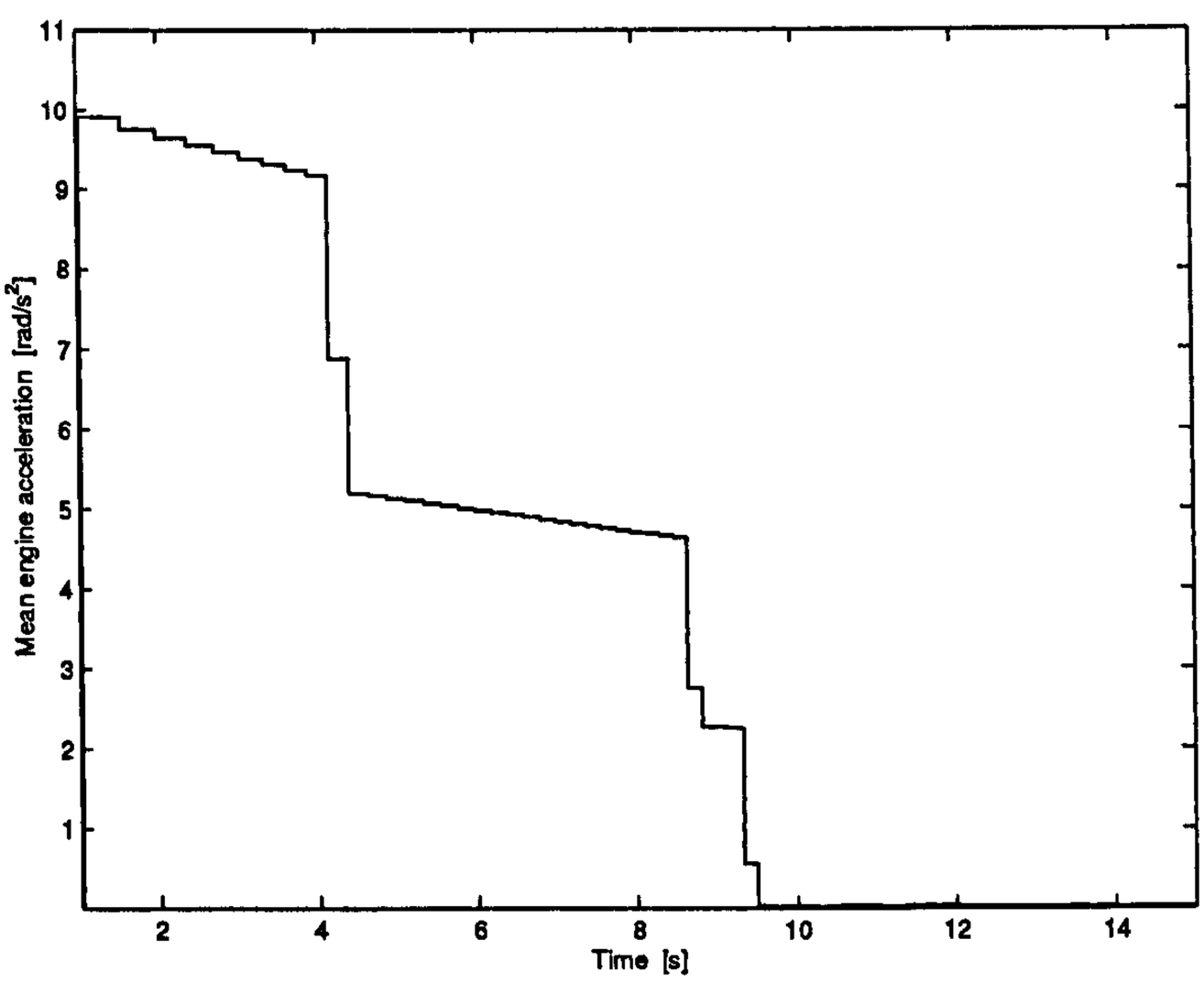

Figure 2.13: Predicted mean acceleration of Engine B from starting until steady state

2.5 Discussion and conclusions

This chapter presents a dynamic model for a single cylinder DI four-stroke Diesel engine which can simulate engine performance under both transient and steady-state operating conditions. The model has been implemented in SIMULINK. Validation has been performed for two types of Diesel engines, one for transient response and the other for steady state. Predicted profiles of the instantaneous engine speeds through the transient and steady state are in good agreement with measurements. Inertia of the dynamometer and the stiffness and damping of the coupling are also included, enabling a variety of engine tests to be carried out. A mean friction model that includes engine friction components for the piston assembly, the crankshaft bearings, the valve train, the pumping losses and the pumps, is used. One reason for the discrepancy between the measured and predicted angular velocity at high engine speeds, as shown in Figure 2.4, may be due to the mean friction model. An instantaneous friction model as opposed to a mean friction model, should improve predictions.

In Chapter 3, work is presented that improves the friction model and so reduces the simulation inaccuracies. Other reasons for errors are inaccuracies in the values of the model parameters which can be tuned to improve the model prediction. Chapter 5 includes work to obtain the engine parameters by means of numerical inversion procedures. In Chapter 4, the inertia variations effects are taken in consideration and a complete engine model is developed by adding the thermodynamic aspects. Since engine events for control and estimation are generally periodic with respect to crank-angle rather than time, also because sensor sampling in engine management systems is generally based on crank angle events, rather than the real-time clock, the model of Chapter 4 is developed in the crank angle domain.

Chapter 3

Instantaneous Friction Components Model

3.1 Introduction

As discussed in Section 2.5, one main source of modelling errors results from limitations in the friction model, especially at high engine speeds during transient response. This chapter extends the friction model to reduce the simulation errors. Since, the engine models must be efficient and accurate, and simulation run-times should not be excessive, the engine friction model should represent the relevant trends but be relatively simple to compute. The components of the engine friction model are mostly based on theoretical considerations, namely Reynolds equation and dynamic analysis. In addition, new equations for the friction components of ring assembly, bearing mixed lubrication and valve train are included. In Chapter 2, a mean simplified friction torque model is assumed, this does not accurately represent the engine trends at high engine speeds during transient response. The model is extended in this chapter to include instantaneous engine friction behaviour, oil viscosity variations and additional detailed effects of engine friction components.

The friction model consists of friction due to the piston assembly, the bearing, the valve train and the auxiliaries. These components are individually computed

and summed to find the overall friction torque. Thus the relative percentage contribution of each of the above components can be evaluated using the proposed model.

The fact that ignition takes place in the combustion chamber does not necessarily mean that the engine will successfully start. Many factors contribute to a successful start and all of them are temperature dependent. One of them, the calculation of engine friction during starting, depends on the oil viscosity. In [SBTM01], examination of the magnitude and variation of the engine friction mean effective pressure under cold start and warm-up is carried out. Investigation of changes in friction mean effective pressure associated with operating conditions, particularly the effect of start temperature and magnitude of friction contributions made by the major component assemblies are presented. The model in this chapter can simulate instantaneous engine friction during cold-start by including the effect of temperature variations on oil viscosity. The results might be used to match the electrical starter to prevailing conditions in order to achieve optimum engine startability.

The developed friction model is incorporated into the two degree of freedom engine dynamic model developed in Chapter 2. The simulations from this model have a 97% accuracy when compared to experimental data.

Although the friction model in this chapter is mostly developed analytically, the relative contribution of each friction component can be determined empirically. Hence a simple procedure for tuning a relative friction component weights is also developed.

The chapter is arranged as follows. In Section 3.2, the friction model is presented. Some simulation results are presented in Section 3.3, and the predicted behaviour compared with some experimental data. In Section 3.4, the friction model tuning is presented. Finally there is a discussion and the main conclusions are drawn. Details of the derivation of the friction model are presented in Appendix B.

3.2 Friction modelling

The main aim of this chapter is to model the friction torque given by the expression $\sum_{k=1}^{6} T_{fk}$. The friction torque plays a dominant role within the engine dynamic equation, and accurate modelling of this component is very important.

3.2.1 Engine friction model

Engine friction can be modelled to give either mean or instantaneous values. Studies providing mean frictional losses over each cycle include, for example, [Ciu92, Ciu93]. There are two important papers on instantaneous engine friction evaluation. The first paper [RH84] determines the total instantaneous frictional torque by measuring the engine speed and the indicated pressure, but does not include the effect of temperature variation on oil viscosity, and the ring assembly friction analysis is not detailed enough to describe the friction behaviour during lubrication modes. The second study [CRD96] presents a frictional model with three components, ring assembly, loaded bearing and auxiliaries, but neglects valve train, piston skirt and camshaft losses leading to a simplified engine friction model.

The aim of this work is to build a comprehensive friction model for Diesel engines. Theoretical studies are employed to derive engine friction components in order to predict the engine behaviour during all of the engine working modes, from start until high engine speed. The derivation of friction torque for piston assembly, bearing, valve train and auxiliaries are outlined below. Details of the derivations are given in Appendix B.

3.2.2 Piston assembly friction torque

The piston-ring assembly may be responsible for 50-75% of the entire engine friction as mentioned in Section 2.2.3.

Ring friction torques

The piston assembly friction is dominated by the ring friction components [FTT81]. It has been observed that the ring assembly lubrication mode is hydrodynamic

except near the top and bottom dead centre positions where the oil film breaks down. The ring assembly friction torques can be found by assuming that the friction force is equal to the product of the normal load between the ring assembly and the liner, and the friction coefficient. Thus the ring assembly friction torque (from (B.18)) is:

$$T_{f1} = r\,|G(\theta_1)| \left\{ \eta \left[\left(1 - \frac{\mathrm{sgn}(\dot{y})\eta}{\eta + G_3(\theta_1)} \right) \left(\sum_{i=1}^{N} \left(\frac{E_i g_c}{7.07 d_r (\frac{d_r}{B_i} - 1)^3} \right) \pi d_r B_i \right. \right. \right.$$
$$\left. \left. + \sum_{i=1}^{N} a_i \,|p_I - p_{atm}|\, \pi d_r B_i \right) + \left(\frac{|p_I - p_{atm}|\, \frac{\pi}{4} d^2 - M G_1(\theta_1) \dot{\theta_1}^2}{\eta + G_3(\theta_1)} \right) \right]$$
$$- \left(\frac{\eta}{\eta + G_3(\theta_1)} \right) \left(\frac{\mu \dot{\theta}_1 r G(\theta_1)}{O_c} \right) dL_s \Big\}. \qquad (3.1)$$

where

$$G_3(\theta_1) = \frac{L \sqrt{1 - \left(\frac{\delta + r \sin(\theta_1 - \phi)}{L} \right)^2}}{(\delta + r\,|\sin(\theta_1 - \phi)|)}. \qquad (3.2)$$

The coefficient of friction for hydrodynamic lubrication, η, is directly proportional to the piston speed and oil viscosity, and inversely proportional to the ring load [Mcg78]. Stribeck diagrams (see Figure 3.1), obtained from experimental results, are widely used for determining the coefficient of friction. For the coefficient of friction with mixed lubrication, the variation can be approximated by a straight line without significant error. This approximation [MP97] is used in this chapter. Thus

$$\eta = \begin{cases} c_1 - (c_1 - z)\,|\sin\theta_1| & \text{for } 1.5\pi \le \theta_1 \le 2.5\pi, \\ z & \text{otherwise,} \end{cases} \qquad (3.3)$$

where c_1 is the mixed friction coefficient for rings and z is the hydrodynamic friction coefficient given by:

$$z = \sqrt{\frac{\mu \dot{\theta}_1 r\,|G(\theta_1)|}{L_r}}, \qquad (3.4)$$

and L_r is the load per unit length given by:

$$L_r = \sum_{i=1}^{N} \left(\frac{E_i g}{7.07 d_r (\frac{d_r}{B_i} - 1)^3} + |p_I - p_{atm}| \right) B_i. \qquad (3.5)$$

Skirt friction torque

In reciprocating internal combustion engines, the piston skirt profile is designed to prevent local contact due to thermal expansion and to reduce friction losses and piston slap, by ensuring that a proper lubricating oil film thickness is maintained for maximum wedge effect and an appropriate piston pin offset.

The piston skirt friction force is derived by applying Newton's law for viscous friction and can be expressed as:

$$F_{f2} = \left(\frac{\mu \dot{\theta}_1 r G(\theta_1)}{O_c} \right) dL_s \tag{3.6}$$

and the piston skirt friction torque is given as:

$$T_{f2} = \left(\frac{\mu \dot{\theta}_1 r G(\theta_1)}{O_c} \right) dL_s r G(\theta_1). \tag{3.7}$$

3.2.3 Bearings friction torque

The main journal bearings are sited at the crank, both ends of the rod and the camshaft. These are analyzed using the Reynolds approximation to the Navier-Stokes equations. The bearings are treated as axisymmetric and two-dimensional to account for their finite length. The bearings generally operate in the hydrodynamic lubrication mode except around top dead centre. By solving the Reynolds equation, the instantaneous friction torque during hydrodynamic lubrication mode (for $0 \leq \theta_1 < 1.9\pi$ and $2.4\pi < \theta_1 \leq 4\pi$) on the journal bearing is given by:

$$T_{f3} = \left[\frac{F_t \epsilon}{2} + \frac{2\pi \mu \dot{\theta}_1 r_b^3 L_b G_4(\theta_1)}{\sqrt{(c_r^2 - \epsilon^2)}} \right], \tag{3.8}$$

where the geometrical function $G_4(\theta_1)$ is given by:

$$G_4(\theta_1) = \left[1 + \frac{\cos\theta_1}{\sqrt{\left(\frac{L}{r}\right)^2 - \sin\theta_1^2}} \right]. \tag{3.9}$$

Due to the abrupt increase of friction torque shortly after the top dead centre, the mode of the lubrication is mixed, and the friction coefficient, η_{bm}, depends on

the properties of the pair of rubbing materials. η_{bm}, has a negative slope in the Stribeck Diagram (see Figure 3.1) [Ros82], and is given by:

$$\eta_{bm} = c_2 \left(\frac{\mu \dot{\theta}_1}{|p_I - p_{atm}|} \right)^{-n}, \tag{3.10}$$

where c_2 is the mixed friction coefficient for bearings and the index number n is taken as $\frac{1}{3}$. Thus the proposed formula to calculate the bearing friction torque around the top dead centre, for $1.9\pi \leq \theta_1 \leq 2.4\pi$, is

$$T_{f4} = \eta_{bm} r_b \left[\left(\frac{\left(\frac{\pi}{4}\right) d^2 \, |p_I - p_{atm}| - r\dot{\theta}_1{}^2 M \left(\cos\theta_1 + \left(\frac{r}{L}\right)\cos 2\theta_1\right)}{G_5(\theta_1)} \right) \times \left|\cos\left(-2\theta_1 + 4.3\pi\right)\right| \right], \tag{3.11}$$

where $G_5(\theta_1)$ is given by

$$G_5(\theta_1) = \sqrt{1 - \left(\frac{\delta + r\sin(\theta_1 - \phi)}{L} \right)^2}. \tag{3.12}$$

and $|\cos(-2\theta_1 + 4.3\pi)|$ is a correction term to take into account the increase of friction torque (as was observed by [MF89]) shortly after top dead centre. The change from hydrodynamic friction to mixed friction is due to the large load transmitted by the crankshaft to the bearing during the combustion period.

3.2.4 Valve train friction torque

The valve train carries high loads over the entire speed range of the engine. Loads acting on the valve train at lower speeds are primarily due to the spring forces, while at higher speeds the inertia forces of the component masses dominate. Valve train friction accounts for the friction in cam/follower, rocker arm/pivot shaft, camshaft bearings, valve/valveguides, and seals. To simplify the analysis, the valve train is considered as a system represented by the cam/follower and is assumed to operate in the boundary lubrication mode.

The valve train friction torque is formulated to depend on the load and the engine speed, and is given by:

$$T_{f5} = \left(\frac{d_i^4 G_v}{8 d_o^3 N_t} \right) V_l N_v \left(1 - c_3 \dot{\theta}_1\right) r \, |G(\theta_1)| \, . \tag{3.13}$$

where c_3 is a speed coefficient.

3.2.5 Auxiliaries and gear torque losses

This component models the friction due to the unloaded journal bearings, water pump, fuel pump, oil pump, generator and gears. A hydrodynamic lubrication mode is assumed, and the friction coefficient is calculated as for Equation (3.4). If the terms which represent the normal load, oil film pressure and the effective radius and length of the auxiliaries shafts are assumed to be unity, then the friction torque for the auxiliaries is formulated as:

$$T_{f6} = \sqrt{\mu \dot{\theta}_1}. \tag{3.14}$$

3.2.6 Viscosity variations with temperature

The variation of temperature and hence oil viscosity is an important factor in the engine friction calculations. The viscosity of oil decreases with increasing temperature. This trend is typical for Newtonian regimes for oils, where the viscosity is independent of the shear rate. Furthermore, the viscosity of oils increases with pressure. At certain times during hydrodynamic lubrication, the loads increase the oil pressure, which in turn increases the viscosity.

The experimental results used for the validation of the model were obtained from engines using SAE 30 oil. The oil viscosity as a function of temperature and pressure for the SAE 30 oil is determined by a nonlinear least-squares method as an exponential function [Bor97], using data from [Fer86], and is given by:

$$\mu = 7.849 \times 10^{-5} \exp\left[\frac{-8.670 \times 10^{-3} T_o^2 - 1.15311 T_o + 1361}{T_o + 133} + \frac{p_o}{105}\right]. \tag{3.15}$$

In this study only the effect of temperature variations are taken into consideration, because oil pressure has only a minor effect on the engine oil viscosity, hence $p_o = p_{atm}$ is used in Equation (3.15).

3.3 Model simulation and validation

In order to validate the behaviour of the engine friction model with experimental results, the developed friction model is incorporated into the two degree of freedom

single cylinder Diesel engine dynamic model in Chapter 2, using Matlab/SIMULINK [SIM97, Mat97]. The geometrical specifications for the engine are shown in Table G.1 in Appendix G. The measured data under warm-up conditions and the geometrical specifications are taken from [FA97] and [Fil98].

There are three empirical coefficients in Equations (3.3), (3.10) and (3.13) whose values need to be assigned. Coefficient c_1 is the empirical coefficient of the friction coefficient for ring assembly with mixed lubrication, its variation can be approximated by a straight line from the Stribeck diagram without significant error. Coefficient c_2 is the empirical coefficient of friction coefficient for the friction of the bearing during mixed lubrication, and depends on the properties of the pair of rubbing materials. The lubrication in the valve train at lower speeds is in the boundary mode and at high speeds in the mixed mode, so the friction is slightly decreased at high speeds. The expression $(1 - c_3\dot{\theta}_1)$ which includes the empirical coefficient c_3 takes into consideration the slight decrease of the valve train friction coefficient with engine speed [Bis65]. The empirical coefficients are shown in Table 3.1.

Mixed friction coefficient for rings	c_1	0.11
Mixed friction coefficient for bearings	c_2	0.002
Speed effect in valve train friction	c_3	0.00127 [s/rad]

Table 3.1: Empirical coefficients

The friction model is given by Equations (3.1) to (3.14), however, the simulations were performed with Equation (3.1) replaced by the following

$$T_{f1} = \eta r \left|G(\theta_1)\right| \left[\sum_{i=1}^{N} \left(\frac{E_i g_c}{7.07 d_r (\frac{d_r}{B_i} - 1)^3}\right) \pi d_r B_i + \sum_{i=1}^{N} a_i \left|p_I - p_{atm}\right| \pi d_r B_i + \left(\frac{\left|p_I - p_{atm}\right| \frac{\pi}{4} d^2 - M G_1(\theta_1) \dot{\theta_1}^2}{\eta + G_3(\theta_1)}\right)\right]. \quad (3.16)$$

The above equation was obtained by making the assumption that the F_ϵ term in Equation (B.13) is negligible. The maximum value of the $\frac{\eta}{\eta + G_3(\theta_1)}$ term in Equation (3.1) that does not appear in Equation (3.16) is less than 1%. Hence the use of

Equation (3.16) does not significantly affect the simulation accuracy. Note that for improved accuracy, Equation (3.1) should be used.

Figures 3.2 and 3.3 show the instantaneous friction torque obtained from the simulation. Note that for this plot and all other plots in this chapter, one crank shaft cycle represents 4π radians, i.e., two revolutions. The lubrication mode of the ring assemblies is considered to be mixed lubrication near top dead centre. The ring assembly friction torques reach the maximum value after top dead centre where the indicated torque is maximum and its value is approximately equal to twice the ring friction torque at the beginning of the combustion. The lubrication mode of the skirt is in general hydrodynamic and its friction torque is high in the mid-region of the stroke where the piston speed is maximum. The bearing lubrication mode is hydrodynamic except at the points where the indicated pressure is maximum, when there is mixed lubrication and the friction torque is increased substantially; its value is approximately five times the hydrodynamic lubrication friction torque value. The valve train friction torque increases during the intake and exhaust strokes due to the spring stiffness forces being increased.

The simulation simulation speed response is shown in Figure 3.4 and it is seen that there is very good agreement between predicted and experimental engine speed. The maximum relative error is less than 3%.

Figure 3.5 shows the crankshaft angular velocity when the simulation is run without friction and it is seen that the engine speed is increased substantially. Thus it is crucially important to take into consideration the friction model.

Figure 3.6 shows the angular velocity for different oil temperatures. Initially, the engine is assumed to be cranking at a speed of about 350 rpm with an input torque that represents the starter motor torque. Next, the simulation program is switched to the firing indicted torque and this explains why the engine speed decreases at the beginning. At $-5°C$, the angular velocity shows a slow increase in the engine speed up to cycle six. The maximum angular velocity reached at $-5°C$ was 820 rpm. For $0°C$, there is a gradual increase in the angular velocity beginning at cycle four, and reaching a maximum of 950 rpm. At $10°C$, a smooth

and fast increase in the angular velocity begins at cycle two, reaching a maximum speed of 1180 rpm. This trend is due to the effect of start temperature on the oil viscosity.

3.3.1 Comparison between friction models

The aim of this section is to compare between the friction models of the engine components. Figure 3.7 shows the average values of the engine friction components over each cycle for five cycles during transient response, the results obtained by using the instantaneous friction model (Equations 3.1-3.14). The individual contributions to the total friction torque are shown in Table 3.2

Friction model	*Ring* | *Skirt*	*Bearing*	*Valves*	*Aux.*
Instantaneous, Equations (3.1-3.14)	40.3% | 15.7%	29.1%	8.8%	6.1%
Mean, Equations (2.13-2.25)	52%	18%	22%[1]	8%

Table 3.2: Individual contribution of the friction components

Figure 3.8 shows the values of the mean engine friction components model presented in Chapter 2 (Equations (2.13)-(2.25)), for five cycles during transient response. The individual contributions to the total friction torque are shown in Table 3.2. The friction components of pumping, valve train and pump friction torque correlations in the mean friction model are obtained by means of motoring (without firing) friction measurements. This type of testing involves rotating the engine with a motoring dynamometer and recording the torque required to maintain a constant speed. By removing components from the engine it is possible to determine their contribution to friction, such an approach cannot capture the friction trends during firing.

For the purpose of comparison between different models of the auxiliaries friction, the following model from [CRD96] is considered:

$$T_{f6} = 2.02 L_{eq} R_{eq}^2 \mu \dot{\theta}_1. \tag{3.17}$$

Here, the models represented by Equation (2.25), (3.14) and (3.17): are named

[1] Combined with the pumping losses torque.

Model I, Model II and Model III respectively. Model I is obtained from motoring data and dimensional analysis which can give reasonable results in the range where the data have been taken to correlate the losses. Models II and III are analytically based using the hydrodynamic lubrication assumption and Newton's viscous law respectively. Table 3.3 shows the mean friction of the auxiliaries over all the engine speed range. Figure 3.9 shows the auxiliaries friction component response from three models. It shows that the Model I and Model III responses are quite close up to cycle six, then Model II and Model III response become closer as the engine speed increases. The individual relative error with respect to the mean value are also shown in Table 3.3 and the deviation between the models prediction is not too high.

	Mean friction	*Relative error*
Model I (Equation 2.25)	1.85 Nm	29%
Model II (Equation 3.14)	1.33 Nm	-7.2%
Model III (Equation 3.17)	1.12 Nm	-21.8%

Table 3.3: Mean friction of auxiliaries

The mechanical friction in Diesel engines can contribute 15% from overall engine losses [PF86, TC99] and the auxiliaries about 10% from the mechanical friction, i.e, 1.5% of the overall engine losses. This is evidence that the auxiliaries losses play a minor effect and a simplified model can be used with confidence.

3.4 Friction model tuning

The main aim of this work is to predict the Diesel engine friction components analytically with sufficient accuracy in order to use the model for control and estimation. For further improved prediction of crankshaft speed, the friction term is modified to include six weighting coefficients, $\alpha_1, \ldots, \alpha_6$,

$$T_I - \sum_{k=1}^{6} \alpha_k T_{fk} - T_r = J_1(\theta_1)\ddot{\theta}_1 + T_S + T_D. \tag{3.18}$$

These coefficients are included to account for parameter and modelling un-

certainties, and their values can be estimated using experimental data of cylinder pressure and instantaneous crankshaft angular speed. Based on the numerical procedure (algorithm) described in Appendix C, weighting coefficients which minimize the difference between the measured and predicted speeds are determined, the values are shown in Table 3.4.

Rings assembly	α_1	0.9895
Piston skirt	α_2	0.9877
Bearings hydrodynamic	α_3	0.9550
Bearing mixed	α_4	0.8320
Valve train	α_5	0.9500
Auxiliaries	α_6	0.9100

Table 3.4: Weighting coefficients of friction correlations

There is no guarantee of convergence of the algorithm, but for the example presented in this chapter, it always converged. From Table 3.4, the values of the weighting coefficients are close to one and it is noted that values one give the results of the analytical model.

Figure 3.10 shows the predicted and measured fluctuation of the crankshaft instantaneous angular velocity for one cycle during low idle speed. The predicted and measured values are in phase. The predicted value is slightly higher during intake stroke and there is excellent agreement during the other strokes. The figure also includes the predicted velocity with the weighting coefficients included, and it can be seen that this is closer to the measured speed.

Figure 3.11 shows the predicted and measured instantaneous engine speeds during transient response from low idle speed to high engine speed with the weighting coefficients included, there is very little difference between them and the curves are almost co-incident. Figure 3.12 illustrates the percentage error between the measured and predicted speeds for Figures 3.11 and 3.4. Note the beating behaviour which shows the small difference between the frequencies of the predicted and measured speeds.

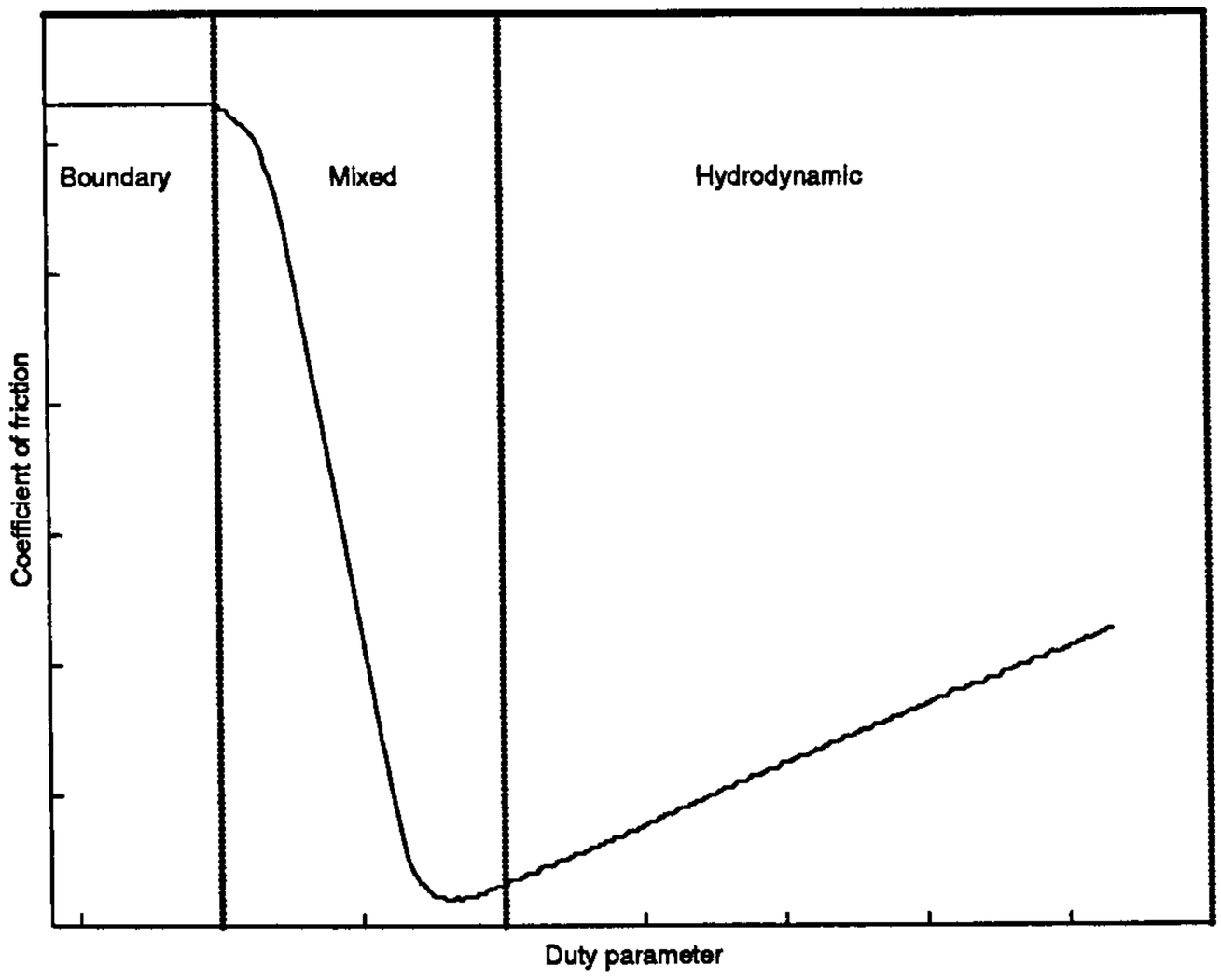

Figure 3.1: Stribeck diagram showing regimes of lubrication [Ros82]

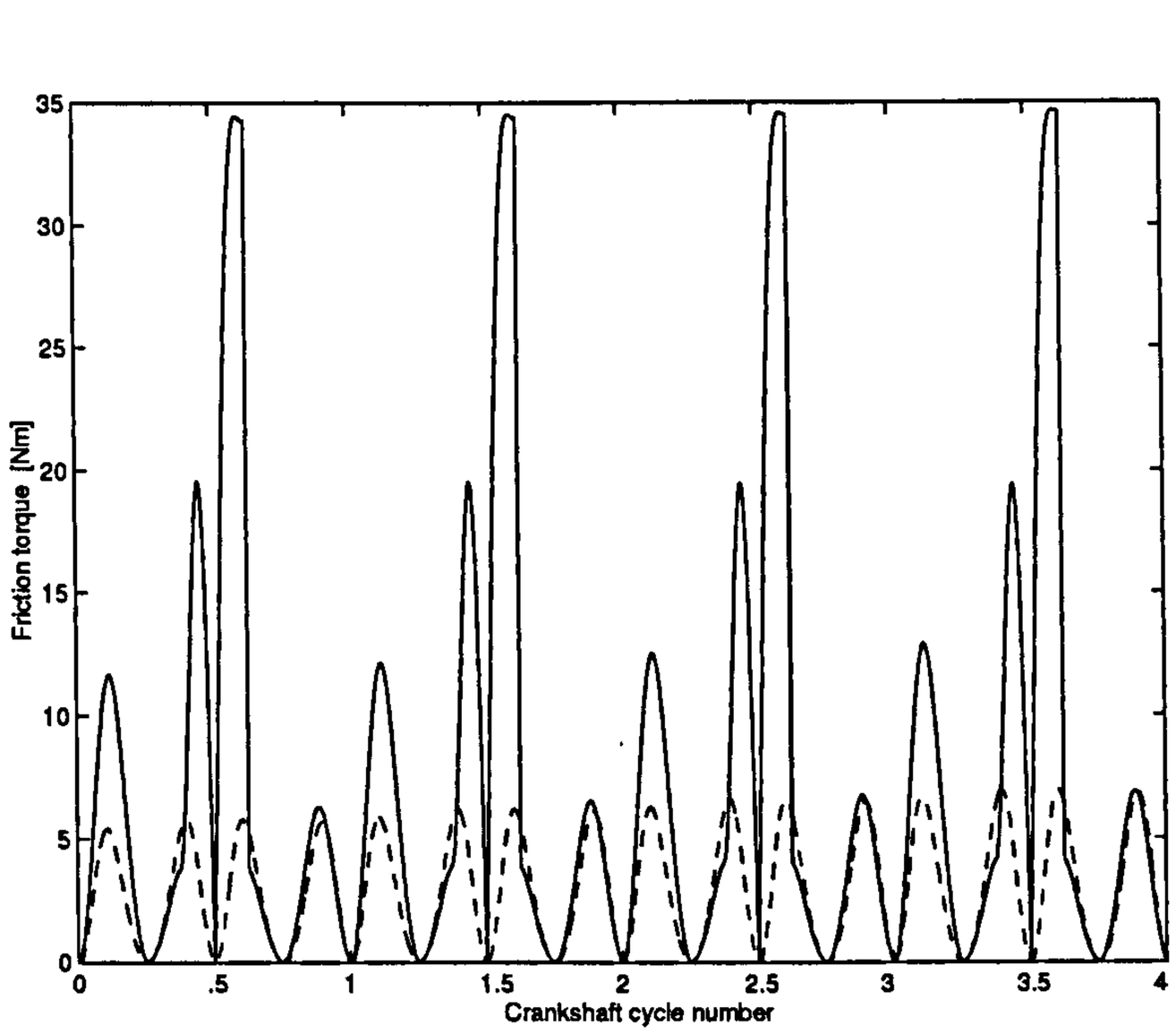

Figure 3.2: Predicted instantaneous friction torque during transient response for ring assembly (——) and skirt (- - -){one crankshaft cycle= 4π }

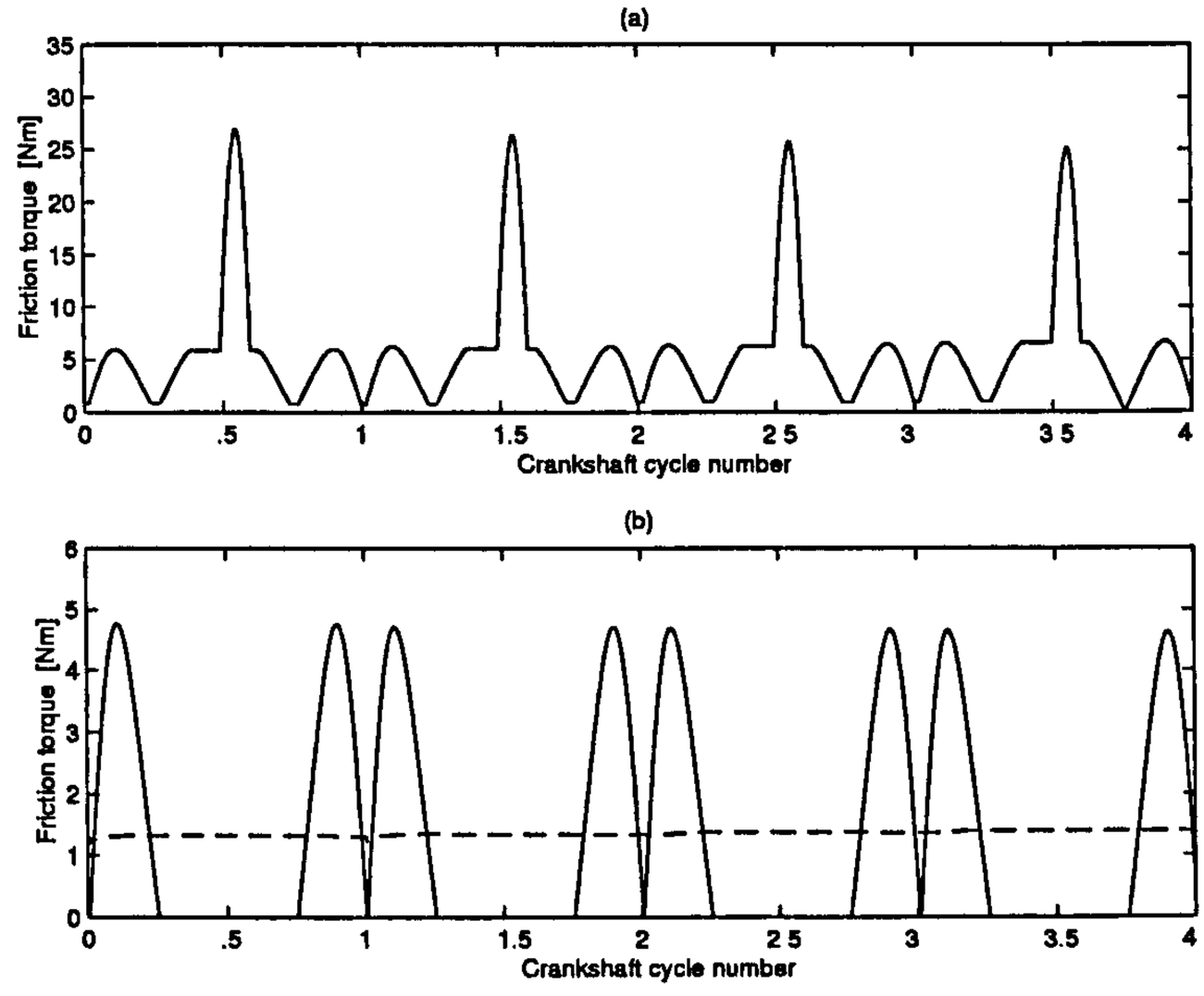

Figure 3.3: Predicted instantaneous friction torque during transient response for:(a) bearings(——), (b) valve train (——), and auxiliaries (- - -) {one crankshaft cycle= 4π }

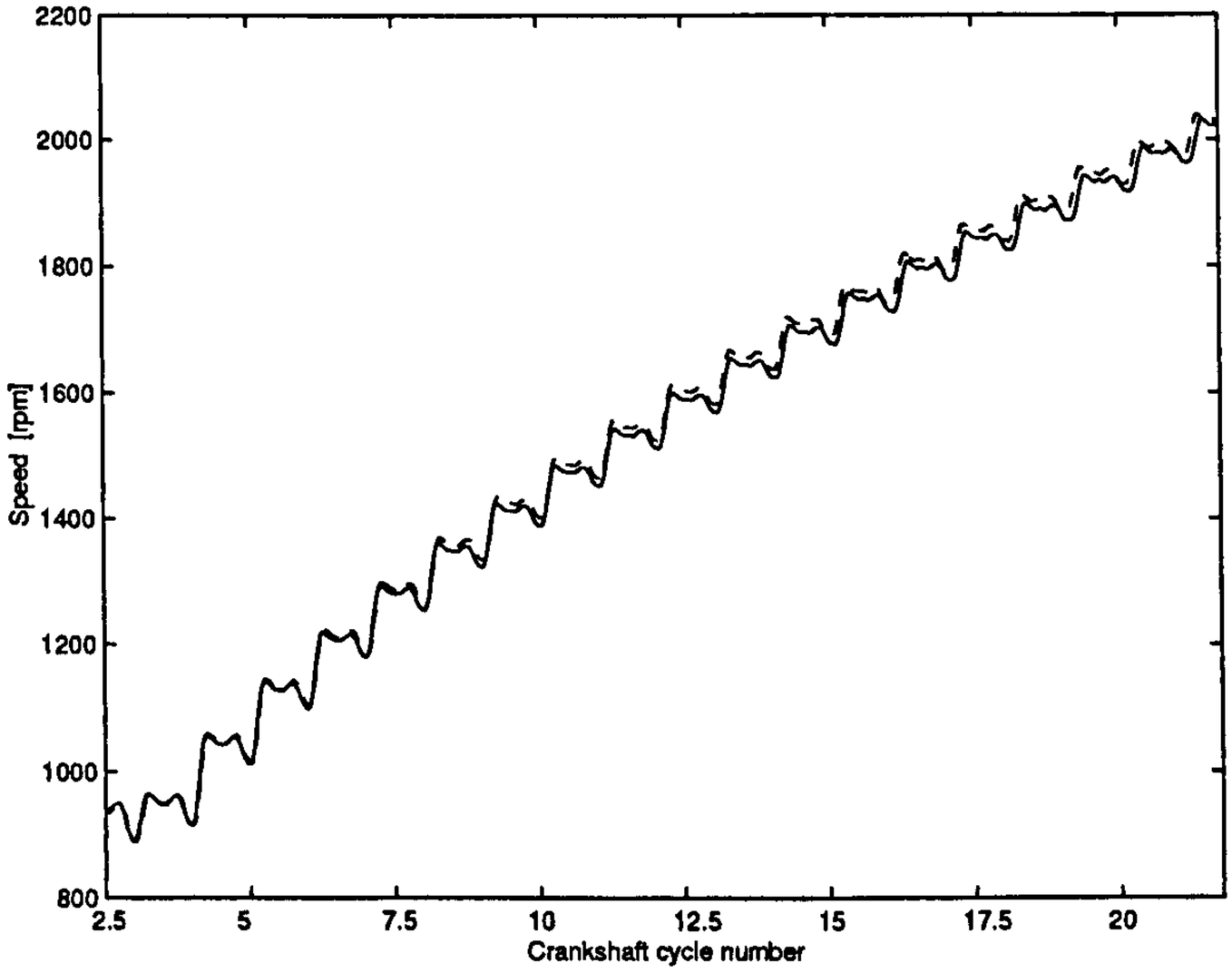

Figure 3.4: Comparison between the predicted (——) and measured (- - -) instantaneous speed of the engine during transient response [FA97] {one crankshaft cycle= 4π }

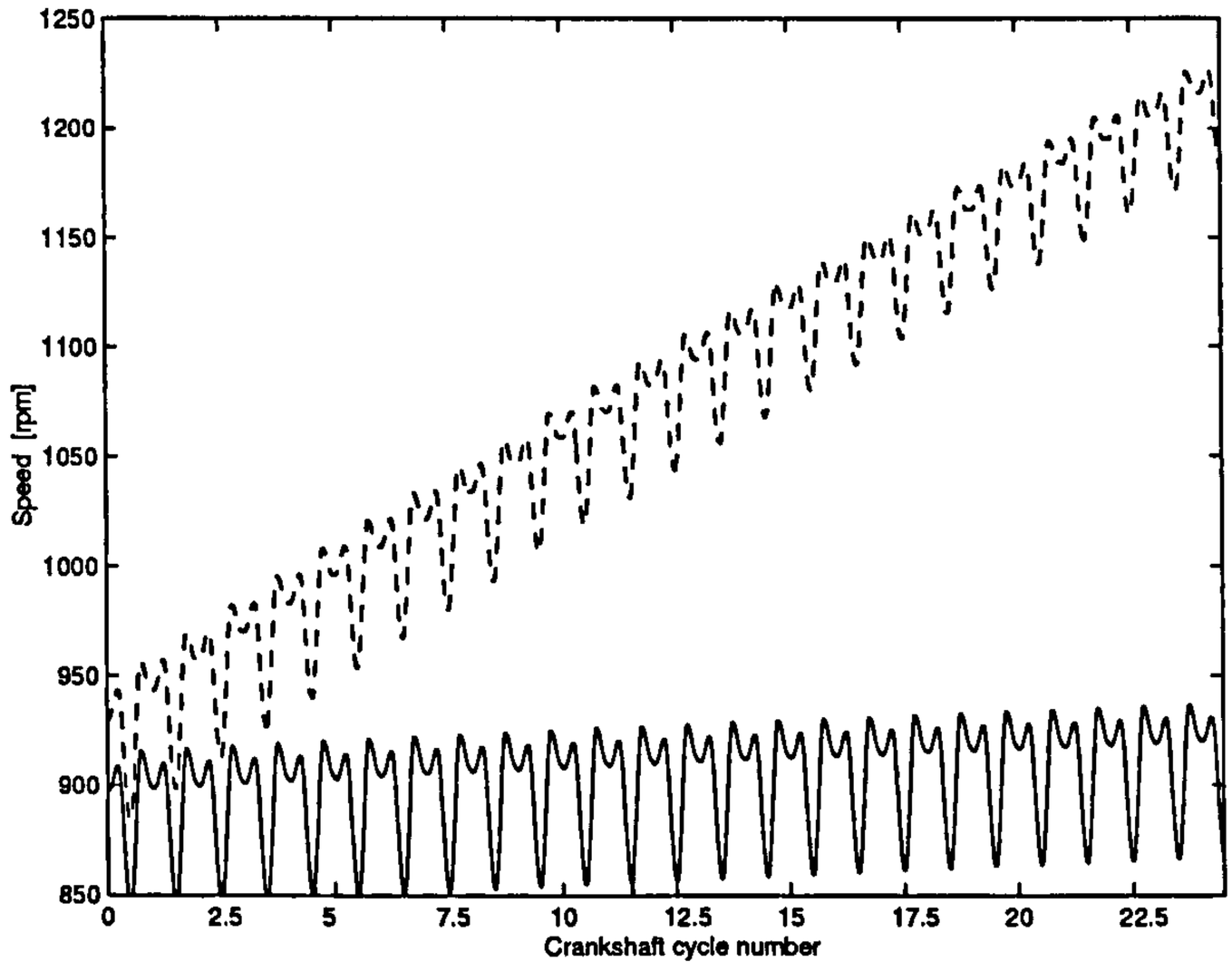

Figure 3.5: Predicted Instantaneous crankshaft speed, with friction (——) and without friction (- - -){one crankshaft cycle= 4π }

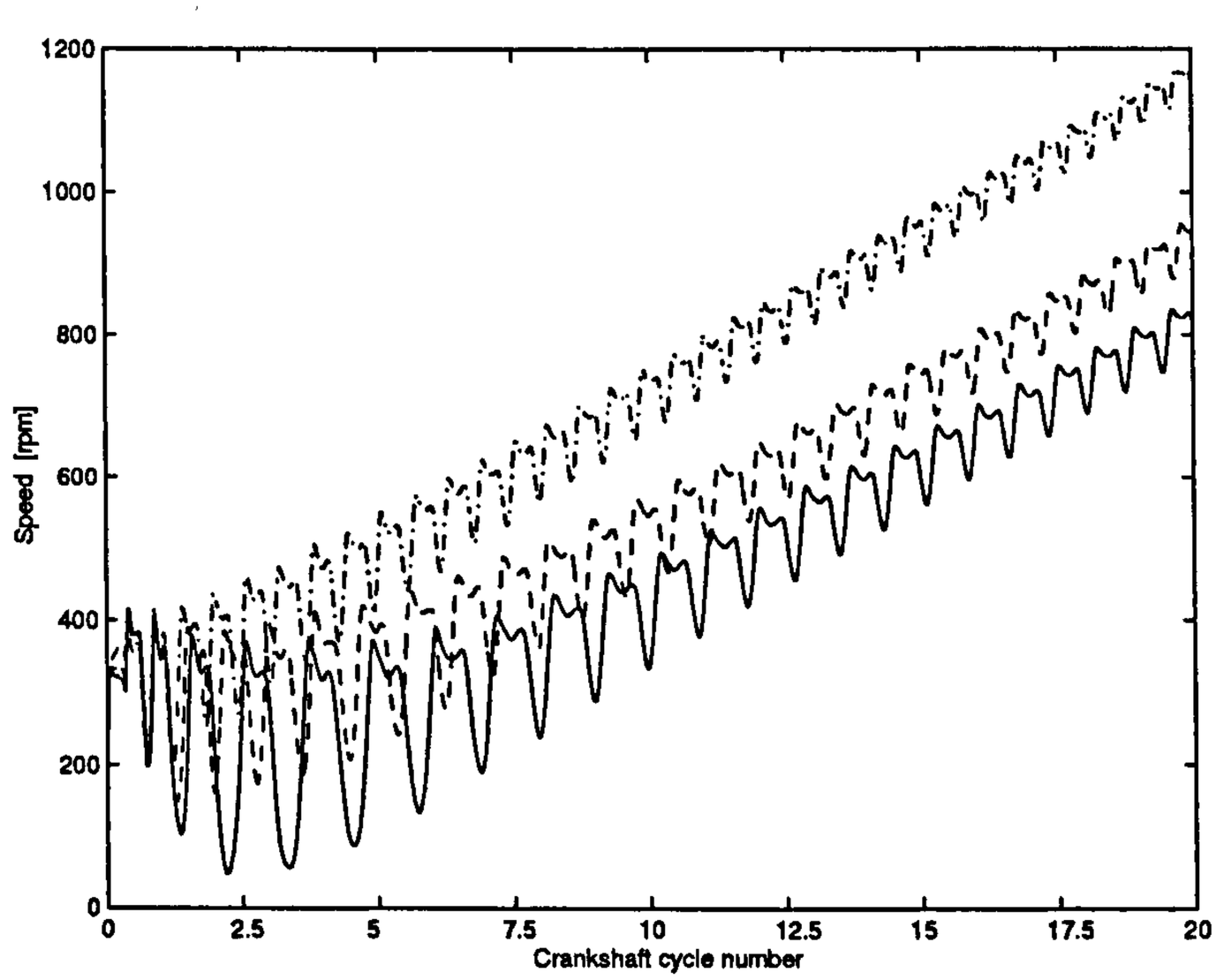

Figure 3.6: Predicted instantaneous crankshaft speed at cold-start, −5°C oil temperature (——), 0°C oil temperature (- - -) and 10°C oil temperature (- · - ·){one crankshaft cycle= 4π }

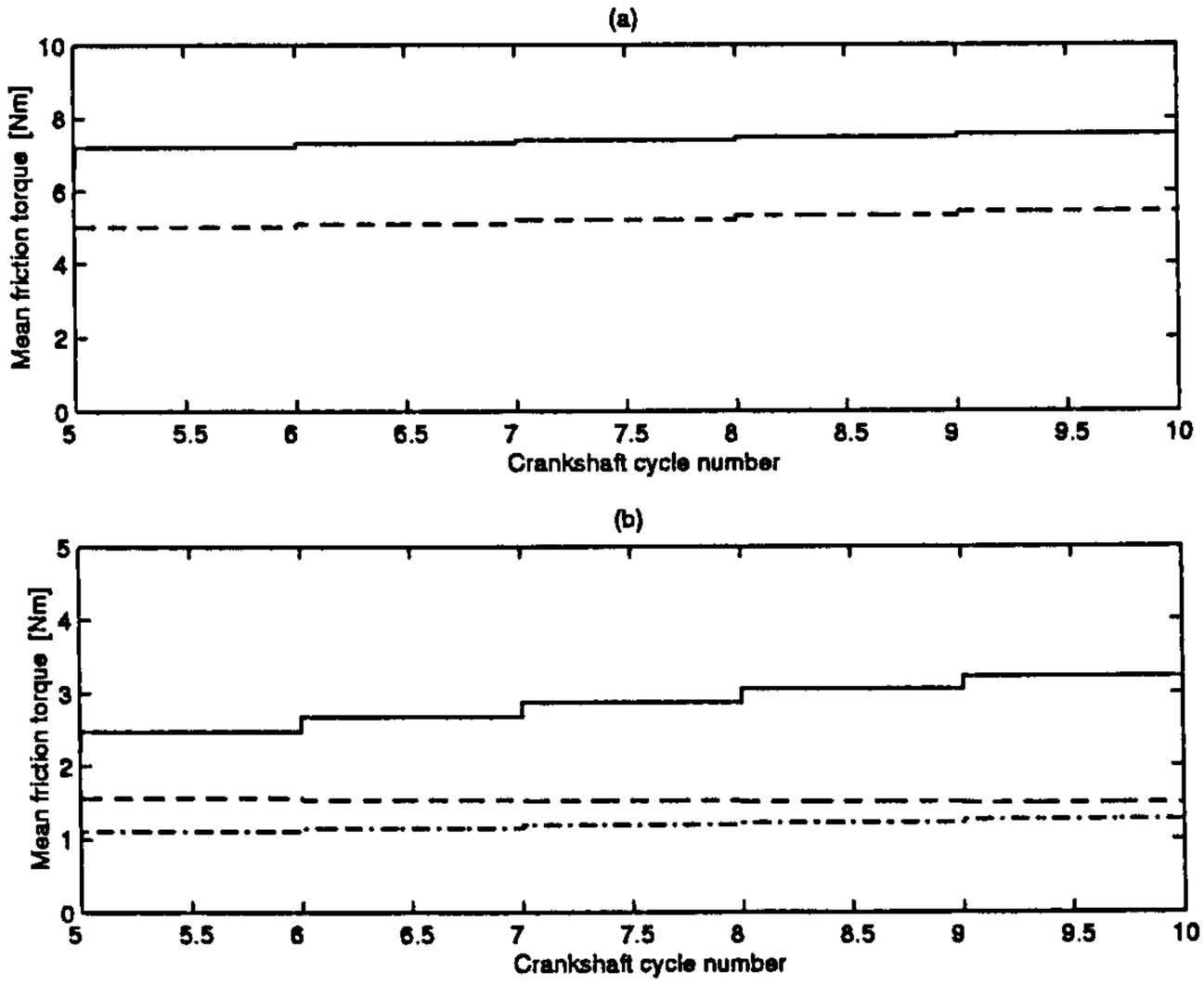

Figure 3.7: Predicted mean friction torque for every cycle (Equations 3.1-3.14):(a) rings(——) and bearings (- - -), (b) skirt (——), valve train (- - -) and auxiliaries (- · - ·){one crankshaft cycle= 4π }

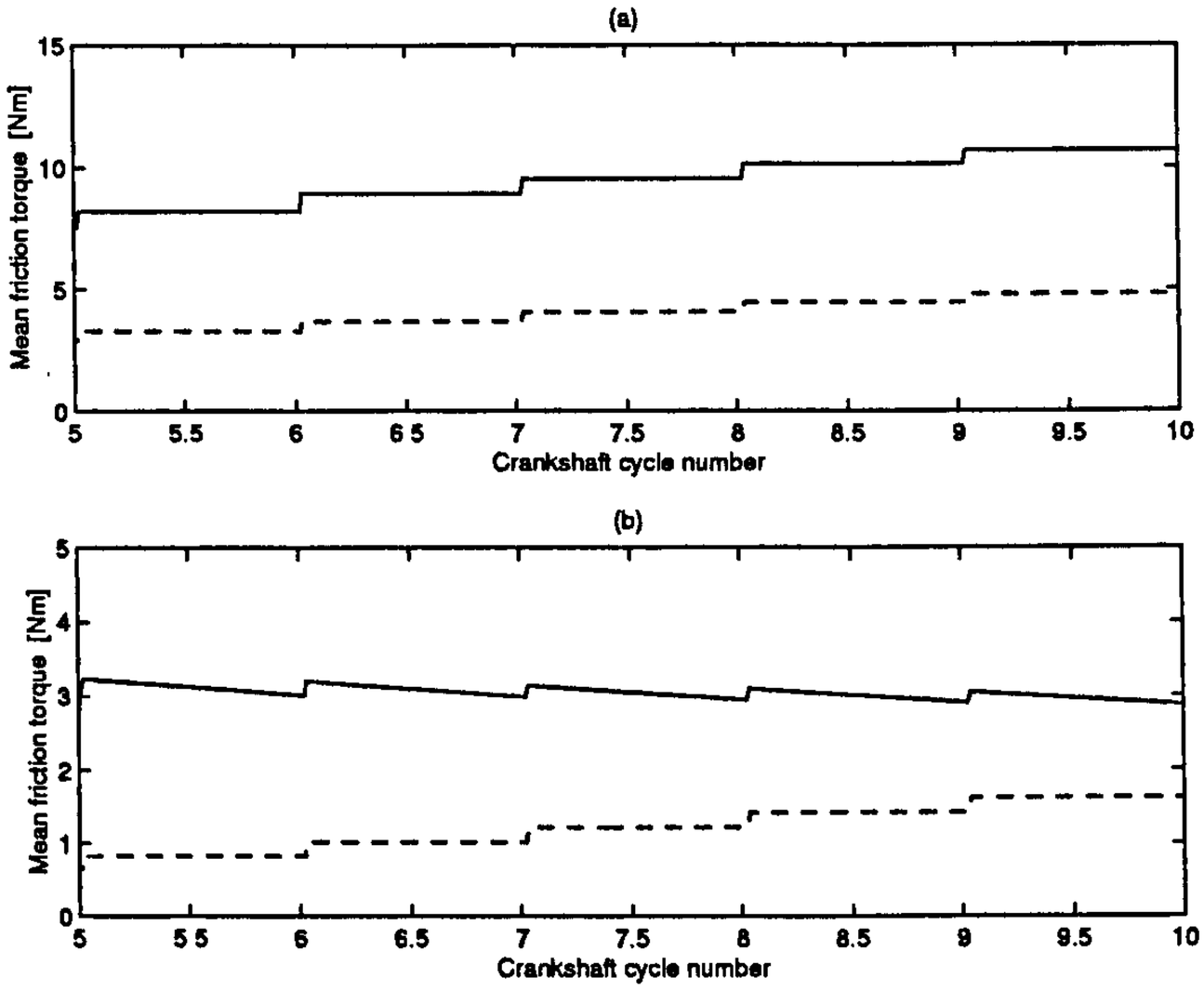

Figure 3.8: Predicted mean friction torque for every cycle (Equations 2.13-2.25):(a) piston assembly (——) and pumping & valve train (- - -), (b) bearings (——)and auxiliaries (- - -) {one crankshaft cycle= 4π }

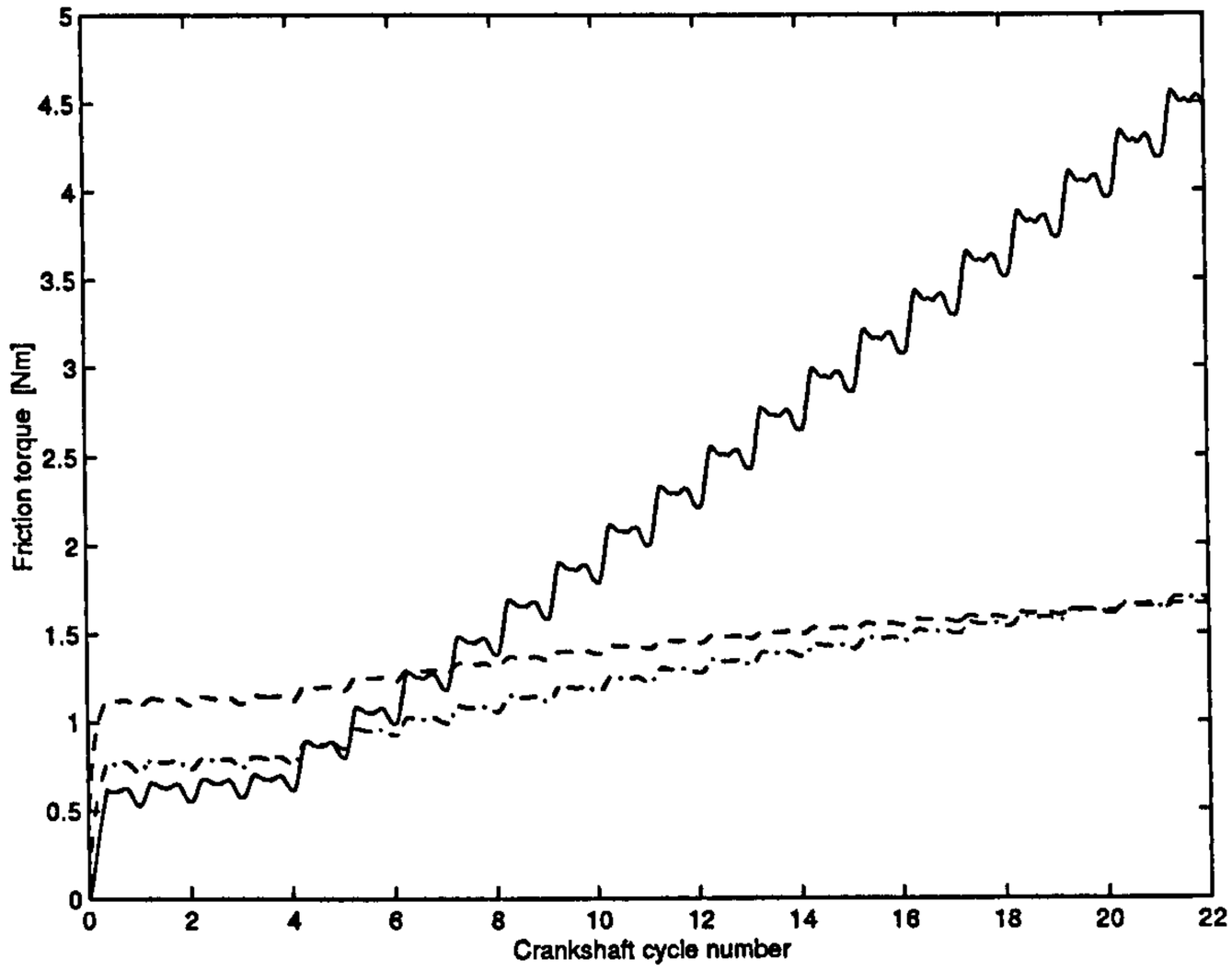

Figure 3.9: Predicted friction torque for: pump (Equation 2.25) (——), auxiliaries (Equation 3.14) (- - -) and auxiliaries (Equation 3.17) (-·-·-) {one crankshaft cycle= 4π }

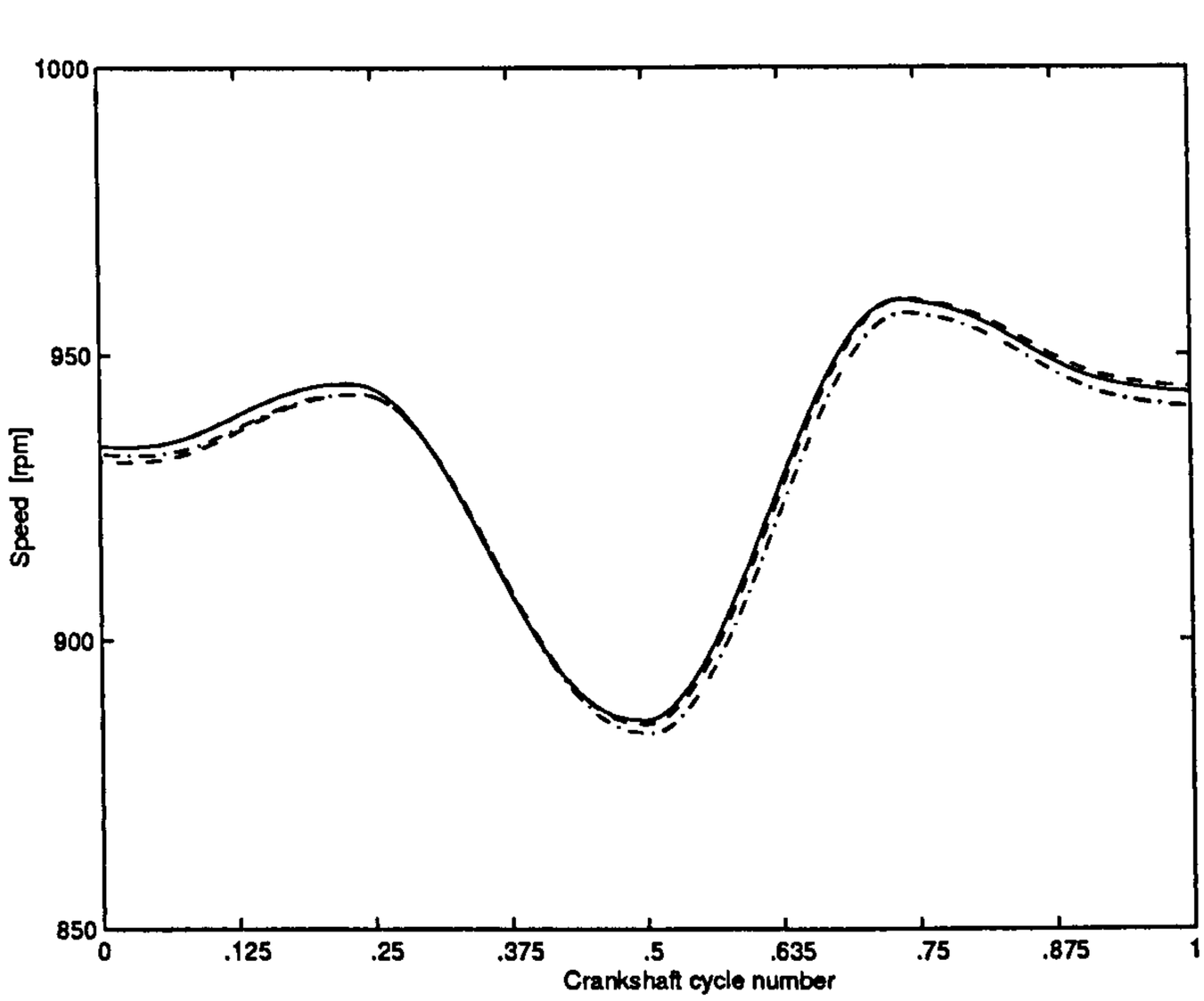

Figure 3.10: Comparison between the predicted (- · - ·), predicted with weighting coefficients (——) and measured (- - -) instantaneous speed cycle of the engine during low idle speed [FA97] {one crankshaft cycle= 4π }

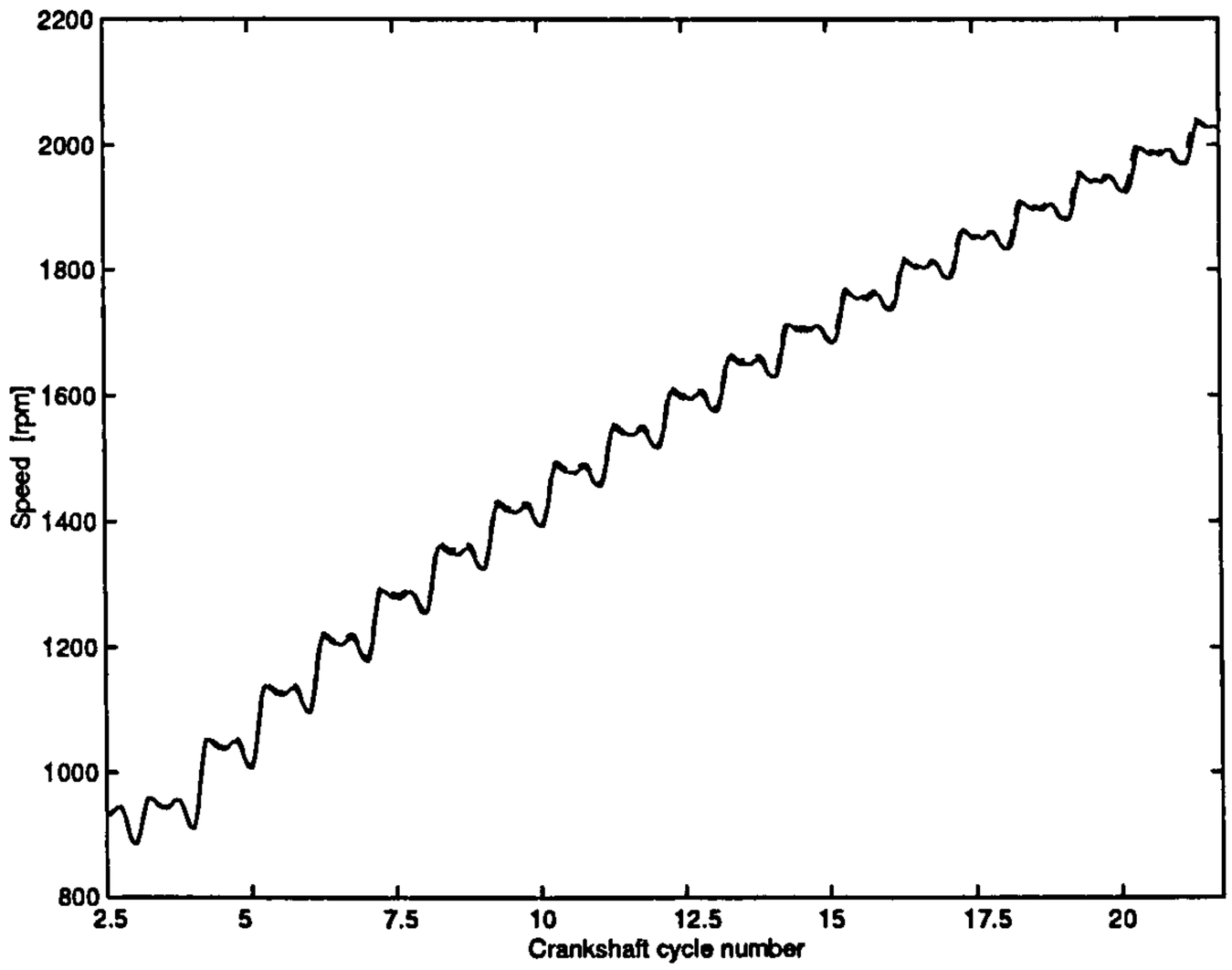

Figure 3.11: Comparison between the predicted with weighting coefficients (——) and measured (- - -) instantaneous speed of the engine during transient response [FA97] {one crankshaft cycle= 4π }

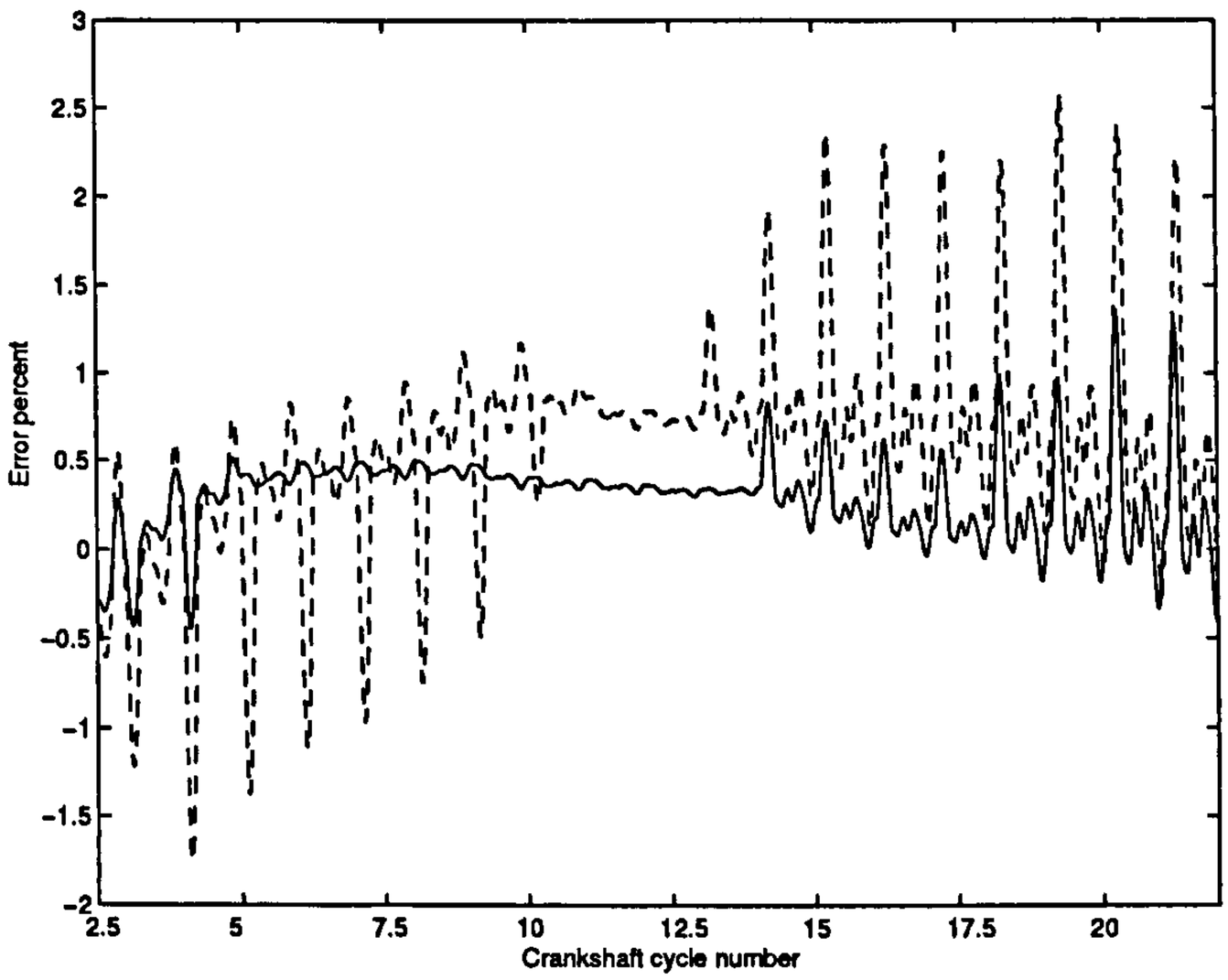

Figure 3.12: Relative percentage error between measured and predicted speed, for Figure 3.11 (——) and Figure 3.4 (- - -) {one crankshaft cycle= 4π }

3.5 Discussion and conclusions

This chapter presents a comprehensive friction model for a single cylinder Diesel engine. The engine friction model is simple enough to be computationally efficient, but complete enough to capture the relevant trends, so it can be meaningfully incorporated into overall engine control models. New equations for the friction of the ring assembly, bearings and valve train are presented. The friction model can simulate instantaneous engine friction behaviour under transient and cold-start operating conditions. The model describes engine friction in term of the following components: (a) rings assembly, (b) skirt, (c) crankshaft, connecting rod and camshaft bearings, (d) valve train and (e) auxiliaries. The friction torque components are derived by theoretical analysis.

There is excellent agreement between the measured data and the predicted results for crankshaft instantaneous angular velocity and the simulations follow the speed fluctuation profile well for low idle speeds and during transient response (from low idle speed to high engine speed without load). The model also simulates temperature-viscosity changes. The simulation results from Figure 3.6 show the engine startability is improved when the oil temperature is increased. The model predictions fall within 3% of the experimental data. To improve the model, weights for the friction components are tuned by numerical optimization using experimental data. After tuning, there is better agreement between the model predictions and experimental data of crankshaft speed.

Chapter 4

Engine Model Including Dynamic and Thermodynamic Effects

4.1 Introduction

To complete the engine model, so that it may be used for estimation and control designs, the thermodynamic aspects that describe the relationship between the fuelling and the indicated pressure should be included. In this chapter, a thermodynamic model is developed and combined with the dynamic model of Chapter 2 and instantaneous friction model Chapter 3 to give an over-all engine model.

For linear engine models, [HF71, FG74, FW76] used identification schemes to obtain discrete engine transfer function utilizing Pseudo Random Binary Sequences as the plant input. Local linearised continuous models [WTW77, KP99] which are derived from frequency domain identification methods are also available. These approaches can only be approximately represent the engine transient response.

A number of different models have been developed for the purpose of Diesel engine control and estimation. In [JKS+91], a mean value model is used. The mean value model assumes average values of pressure, temperature, and mass flow in the submodels. Steady state or transient performance data can be used to find parameters constants in submodel equations. This type of model can only predict average behaviour of engines and cyclic variations are not considered. Diesel en-

gine models for an electronic control simulator were developed in [Wat84, GRH89]. The in-cylinder combustion process was included by using a single zone model, and a filling and emptying modelling technique. In [Wat84], the compromise between accuracy and computer time is discussed. These models do not predict in-cycle crankshaft angular speed variations. In [KM95], hybrids of two models, a mean torque production model and a simplified cylinder-by-cylinder model, are investigated in order to provide control engineers with tools for developing control and diagnostic algorithms.

Nonlinear engine control and diagnostics have aroused great interest in an effort to enhance dynamic engine performance. Recently, non-linear transient simulations of the Diesel engine in order to predict engine torques and speeds have been carried out in both [FA97] and [LCH97]. Engine control schemes generally operate on engine events which are periodic in the crank-angle domain, rather than on a real-time clock. Hence, for the purposes of model-based control and fault-diagnostic schemes, it is preferable that the engine state variables are based in the crank-angle domain rather than the time domain. Also, since events associated with crankshaft angle can take place in between the time steps, there results a discrepancy between actual crankshaft event occurrence and the discrete-time-detection of the crankshaft by time-step simulated system. In both [FA97] and [LCH97], the simulations are performed in the time domain. Additionally, inertia variations are not included in either model. Furthermore, the instantaneous friction components model included in [LCH97] does not take into consideration the viscosity variation with temperature, and the empirical coefficients of the friction components have to be calibrated for each type of engine.

In this chapter a combined dynamic, instantaneous friction and thermodynamic engine model is developed in the crank angle domain and used to predict the in-cycle variations of the engine states. Engine events for control and estimation are generally periodic with respect to crank-angle rather than time. Also, because sensor sampling in engine management systems is generally based on crank angle events, rather than time, an engine model totally based in the crank-angle

domain is developed. The proposed model takes into consideration the inertia variations of the crankshaft assembly. The model treats the cylinder strokes and the manifolds as thermodynamic control volumes by using the filling and emptying method, solving energy and mass conservation equations with submodels for combustion and heat transfer. The model has been implemented in Matlab/SIMULINK [Mat97, SIM97] and in-cycle calculations are performed at each sampling instance.

In Section 4.2 the engine dynamic model of Chapter 2 is improved by computing the inertia variations of the crankshaft assembly and transforming to the crank angle domain. In Section 4.3 cylinder volume and area are presented. The thermodynamic model presented in Section 4.4 is based on the filling and emptying method. Three thermodynamic control volumes are considered; the inlet manifold, the cylinder and the exhaust manifold. In Section 4.5 the implementation of the combined model is described, followed by some simulation results to show the model behaviour and validation. Model sensitivity is presented in Section 4.6. Finally, there is a discussion and some conclusions are drawn.

4.2 Engine dynamic model

4.2.1 Inertia variations

Reciprocating mechanisms have variable inertia due to the change of geometry through a crank revolution. The piston and connecting rod masses change their position relative to the crankshaft axis and hence change the effective inertia about this axis. The same path is followed by these parts during each revolution of the crankshaft and thus the inertia variation is smooth and periodic. A variable inertia (with respect to the crankshaft rotational axis) as a function of the crankshaft position is used. For a given crank-angle, the inertia with respect to the centre line of the crankshaft is defined by considering the equivalent inertia of the piston, connecting rod, and crankshaft assembly [Rao90, LS99, DHS99, HS94]. In this

study the piston pin offset is taken into consideration during the analysis of the variable inertia.

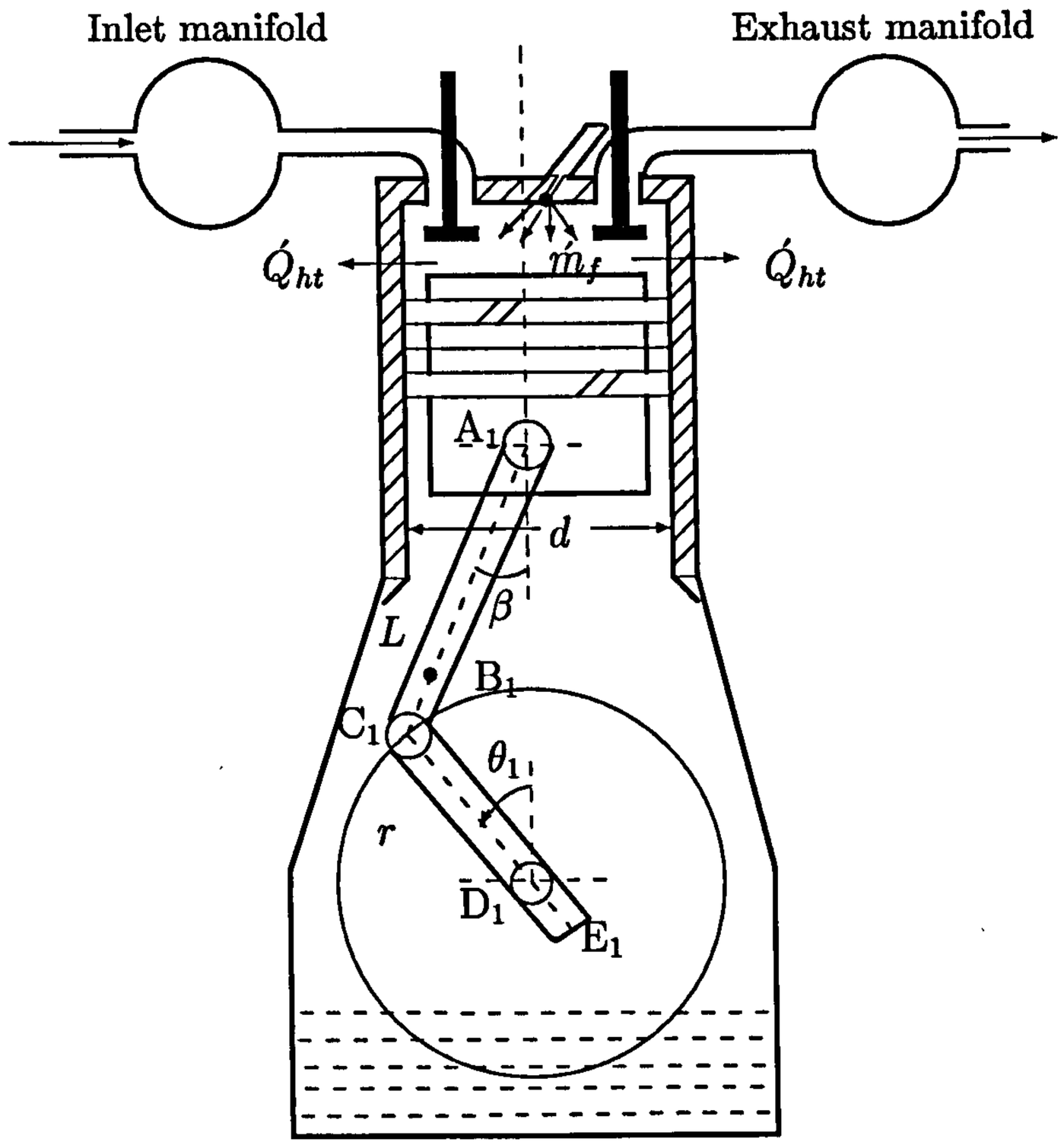

Figure 4.1: Single-cylinder Diesel engine

The crank-angle varying inertia of an engine crankshaft assembly is derived in Appendix D and is given by:

$$\begin{aligned} J_1(\theta_1) &= J_c + m_c(Fr)^2 + J_R\left[\left(\frac{r}{L}\right)^2 \frac{1}{\lambda(\theta_1)}\cos^2(\theta_1-\phi)\right] \\ &+ m_p r^2\left(\sqrt{\frac{1-\lambda(\theta_1)}{\lambda(\theta_1)}}\cos(\theta_1-\phi)+\sin(\theta_1-\phi)\right)^2 \\ &+ m_R r^2(1-\hbar)^2\cos^2(\theta_1-\phi) \\ &+ m_R r^2\left(\hbar\sqrt{\frac{1-\lambda(\theta_1)}{\lambda(\theta_1)}}\cos(\theta_1-\phi)+\sin(\theta_1-\phi)\right)^2 \end{aligned} \tag{4.1}$$

and

$$\begin{aligned}\frac{\partial J_1(\theta_1)}{\partial \theta_1} &= 2J_R\Bigg[\left(\frac{r}{L}\right)^3 \frac{\sqrt{1-\lambda(\theta_1)}}{\lambda(\theta_1)^2}\cos^3(\theta_1-\phi) - \left(\frac{r}{L}\right)^2 \frac{1}{\lambda(\theta_1)}\cos(\theta_1-\phi) \\ &\quad \times \sin(\theta_1-\phi)\Bigg] - 2m_R(1-\hbar)^2 r^2 \cos(\theta_1-\phi)\sin(\theta_1-\phi) \\ &\quad -m_R r^2\left(\hbar\sqrt{\frac{1-\lambda(\theta_1)}{\lambda(\theta_1)}}\cos(\theta_1-\phi) - \sin(\theta_1-\phi)\right) \\ &\quad \Bigg[-\left(\frac{r\hbar}{L\sqrt{\lambda(\theta_1)^3}}\right)\cos^2(\theta_1-\phi) - \cos(\theta_1-\phi) + \hbar\sqrt{\frac{1-\lambda(\theta_1)}{\lambda(\theta_1)}} \\ &\quad \times \sin(\theta_1-\phi)\Bigg] - m_p r^2\left(\sqrt{\frac{1-\lambda(\theta_1)}{\lambda(\theta_1)}}\cos(\theta_1-\phi) + \sin(\theta_1-\phi)\right) \\ &\quad \Bigg[\left(\frac{r}{L\sqrt{\lambda(\theta_1)^3}}\right)\cos^2(\theta_1-\phi) - \cos(\theta_1-\phi) \\ &\quad +\sqrt{\frac{1-\lambda(\theta_1)}{\lambda(\theta_1)}}\sin(\theta_1-\phi)\Bigg] \end{aligned} \tag{4.2}$$

where J_c is the moment of inertia of the crankshaft, J_R is the moment of inertia of the connecting rod, m_c is the mass of the crankshaft, m_R is the mass of the connecting rod, m_p is the mass of the piston, $\hbar$ is the length ratio of C_1B_1 to C_1A_1, and F is the length ratio of E_1D_1 to D_1C_1 as shown in Figure 4.1.

In this thesis, the derivative of some variable, x with respect to time is denoted by $\dot{x}$ and the derivative with respect to crank angle by $\acute{x}$.

By substituting Equation (2.10) into the Equations (2.1), and rearranging, the system equations are given as:

$$\ddot{\theta}_1 = \frac{1}{\tau}\left[T_I(\theta_1) - \left[MrG(\theta_1)G_1(\theta_1) + \frac{1}{2}\frac{\partial J_1(\theta_1)}{\partial \theta_1}\right]\dot{\theta_1}^2 - \sum_{k=1}^{5} T_{fk} - T_S - T_D\right], \tag{4.3}$$

$$\ddot{\theta}_2 = \frac{1}{J_2}\left[T_D + T_S - T_L\right]. \tag{4.4}$$

where the moment of inertia of crankshaft assembly and the reciprocating parts, τ, is given by $\tau = \left(J_1(\theta_1) + MrG(\theta_1)G_2(\theta_1)\right)$.

To develop an engine dynamic model in the crank angle domain, consider the crankshaft angle θ_1 as an independent variable. Then the independent variable

transformation can be obtained from [WKR97] as follows:

$$\dot{\theta}_1 = \frac{d\theta_1}{dt} = \omega_1(\theta_1), \tag{4.5}$$

$$\ddot{\theta}_1 = \omega_1 \frac{d\omega_1}{d\theta_1}, \tag{4.6}$$

$$\dot{\theta}_2 = \omega_1 \frac{d\theta_2}{d\theta_1} = \omega_2(\theta_1), \tag{4.7}$$

$$\ddot{\theta}_2 = \frac{d\omega_2}{dt} = \omega_1 \frac{d\omega_2}{d\theta_1}. \tag{4.8}$$

From Equation (4.7), the relationship between the dynamometer angular position θ_2 and the independent variable θ_1 is given by:

$$\int_0^{\theta_2} d\theta_2 = \int_0^{\theta_1} \frac{\omega_2(\theta_1)}{\omega_1(\theta_1)} d\theta_1 \Rightarrow \theta_2 = \int_0^{\theta_1} \frac{\omega_2(\theta_1)}{\omega_1(\theta_1)} d\theta_1. \tag{4.9}$$

By substituting Equations (4.5), (4.6) and (4.8) into the Equations (4.3) and (4.4), the system equations in the crank-angle domain is given by:

$$\acute{\omega}_1 = \frac{1}{\tau\omega_1}\left[T_I(\theta_1) - \left[MrG(\theta_1)G_1(\theta_1) + \frac{1}{2}\frac{\partial J_1(\theta_1)}{\partial\theta_1}\right]\omega_1^2 - \sum_{k=1}^{5} T_{fk} - T_S - T_D\right], \tag{4.10}$$

$$\acute{\omega}_2 = \frac{1}{J_2\omega_1}\left[T_D + T_S - T_L\right]. \tag{4.11}$$

4.3 Cylinder volume and Area

From the piston-crank mechanism, the cylinder volume is

$$V = \frac{V_d}{c-1} + \frac{\pi d^2}{4}\left[\sqrt{(r+L)^2 - \delta^2} - \left(\sqrt{L^2 - (\delta + r\sin(\theta_1 - \phi))^2} + r\cos(\theta_1 - \phi)\right)\right] \tag{4.12}$$

The cylinder heat transfer area is given by

$$A = \alpha\frac{\pi d^2}{4} + \pi d\left[\sqrt{(r+L)^2 - \delta^2} - \left(\sqrt{L^2 - (\delta + r\sin(\theta_1 - \phi))^2} + r\cos(\theta_1 - \phi)\right)\right] \tag{4.13}$$

where $\alpha > 2$ for a non-flat piston and cylinder head, and $\alpha = 2$ for a flat piston top and cylinder head bottom. The derivative with respect to crank angle of Equation (4.12) is

$$\dot{V} = \frac{\pi d^2}{4} r \left[\sin(\theta_1 - \phi) + \frac{\cos(\theta_1 - \phi)(\delta + r\sin(\theta_1 - \phi))}{\sqrt{L^2 - (\delta + r\sin(\theta_1 - \phi))^2}} \right]. \tag{4.14}$$

4.4 Thermodynamic modelling

4.4.1 Conservation of mass and energy

The filling and emptying method [WJ82] treats the cylinder and each manifold as a thermodynamic control volume for the engine given in Figure 4.1. Using the first law of thermodynamics for an open system and the ideal gas law, the temperature differential equation can be written as [WJ82, Wat84]:

$$\dot{T} = \left[\left(\sum_j \dot{Q}_{htj} + \sum_{in} h_{oin}\dot{m}_{in} - \sum_{out} h_{0out}\dot{m}_{out} + \dot{m}_f h_{for} - u\dot{m} \right) \frac{1}{m} - \frac{RT}{V}\dot{V} - \frac{\partial u}{\partial F}\dot{F} \right] / \frac{\partial u}{\partial T}. \tag{4.15}$$

where subscript j denotes surfaces with different rates of heat transfer, Q includes heat released by combustion, h_0 is the stagnation enthalpy, hence implicitly accounting for kinetic energy, u is the specific internal energy, P and T are control volume pressure and temperature respectively and m is the mass. Derivation and application of Equation (4.15) to cylinder and manifolds control volumes are illustrated in Appendix D.

The specific internal energy u is assumed to be a function of temperature T and the equivalence ratio F only (for the definition of F, see Equation (4.20)). Since dissociation effects are small [Wat84], the influence of pressure is neglected. A curve fit of combustion product data as a continuous function is used [WJ82], based on absolute zero temperature of the elements. Thus

$$u = u(T, F). \tag{4.16}$$

The gas constant R is given by

$$R = \frac{0.278 + 0.02F}{1 + f_s F} \tag{4.17}$$

where f_s is the stoichiometric fuel air ratio.

Mass conservation for both air and fuel is required. Considering the total mass (fuel and air) gives

$$\acute{m} = \sum_{in} \acute{m} - \sum_{out} \acute{m} + \sum \acute{m}_{bf}. \tag{4.18}$$

The total mass is given by

$$m = m_a + m_{bf}, \tag{4.19}$$

where m_a is the mass of the air and m_{bf} is the mass of the burnt fuel. The fuel-air equivalence ratio is defined as

$$F = \frac{f}{f_s}, \tag{4.20}$$

where f is the fuel air ratio. The term $\acute{F}$ in Equation (4.15) is given by [Wat84];

$$\acute{F} = \left[\frac{1 + f_s F}{m}\right] \left[\frac{1 + f_s F}{f_s} \acute{m}_{bf} - F\acute{m}\right]. \tag{4.21}$$

4.4.2 Ports and valves mass flow rates

A one-dimensional model for flow through a valve (or port), using the analogy of an orifice having an equivalent area, is used. Applying the energy equation from upstream to downstream for isentropic steady flow, and assuming that the inlet velocity is negligible, for subsonic flow $P_d/P_u > (2\gamma_s/(\gamma_s + 1))^{(\gamma_s/(\gamma_s - 1))}$, the mass flow rate has the form,

$$\acute{m} = C_d A_v P_u \sqrt{\left(\frac{2\gamma_s}{\gamma_s - 1}\right) \frac{1}{RT_u} \left[\left(\frac{P_d}{P_u}\right)^{\frac{2}{\gamma_s}} - \left(\frac{P_d}{P_u}\right)^{\frac{\gamma_s + 1}{\gamma_s}}\right]}, \tag{4.22}$$

where C_d is the discharge coefficient, γ_s is the specific heat ratio and A_v is the valve or port area.

For sonic flow $P_d/P_u \leq (2\gamma_s/(\gamma_s + 1))^{(\gamma_s/(\gamma_s - 1))}$, the mass flow rate has the form

$$\acute{m} = C_d A_v P_u \sqrt{\frac{\gamma_s}{RT} \left(\frac{2}{\gamma_s + 1}\right)^{\left(\frac{\gamma_s + 1}{\gamma_s - 1}\right)}}. \tag{4.23}$$

4.4.3 Combustion

Many combustion models have been discussed in [Hey88, WJ82, Ram89]. The single zone model proposed in [Wat84] is used here, because it is widely accepted and can be used to predict both premixed and diffusion burning. The ignition delay (ID) equations as a function of cylinder pressure and temperature can be used to calculate the start of the combustion [Hey88];

$$ID = 3.45 \left(\frac{P}{101.3} \right)^{-1.02} e^{\frac{2100}{T}}, \tag{4.24}$$

with the constraint

$$\int_{\theta_{inj}}^{\theta_{ign}} \frac{d\theta}{ID} = 1 \tag{4.25}$$

where θ_{inj} is the angle at injection and θ_{ign} is the angle at ignition. The normalised premixed burning rate is given by:

$$\acute{m}_{fpre} = k_{p1} k_{p2} \theta_{norm}^{k_{p1}-1} \left(1 - \theta_{norm}^{k_{p1}}\right)^{k_{p2}-1} \tag{4.26}$$

while the normalised diffusion burning rate is given by:

$$\acute{m}_{fdiff} = k_{d1} k_{d2} \theta_{norm}^{k_{d1}-1} e^{-k_{d1} \theta_{norm}^{k_{d2}}} \tag{4.27}$$

where θ_{norm} is non-dimensional angle, increasing from 0 at start of combustion to 1 at the end of combustion. The parameters k_{p1}, k_{p2}, k_{d1} and k_{d2} have been correlated with fundamental factors having the strongest influence on the combustion rate. The best fit values of these parameters for a range of direct injection Diesel engines are presented in [Wat84].

The fraction of the total fuel that goes to the premixed burning, χ, is given by [Wat84]:

$$\chi = 1 - 0.926 F^{0.37} ID^{-0.26}. \tag{4.28}$$

Assuming complete combustion in 125 degrees of crank angle, the normalised angle is defined as:

$$\theta_{norm} = \frac{\theta_1 - \theta_{ign}}{125}. \tag{4.29}$$

Finally, the fuel burning rate is given by [Wat84]:

$$\acute{m}_{fnorm} = \chi \acute{m}_{fpre} + (1 - \chi) \acute{m}_{fdiff}. \tag{4.30}$$

and

$$\dot{m}_{bf} = \frac{m_f \dot{m}_{fnorm}}{\theta_{com}} \tag{4.31}$$

where θ_{com} is the combustion period in degrees.

4.4.4 Cylinder heat transfer

An instantaneous convective heat transfer is defined by,

$$\dot{Q}_{ht1} = h_{con} A_v (T - T_w) \tag{4.32}$$

where h_{con} is the heat transfer coefficient based on forced convection and is given by [BN87],

$$h_{con} = 130 V^{-0.06} P^{0.8} T^{-0.4} (N_p + 1.4)^{0.8} \tag{4.33}$$

where N_p is the mean piston speed and T_w is the cylinder wall temperature. The primary sources of radiative heat transfer in Diesel engines are the high temperature burned gases and soot particles. Following work in [AH86], the instantaneous radiant heat transfer can be expressed as:

$$\dot{Q}_{ht2} = \varepsilon \sigma A_v (T_{rad}^4 - T_w^4) \tag{4.34}$$

where ε is the apparent grey-body emissivity, σ is the Stephan-Boltzman constant and T_{rad} is the apparent radiant temperature. The adiabatic flame temperature, $T_{(F=1.1)}$, is the temperature of the hydrocarbon and air combustion products, when fuel air ratio is slightly greater than stoichiometric ($F = 1.1$). The apparent radiant temperature T_{rad} is calculated as the mean of the adiabatic flame temperature and the average bulk gas temperature, i.e.

$$T_{rad} = \frac{T + T_{(F=1.1)}}{2}. \tag{4.35}$$

The temperature of combustion products at $F = 1.1$ is computed from a correlation of instantaneous air temperature and pressure as in [AH86]

$$T_{F=1.1} = (1 + 0.0002317(T - 950))(2726.3 + 0.906P - 0.003233P^2) \tag{4.36}$$

for $800K < T < 1200K$, and

$$T_{F=1.1} = (1 + 0.000249(T - 650))(2487.3 + 4.7521P - 0.11065P^2 + 0.000898P^3) \tag{4.37}$$

for $450K < T < 800K$.

The apparent emissivity is assumed to vary linearly between [0.9 to 0] over the expansion stroke. The cylinder wall temperature is updated at each step by using the one-dimensional heat conduction model, and an electrical analogy model, shown in Figure 4.2:

$$\dot{Q}_{ht1} + \dot{Q}_{ht2} = \frac{(T_w - T_{coolant})}{R_{wc} + R_w} \tag{4.38}$$

where $R_{wc} = \frac{1}{h_{coolant}A}$ is the thermal resistance from wall to coolant. The thermal resistance for conduction through the wall is $R_w = \frac{t}{KA}$, where t is the wall thickness and K is the thermal conductivity. A fourth order polynomial equation in T_w is obtained and the ith solution gives the wall temperature.

$$\frac{(T - T_w)}{R_{gw}} + \varepsilon\sigma A(T_{rad}^4 - T_w^4) = \frac{(T_w - T_{coolant})}{R_{wc} + R_w} \tag{4.39}$$

where $R_{gw} = \frac{1}{h_{con}A}$ is the thermal resistance from gas to wall. Thus the cylinder heat release rate can be calculated from Equations (4.32) and (4.34):

$$\dot{Q}_{ht} = \dot{Q}_{ht1} + \dot{Q}_{ht2} \tag{4.40}$$

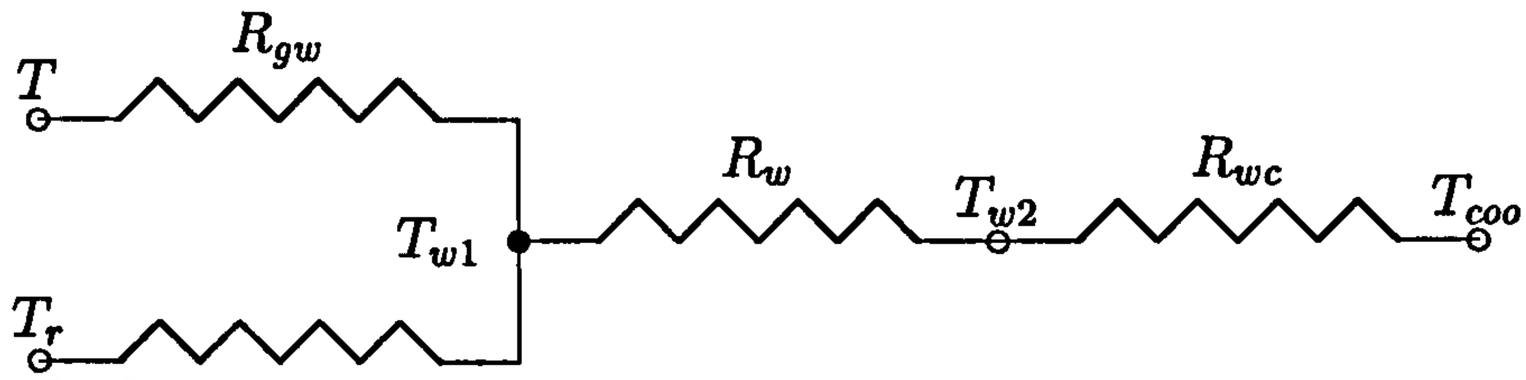

Figure 4.2: Thermal resistance for the cylinder

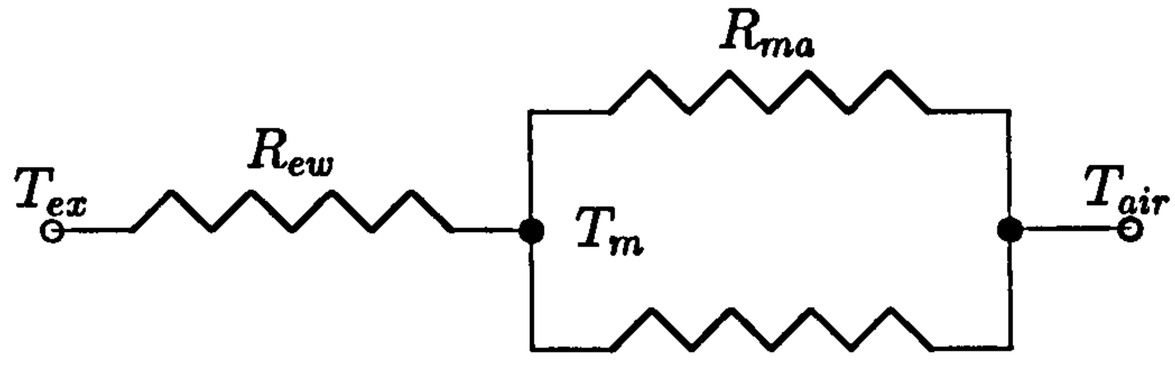

Radiation resistance.

Figure 4.3: Thermal resistance for the exhaust manifold

4.4.5 Exhaust manifold heat transfer

The exhaust gas flow is considered to be turbulent. The forced heat convection between the exhaust gas and the manifold wall, the natural convection, and the radiation between the manifold and ambient air are taken into account. The conductive heat transfer through the wall thickness is neglected. An electrical analogy model is shown in Figure 4.3. The manifold is assumed to have a cylindrical shape, and homogeneous gas and wall temperatures. The heat transfer rate from exhaust gas to manifold is given by

$$\dot{Q}_{ht} = h_f A_m (T - T_m) \tag{4.41}$$

The heat transfer rate from manifold to air is given by

$$\dot{Q}_{ma} = h_n A_m (T_m - T_{air}) \tag{4.42}$$

The heat transfer rate due to radiation is given by

$$\dot{Q}_r = \varepsilon \sigma A_m (T_m^4 - T_{air}^4) \tag{4.43}$$

h_f is the forced heat convective coefficient given by [ZPHS92]

$$h_f = 0.023 \frac{K}{D_i} R_e^{0.8} P_r^{0.3} \tag{4.44}$$

where R_e is the Reynolds number and P_r is the Prandtl number:

$$R_e = \frac{\varpi D_i}{\nu_g} \tag{4.45}$$

$$P_r = \frac{C_p \mu_g}{K} \tag{4.46}$$

where ν_g is the kinematic viscosity, D_i is the inner manifold diameter and C_p is the specific heat and ϖ is the average exhaust gas flow rate. The dynamic viscosity μ_g can be calculated from [Ram89]:

$$\mu_g = \frac{3.3 \times 10^{-7} T^{0.7}}{1 + 0.027F}. \tag{4.47}$$

The average flow rate ϖ is given by [ZPHS92]:

$$\varpi = \frac{NV}{120(\frac{\pi D_i^2}{4})}. \tag{4.48}$$

The natural heat convective coefficient h_n is given by [ZPHS92]:

$$h_n = 0.53 \frac{K}{D_o} (G_r P_r)^{0.25} \tag{4.49}$$

where G_r is the Grashof number [ZPHS92]:

$$G_r = \frac{g\varsigma(T_m - T_{air})(0.9D_o)^3}{\nu_g^2} \tag{4.50}$$

where g is the gravitational acceleration, D_o is the outer manifold diameter and ς is the volumetric coefficient and is taken as equal to $\frac{1}{T_{air}}$[Ozi85]. Applying the energy conservation principle to the volume, a fourth order polynomial equation in T_m is obtained. The solution to this equation gives the manifold temperature which can be substituted into Equation (4.41) to calculate the manifold heat transfer rate:

$$T_m - T + \frac{D_o}{D_i}\frac{h_n}{h_f}(T_m - T_{air}) + \frac{D_o}{D_i}\frac{\sigma\varepsilon}{h_f}(T_m^4 - T_{air}^4) = 0. \tag{4.51}$$

4.5 Model implementation and simulation

4.5.1 Model implementation

The complete model is implemented using Matlab/SIMULINK [Mat97, SIM97]. Figure 4.4 shows the structure of the SIMULINK model for the engine analytical model. There are ten blocks, representing the overall engine model. The inputs

are air flow rate, fuel flow rate, ambient conditions and engine parameters. The outputs of the engine model are speed, crankshaft angular position and other states. The engine dynamic model block contains the equations of Chapter 2; Sections (2.2.1-2.2.2), Chapter 3; Section 3.2, and Chapter 4; Sections 4.2, 4.3, and 4.4.

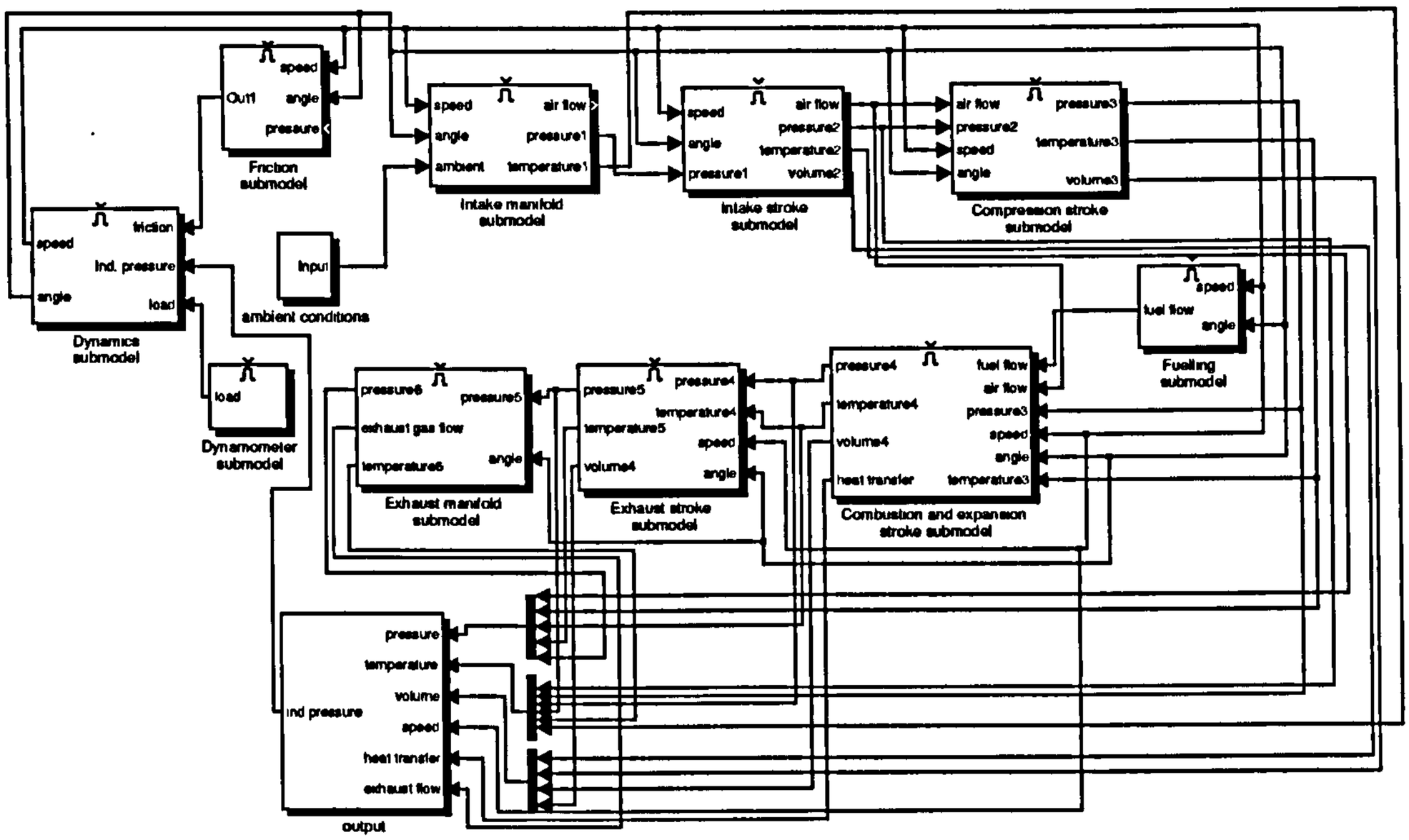

Figure 4.4: Analytical model representation using SIMULINK

The integration step for the program is chosen to be one crank-angle degree. The indicated torque from the cylinder is updated at each step, and then used in the nonlinear dynamic model to update the instantaneous crankshaft angular velocity. The current simulation program is executed on a 400 MHZ Pentium II PC, and the simulation takes about 8 seconds for a 720 degree engine cycle at an engine speed of 950 rpm.

4.5.2 Model behaviour and validation

In order to validate the transient behaviour of the engine model with experimental results, a F1L 210 DEUTZ MAG DI single cylinder Diesel engine is used. The measured data engine are taken from [LCH97]. This engine was selected because it is fully-instrumented and set-up for warm-up and cold start conditions at

Wayne State University, also the engine parameters for running thermodynamic model were available. The geometrical specifications for this Engine are shown in Table G.3 in Appendix G, and are taken from [LCH97] and [GH88]. Comparisons between the predicted and measured values of the indicated pressure and the crankshaft instantaneous angular velocity for a single cycle during firing are shown in Figures 4.5 and 4.7 respectively. Figure 4.5 shows a comparison between the predicted and measured cylinder gas pressure with firing at no load and an average engine speed of 1795 rpm and the fuelling rate is 25 mm^3per cycle. The overall agreement between the measured and predicted curves is good. The gas pressure during the exhaust stroke is slightly overestimated. Differences in engine timing, real heat transfer and heat release between the real engine and simulated engine may also account for the differences. The slight underestimation of the engine pressure during the combustion stroke may also be due to the fact that a single zone combustion model is used here. Figure 4.6 shows the difference between measured and predicted cylinder gas pressure. The maximum difference is about 3.8 bar for a small duration near the top dead centre, where the measured gas pressure is about 51 bar, giving a relative percentage error of about 7.5%.

As shown in Figure 4.7, the slight underestimation of the gas pressure during combustion has resulted in a minor underestimation of the instantaneous engine speed with reciprocating and inertia variations, near the TDC. In addition, the slight underestimation of the instantaneous engine speed with reciprocating and inertia variations after the mid-exhaust stroke is due to the gas pressure overestimation. Other reasons for the error include inaccuracies in the engine model parameters and errors in modelling friction behaviour. The overall agreement between the measured and predicted curves is good. Figure 4.7 also shows that the predicted crankshaft instantaneous angular velocity of the model with the reciprocating and inertia variation terms removed (the terms associate with the ω_1^2 term in Equations (4.10)). When the simulation is performed for the model without the reciprocating and inertia variation terms, the speed profile has overestimation except at the end of the intake stroke, the start of the compression stroke and

after the middle of the exhaust stroke. This demonstrates the importance of the incorporation of the reciprocating and inertia variation terms. The difference is more marked at high engine speeds due to the dependence of $\dot{\omega}_1$ on the ω_1^2 term (Equations (4.10)).

The predicted inlet flow is shown in Figure 4.8. The normalized rate of heat release is shown in Figure 4.9. The high left peak in the curve represents the premixed phase. Combustion of fuel mixed with air to within the flammability limits during the ignition delay period occurs rapidly in a few crank angle degrees. When this burning mixture is added to the fuel it burns during this phase, and a high heat release rate is characteristic of this phase. The low right peak is the diffusion phase; once the fuel and air premixed during the ignition delay have been consumed, the burning rate is controlled by the mixture available for burning. The heat released decreases as this phase progresses as seen in Figure 4.9.

The model is tested for cold conditions, where the cylinder wall temperature remains at a room temperature of 30 °C. Figure 4.10 shows the comparison between predicted and measured cylinder gas pressure. Figure 4.11 shows the good agreement between predicted and measured instantaneous engine speeds, especially at high engine speeds.

The rate of change of the engine inertia is shown in Figure 4.12. $\frac{\partial J_1(\theta_1)}{\partial \theta_1}$ is a bounded periodic function with an average value of zero. Therefore, although there are periods during crank rotation when the velocity term has a positive effect and other periods where it has a negative effect, the net effect for a complete rotation is zero. The physical reason for this term is that, as the inertia decreases and less work is required for motion, it appears as if energy is added to the system. Similarly, as the inertia increases and more work is required, energy appears to be removed from the system. In the same figure, the inertia of the crank assembly is not constant, but it is a function of crank-angle. Due to the attachment of the big end of the connecting rod with the crankshaft, the maximum crank assembly inertia is near $\frac{\pi}{2}$ and $\frac{3\pi}{2}$ of the crankshaft angular position and the minimum is near 0 and π.

The instantaneous torque produced by the engine at 40 mm^3 of fuel per cycle for four engine cycles is shown in Figure 4.13. The maximum torque value represents the maximum pressure in the cylinder during the combustion stroke as illustrated in the same figure. The fluctuations in engine torque during the cycle, result in variations of the instantaneous crankshaft rotational speed.

The convection and radiation heat transfer from the cylinder is shown in Figure 4.14. In the vicinity of ignition at top dead centre, the magnitude of the heat transfer is high. This is due to a high gas temperature inside the combustion chamber at that moment, as seen in Figure 4.15.

Figure 4.16 shows the pressure-volume diagram. The compression curve behaviour is similar to the expansion curve. Since both the compression of the unburnt mixture prior to combustion and expansion of the burnt gases following the end of combustion are close to an adiabatic isentropic process, the observed behaviour is as expected; the compression and expansion processes fit well with the polytropic relation $PV^{1.3}$ = constant. The pressure increases smoothly to reach its maximum value after TDC.

The rate of the equivalence ratio at a fuel per cycle of 40 mm^3 is presented in Figure 4.17. Since only air exists during the compression stroke, there is a zero or small equivalence ratio. Once the injection starts, the equivalence ratio increases with a constant rate of change because the intake valves are closed and a constant fuel injection rate is assumed. After the completion of the injection the equivalence ratio is constant until all the fuel is burnt.

The exhaust gas temperature is shown in Figure 4.18. Initially, the manifold temperature is from the previous cycle. Then when the gas enters in from the combustion chamber, the heat transfer by convection and radiation takes place leading to a decrease in the exhaust gas temperature. In reality, the cylinder gas is mixed with the manifold exhaust gas which leads to a more gradual temperature increase. This assumption does not affect the application of the model for estimation and control.

4.6 Model sensitivity

To check the overall model sensitivity, the engine parameters are perturbed ±3%, ±8%, and ±15% respectively. The absolute percent mean relative error is given by $100 \times \left| \left(\frac{\int_0^{\theta_1} ((\dot{\theta}_{meas.} - \dot{\theta}_{sim.})/\dot{\theta}_{meas.}) d\theta_1}{\int_0^{\theta_1} d\theta_1} \right) \right|$. The model sensitivity values are shown in Table 4.1. From the result, the model behaves reasonably with respect to system parameter changes.

Absolute percent mean relative error of the engine speed at parameters perturbation ±3%	8.58%
Absolute percent mean relative error of the engine speed at parameters perturbation ±8%	12.28%
Absolute percent mean relative error of the engine speed at parameters perturbation ±15%	18.87%

Table 4.1: Model sensitivity

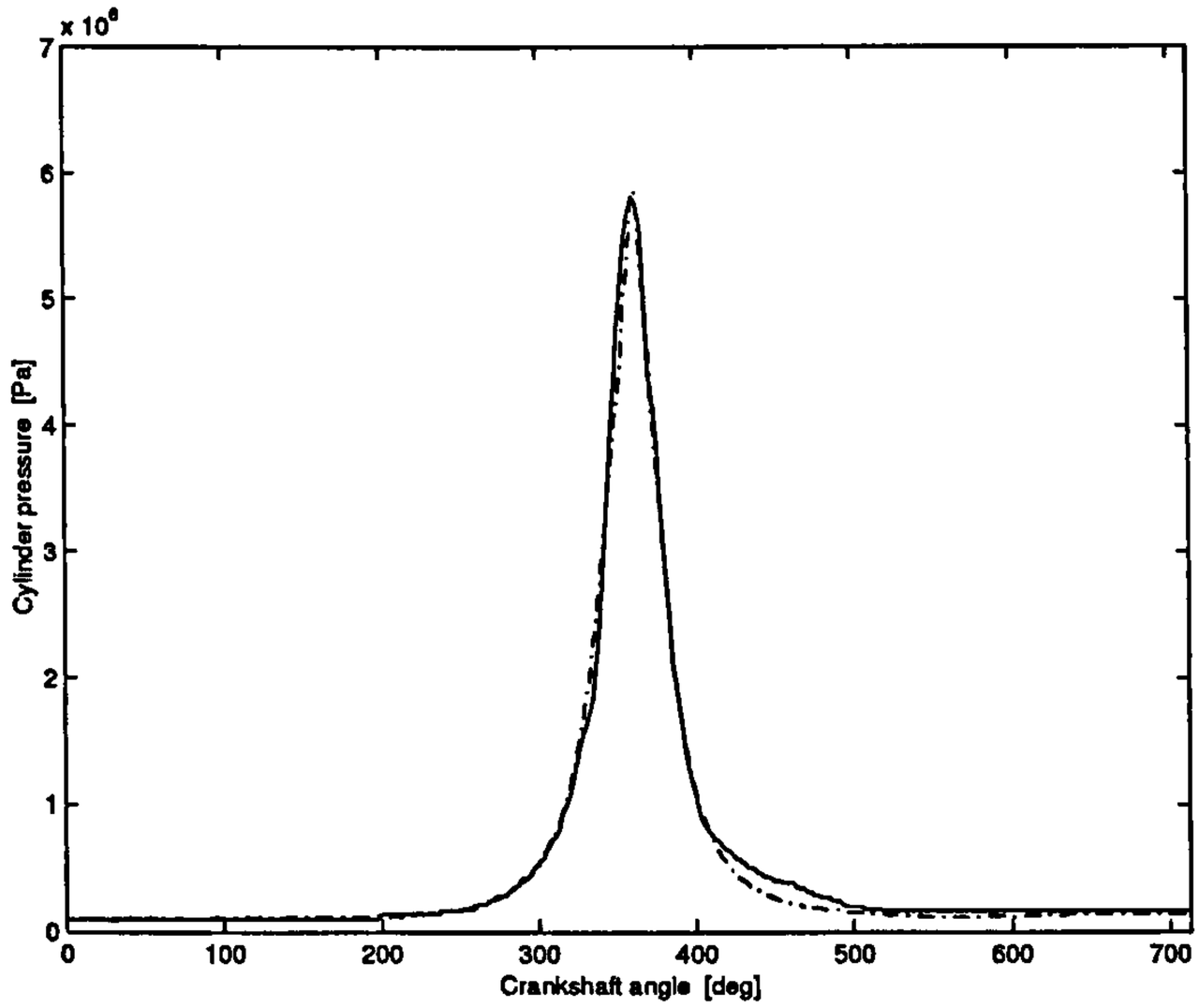

Figure 4.5: Comparison between predicted (——) and measured [LCH97](- · - ·) cylinder gas pressure under firing

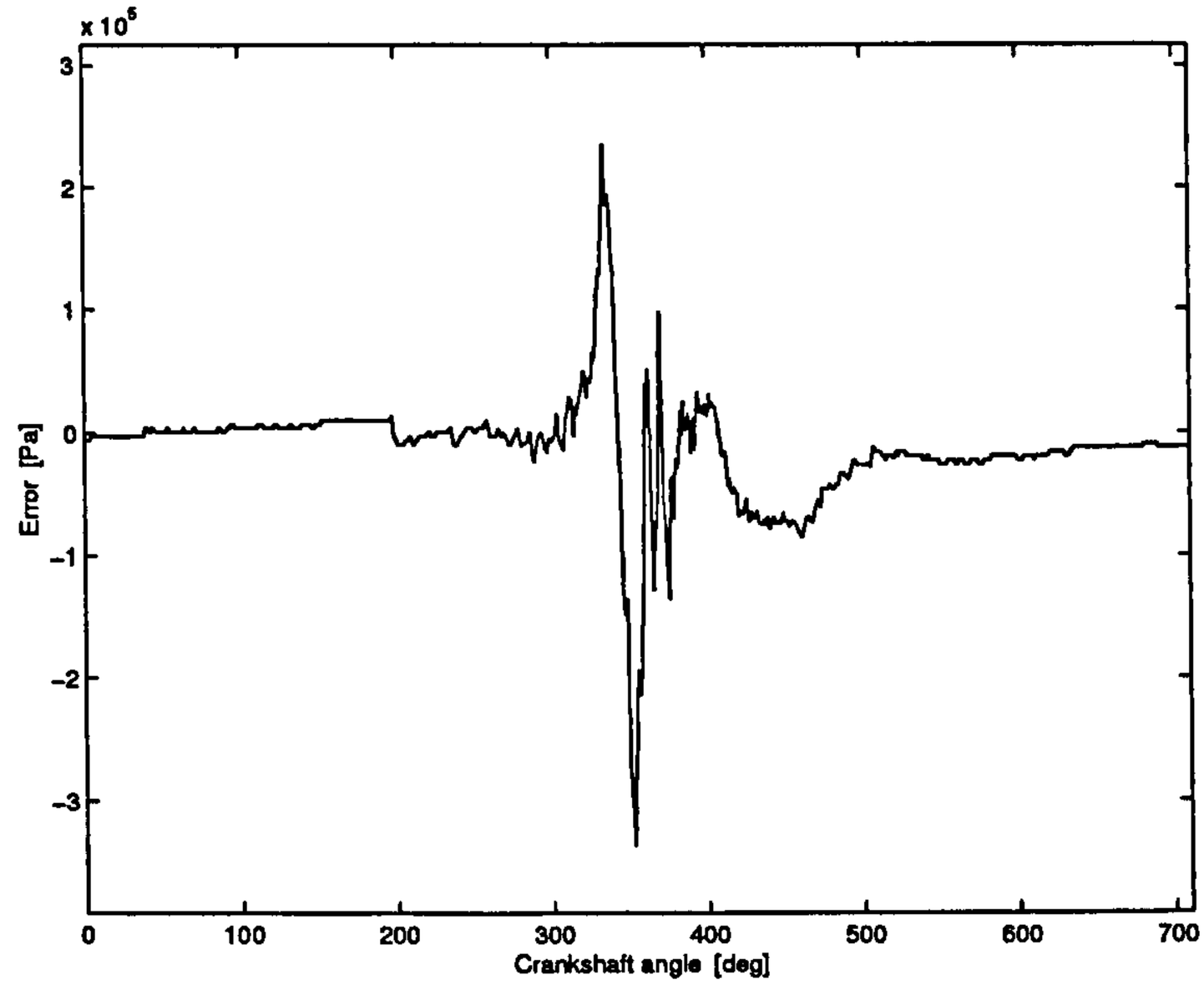

Figure 4.6: Error between measured and predicted pressure

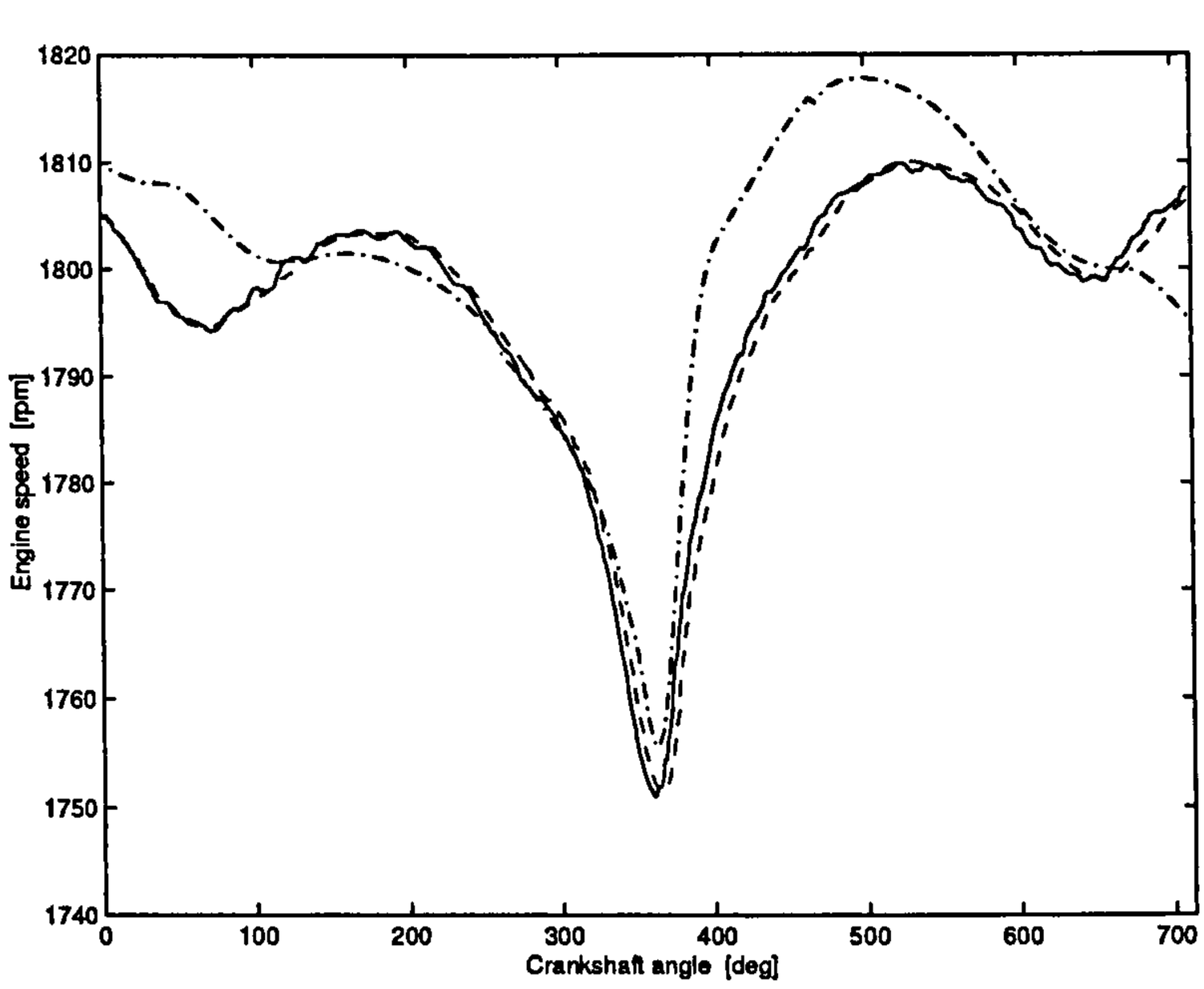

Figure 4.7: Comparison between predicted speed with reciprocating and inertia variation (——), predicted speed without reciprocating and inertia variation (- · - ·) and measured speed [LCH97](- - -).

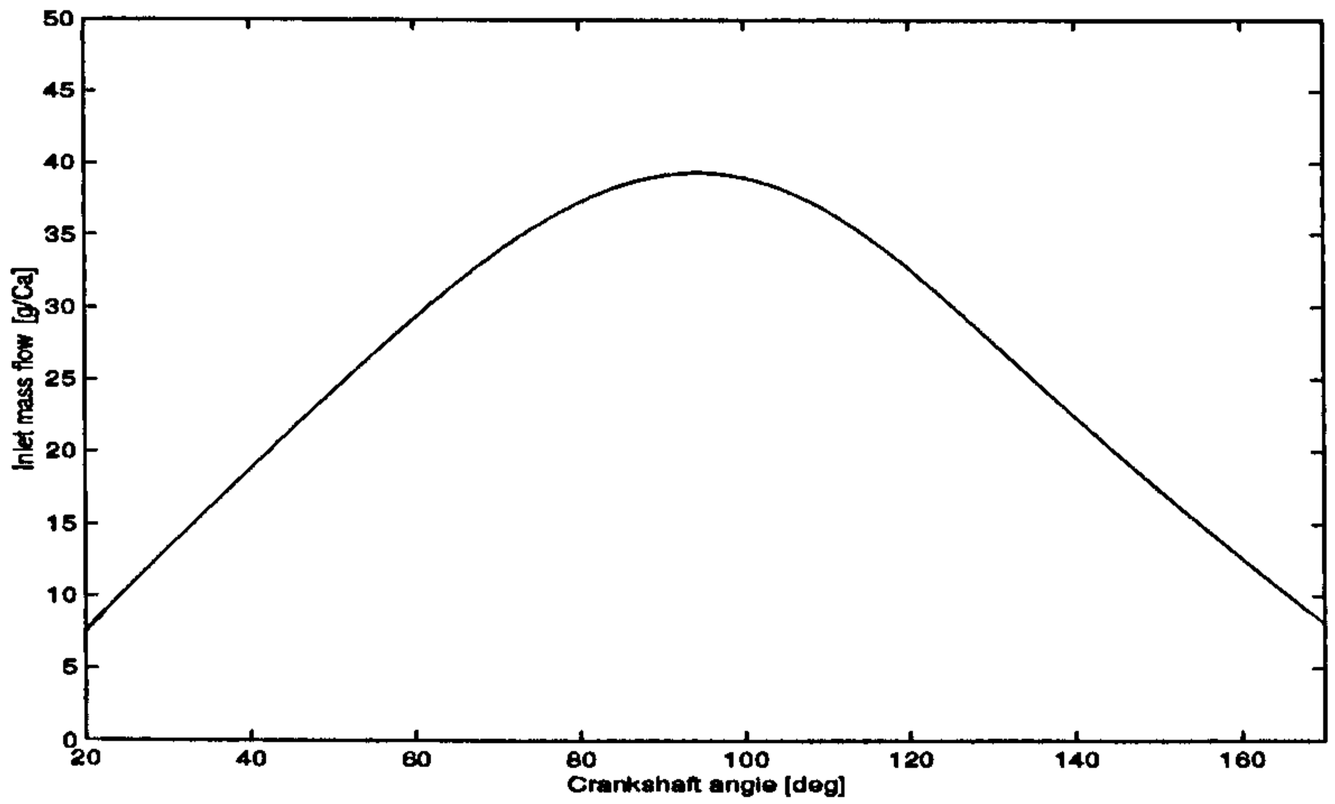

Figure 4.8: Predicted flow rate through the inlet valve

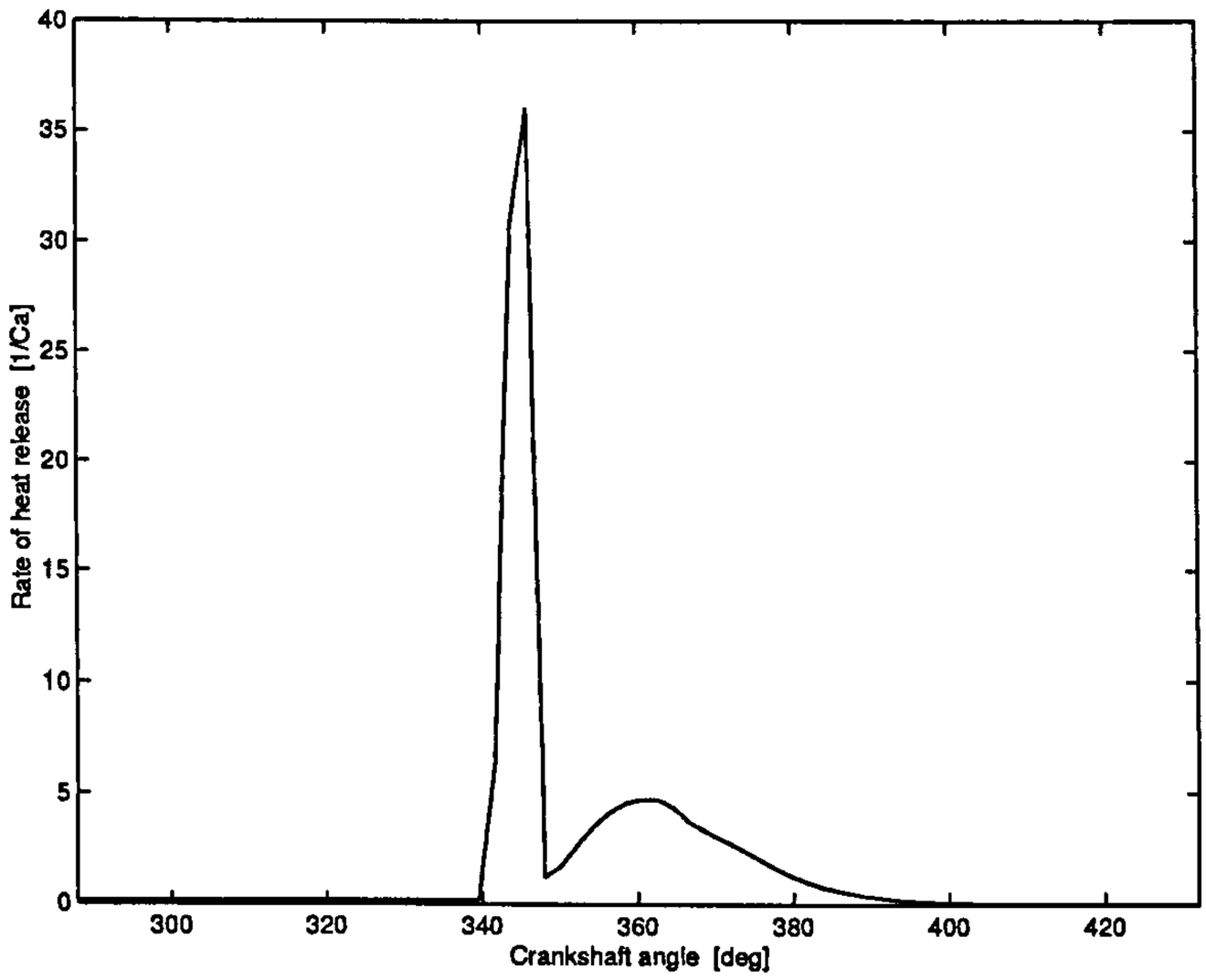

Figure 4.9: Predicted normalized heat release at fuel per cycle of 25 mm^3

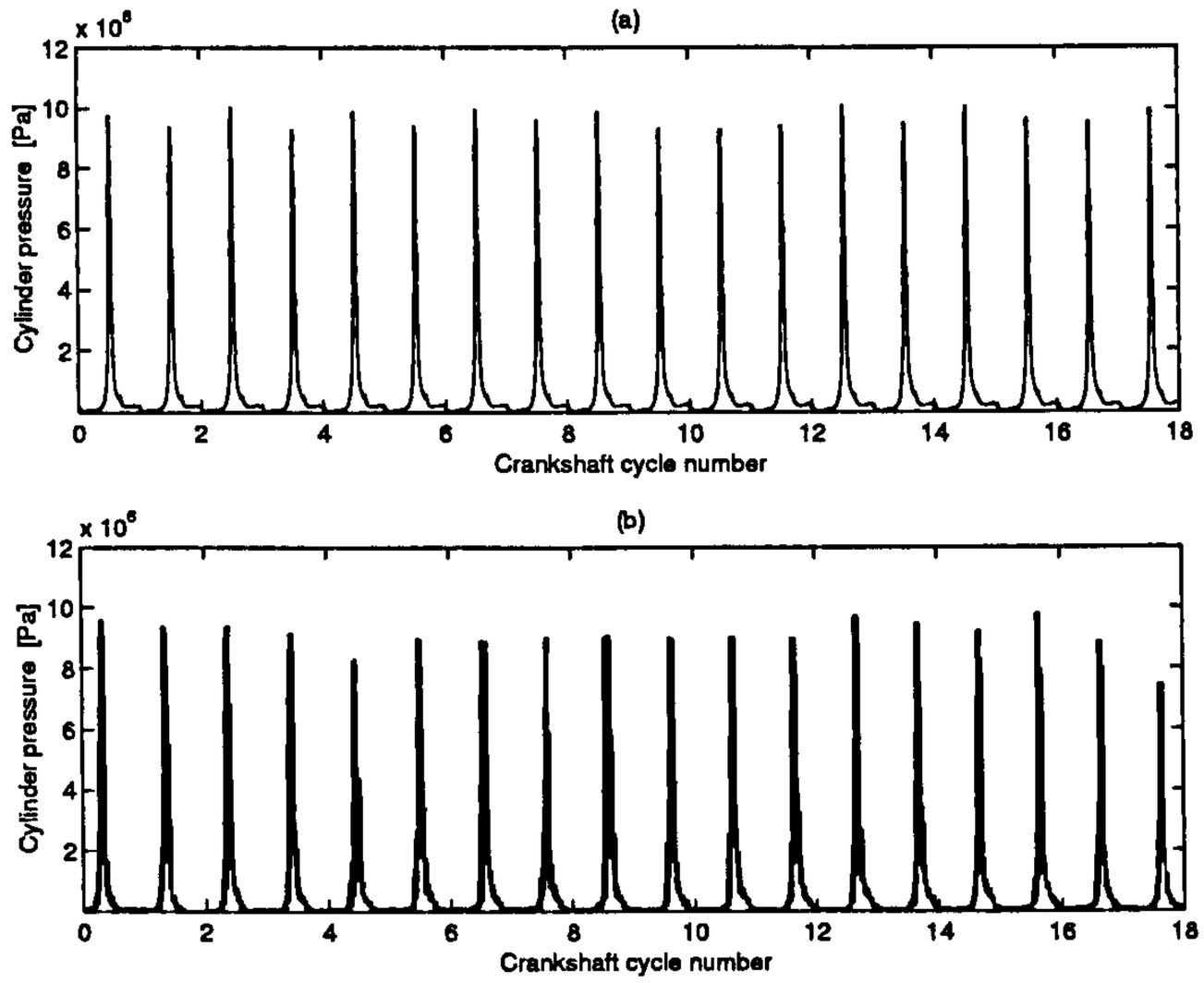

Figure 4.10: Cylinder gas pressure (a) Predicted, (b) Measured [LCH97]

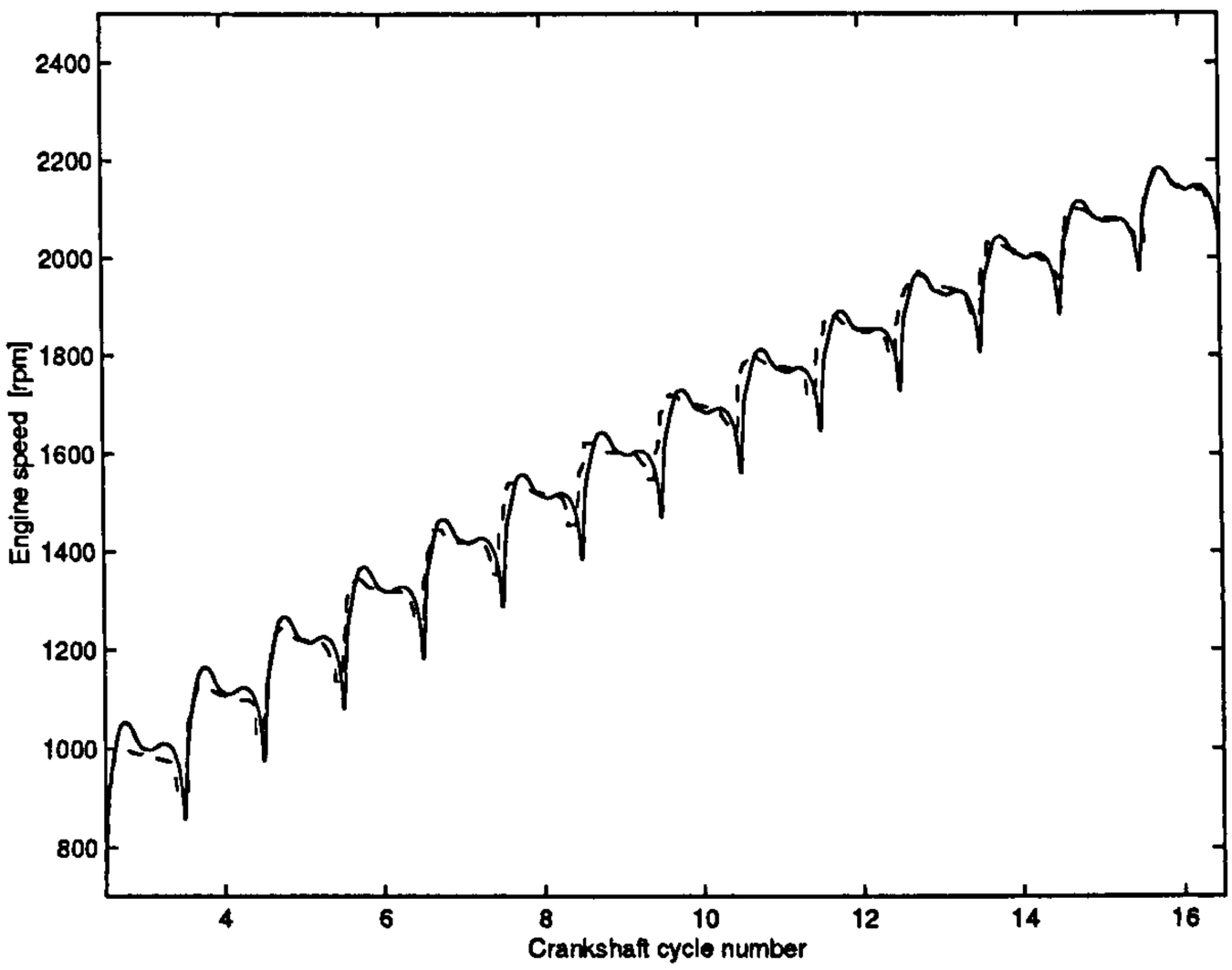

Figure 4.11: Comparison between predicted (——), and measured [LCH97] (- - -) instantaneous crankshaft angular velocity

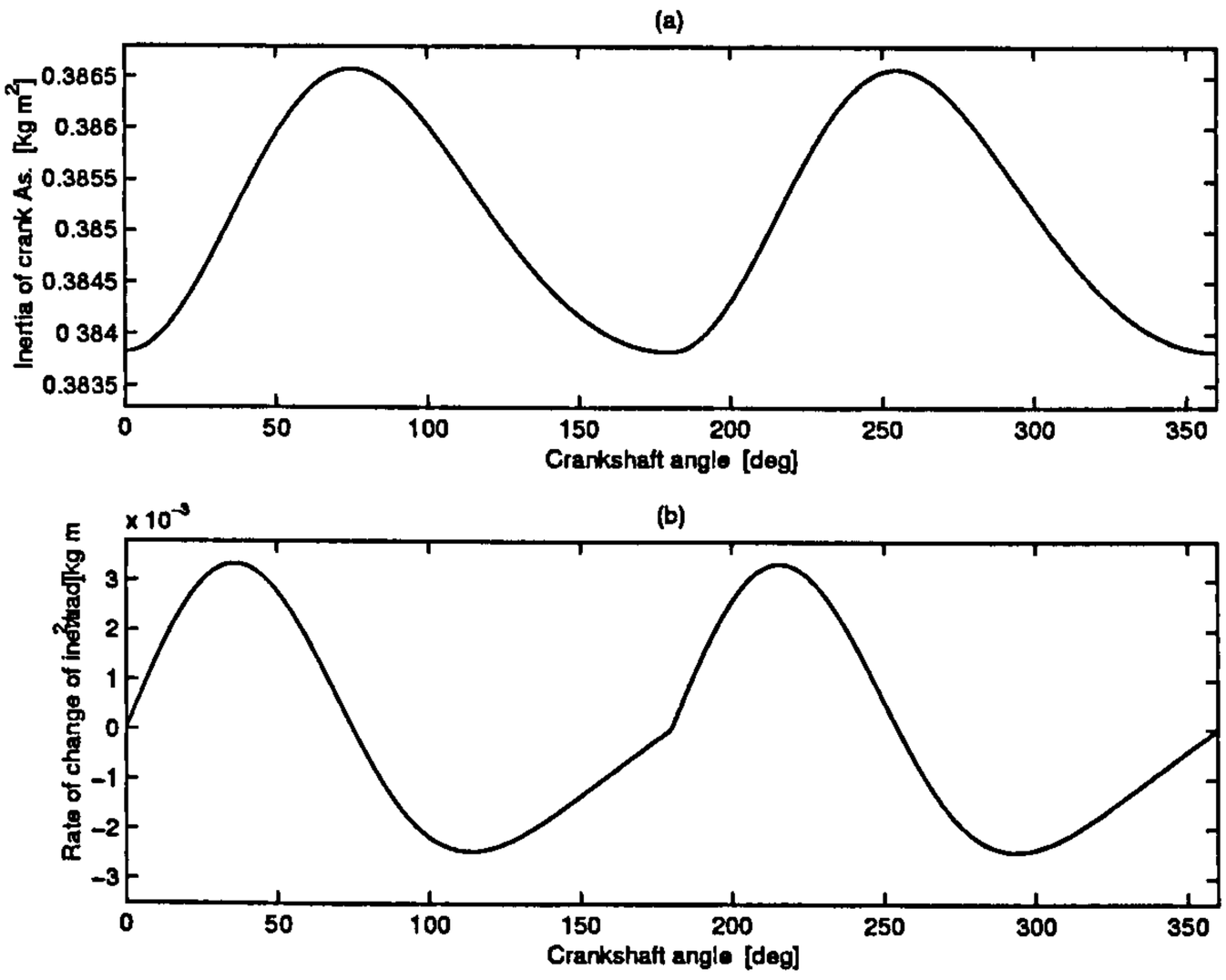

Figure 4.12: (a) Inertia of the crankshaft assembly, (b) rate of change of the inertia for the crankshaft assembly

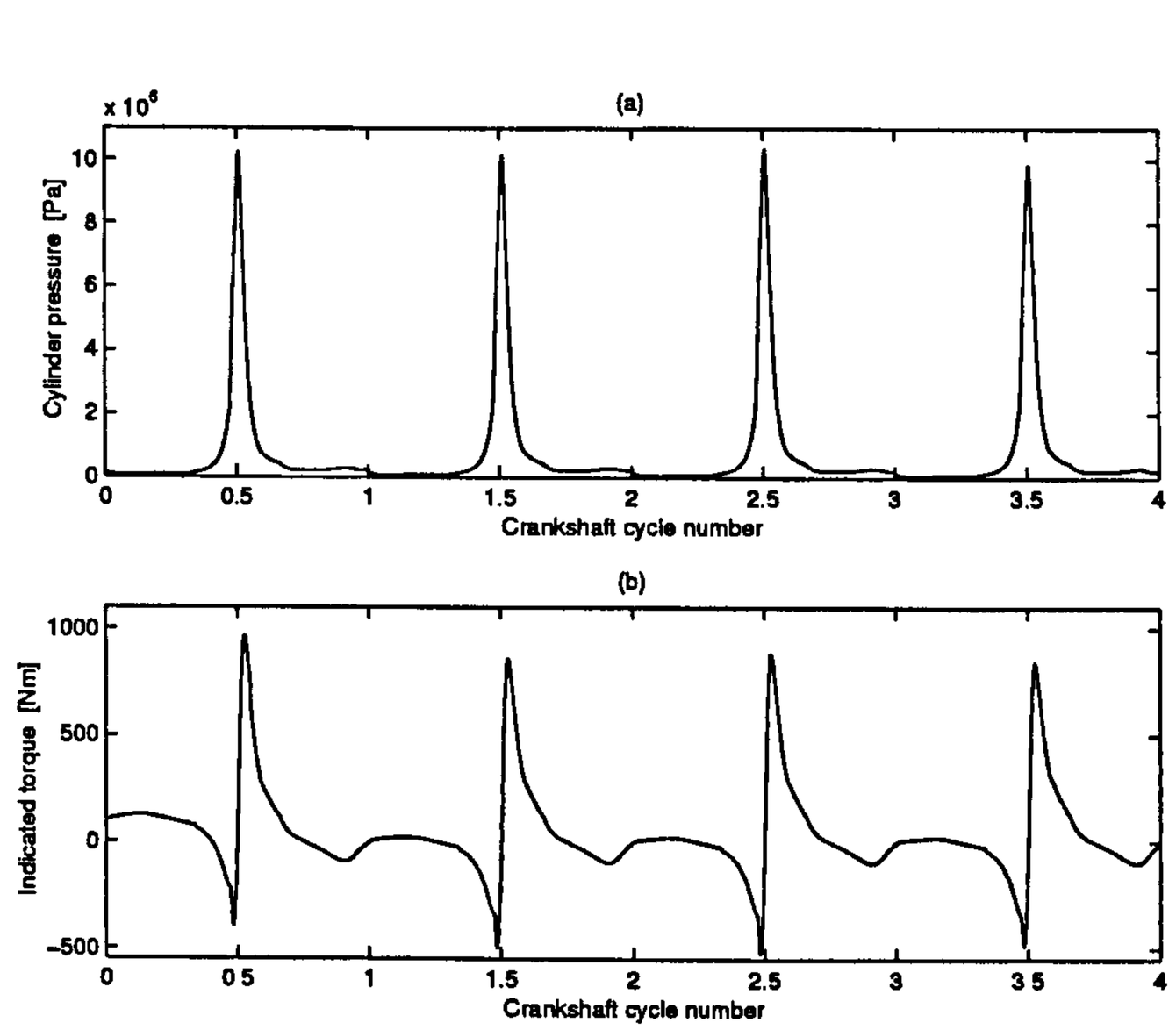

Figure 4.13: (a) Predicted cylinder pressure at fuel per cycle of 40 mm^3, (b) predicted indicated torque at fuel per cycle of 40 mm^3

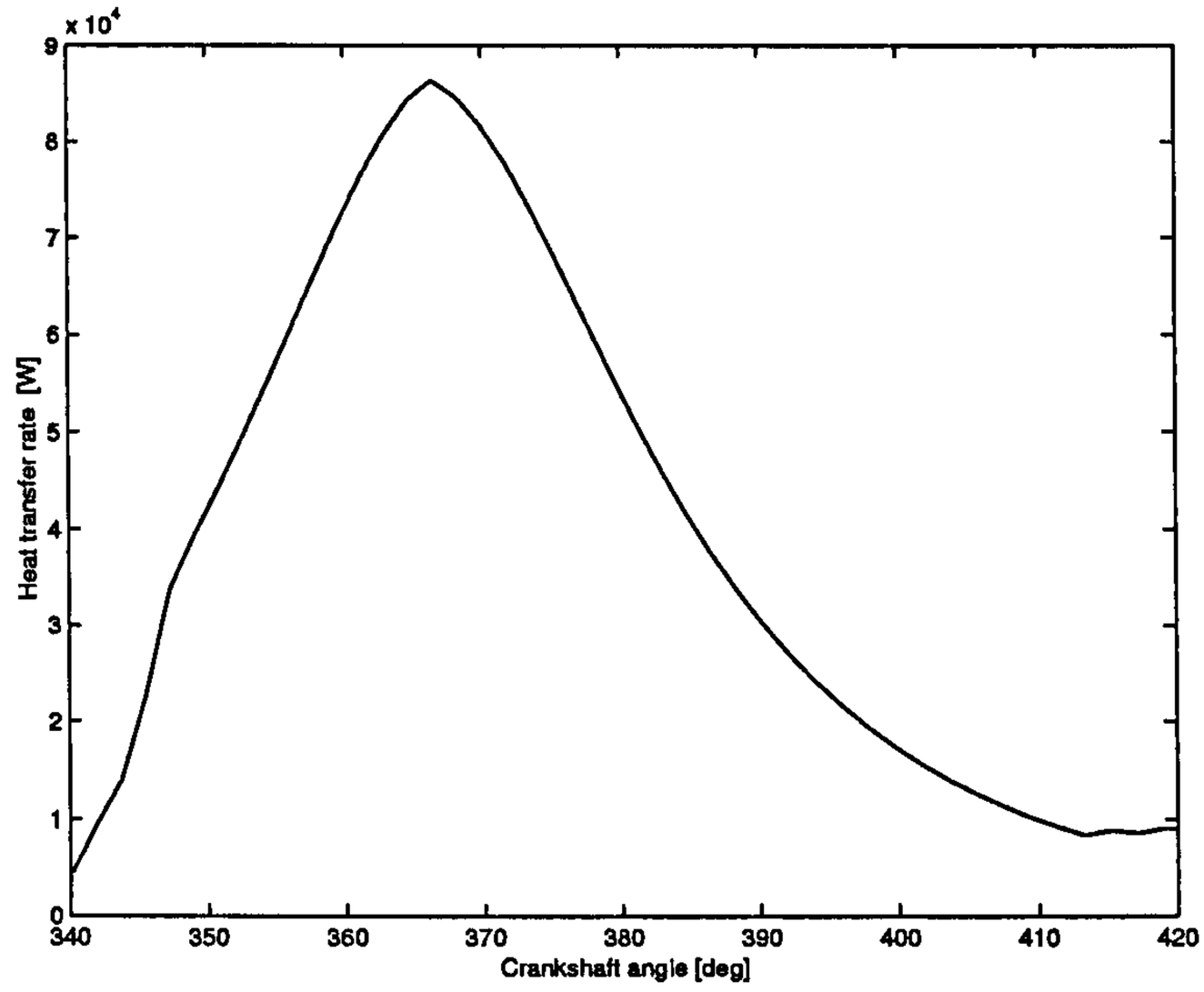

Figure 4.14: Predicted wall heat transfer rate as a function of the crankshaft angle at fuel per cycle of 40 mm^3

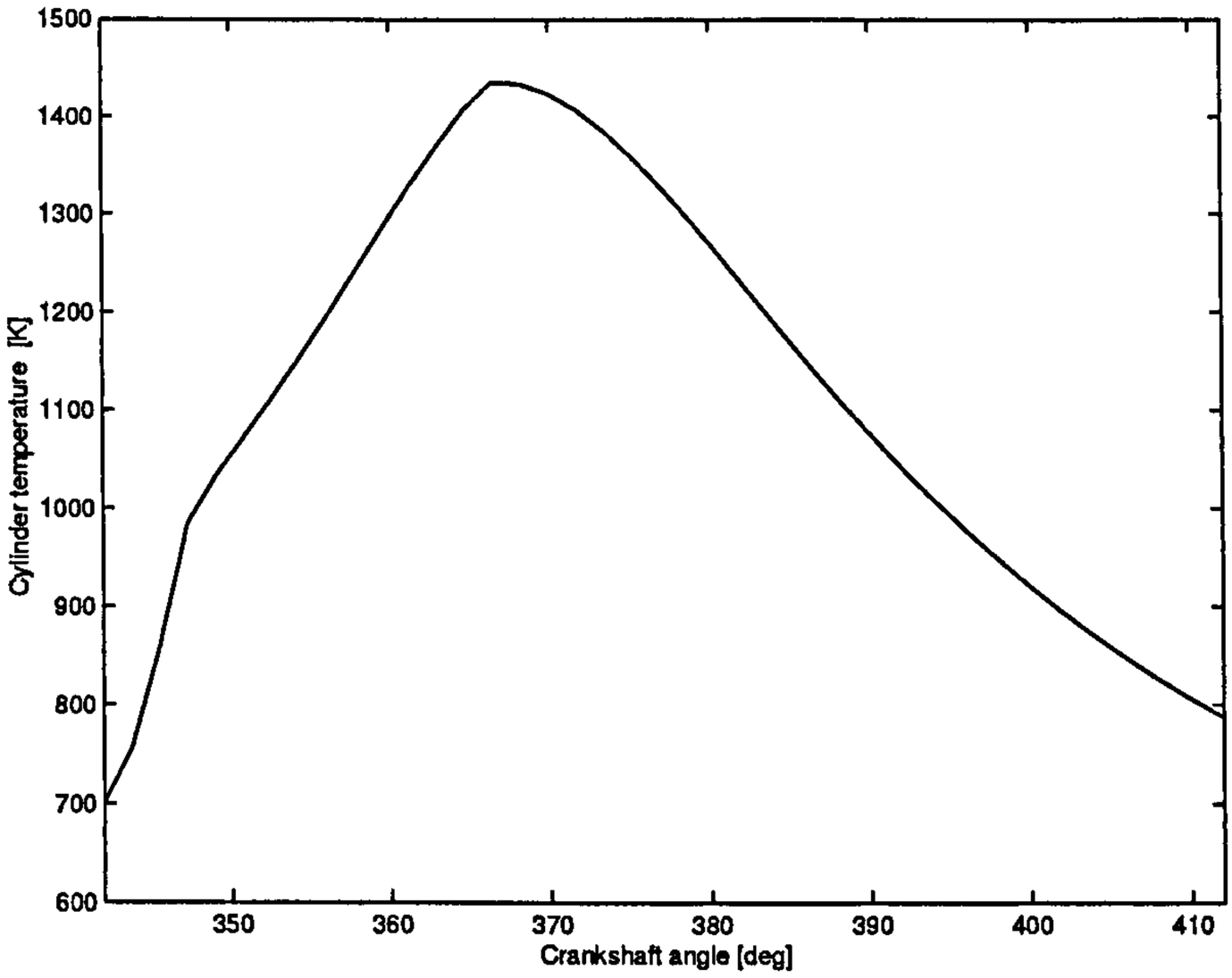

Figure 4.15: Predicted gas temperature profile as a function of the crankshaft angle at fuel per cycle of 40 mm^3

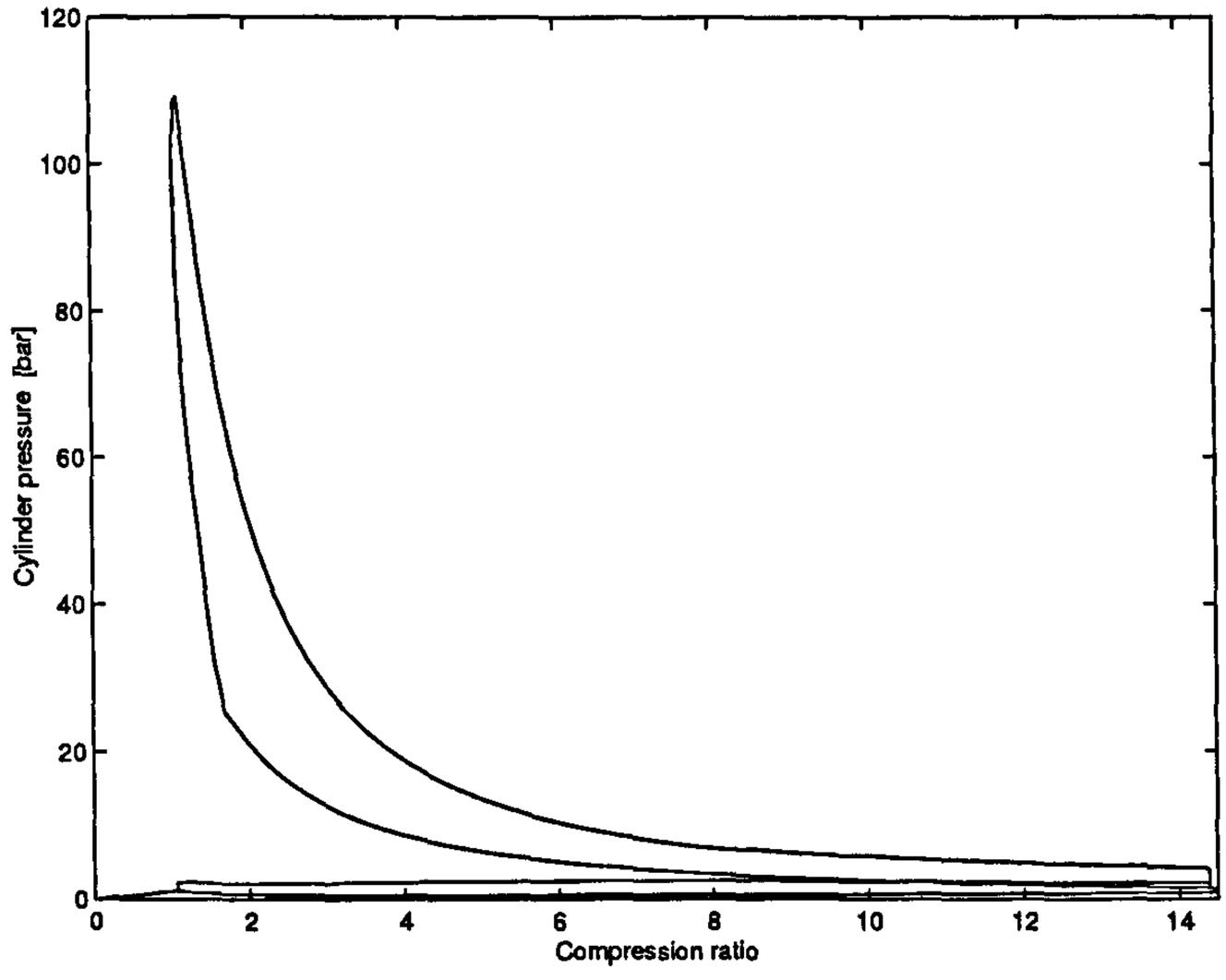

Figure 4.16: Predicted pressure-volume diagram

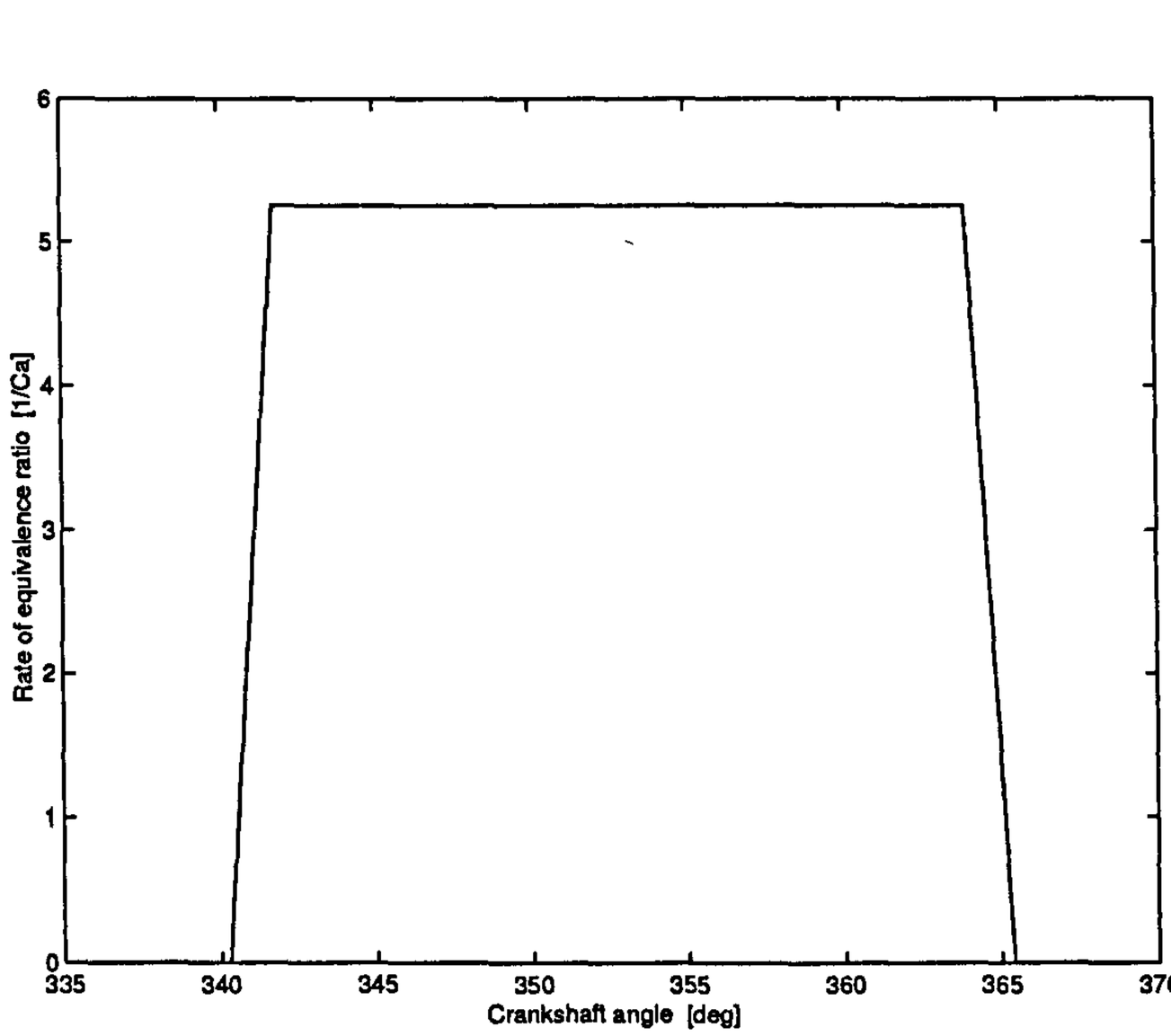

Figure 4.17: Predicted rate of the equivalence ratio for the mixture inside the cylinder

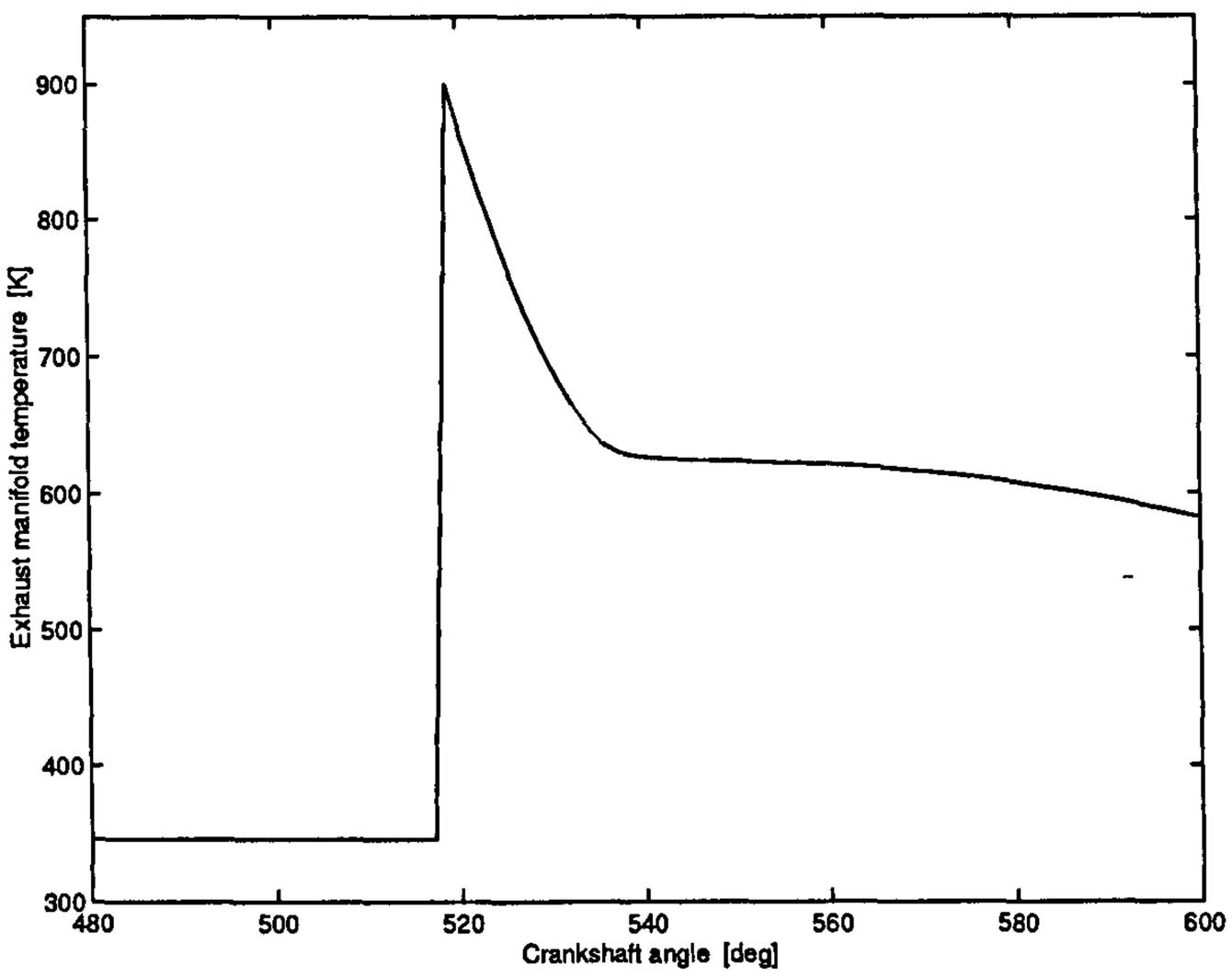

Figure 4.18: Predicted exhaust manifold temperature

4.7 Conclusions

This chapter presents a detailed nonlinear Diesel engine model. The detailed model composes of dynamic model, instantaneous friction model and thermodynamic model in the crank-angle domain. The model is used to predict the in-cycle variation of engine states for both transient and steady-state operating conditions. The model has been implemented in SIMULINK. The model has been validated using measurement from a F1L 210 DEUTZ MAG DI single cylinder Diesel engine. Predicted profiles of the cylinder gas pressure and the instantaneous crankshaft angular velocity through the transient under cold start conditions are in good agreement with measurements. The in cycle inertia variations of the crankshaft is taken into consideration. The importance of including inertia variations is demonstrated.

Chapter 5

Parameter Estimation Based on a Numerical Inversion Technique

5.1 Introduction

As pointed out in Chapter 2 another source of model errors is inaccuracies in system parameters. This chapter presents a method to obtain certain engine parameters by means of a numerical inversion of the dynamical model of a single-cylinder Diesel engine. Thus from data of crankshaft velocity, indicated torque, dynamometer angular velocity and applied load, engine parameters can be estimated. This has two possible applications. First, the engine model parameters, inaccuracies in which is a main source of modelling errors, can be tuned, so improving the modelling accuracy. Second, due to the variety of Diesel engine applications, there is a demand for different types of engines; so the model can be used as a design tool to fulfill customer requirements. The numerically inverted engine dynamic model can be used to design new Diesel engine families. The numerical analysis technique is implemented during both transient and steady state engine response to estimate the parameters.

Inversion of an engine dynamic model has been established as an effective tool for studying engine performance and contributing to design evaluation and new developments. Previous efforts in the area of inverting an engine dynamic model

can be found in [Riz89, ZR93, COC89]. The main aim of these works is to invert the engine dynamic model to describe the relationship between the combustion pressure and engine angular velocity.

In the next section, a numerical inversion technique is presented. In Section 5.3, the numerical technique is applied to the engine model and a brief description of a SIMULINK [SIM97] implementation is presented. The numerical inversion procedure is illustrated by simulation results which are presented in Section 5.4. The inverted model sensitivity is presented in Section 5.5. The engine parameters predicted by numerical inversion are validated through comparison with physical values from two different engines. A comparison between the measured crankshaft velocity and the engine crankshaft velocity predicted by the inverted parameters is also presented. Finally, there is a discussion and some conclusions are drawn.

5.2 Numerical inversion technique

5.2.1 Numerical inversion technique for Engine dynamic model

Let there be n unknown system parameters in the vector $\mathbf{p} \in \mathbb{R}^{n\times 1}$. The dynamic Equations (2.1) and (2.2), can be expressed as a function of $\mathbf{p}$,

$$f(\mathbf{p}) = 0. \tag{5.1}$$

Thus given the measured data, engine angular velocity, indicated torque, dynamometer angular velocity and dynamometer load, Equation (5.1) provides a single equation in the n unknown elements of $\mathbf{p}$. However, to find $\mathbf{p}$, n independent equations are required. These equations are generated by evaluating f at discrete time intervals, $t_1, t_2, \cdots, t_n$. In order to numerically invert the engine dynamic model, the system equations are expressed as functions of an engine parameters vector $\mathbf{p} \in \mathbb{R}^{n\times 1}$.

The engine dynamic Equations (2.1) and (2.2), can now be expressed by n nonlinear equations:

$$f_1(p_1, p_2, \ldots, p_n, t_1) = 0$$

$$\begin{aligned} f_2(p_1, p_2, \ldots, p_n, t_2) &= 0 \\ &\vdots \quad \vdots \\ f_n(p_1, p_2, \ldots, p_n, t_n) &= 0 \end{aligned}$$

This system of n nonlinear equations in n unknowns can alternatively be represented by defining a vector $F \in \mathbb{R}^{n\times 1}$

$$\begin{aligned} F(p_1, p_2, \ldots, p_n) &= (f_1(p_1, p_2, \ldots, p_n), f_2(p_1, p_2, \ldots, p_n), \ldots, \\ & f_n(p_1, p_2, \ldots, p_n))^T = 0. \end{aligned} \tag{5.2}$$

Equation (5.2) can be written as:

$$\mathbf{F(p)} = 0. \tag{5.3}$$

Let $\mathbf{p_0}$ be an initial estimate of $\mathbf{p}$ known to be in the vicinity of the actual solution of $\mathbf{F(p)}$. $\mathbf{F(p)}$ can now be expanded in a Taylor series about this point:

$$\begin{aligned} f_1(p_1, p_2, \ldots, p_n) &= f_{01} + \left.\frac{\partial f_1}{\partial p_1}\right|_0 (p_1 - p_{01}) + \left.\frac{\partial f_1}{\partial p_2}\right|_0 (p_2 - p_{02}) + \ldots \\ f_2(p_1, p_2, \ldots, p_n) &= f_{02} + \left.\frac{\partial f_2}{\partial p_1}\right|_0 (p_1 - p_{01}) + \left.\frac{\partial f_2}{\partial p_2}\right|_0 (p_2 - p_{02}) + \ldots \\ &\vdots \qquad\qquad\qquad\qquad \vdots \\ f_n(p_1, p_2, \ldots, p_n) &= f_{0n} + \left.\frac{\partial f_n}{\partial p_1}\right|_0 (p_1 - p_{01}) + \left.\frac{\partial f_n}{\partial p_2}\right|_0 (p_2 - p_{02}) + \ldots \end{aligned} \tag{5.4}$$

The zero subscript indicates that the functions and all partial derivatives are evaluated at $\mathbf{p_0}$. By setting $\mathbf{F(p)} = 0$ in (5.4) gives n equations in the n unknowns $p_1, p_2, \cdots, p_n$. These equations can be solved using a generalized Newton-Raphson method:

$$\begin{bmatrix} p_1 \\ p_2 \\ \vdots \\ p_n \end{bmatrix} \approx \begin{bmatrix} p_{01} \\ p_{02} \\ \vdots \\ p_{0n} \end{bmatrix} - \left.\begin{bmatrix} \frac{\partial f_1}{\partial p_1} & \frac{\partial f_1}{\partial p_2} & \cdots & \frac{\partial f_1}{\partial p_n} \\ \frac{\partial f_2}{\partial p_1} & \frac{\partial f_2}{\partial p_2} & \cdots & \frac{\partial f_2}{\partial p_n} \\ \vdots & \vdots & \vdots & \vdots \\ \frac{\partial f_n}{\partial p_1} & \frac{\partial f_n}{\partial p_2} & \cdots & \frac{\partial f_n}{\partial p_n} \end{bmatrix}^{-1}\right|_0 \begin{bmatrix} f_{01} \\ f_{02} \\ \vdots \\ f_{0n} \end{bmatrix}. \tag{5.5}$$

The Newton-Raphson method one of the most powerful methods for solving one-dimensional or multi-dimensional and systems of nonlinear equations [BF97], gives rapid convergence, the accuracy approximately doubling with each iteration [Mat92].

5.3 Implementation of the numerical inversion technique

5.3.1 Parameter inversion technique

The numerical inversion technique is implemented for two different engine operating modes, transient and steady state. The transient response is used to estimate three parameters, that is $\mathbf{p} = (J_1, M, J_2)^{\mathcal{T}}$. Six parameters are estimated for the steady state response, that is $\mathbf{p} = (S, D, d, r, L, D_{iv})^{\mathcal{T}}$.

The discrete time intervals $t_1, t_2, \cdots, t_n$, are uniformly spaced over a cycle for the steady state response, although the accuracy appears not to be affected by the time intervals. However, since the engine speed varies during the transient response, the data must be sampled at the same angular position in each cycle. Thus the time interval is nonuniform for the transient response.

From simulation data, it was evident that for the transient response, the initial estimates needed to be within about 60% of their actual values for convergence. However, for the steady state estimations, the parameters always converged.

Prior to sampling, the angular velocity and indicated torque data were averaged over each cycle to reduce noise and fluctuations resulting from high order crankshaft vibrations and the reactive forces from the engine and dynamometer mountings, also to improve the convergence of the technique, as shown in Figure 5.1.

5.3.2 Matlab/SIMULINK implementation

The technique is implemented using Matlab/SIMULINK. Figure 5.2 shows the structure of the SIMULINK model for the numerical inversion technique. The input block contains the measured data, crankshaft velocity, indicated torque, dy-

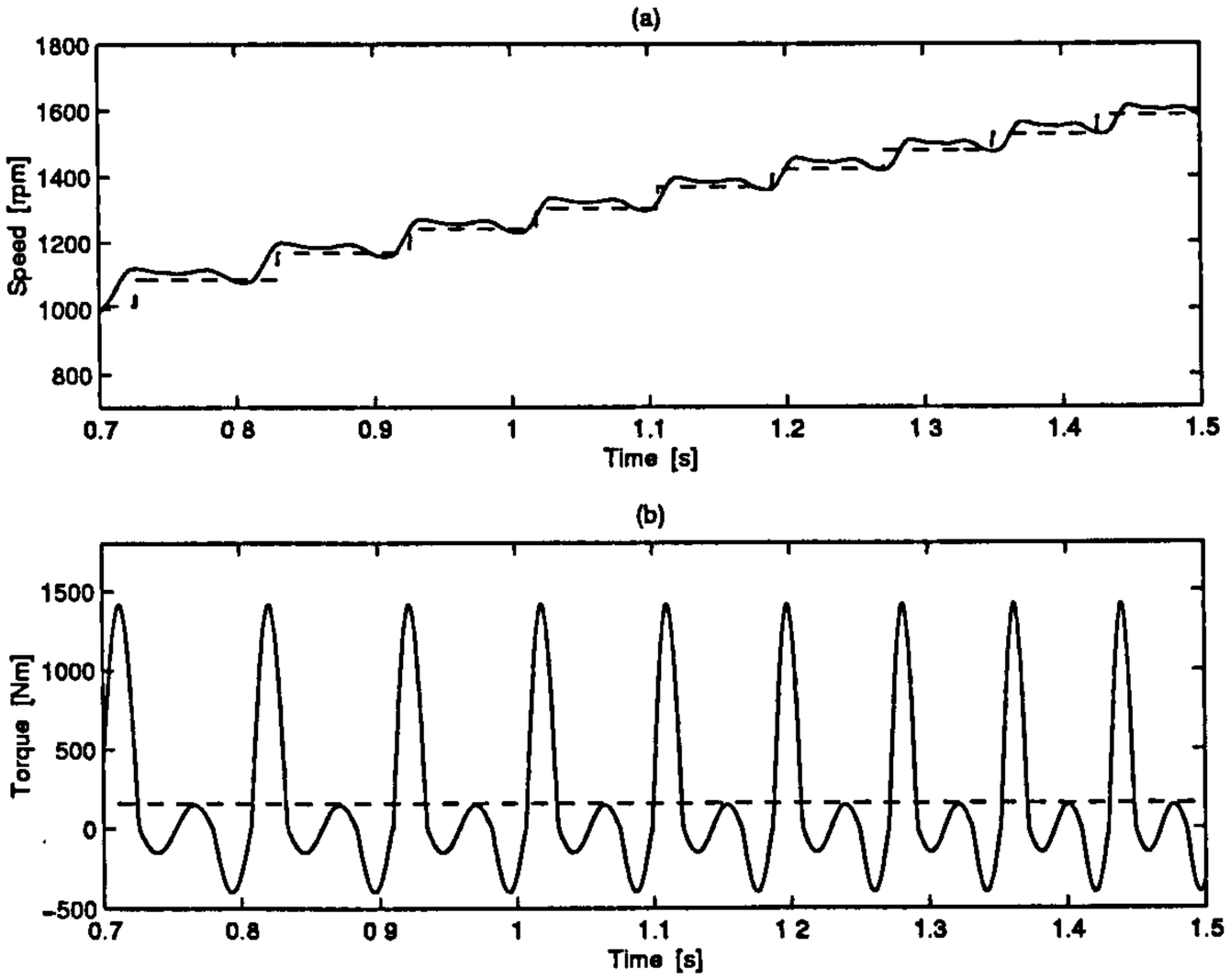

Figure 5.1: (a) Engine speed: before averaging (——) and after averaging (- - -), (b) Indicated torque: before averaging (——)and after averaging (- - -)

namometer velocity and applied load. The output block contains the engine and dynamometer parameters and speed comparison diagrams. The numerical inversion block uses the Newton-Raphson method to estimate the system parameters from the input data. The engine dynamic model block contains the model described in Chapter 2. A comparison of the estimated crankshaft velocity with the measured data is performed in the comparison block. A variable-step Runge-Kutta (4,5) method was used for the simulation.

5.4 Results and model validation

In order to validate the numerical inversion model, both transient and steady state estimations were performed for two single cylinder Diesel engines, labeled A and B, using the same dynamometer. The measured data as well as the engine parameters for engine A are taken from [FA97] and [Fil98], and for engine B are provided by [Kah98].

An initial estimate of J_1 is made from a knowledge of the moments of inertia of the large flywheels, crankshafts, rotating parts of connecting rods and main

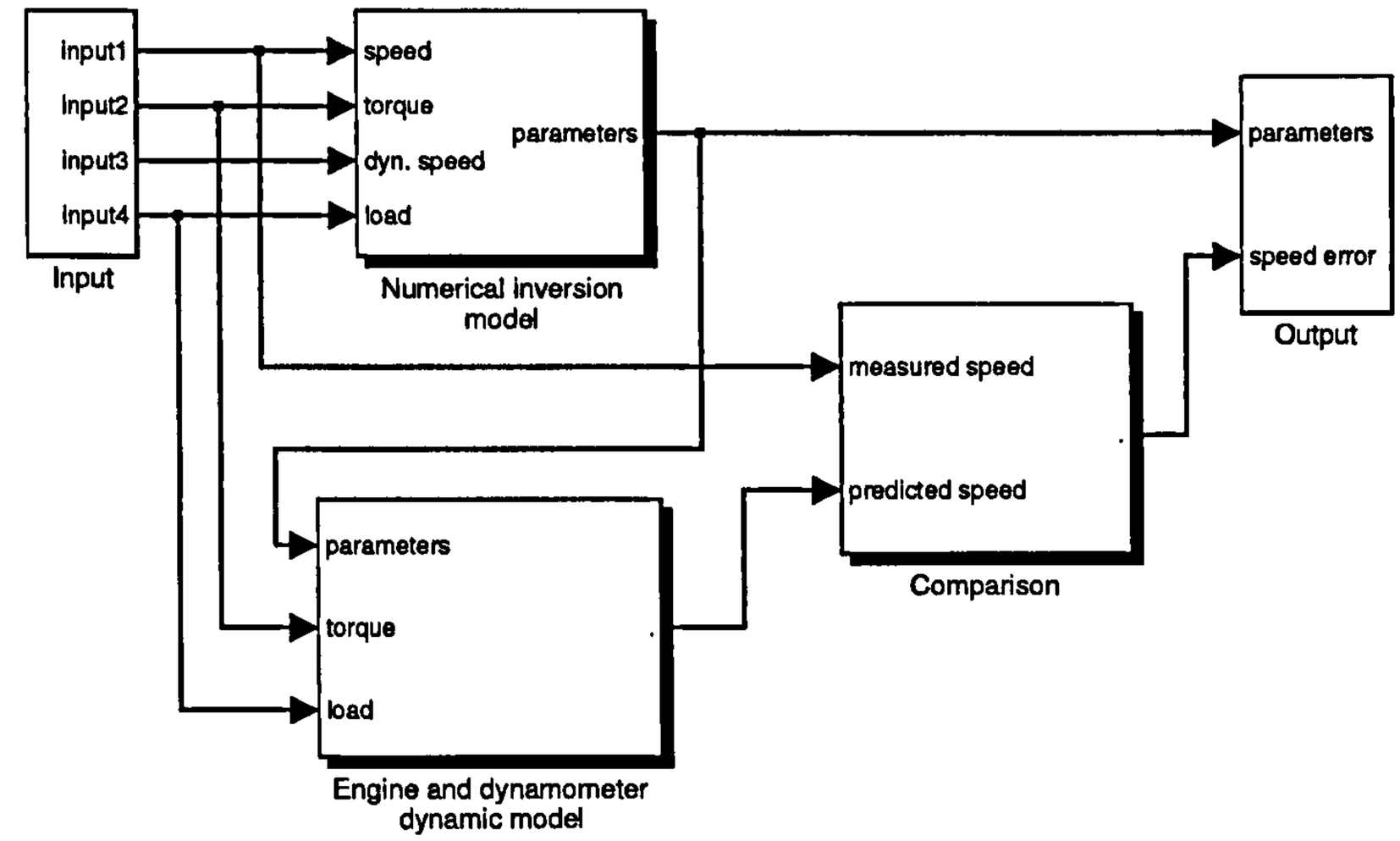

Figure 5.2: Numerical inversion model representation using SIMULINK

Parameter	Units	Predicted Values	Actual Values	Error
d	[mm]	129.7	130.0	0.230%
r	[mm]	079.8	080	0.250%
L	[mm]	267.0	269.3	0.854%
D_{iv}	[mm]	30	30	0.000%
J_1	[kgm^2]	1.4180	1.400	1.286%
M	[kg]	1.100	1.080	1.852%

Table 5.1: Engine A estimated parameters

gears. The predicted values are slightly less than the estimates obtained from the numerical inversion model as shown in Tables 5.1 and 5.2. These discrepancies arise from the fact that the system is time variant and the measured data are averaged at each cycle during the transient response, and the inertia of auxiliary systems (alternator, water pump, fuel pump, oil pump, and camshaft) contribute to the engine moment of inertia. The equivalent masses, M, are approximately computed by considering the mass of pistons, rings, wrist pins, and the small end of connecting rods. These values are slightly less than the estimates obtained from the model as shown in Tables 5.1, and 5.2. These discrepancies arise due to the averaging of data at each cycle and due to the small amount of mass near the small end also contributing to the reciprocating motion. The other values, D_{iv}, d,

r, and L are very close to the estimated values.

The dynamometer inertia, J_2, is approximately calculated by assuming that it is mostly due to the fluid coupling load cell. Because the coupling also contributes to the dynamometer inertia, this value is less than the estimate obtained from the numerical inversion model. The values of S and D are very close to the estimated values as shown in Table 5.3.

Parameter	Units	Predicted Values	Actual Values	Error
d	[mm]	100.7	100.0	0.700%
r	[mm]	62.9	62.5	0.640%
L	[mm]	220.0	218.8	0.550%
D_{iv}	[mm]	28.2	28.0	0.714%
J_1	[kgm^2]	2.223	2.200	1.045%
M	[kg]	1.730	1.700	1.765%

Table 5.2: Engine B estimated parameters

To test the accuracy of the estimated parameters, the crankshaft angular velocity computed using the inverted parameters is compared with measured data for both engines. Almost no external load is imposed by the dynamometer for the first two seconds, so the engine accelerates from low idle speed and passes through the entire speed range until it is at high engine speed as shown in Figure 5.3. The engine accelerates because the net torque value is positive. The overall agreement between the measured and estimated speeds is very good.

Figure 5.4 shows the predicted and measured angular velocities of Engine B during the steady-state. It is noted that these are in good agreement.

Parameter	Units	Predicted Values	Actual Values	Error
J_2	[kgm^2]	0.3775	0.3700	2.027%
S	[Nm/rad]	19153.5	19200	0.242%
D	[Nm/(rad/s)]	125	125	0.000%

Table 5.3: Dynamometer estimated parameters

An additional check on the validity of the numerical inversion model can be performed by mapping the vector $(\mathbf{F}(\mathbf{p}))^{\mathcal{T}} \in \mathbb{R}^n$ into the real line $\mathbb{R}$. A geometric representation for $n = 2$ (for parameters d and r) for both engines are given in

Figures 5.5 and 5.6; it is clear that the value of d and r obtained from graphical intersection and numerical solution are identical.

5.5 Inverted model sensitivity

To test the sensitivity of the numerical inversion model to perturbations in the data, the values of the measured crankshaft angular velocity were perturbed by a small offset. Simulations were performed for Engine A, and the numerical solution converged to a new set of parameters. Figure 5.7 shows the crankshaft angular velocity profiles of measured data, perturbed down and perturbed up. The tuning test is implemented assuming that Engine A achieves the same power profile at all speed modes. The comparison between the results in Table 5.1 and Table 5.4 shows that the inverted model is not over-sensitive.

Parameter	Units	Predicted shift up	predicted shift down
d	[mm]	125.0	134.6
r	[mm]	76	83
L	[mm]	225	281
D_{iv}	[mm]	33	27
J_1	[kgm^2]	1.416	1.420
M	[kg]	1.06	1.095

Table 5.4: Estimated parameters

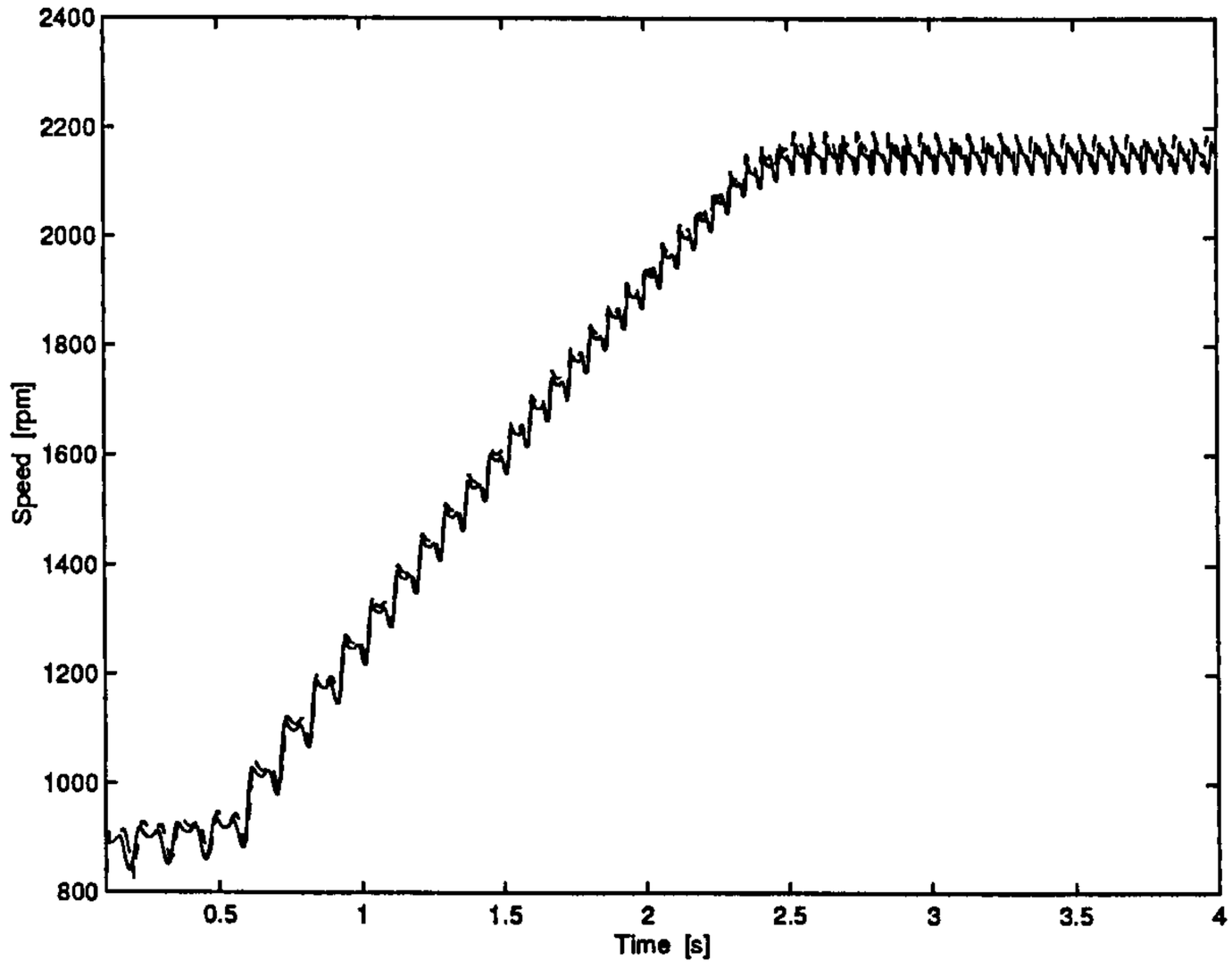

Figure 5.3: Comparison between the predicted (which is calculated from the inverted parameters) (——) and measured [FA97] (- - -) instantaneous speed of Engine A

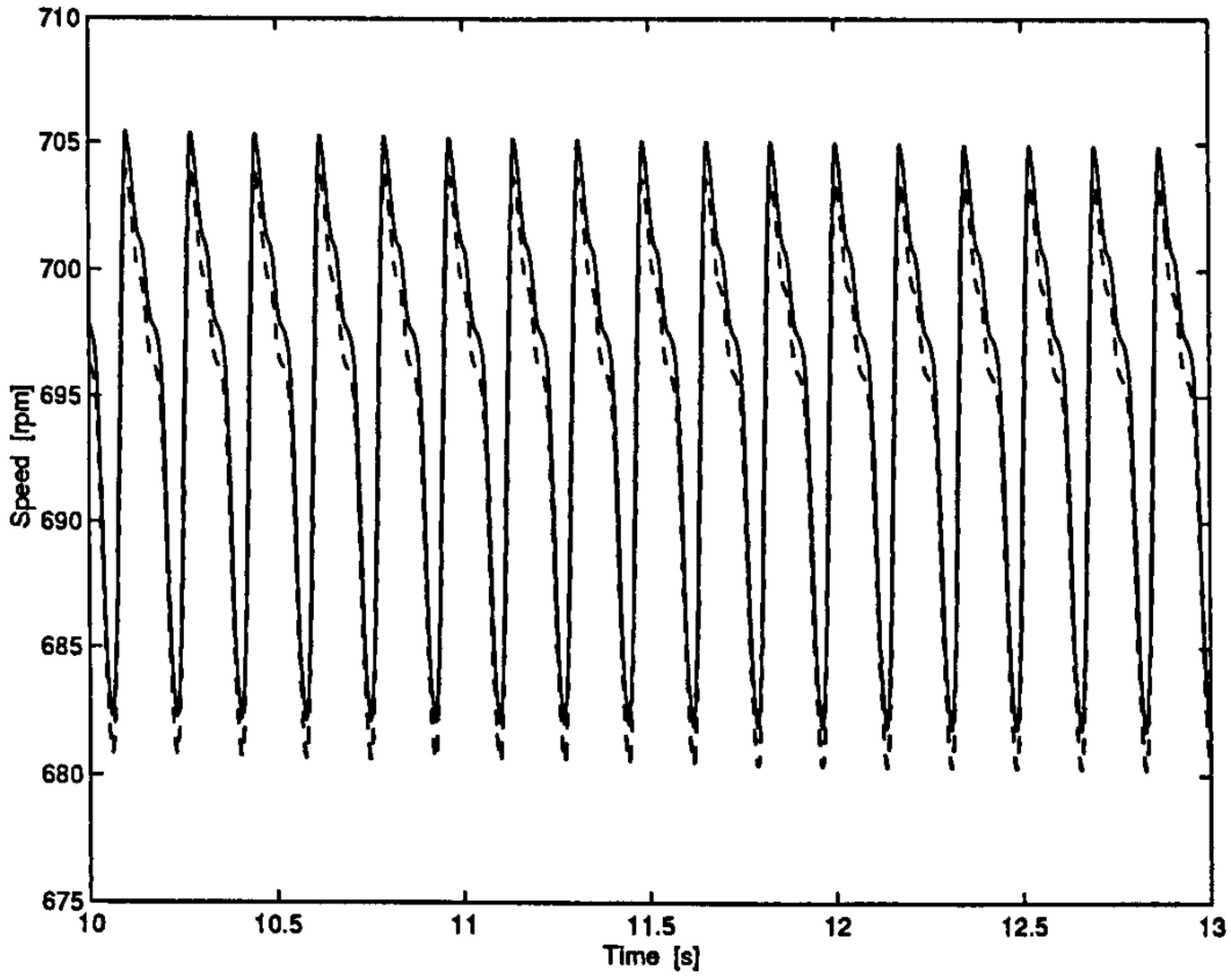

Figure 5.4: Comparison between the predicted (which is calculated from the inverted parameters) (——) and measured [Kah98] (- - -) instantaneous speed of Engine B

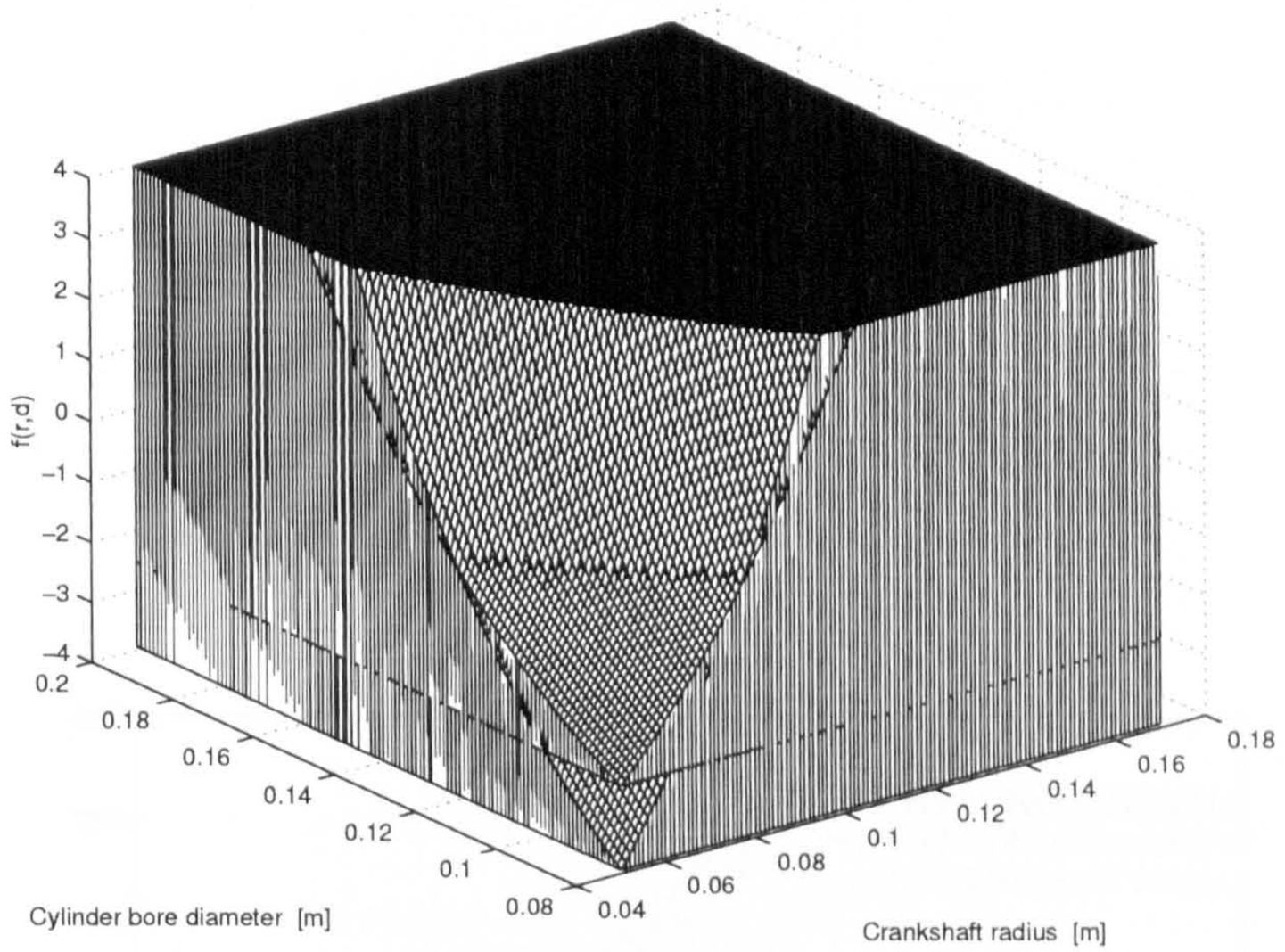

Figure 5.5: Graphical representation for cylinder bore and crankshaft radius of Engine A

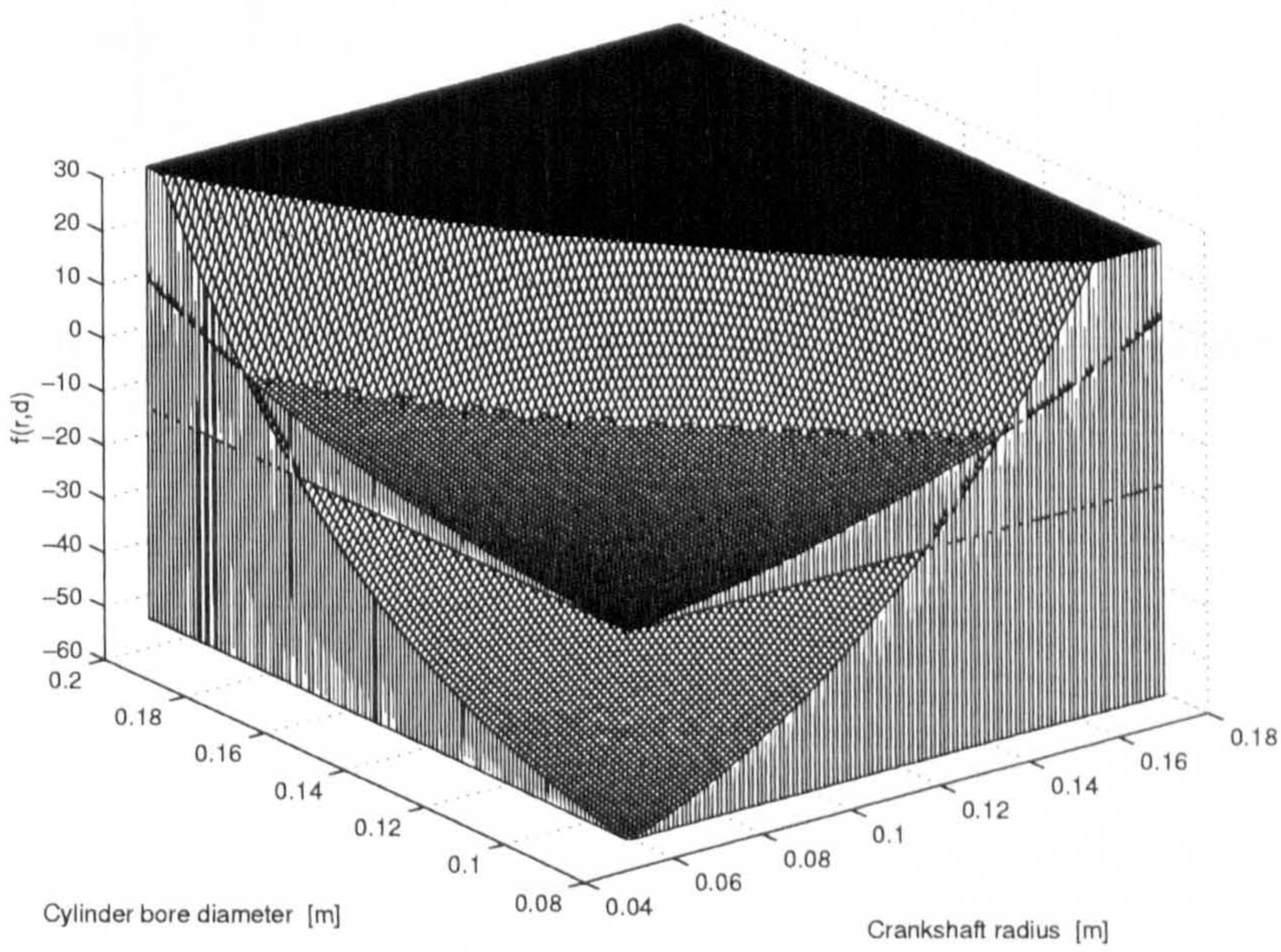

Figure 5.6: Graphical representation for cylinder bore and crankshaft radius of Engine B

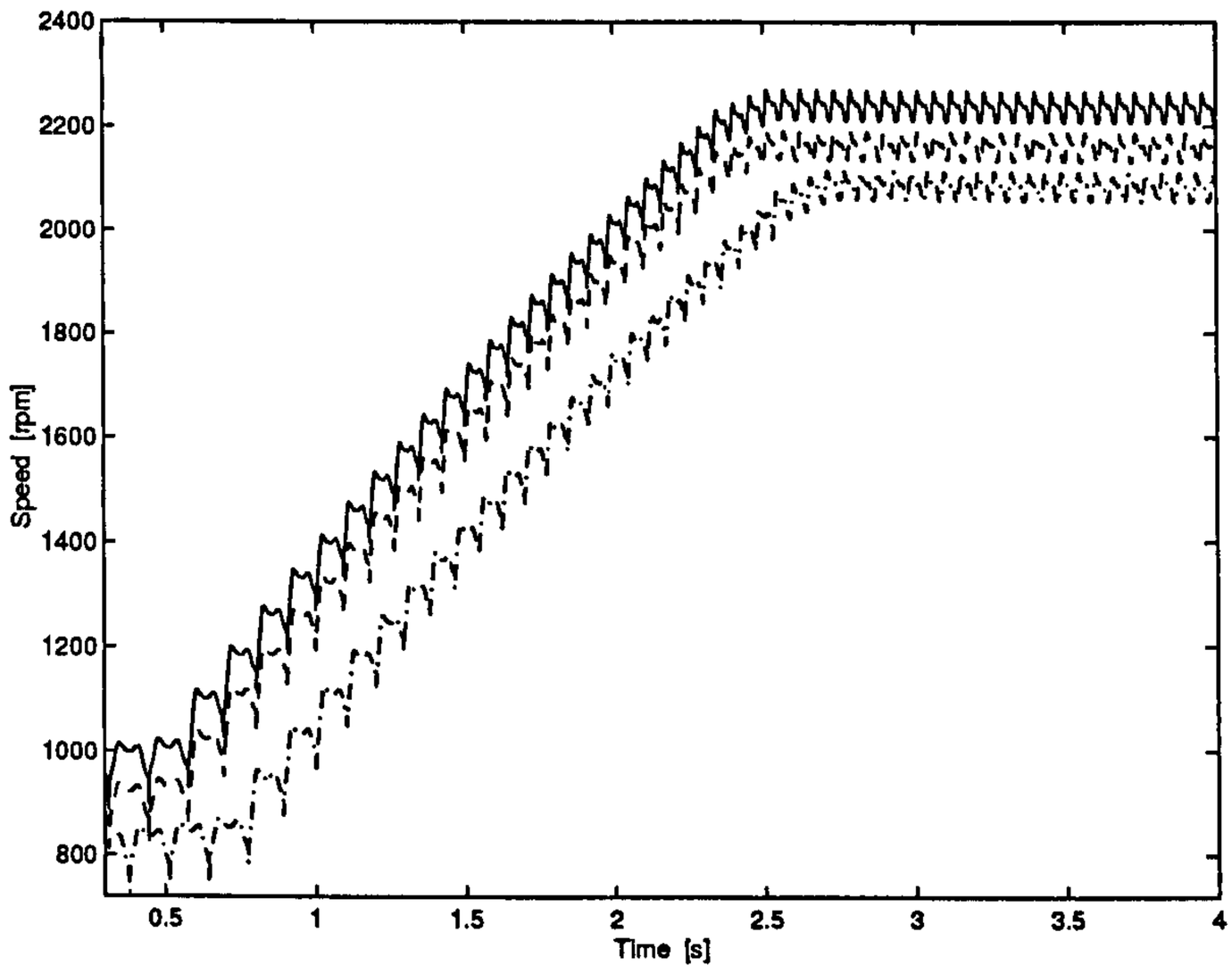

Figure 5.7: Measured [FA97] (- - -), positive offset (——) and negative offset (- · - ·) crankshaft angular velocity profiles of Engine A

5.6 Discussion and conclusions

This chapter presents a numerical inversion method for the dynamic model of a single cylinder Diesel engine. The method can invert the dynamic model parameters at transient and steady state conditions. The inversion model is based on the Newton-Raphson method due to its rapid convergence, the accuracy approximately doubling with each iteration. The input data, crankshaft velocity, indicated torque, dynamometer velocity and applied load is used to calculate the inverted parameters. These are used by the dynamic model to compute the engine angular velocity profile. Predicted profiles of the engines speed calculated from inverted parameters through the transient and steady states are in excellent agreement with measurements. Although a regression technique could also be used to estimate the parameters, the approach presented here is fast and works well.

The main conclusions of this chapter are:

- The numerical inversion model can be used to improve engine dynamic modelling accuracy by estimating more exact parameters.
- The inverted dynamic model parameters have been validated with physical values and are in excellent agreement.
- The numerical inversion model could be used as an engine design tool and for engine design validation.

Chapter 6

Indicated and Load Torque Estimation Using Sliding Mode

6.1 Introduction

Indicated torque has much information regarding the engine performance, such as fuel burning rate, combustion heat release rate and air fuel ratio. It may also be utilised for fault diagnosis of engine combustion and fuel injection timing. For instance, engine misfire or mistiming of fuel injection will increase exhaust gas emissions and will reduce the indicated torque, causing a reduction in engine performance. Indicated torque can be calculated from the measurements of cylinder indicated pressure. However, pressure sensors are expensive and indicated pressure is difficult to access. Therefore, the estimation of indicated torque from an engine dynamic model has significant potential benefit. The estimation accuracy of the indicated torque is affected by the load torque imposed on the engine. Without this estimate crankshaft effects from the load torque can be incorrectly attributed to indicated torque variations, and costly false estimations can result. This chapter describes a nonlinear observer that can be used to estimate both the engine indicated torque and load torque based on low cost measured and more accessible variables.

The measured variables are instantaneous angular velocities and angular dis-

placements of the engine crank shaft and the dynamometer coupling. The dynamic engine model used in this chapter is a suitable candidate for model-based diagnostics since oscillatory engine states are intrinsic in the model and can be related to engine failures. Also, inclusion of the inertia variation with piston pin offset effects, especially at high engine speeds, significantly decreases the occurrence of false diagnostics due to more accurate pressure estimation, and can predict Diesel engine behaviours. Large inertial force errors, caused by the highly nonlinear nature of engine geometry, limit the use of other cylinder pressure estimation schemes.

One of the underlying assumptions in the design and analysis of the sliding mode observer systems is that the control can be switched from one value to another infinitessimally fast. In practice, this must take a finite time, and this causes a chattering effect.

Estimation of cylinder pressure by using crank shaft angular velocity is investigated in many papers in the literature. For examples, papers [CC93, Riz89, COC89], consider linear models for the engine dynamic model. Thus, modelling errors increase significantly when the engine is operated at high speed. In [RZ94, ZR93, SRTL92], nonlinear inertia variations and load effects are not explicitly explored, and this leads to inaccuracy of the indicated torque estimation. [KRW99], applies the unknown input observer (UIO) methodology to estimate engine torque in a multi cylinder engine. This works in a mostly linear problem setting and thus is most suitable for steady state (constant speed) applications. Since some matrix transformations are required when performing the UIO methodology, the physical representation of the state variables of the UIO is not explicit and the computational load is relatively high.

Torque estimators based on sliding mode observers can be found in [KM94, CM97, SM95]. All these estimators are implemented in the time domain. Engine events such as, fuel injection, valve opening, etc however are periodic with crank angle. So it is more beneficial to design control and observation schemes that operate in the crank angle domain. Estimation of indicated torque from the crankshaft angular velocity measurement has been investigated by [RDW95, WKR97]. In

[WKR97] a crank angle based model is used to design the observer and crankshaft angular velocity is sampled uniformly at discrete crank angle intervals. But the limitations of their work are:

- nonlinear inertia variations are not included, this will affect the indicated torque estimation accuracy at high engine speed,

- the load torque is ignored, this significantly affect the accuracy of the indicated torque estimation,

- the observer gain function does not represent the real topology of the indicated pressure during the engine stroke (from intake to exhaust) which still gives a certain amount of chatter,

- the dynamometer coupling position was calculated by integrating the ratio between the dynamometer and engine speeds, so any measurement bias will increase with the crank angle leading to divergence.

In this chapter a technique is presented to design a robust observer to estimate the indicated torque and load torque. The developed observer is based on the two degree of freedom engine dynamic model described in Chapter 2, and transformed into the crank angle; Section 4.2. The sliding mode observer is chosen for this study because of its robustness and convergence. The estimated torque from this observer has a good accuracy when compared to experimental data.

The chapter is arranged as follows. In the next section, the engine dynamic model is summarized. In Section 6.3, the observer design, observer stability and selection of the observer gain are investigated. Simulation results are presented in Section 6.4, and the estimated behaviour compared with experimental data. In Section 6.5, the observer sensitivity is presented. Finally there is a discussion and the main conclusions are drawn.

6.2 Engine dynamic model

6.2.1 System description

Figure 2.1 shows a model of an engine coupled to a dynamometer. The model is discussed in detail in Chapter 2; transformed into crank angle domain and includes the inertia variations; Section 4.2.

6.2.2 Friction model

The friction torque terms include the hydrodynamic bearing friction torque, T_{f3}, Equation (3.8); the valve train friction torque, T_{f5}, Equation (3.13); and auxiliaries losses torque, T_{f6}, Equation (3.14), as discussed in Chapter 3. The piston assembly friction T_{f1} given by Equation (3.1) is a function of the indicated pressure. In order to simplify the observer and enable stability analysis, an alternative piston assembly friction, as given by [Bis65], is taken as

$$T_{f1} = 42.8 \left[\frac{(c)^{0.20} r V_d}{d} \right] \omega. \tag{6.1}$$

[Bis65] gives the expression as a mean effective pressure. Here it is transformed to a torque as discussed in Chapter 2.

6.2.3 State space representation

Let the states of the dynamic model be defined as $x_1 = \omega_1$, $x_2 = \omega_2$, $x_3 = \theta_2$. The state space representation of Equations (4.10) and (4.11) can then be written as:

$$\dot{x}_1 = \frac{1}{\tau x_1} \left[T_i(\theta_1) - \left[M r^2 G(\theta_1) G_1(\theta_1) + \frac{1}{2} \frac{\partial J_1(\theta_1)}{\partial \theta_1} \right] x_1^2 - \sum_{k=1}^{5} T_{fk} - S(\theta_1 - x_3) - D(x_1 - x_2) \right], \tag{6.2}$$

$$\dot{x}_2 = \frac{1}{J_2 x_1} \left[S(\theta_1 - x_3) - D(x_1 - x_2) - T_L \right], \tag{6.3}$$

$$\dot{x_3} = \frac{x_2}{x_1}, \tag{6.4}$$

6.3 Nonlinear sliding mode observer design

This section examines a sliding mode observer methodology for the estimation of unknown inputs. The hint to the solution lies in constructing a supplementary dynamic system described by differential equations with a discontinuous switching component, and then intentionally create a sliding motion in the supplementary system [ES98, HGH93]. According to the developed engine dynamic model, an indicated torque and load torque estimator is designed using a sliding mode observer. If the crank shaft angular velocity, $\omega_1 = x_1$, the coupling velocity, $\omega_2 = x_2$, and the coupling displacement, $\theta_2 = x_3$, are measured, then the output equations are

$$y_1 = x_1 \tag{6.5}$$

$$y_2 = x_2 \tag{6.6}$$

$$y_3 = x_3 \tag{6.7}$$

The observer is designed as follows:

$$\dot{\hat{x}}_1 = \frac{1}{\tau y_1}\left[\hat{T}_i(\theta_1) - \left[Mr^2G(\theta_1)G_1(\theta_1) + \frac{1}{2}\frac{\partial J_1(\theta_1)}{\partial \theta_1}\right] y_1^2 - \sum_{k=1}^{5} T_{fk} - S(\theta_1 - y_3) - D(y_1 - y_2)\right], \tag{6.8}$$

$$\dot{\hat{x}}_2 = \frac{1}{J_2 y_1}\left[S(\theta_1 - y_3) - D(y_1 - y_2) - \hat{T}_L\right], \tag{6.9}$$

$$\dot{\hat{x}}_3 = \frac{y_2}{y_1}. \tag{6.10}$$

where ($\hat{}$) refers to the estimated variable. The term x_3 is equal to the integral of the ratio between the dynamometer and engine speed, $\frac{y_2}{y_1}$, but even if there is a small offset at the beginning, it is going to increase with respect to the crank angle

leading to divergence in the estimated parameters. Instead, unlike in [WKR97], the dynamometer angular position is measured. Let the estimated engine torque be formulated as

$$\hat{T}_i(\theta_1) = -m_1 \operatorname{sgn}(s_1) A_p r G(\theta_1) \tag{6.11}$$

where m_1 is positive scalar quantity (indicated torque observer gain), $s_1 = (G(\theta_1)(\hat{x}_1 - y_1))$ and sgn is the signum function, which is given in Equation (2.15).

Let the estimated load torque be

$$\hat{T}_L = -m_2 \operatorname{sgn}(s_2)(|s_2| + \delta(\theta_1)) \tag{6.12}$$

where m_2 is positive scalar quantity (load torque observer gain), $s_2 = (\hat{x}_2 - y_2)$ and $\delta(\theta_1)$ is a function that represents the difference between the measured engine and the coupling speeds without load for one engine cycle. In cases where the engine is connected to the vehicle transmission, $\delta(\theta_1)$ represents the difference between the measured engine and the transmission output shaft speeds. This function captures differences in speed measurements in the real world due to, for example, damping, backlash, clearance, etc. The load torque on Diesel engines can be estimated by using the proposed method.

Researchers have proposed several algorithms to select the gains of the observer, e.g., Constant gain, Kalman Filter, extended Kalman Filter, Pole-placement method and Frequency Shaping Method [UGS99].

If the estimation errors are written as:

$$e_1 = (\hat{x}_1 - x_1), \quad e_2 = (\hat{x}_2 - x_2), \quad e_3 = (\hat{x}_3 - x_3)$$

then from Equations (6.2)-(6.4) and (6.8)-(6.10) the following error system is obtained

$$\dot{e_1} = \frac{1}{\tau y_1}\left[-T_i(\theta_1) - m_1 \operatorname{sgn}(G(\theta_1)(\hat{x}_1 - y_1)) A_p r G(\theta_1)\right], \tag{6.13}$$

$$\dot{e_2} = \frac{1}{J_1 y_1}\left[T_L + m_2 \operatorname{sgn}(\hat{x}_2 - y_2)(|(\hat{x}_2 - y_2)| + \delta(\theta_1))\right], \tag{6.14}$$

$$\dot{e_3} = 0. \tag{6.15}$$

If $e_3 = 0$, there is a sufficient value of the gains m_1, m_2, such that the reachability condition (sign condition) is satisfied. This generates sliding modes, such that e_1, $e_2 \to 0$ when $\theta_1, \theta_2 \to \infty$. This implies

$$\hat{T}_i(\theta_1) = -m_1 \operatorname{sgn}(G(\theta_1)(\hat{x}_1 - y_1))A_p r G(\theta_1) \approx T_i(\theta_1), \tag{6.16}$$

$$\hat{T}_L = -m_2 \operatorname{sgn}(\hat{x}_2 - y_2)(|(\hat{x}_2 - y_2)| + \delta(\theta_1)) \approx T_L. \tag{6.17}$$

From a mathematical viewpoint, the model used in the design of an observer structure must be close to the physical model, if an accurate estimation is desired. It is noted that the mathematical model used in this chapter is a nonlinear dynamic model, and ables to predict the engine behaviour during transient response.

6.3.1 Stability of the observer

Lemma 1 *If the estimation error $e_3 = 0$, there are sufficiently large gains m_1 and m_2 such that the sign of Equations (6.13) and (6.14) will be dominated by sign of the terms $-m_1 \operatorname{sgn}(G(\theta_1)(\hat{x}_1 - y_1))A_p r G(\theta_1)$ and $-m_2 \operatorname{sgn}(\hat{x}_2 - y_2)(|(\hat{x}_2 - y_2)| + \delta(\theta_1))$ respectively, leading to $e_1, e_2 \to 0$ as $\theta_1, \theta_2 \to \infty$ such that the sign condition is satisfied [Utk78, UGS99], then*

$$\hat{T}_i(\theta_1) \approx T_i(\theta_1) \tag{6.18}$$

and

$$\hat{T}_L \approx T_L \tag{6.19}$$

Proof: From Equation (6.15)

$$\dot{e_3} = 0, \tag{6.20}$$

the lemma can be proved by defining a Lyapunov function as follows

$$\ell(e_3) = \alpha e_3^2 \tag{6.21}$$

where α is any positive number, and suppose the system equation is given as $F(e_3)$. Then the system is stable if

$$F(e_3).\nabla \ell(e_3) \leq 0, \tag{6.22}$$

which gives

$$2\alpha e_3 \dot{e_3} \tag{6.23}$$

by substituting Equation (6.15) into Equation (6.23) yields

$$F(e_3).\nabla \ell(e_3) = 0. \tag{6.24}$$

Hence the system is stable, and $e_3 = 0$. ■■

6.3.2 Construction of the indicated torque observer gain

The sliding mode is used such that the estimated torque gain (m_1) is constant. The estimation results using constant gains are shown in Figure 6.1, where the solid line is the measured indicated torque and the dashed line is the estimated torque. The solid area in Figure 6.1 (b) results from the high frequency switching at high observer gain. While bad estimation results are obtained using low observer gain, a strong chattering exists in the estimated indicated torque at high observer gain. The measured data which are used for the comparison in Figure 6.1 are taken from [FA97] and [Fil99]. The geometrical specifications for the engine are shown in Table G.1, in Appendix G.

It was found that the chattering behaviour can be eliminated by varying the observer gain as a function of crank-angle. Since the indicated torque is strongly dependent on the indicated cylinder pressure, the observer gain has a relationship with the indicated cylinder pressure. Thus the observer gain is defined to be a function of the stroke. The magnitude of the gains should be large enough to satisfy the sign condition. The observer gain is selected to be equal for both the exhaust and the intake strokes. For the gain during the combustion and expansion stroke, it is sufficient to set the observer gain value to be approximately equal to the maximum value of the cylinder indicated pressure. Figure 6.2 shows the observer gain as a function of the engine crank shaft angle.

The benefit of using a variable observer gain as a function of crank angle is seen in Figure 6.3, where subplot (a) is the indicated torque relative error when using a variable observer gain, while subplot (b) represents the indicated torque

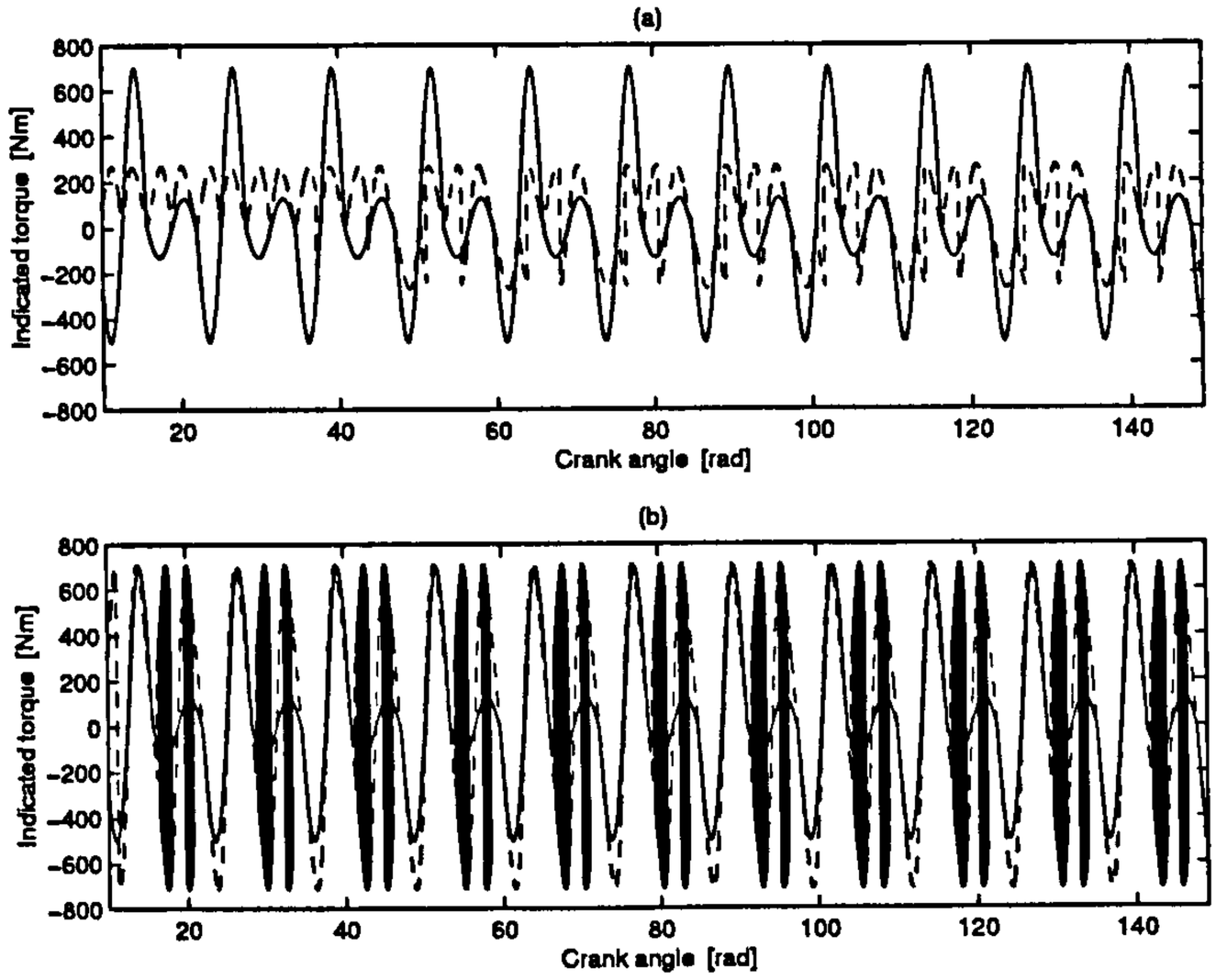

Figure 6.1: Comparison between estimated (- - -) and measured (——) [FA97] cylinder indicated torque : (a) with low observer gain (m_1=20000) and (b) with high observer gain (m_1=5300000)

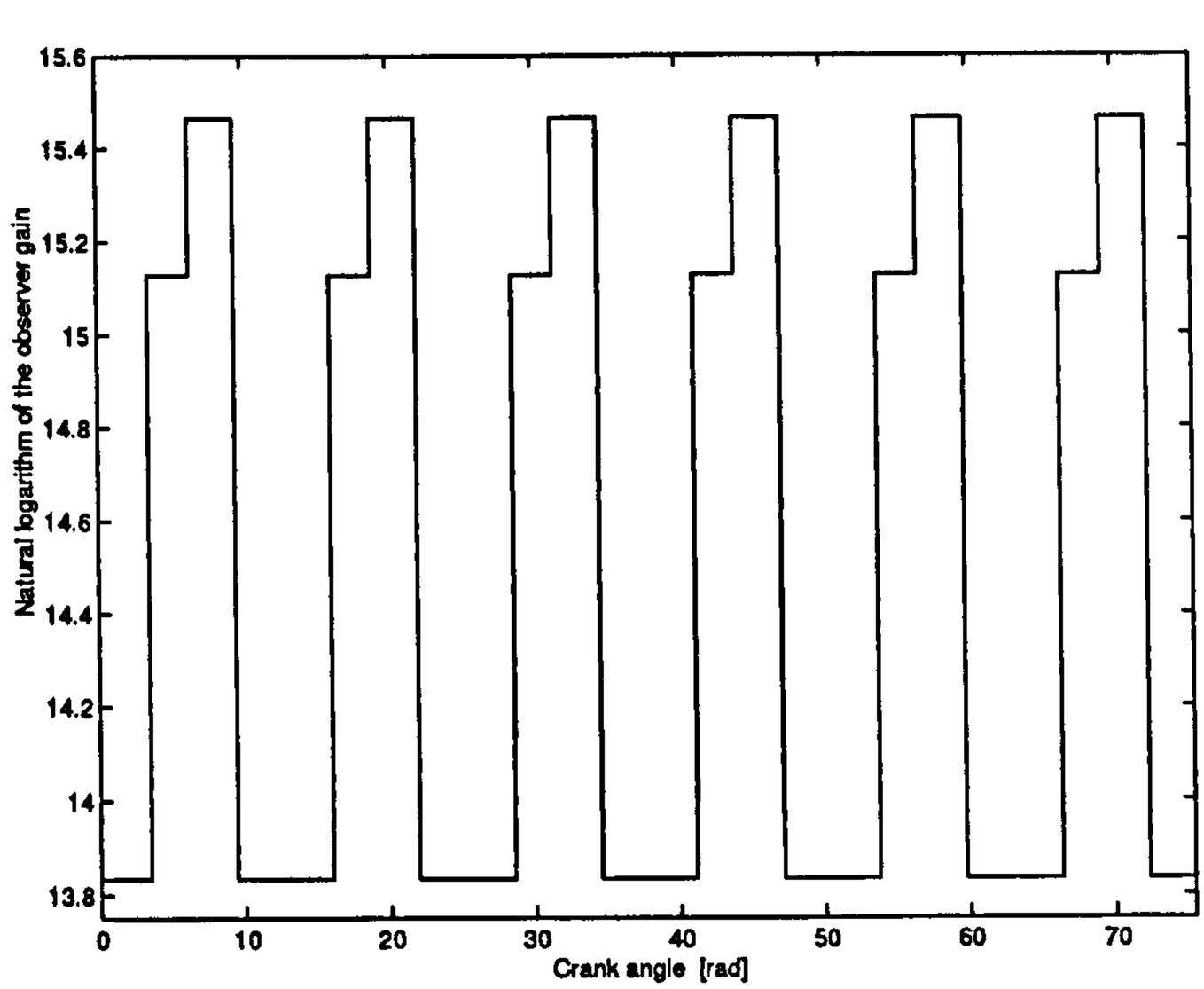

Figure 6.2: Observer gain as a function of the engine crank shaft angle

relative error when using fixed high observer gain. It is clear that the estimation accuracy is improved with variable gain.

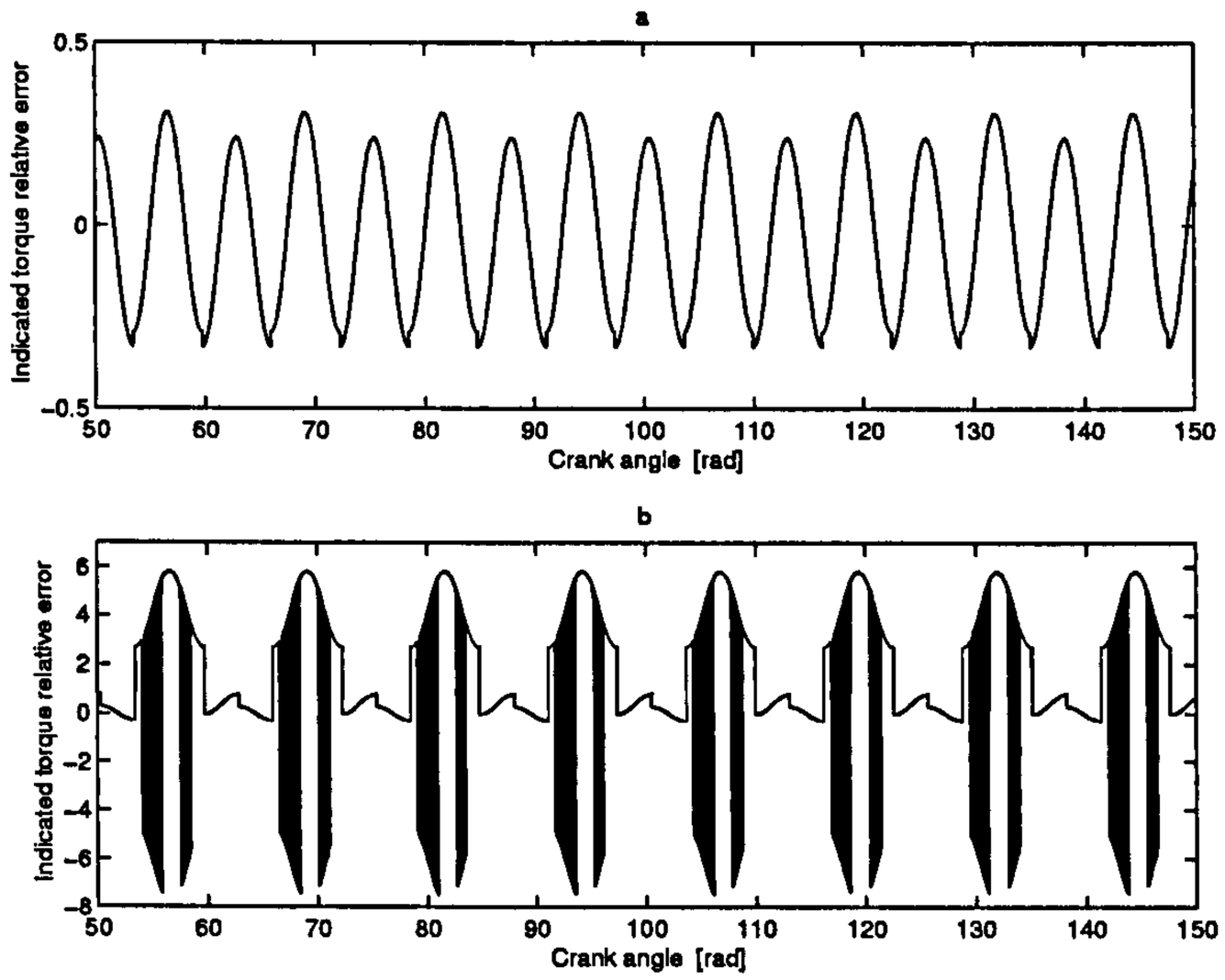

Figure 6.3: Indicated torque relative error: (a) with variable observer gain and (b) with constant observer gain

6.4 Observer simulation and validation

In order to validate the behaviour of the observers with experimental results, the two degree of freedom single cylinder Diesel engine dynamic model, developed in Chapter 2 and the transformation into crank angle domain in Section 4.2 is used. The geometrical specifications for the engine are shown in Table G.1. The measured data are taken from [FA97] and [Fil99].

The validation of the sliding mode observer is carried out during transient engine response, and the engine speed is used to estimate the indicated torque is shown in Figure 6.4. Figure 6.5 shows that the observer has converged to the correct indicated torque after about two engine cycles. A comparison between the estimated and measured indicated engine torque shows a good agreement.

The estimation accuracy of the indicated torque is affected by the load torque imposed on the engine. Figure 6.6 shows a comparison between the measured and estimated engine indicated torque, where the observer tries to compensate the load imposed on the system, by giving a negative torque at certain crank shaft angle positions. This gives inaccurate estimations. To overcome this problem, a load torque observer is added to the system, and the combined observer, gives better estimation accuracy, Figure 6.7. A comparison between relative indicated torque error with and without load estimation is shown in Figure 6.8 and it is clear that load estimation significantly improves observer predictions.

An arbitrary load is imposed on the engine to study the validity of the load observer. Figure 6.9 shows a comparison between the imposed and estimated loads, where there is good agreement, confirming accurate estimation of the indicated torque.

6.5 Sensitivity of the observer

Two different types of tests are carried out on the estimation of indicated torque to test the sensitivity of the observer. In the first test (0.15) white noise power is used to represent measurement noise of the crank shaft angular velocity, Figure 6.10. Table 6.1 gives the estimation error of the indicated torque for different tests. The absolute percent mean relative error is given by $100 \times \left| \left(\frac{\int_0^{\theta_1} \left((T_i - \hat{T}_i)/T_i \right) d\theta_1}{\int_0^{\theta_1} d\theta_1} \right) \right|$. The validity of the estimated torque with noisy speed signals is shown in Figure 6.11, and there is a slight increase in the percent mean relative error as shown in Table 6.1.

The second test is carried out by assuming engine parameters and friction perturbation; the engine parameters are perturbed ±3% and ±7% and the friction is perturbed ±7% and ±15% respectively. The estimation error from Table 6.1 indicates that the observer is not sensitive to the perturbations and converges with reasonable accuracy. The estimation of the indicated torque at parameters and friction perturbations of ±7% and ±15% respectively is shown in Figure 6.12.

Absolute percent mean relative error of the indicated torque with white noise in speed signals	4.04%
Absolute percent mean relative error of the indicated torque with parameters and friction perturbations of ±3% and ±7% respectively	2.93%
Absolute percent mean relative error of the indicated torque with parameters and friction perturbations of ±7% and ±15% respectively	6.30%

Table 6.1: Estimation errors for various conditions

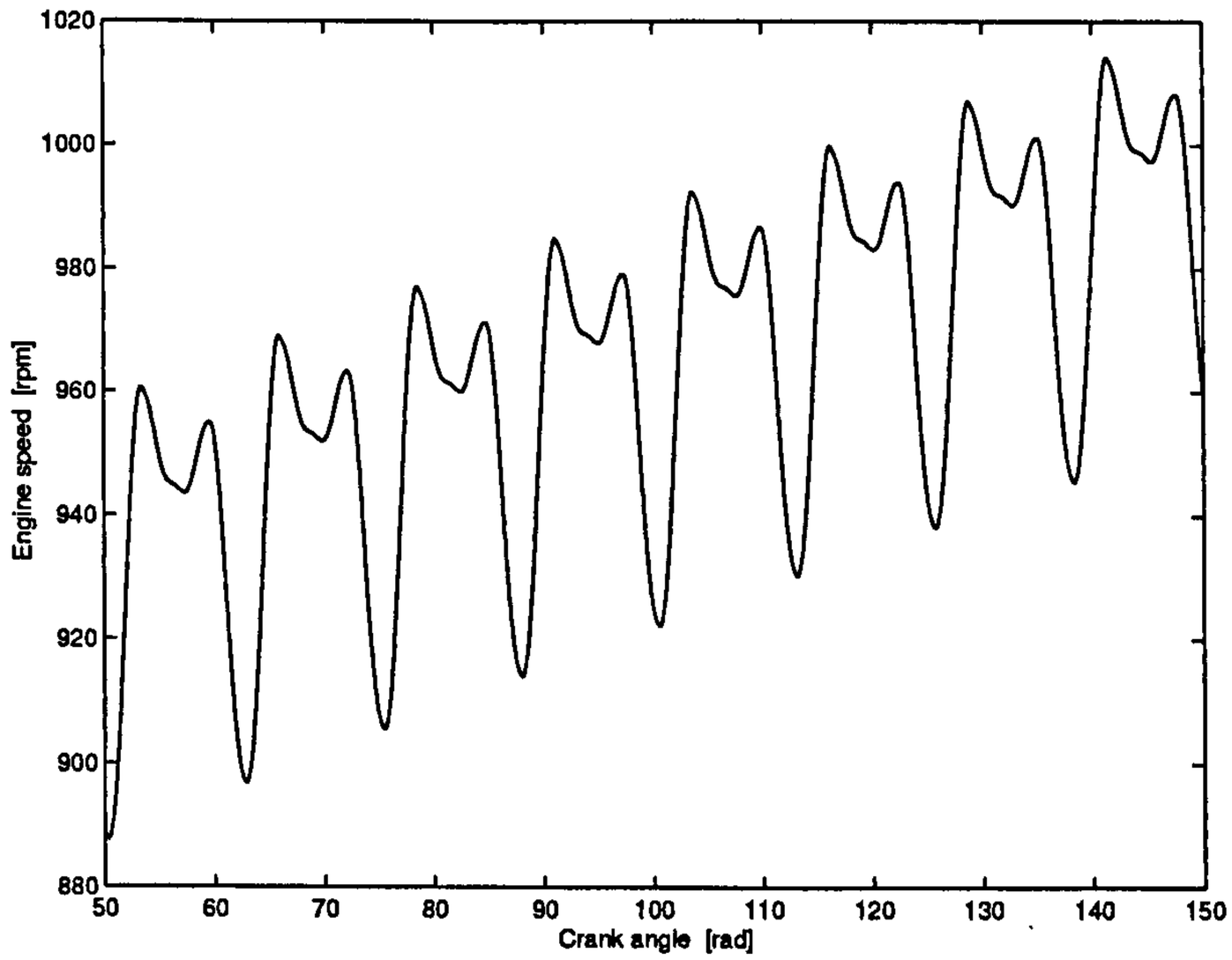

Figure 6.4: Measured engine speed [FA97]

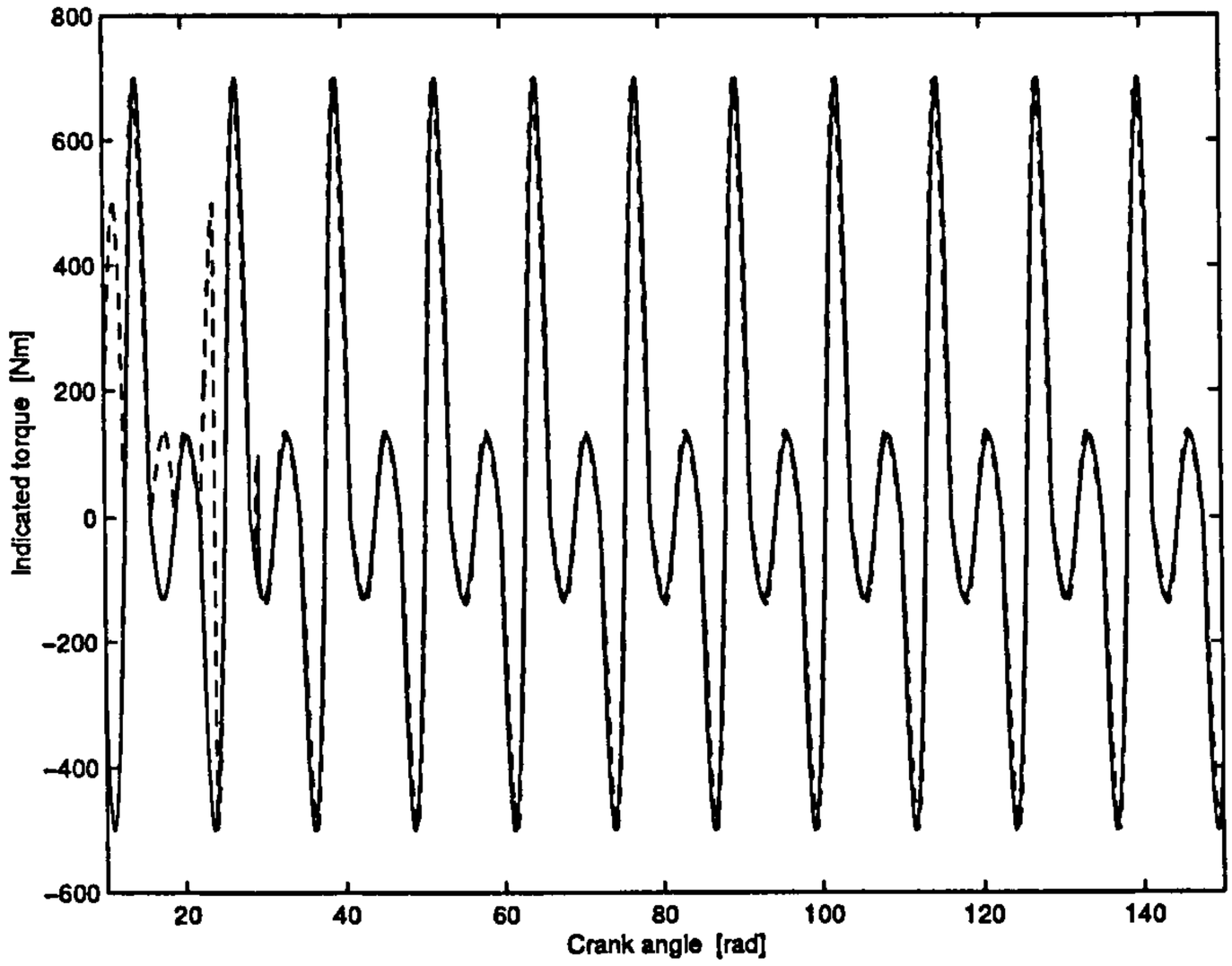

Figure 6.5: Comparison between measured (——) [FA97] and estimated (- - -) engine indicated torque

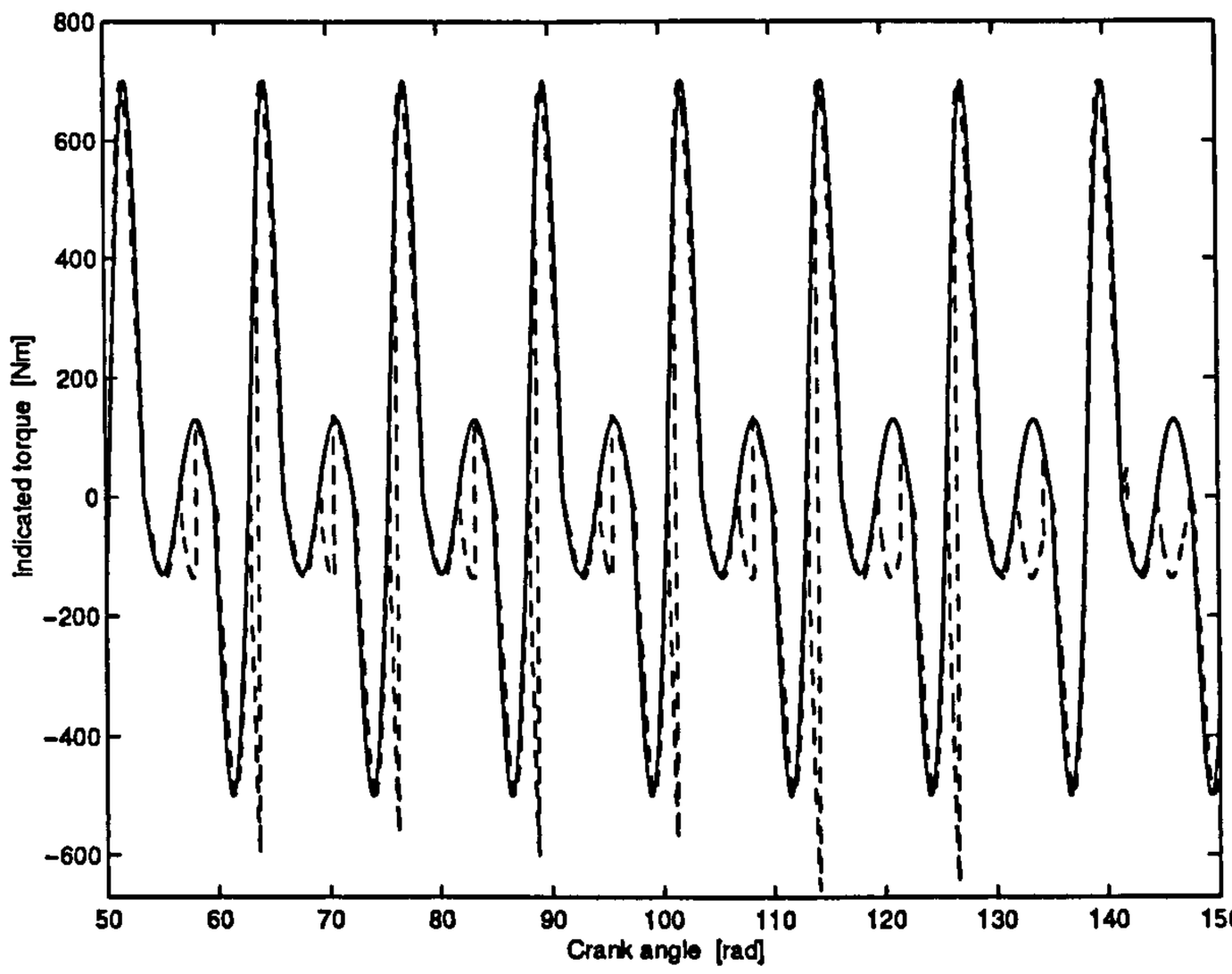

Figure 6.6: Comparison between measured (——) [FA97] and estimated (- - -) engine indicated torque without load estimation

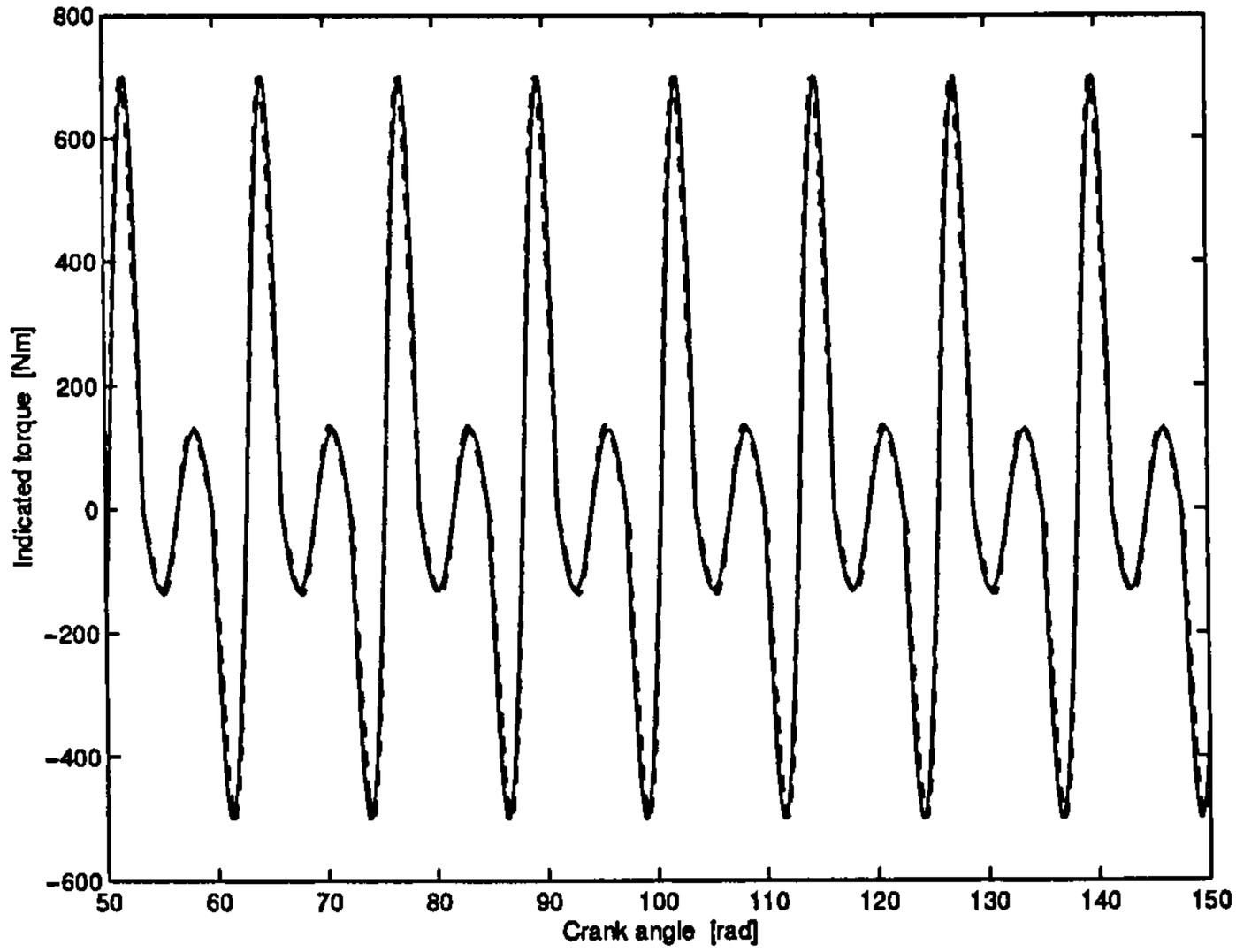

Figure 6.7: Comparison between measured (——) [FA97] and estimated (- - -) engine indicated torque with load estimation

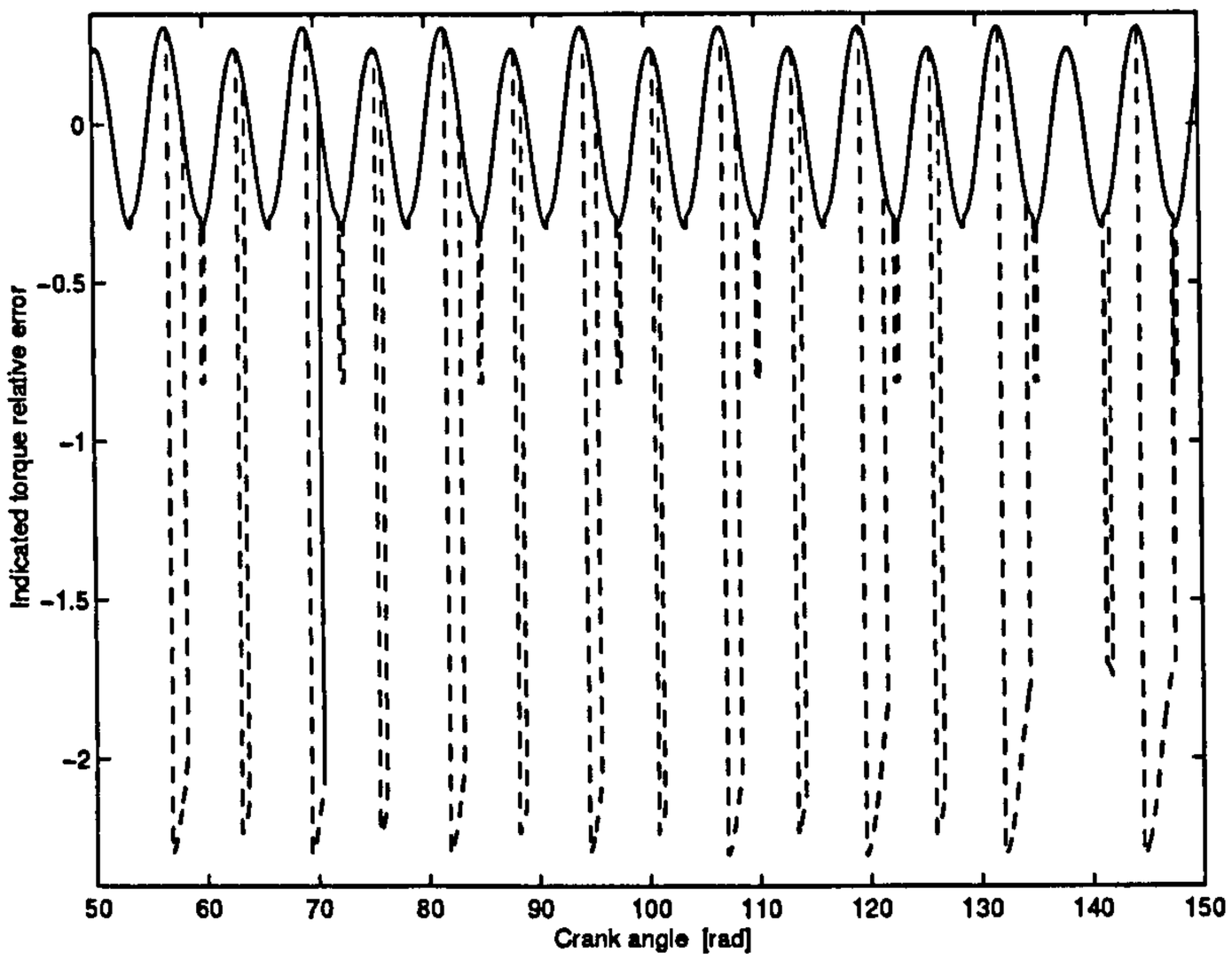

Figure 6.8: Indicated torque relative error with load estimation (——) and (- - -) without load estimation

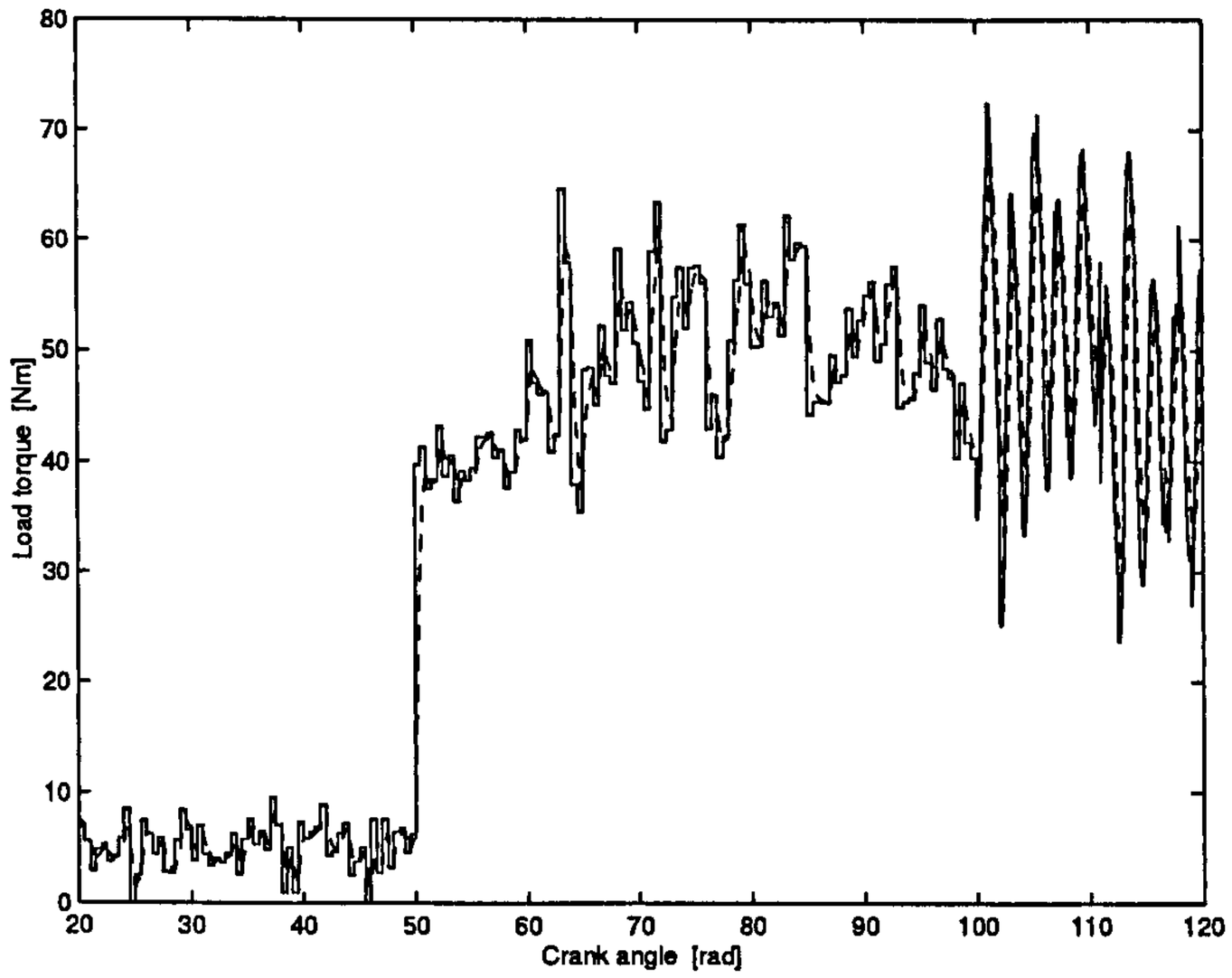

Figure 6.9: Comparison between reference (——) and estimated (- - -) load torque

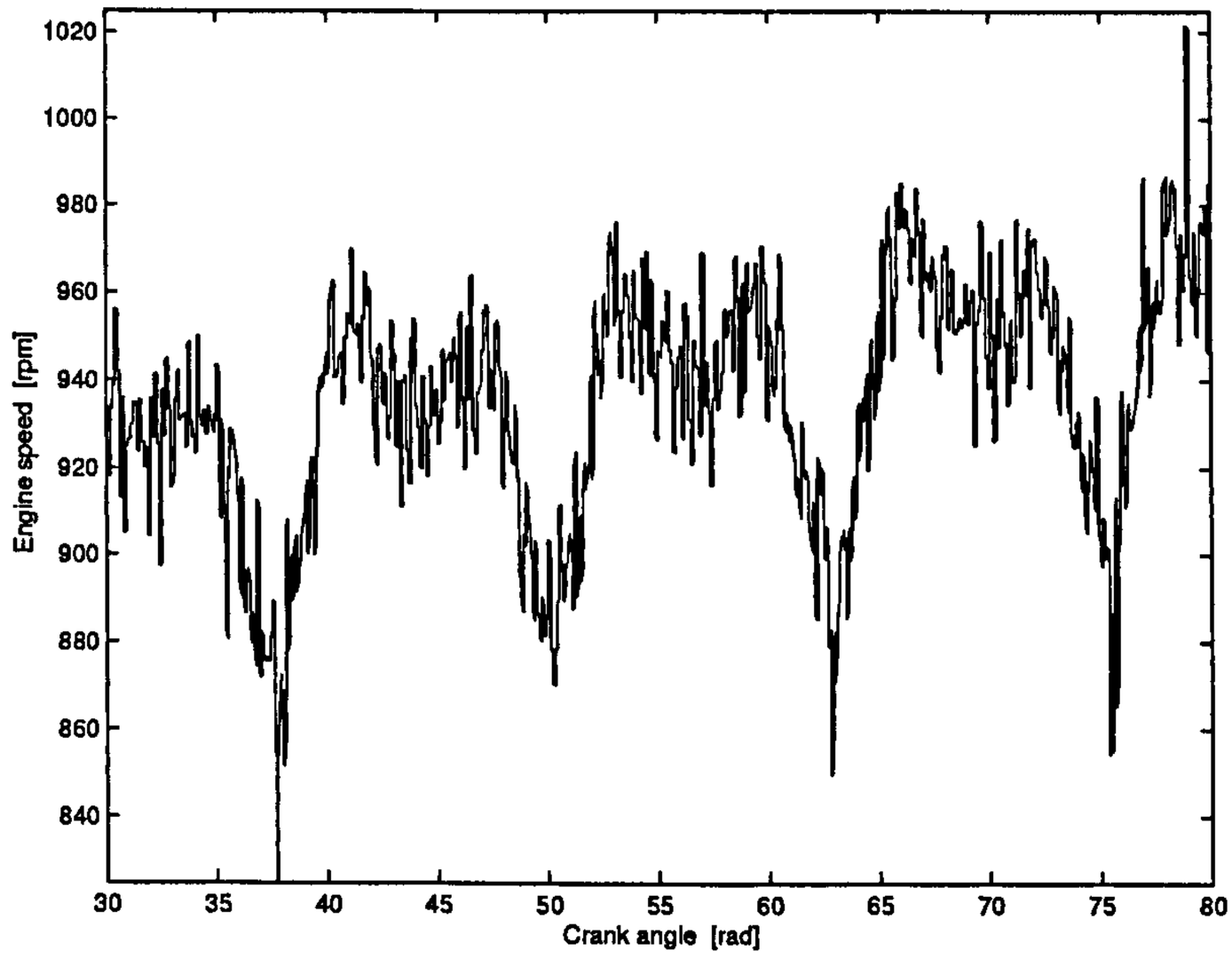

Figure 6.10: Measured engine speed with noise

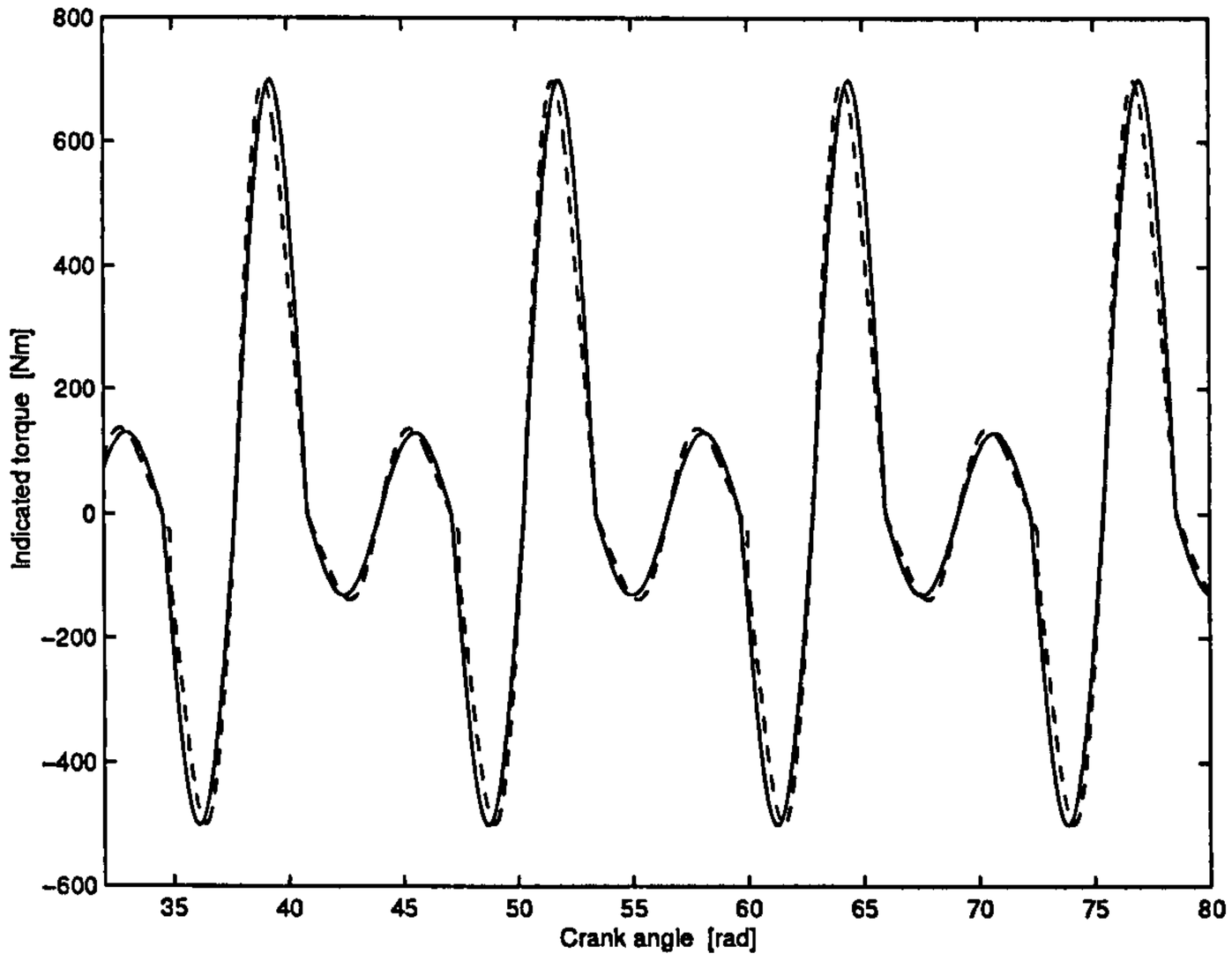

Figure 6.11: Comparison between measured (——) [FA97] and estimated (- - -) engine indicated torque from noisy speed

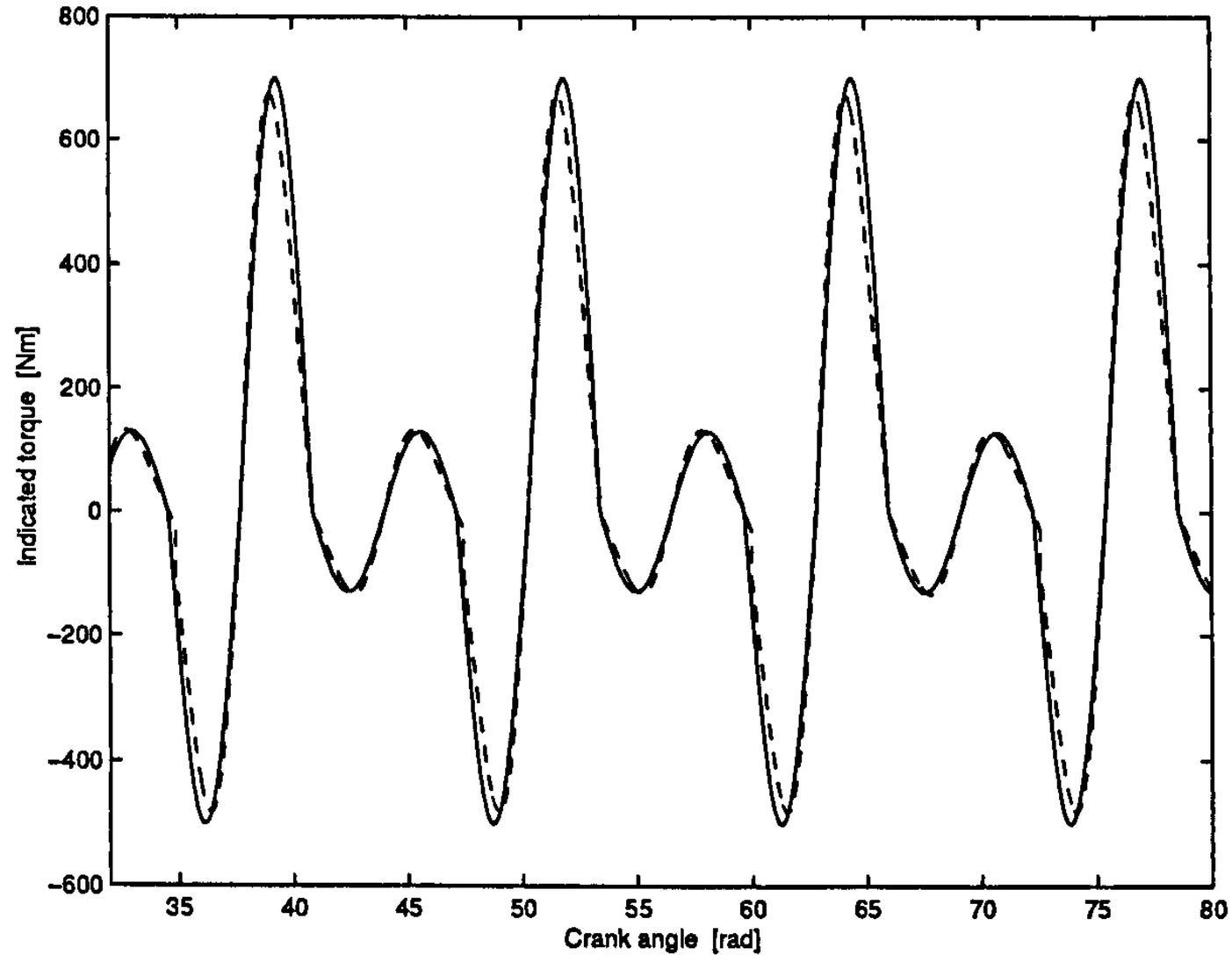

Figure 6.12: Comparison between measured (——) [FA97] and estimated (- - -) engine indicated torque with parameters and friction perturbation

6.6 Discussion and conclusions

A nonlinear observer is designed in this chapter to estimate both the engine indicated and load torques. The estimated torque has a good accuracy when compared to experimental data. Due to its good stability and fast convergence properties, a sliding mode observer was employed. This chapter shows that the estimation accuracy of the indicated torque is improved when the estimation of engine load is considered. The observers are based on low-cost measured and easily accessible variables, and estimate unknown inputs which need expensive sensors to measure and are not easily accessible. The dynamic engine model used includes inertia variations with piston pin offset effects, which significantly decreasing the occurrence of false diagnostics due to more accurate pressure estimation, and can predict Diesel engine behaviours. The sliding gain of the indicated torque estimator is selected as a nonlinear function of engine crank angle in order to reduce the chattering effect. In addition, the stability of the observers are proven to guarantee convergence.

In Chapter 7, an alternative approach using artificial neural networks for Diesel engine indicated torque estimation is investigated.

Chapter 7

Indicated Torque Estimation Based on Neural Networks

7.1 Introduction

The Diesel engines industry has embraced the revolution in electronics and digital technology that has been occurring for the past thirty years. Advances have included microprocessor control of electronic fuel ignition systems based on sensors feedback. In addition to stricter efficiency regulations and competitive designs meant to attract consumers, the main impetus for these controllers has been ever tighter regulations on allowable pollutants from engine combustion. These regulations have spurred ever more complex methods for controlling the fuel air ratio to reduce emission levels. Lately, nonlinear control techniques for Diesel engines have been used for emission control [BDV+99], including the application of artificial neural networks. Artificial neural networks derive their name from the neural network in the human brain. Biology posits that the human brain is composed of millions of neurons in a complex network with the capability of learning patterns given to it.

These learning capabilities make neural networks a prime candidate for many engineering applications, including Diesel engines modelling, estimation and control. In [BDV+94, Bra94], the neural network is used to predict transient changes

in emissions levels following rapid changes in engine operating condition and was used to predict emissions during a legislative drive cycle. In [DBV+99], neural networks were used in a powertrain controller to identify the ideal set points for engine speed and load to minimise fuel consumption and emissions during steady driving.

The application of artificial neural networks for model based fault detection with parity equations is presented in [SI02]. The authors illustrated that the fault detection algorithms, which employ the method of parity equations, were successfully implemented and tested in real time with a 2-litre Diesel engine. In [GMM+99], a comparison between three different condition monitoring techniques is presented, and one of the techniques is the use of neural networks. The purpose of their study was to detect faults during combustion in one of the five cylinders of the Diesel engine using the torsion signal at the crankshaft of the engine. The standard backpropagation algorithm is used to train the neural networks; the torsional signal is used as an input pattern and the output layer represents one class of defect. In [Mes01], an artificial neural network is trained to examine the accuracy of the measured data and allocate a confidence level to each signal for a 6-cylinder turbocharged Diesel engine. The neural network is trained to classify and consequently recognize faulty and healthy behaviour of the engine for a wide range of operating conditions. In [PKG00], the learning capability of artificial neural networks is employed for the real-time diagnosis of potential faults for a turbocharger. The input vector is taken as the series of the harmonic peaks of the power spectral density components of the vertical velocity of the bearings and the output vector is the quantified parameters of the potential faults. The application of the technique to a novel turbocharger with vibration data obtained under working conditions showed promising results.

The research described in this chapter investigates the application of ANNs to Diesel engine estimation, and suggests a new three-term backpropagation (BP) algorithm for the training of the network. This three-term BP algorithm improves the training rate and robustness, at the same time keeping computational com-

plexity low. This chapter shows that the three-term BP algorithm is superior to the standard backpropagation training method.

The chapter is organized as follows. In Section 7.2, the new backpropagation algorithm is presented. In Section 7.3, indicated torque estimation based on artificial neural networks is presented. A discussion is presented and some conclusions are drawn in Section 7.4.

7.2 A new three-term backpropagation algorithm

7.2.1 Background

The standard backpropagation (BP) algorithm is commonly used for training Artificial Neural Networks (ANNs) [RM86]. Training is usually done by iterative updating of weights, employing the negative gradient of a mean-square error function. The error signal is the product of the difference between desired and actual output values and the slope of a sigmoidal activation function. This error signal is then backpropagated to the lower network layers. Traditionally, two parameters, called learning rate (LR) and momentum factor (MF), are used for controlling the weight adjustment along the steepest descent direction and for dampening oscillations. However, its convergence rate can be relatively slow, especially for networks with more than one hidden layer. The reason for the slow convergence rate of the conventional BP algorithm is the saturation behaviour of the activation function used for the network layers. Since the output of a unit exists in the saturation area, the corresponding descent gradient takes a very small value, even if the output error is large, leading to very little progress in the weight adjustment.

The problem of improving the efficiency and convergence rate of the backpropagation algorithm has been investigated by a number of researchers. Jacobs [Jac88] proposed dynamically varying the learning rate and the momentum factor by a fixed step, based on observing the error signals. This approach has been proven to work well for many cases, but the fixed step variations may lead the

system to jump to undesirable regions of the weight space, resulting in divergence. The individual learning rates for each component of the weights vector need to be determined separately, and like the conventional BP algorithm, convergence rates are very slow. In addition, a large number of trial runs are required before arriving at the right learning parameter values.

Ooyen and Neihuis [ON92] proposed a different error cost function, and the use of a second-order Newton's method to optimize the training terms. This approach uses the Pseudo-inverse of the Hessian matrix; however the storage requirements increase quadratically with the number of weights, making the method impractical. The approach of [RIV91] does not use high-order derivatives but dynamically re-scales the variables of the cost function in order to optimize the decrease in the cost function. [YC97, YCC95] considered dynamic learning rate and momentum factor optimization of the BP algorithm using a family of approaches exploiting the derivative with respect to the learning rate and the momentum factor. These approaches do not need to explicitly compute the first and second-order derivatives in weight space, but use information gathered from the forward and backward procedures.

In [SII96], a genetic algorithm for self-adaptation to accelerate the steepest descent rate is presented. The idea is to take the learning rate of the previous step, to increase and decrease it slightly, to evaluate the cost function for both new values of the learning rate, and to choose the one that gives the lower value of the cost function. [FHP96] presented a new incremental learning method for pattern recognition, which employs bounded weight modification and structural adaptation learning rules and applies initial knowledge to constrain the learning process. [KII91] investigated the behaviour of the BP algorithm with a small constant learning rate with stationary, random input environments. The sequence of weight estimates can be approximated by ordinary differential equations, in the sense of weak convergence of a random processes as the learning rate tends to zero. [GM96] proved the Rosenblatt's perceptron convergence (PC) theorem for the BP algorithm, stating that pattern mode backpropagation converges to an optimal

solution for linearly separable patterns.

[KP95] presented a Lagrange multiplier approach for the minimization of a cost function in order to improve convergence. [YC00] proposed an approach for finding optimal weights for feed-forward neural networks. The rationale behind the approach was to reduce the initial network error whilst preventing the network from getting stuck with initial weights. This approach ensures that the outputs of the hidden units are in the active region, i.e. where the derivative of the activation function has a large value. From the outputs of the last hidden layer and the given output pattern, the optimal values of the last layer of weights are evaluated by a least-squares method.

[KP99] proposed an algorithm based on extrapolation of each individual interconnection weight to accelerate the BP algorithm. This requires the error surface to have a smooth variation along the respective axes, so that extrapolation is possible. For performing extrapolation, at the end of each epoch, the BP algorithm convergence behaviour of each network weight is individually examined. [CC99] presented an approach based on the least-squares method to determine the weights between the output layer and the hidden layer, in order to maintain convergence. In the neighborhood of local minima, a penalty function optimization method is employed. [APT99] studied the escaping behaviour of the BP algorithm in the vicinity of temporary minima for a network with an arbitrary number of input units, two hidden layer units and one output unit. Temporary minima correspond to the phase when the network remains in the vicinity of critical points of the plane trajectory, and are in fact saddle points. At these points the network moves away slowly from the critical points, because the largest eigenvalue of the Jacobian matrix of the linearized system is very small and therefore evolves very slowly. However, as training continues, small perturbations in the coefficients of the system are reflected in small perturbations in the eigenvalues, and causes them eventually to bifurcate. At that point, the largest eigenvalue evolves at a much faster rate, and the error curve drops to a significantly lower level.

Some of the proposed modifications of BP algorithms require complex and

costly calculations at each iteration, which offset their faster rates of convergence. Another disadvantage of most acceleration techniques is that often they must be tuned to fit a particular application. Hence, the reduction of the training time by increasing the convergence rate and decreasing learning stalls whilst maintaining the simplicity of the standard two-term BP algorithm is the main aim of this section. A new approach to calculate the change of weight for the link joining the jth unit to the ith unit is presented. In this approach, a third term is proposed in addition to the usual LR and MF terms, this being a proportional factor (PF). This new three-term algorithm can be viewed as being analogous to the common three-term PID algorithm used in feedback control. The viability of this approach is demonstrated on three problems. The results show that the proposed approach out-performs the conventional BP algorithm in terms of convergence speed and the ability to escape from learning stalls.

7.2.2 The standard BP algorithm

The back-propagation algorithm for multi-layer networks is a gradient descent procedure used to minimize a least-square objective function (error function). Assume a batch of training sample pairs: $(I_1, T_1), \cdots, (I_n, T_n)$, where I_s, $1 \leq s \leq n$, represent the sth input in the batch, and $T_s, 1 \leq s \leq n$, is the corresponding desired output (target). For arbitrary number of neurons in the hidden layers, the least-square objective function in the weight space of the networks is

$$E = \frac{1}{nZ_M} \sum_{s=1}^{n} [T_s - O_s^M]^T [T_s - O_s^M], \tag{7.1}$$

where O_s^M is the output vector of an M-layered network with I_s as input, and Z_M is the number of output neurons.

Let W be a vector formed by all the network weights and $\nabla E(W(k))$ be the gradient of E at $W = W(k)$, with $k = 1, 2, 3, \cdots, N$, being the iteration number of the weight vector. The two-term back-propagation algorithm with a momentum term is given by:

$$\Delta W(k) = \alpha(-\nabla E(W(k))) + \beta \Delta W(k-1), \tag{7.2}$$

where α and β are the learning rate (LR) and momentum factor (MF) respectively, and $\Delta W(k) = W(k+1) - W(k)$.

The feed-forward computations of the network with I_s presented to the input layer are given by

$$o_{s,i}^m = f([W_i^m(k+1)]^T O_s^{m-1}), \tag{7.3}$$

where $o_{s,i}^m$, $1 \le i \le Z_m$, denotes the ith output of layer m, $1 \le m \le M$; $f(\cdot)$ is the activation function (usually chosen as the logistic or tanh functions); $W_i^m(k+1)$ is a sub-vector of $W(k+1)$, consisting of all the weights from the neurons of layer $m-1$ to $o_{s,i}^m$; and $O_{s,i}^{m-1}$ is a vector formed by all the outputs of layer $m-1$ (including a unity output, which is used as a reference to bias the next layer) and is given by

$$O_{s,i}^{m-1} = \begin{cases} [1 \quad O_{s,1}^{m-1} \cdots O_{s,Z_m}^{m-1}]^T & \text{for } m > 1, \\ [1 \quad I_s^T]^T & \text{for } m = 1. \end{cases} \tag{7.4}$$

7.2.3 Proportional factor term

The BP algorithm given by (7.2) is modified by adding an extra term in order to increase the BP learning speed and avoid learning stalls. This term is proportional to $e(W(k))$ which represents the difference between the output and the target at each iteration. For batch learning, $e(W(k)) = [e_s \quad e_s \quad \dots \quad e_s]^T$, where the vector e is of appropriate dimension and $e_s = \sum_{s=1}^{n} [T_s - O_s^M]$.

The modified BP algorithm is hence

$$\Delta W(k) = \alpha(-\nabla E(W(k))) + \beta \Delta W(k-1) + \gamma e(W(k)), \tag{7.5}$$

where γ is the proportional factor (PF). It is noted that the BP algorithm given by (7.5) has three terms, one proportional to the derivative of $E(W(k))$, another proportional to the previous value of the incremental change of the weights and a third term proportional to $e(W(k))$. These three terms can be viewed as being analogous to the three terms in a PID controller, commonly used in feedback control applications.

7.2.4 Stability analysis and optimization procedures

The stability of the modified three-term BP algorithm has been analyzed. The detailed stability analysis of the algorithm is provided in Appendix E. The stability study is used to derive conditions that must be satisfied by the learning parameters in order to guarantee stability. Necessary and sufficient conditions for the convergence and stability behaviour of the three-term backpropagation algorithm are also established. It is shown that if the coefficients of the three-term BP algorithm satisfy conditions (E.35) and (E.36), then it is guaranteed that the system is stable and will converge to a local minimum. Condition (E.34) may be violated if one of the eigenvalues of matrix F is relatively large. But in most cases all the minima which are of interest lie within a bounded set. Thus the eigenvalues of matrix F are bounded and therefore if α and γ are sufficiently small, all the local minima are stable. In fact, it is proved that if at least one of the eigenvalues of matrix F is negative, then the system becomes unstable. Also it is shown that all local minima of the cost function are the only locally asymptotically stable points for the algorithm.

Efficient BP learning using simultaneously optimized LR, MF and PF terms is presented in Appendix F. A set of recursive formulae is used for calculating the derivatives of the optimization target with respect to LR, MF and PF. This behaves as a feed-forward procedure in the BP algorithm and does not increase the computational complexity. A group of approaches exploiting the derivatives with respect to LR, MF and PF are presented.

7.2.5 Benchmark examples

In this section the convergence behaviour of the three-term BP and standard BP algorithms are compared using three benchmark problems. In most cases the learning rate and momentum factor for the standard BP algorithm are selected such that the solution converges to a local minimum with no further error reduction possible. For the comparisons, three-term BP algorithm uses the same values of

learning rate and momentum factor as the standard BP algorithm. For all the tests, a logistic activation function $\sigma(x) = 1/(1+\exp^{-x})$ is used for the hidden and output nodes of a fully connected forward neural network. The convergence of the learning process is measured by taking the half-sum-of-squared error objective function. The stopping criterion is set to 500 epochs. The error threshold for a successful trial is less than 10^{-3}. The initial values of the weights are selected randomly between $[-2, 2]$. The network maps the input pattern into the corresponding output target value.

Example I

A parity check problem is considered where the input patterns are six dimensional vectors consisting of ones and zeros. The desired output is set to one if the corresponding input pattern is made up of an odd number of ones, otherwise the desired output is zero. A network with two hidden layers containing 6, 8, 5 and 1 units, ordered from the input layer to output layer, was tested. The problem is taken from [YC97].

Test 1

The first test has three groups I, II and III. Each test group uses constant learning parameters and they increase through the groups. The initial weights are randomly selected in the range $[-2, 2]$. The running of the simulation at different initial values of the weight is called a trial. The simulation is run for 350 trials for each group. Selection of relatively high values for the learning parameters is preferable in the BP algorithm to increase the learning speed but this usually leads to instability. The comparative results summarized in Table 7.1 show that based on the percentage of successful trials (i.e. those having error less than 10^{-3} within 500 epochs), the proposed algorithm is more successful than the standard BP algorithm when relatively high values of the learning parameters are selected. Table 7.1 also shows the mean number of epochs for successful trials which gives an indication of the convergence speed, and it is clear that the three-term BP

algorithm has a faster convergence rate than the standard BP algorithm.

	group I		*group II*		*group III*	
	2-term	3-term	2-term	3-term	2-term	3-term
α	1.1	1.1	2	2	7	7
β	0.5	0.5	0.8	0.8	0.9	0.9
γ	-	0.1	-	1.1	-	1.5
no. epochs	460	430	347	260	230	60
no. trials	350	350	350	350	350	350
success rate	93%	92%	71%	88%	32%	85%

Table 7.1: Test 1: Experimental results for the parity problem

Test 2

The second test is carried out by varying randomly the learning parameters through the simulation as follows, $\alpha \in (0, 12]$, $\beta \in (0, 1)$ and $\gamma \in (0, 5]$, also the initial weights are randomly selected in the range $[-2, 2]$. The algorithms are tested on 200 trials. The percentage of successful trials for the standard BP and three-term BP algorithms are 18% and 65% respectively. Some test results are shown in Figures 7.1 and 7.2. The Figures show the behaviour of the network during learning: the standard BP algorithm does not converge, probably due to local minima. However the three-term BP algorithm converges after about 150 and 25 epochs respectively for the three cases considered.

Example II

In the second example the XOR problem is investigated. This is a popular benchmark for neural network training [APT99]. A network with one hidden layer containing 4, 2 and 1 units, ordered from the input layer to output layer, was

tested. The system inputs are:

$$I_{(1)} = \begin{bmatrix} -1 \\ 0 \\ 0 \end{bmatrix}, I_{(2)} = \begin{bmatrix} -1 \\ 1 \\ 0 \end{bmatrix}, I_{(3)} = \begin{bmatrix} -1 \\ 0 \\ 1 \end{bmatrix}, I_{(4)} = \begin{bmatrix} -1 \\ 1 \\ 1 \end{bmatrix} \tag{7.6}$$

and the desired responses (target) of each input vector are $T_{(1)} = 0, T_{(2)} = 1, T_{(3)} = 1, T_{(4)} = 0$.

Test 1

The first test has three groups I, II and III; the learning parameters increase through the groups. These tests are carried out using constant learning parameters through the simulation and the initial weights are selected randomly in the range $[-2, 2]$. The networks are tested on 350 trials for each group. The comparative results for the percentage of successful trials are summarized in Table 7.2. The group I results show that the standard BP behaves better than the three-term BP when relatively small values for the learning parameters are chosen. But with larger learning parameters, the proposed algorithm is more successful than the standard BP algorithm as shown in Table 7.2 and is hence more robust. Relatively high values of the learning parameters increase the BP algorithm convergence rate but usually lead to instability. The comparative results of the mean number of epochs of successful trials is summarized in Table 7.2, and show that the three-term BP algorithm has a faster convergence rate than the standard BP algorithm.

Test 2

The second test is carried out by randomly varying the learning parameters as follows: $\alpha \in (0, 12]$, $\beta \in (0, 1)$ and $\gamma \in (0, 5]$. The initial weights are selected randomly in the range $[-2, 2]$. The simulation is tested for 200 trials. The percentage of successful trials for the standard BP and the three-term BP algorithms are 24% and 61% respectively. Some test results are shown in Figures 7.3 and 7.4. The figures show instances where the network does not converge at all using

	group I		*group II*		*group III*	
	2-term	3-term	2-term	3-term	2-term	3-term
α	1	1	5	5	12	12
β	0.7	0.7	0.9	0.9	0.93	0.93
γ	-	0.95	-	0.95	-	1
no. epochs	355	250	135	70	85	40
no. trials	350	350	350	350	350	350
success rate	95%	88%	56%	82%	15%	75%

Table 7.2: Test 1: Experimental results for the XOR problem

the standard BP algorithm due to local minima. The proposed algorithm helps the system to escape from local minima after 73 and 62 epochs respectively, with errors ranging between 1×10^{-3} and 2×10^{-7}. In addition, the three-term BP algorithm converged to very small steady state errors, which is unlikely to happen with the conventional BP algorithm as shown in Figure 7.4.

Example III

The final example is a function approximation problem [YC97]. A network with two hidden layers containing 1, 12, 8 and 1 units, ordered from the input layer to output layer, was tested. The function to be approximated, $Y = 2f(f(X)) - 1$, with $f(X) = 3.95X(X-1), \quad 0 \leq X \leq 1$. The training set consisting of 100 patterns is randomly drawn with a uniform distribution from the interval $[0, 1]$.

Test 1

The first test has four groups I, II III and IV; the learning parameters increase through the groups. These tests are carried out using constant learning parameters through the simulation and the initial weights are selected randomly in the range $[-2, 2]$. The networks are tested on 350 trials for each group. The comparative results are summarized in Table 7.3. The group I results show that in this

case, the three-term BP performs slightly better than the standard BP with small values of learning parameters, but with a lower success rate. With larger learning parameters, the proposed algorithm is again more successful than the standard BP algorithm.

	group I		*group II*		*group III*		*group IV*	
	2-term	3-term	2-term	3-term	2-term	3-term	2-term	3-term
α	0.4	0.4	0.95	0.95	1.3	1.3	2.1	2.1
β	0.5	0.5	0.5	0.5	0.7	0.7	0.8	0.8
γ	-	2	-	1.2	-	1.4	-	1.6
no. epochs	470	250	385	260	150	80	100	45
no. trials	350	350	350	350	350	350	350	350
success rate	87%	82%	80%	83%	53%	80%	17%	73%

Table 7.3: Test 1: Experimental results for the approximated function problem

Test 2

The second test is carried out by randomly varying the learning parameters as follows: $\alpha \in (0, 12]$, $\beta \in (0, 1)$ and $\gamma \in (0, 5]$. The initial weights are selected randomly in the range $[-2, 2]$. The simulation is tested for 200 trials. The percentage of successful trials for the standard BP and the three-term BP algorithms are 17% and 58% respectively. Some test results for evolution of the error are shown in Figures 7.5 and 7.6 titled (a). The function formed by the trained network is also depicted in Figures 7.5 and 7.6 titled (b). The proposed algorithm helps the system to learn successfully after 10 epochs, with errors 2×10^{-3}.

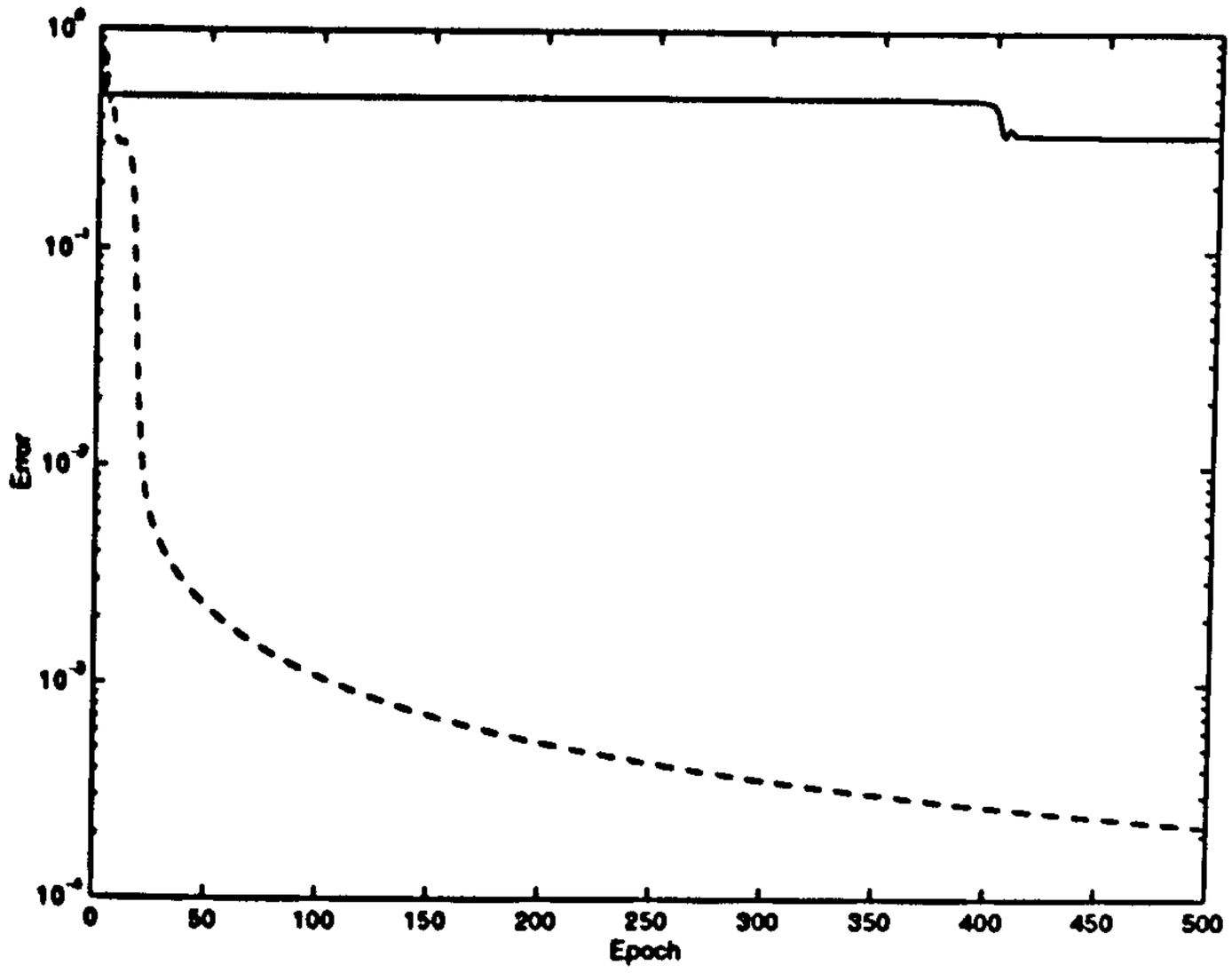

Figure 7.1: Example I (A parity problem): The three-term BP algorithm (- - -) and the BP algorithm (—): Evolution of error ($\alpha = 3$ $\beta = .8$ $\gamma = 1$).

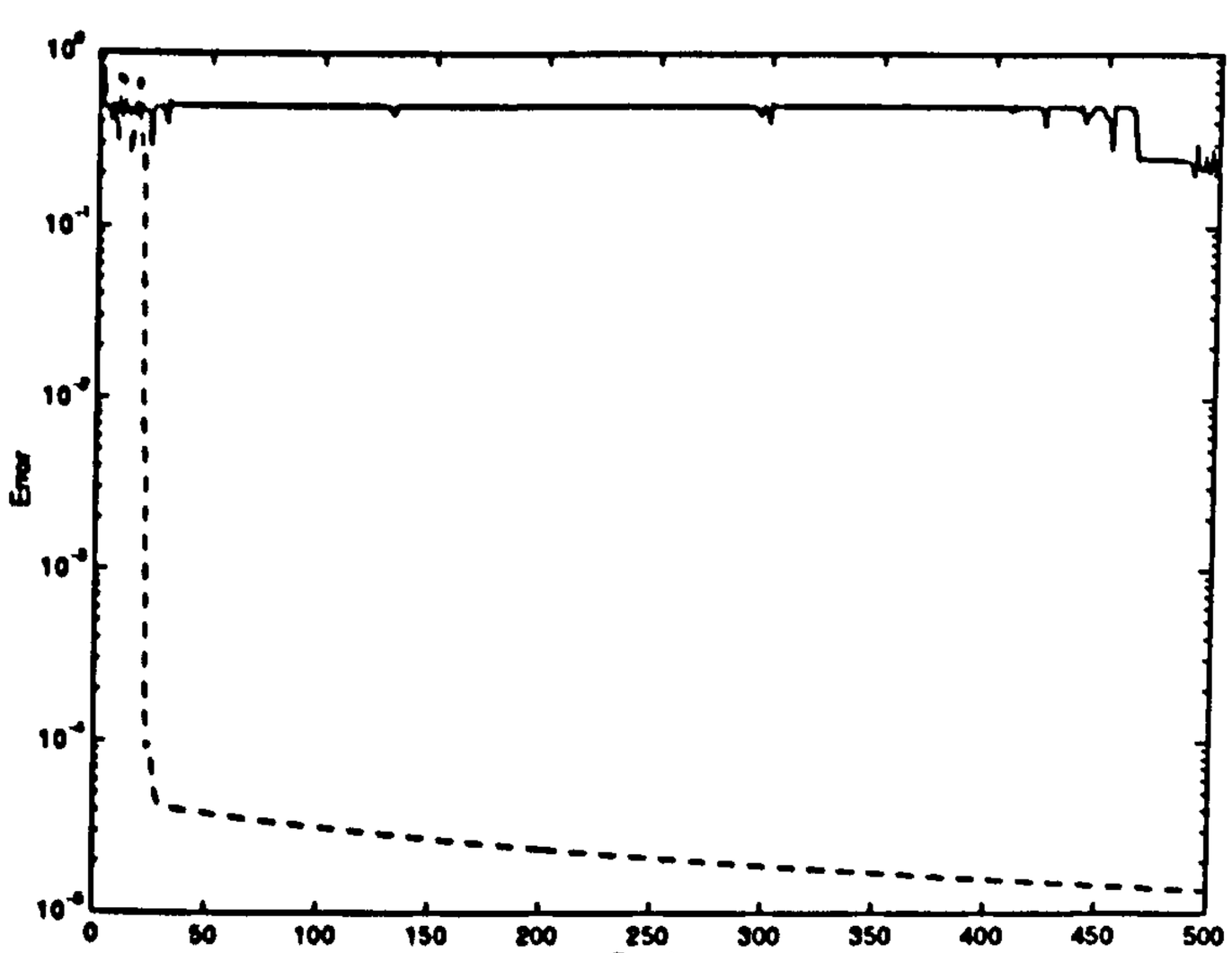

Figure 7.2: Example I (A parity problem): The three-term BP algorithm (- - -) and the BP algorithm (—): Evolution of error ($\alpha = 5.5$ $\beta = .9$ $\gamma = 1.1$).

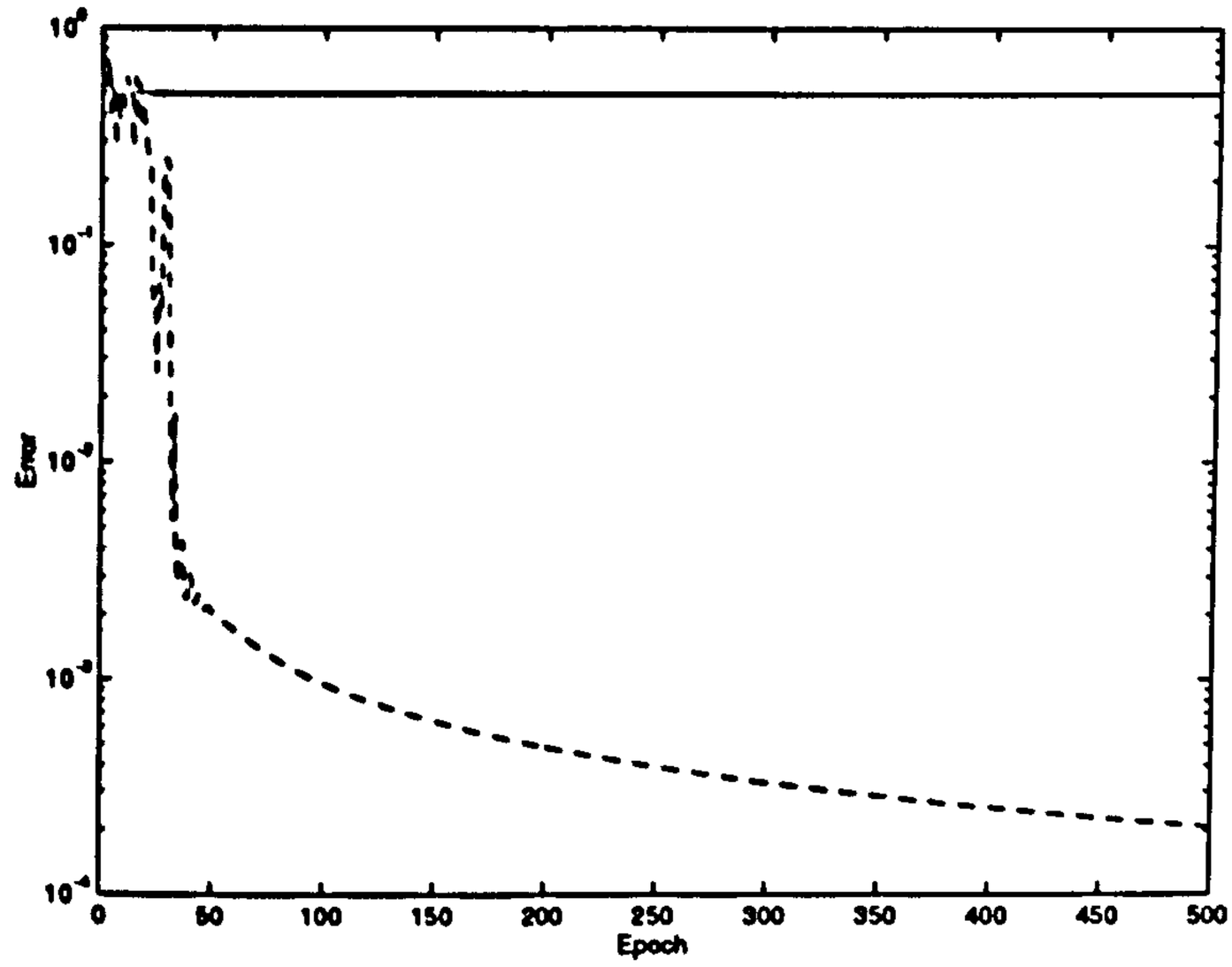

Figure 7.3: Example II (XOR problem) : The three-term BP algorithm (- - -) and the BP algorithm (—): Evolution of error ($\alpha = 1$ $\beta = .92$ $\gamma = 2$).

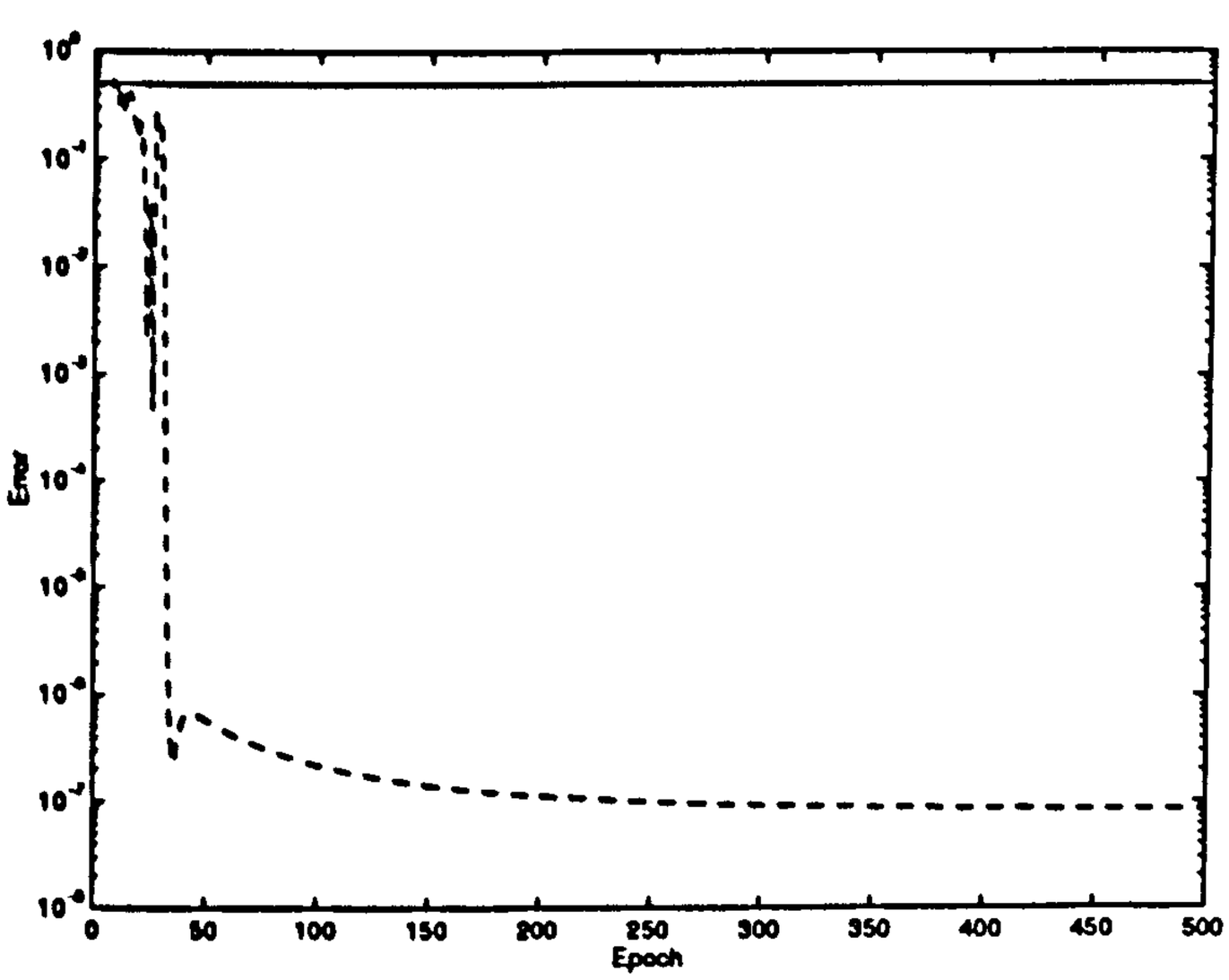

Figure 7.4: Example II (XOR problem) : The three-term BP algorithm (- - -) and the BP algorithm (—): Evolution of error ($\alpha = 5$ $\beta = .9$ $\gamma = .3$).

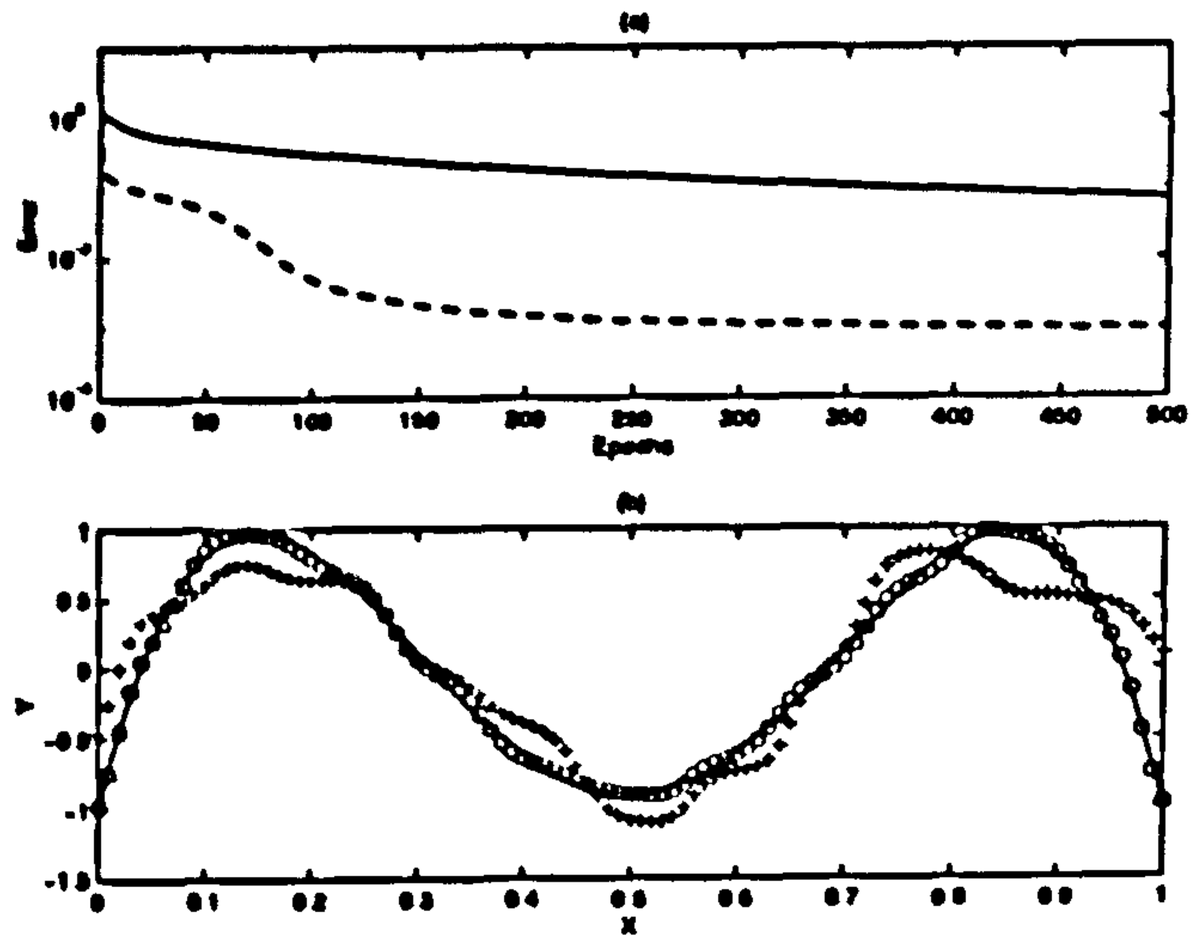

Figure 7.5: Example III (curve fitting problem) : (a) The three-term BP algorithm (- - -) and the BP algorithm (—): Evolution of error, (b) The function to be approximated (—) and approximated by the trained network using the three-term BP algorithm (o o o) and the BP algorithm (+ + +), ($\alpha = 1$ $\beta = .1$ $\gamma = .5$).

7.2.6 Discussion

A new three-term BP algorithm that reduces the number of training epochs and provides escape of the training from learning stalls whilst maintaining the simplicity of standard BP algorithms is presented. A new term is proposed in addition to the LR and MF terms; this being a proportional factor (PF). The comparative test results indicate that the new algorithm offers much higher speeds of convergence than the standard BP algorithm. Consequently, the improvements presented in this chapter provide a more efficient alternative to existing training methods. The results also show that the percentage of successful trials for the three-term BP algorithm was significantly higher than the standard BP algorithm. The proposed algorithm is able to escape from local minima. The three-term BP algorithm is more robust to the choice of initial weights, especially when relatively high values for the learning parameters are selected. The three-term algorithm is applicable to any network with different activation functions.

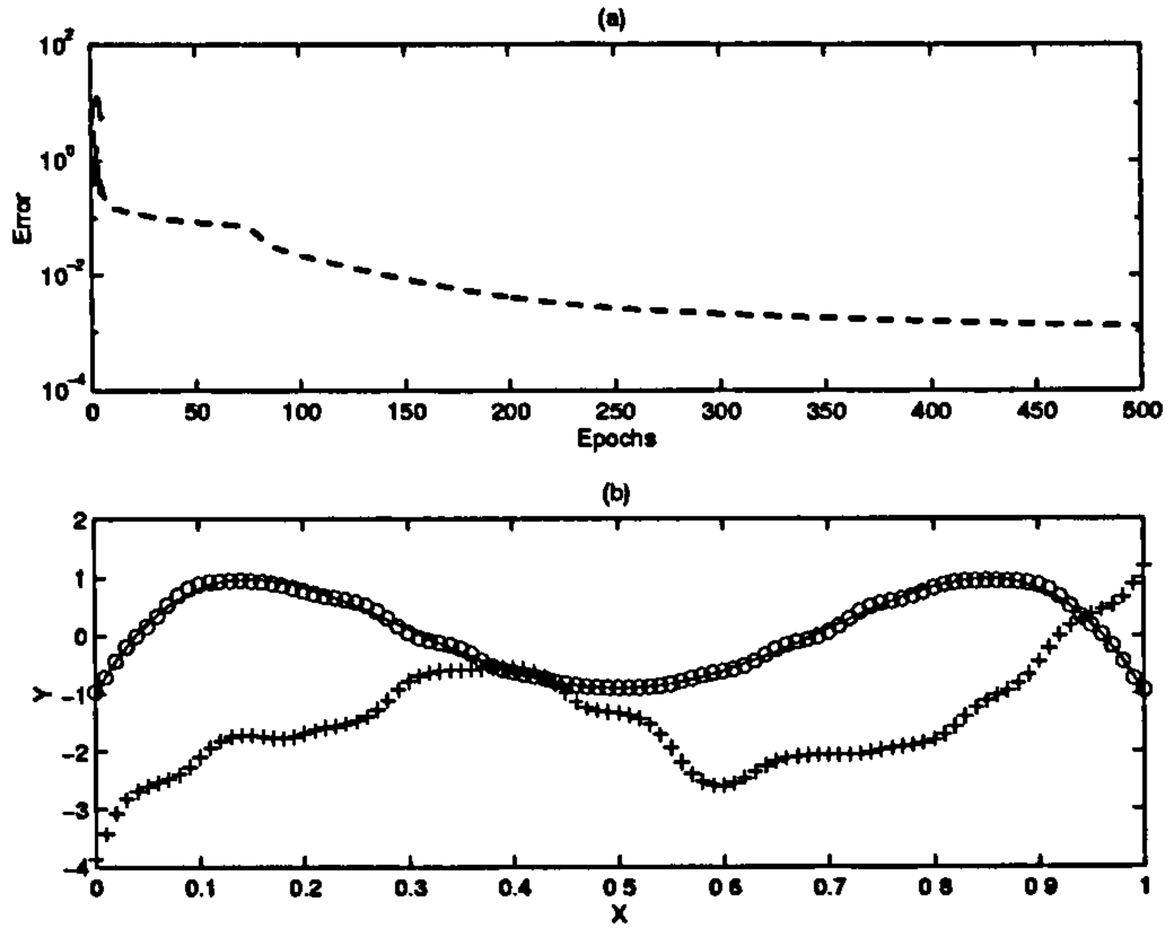

Figure 7.6: Example III (curve fitting problem) : (a) The three-term BP algorithm (- - -) and the BP algorithm (—-): Evolution of error, (b) The function to be approximated (—-) and approximated by the trained network using the three-term BP algorithm (o o o) and the BP algorithm (+ + +), ($\alpha = .4$ $\beta = .5$ $\gamma = 2$).

The proposed algorithm is different from some of the alternative BP algorithms which require complex and costly calculations at each iteration, off-setting their faster rates of convergence. Another disadvantage of most acceleration techniques is that they must often be tuned to fit a particular application.

7.3 Engine indicated torque estimation based on artificial neural networks

The rising complexity of modern automotive engines with an increasing number of actuators and sensors commonly used to minimise emissions and fuel consumption and to maximise engine driveability require a detailed supervision for fault detection and on-board diagnosis. The European Community Directive 98/69/EC requires on-board diagnosis for spark ignition engines and will require it for Diesel engines as of January 2003, mainly to prevent excessive emissions [SI02].

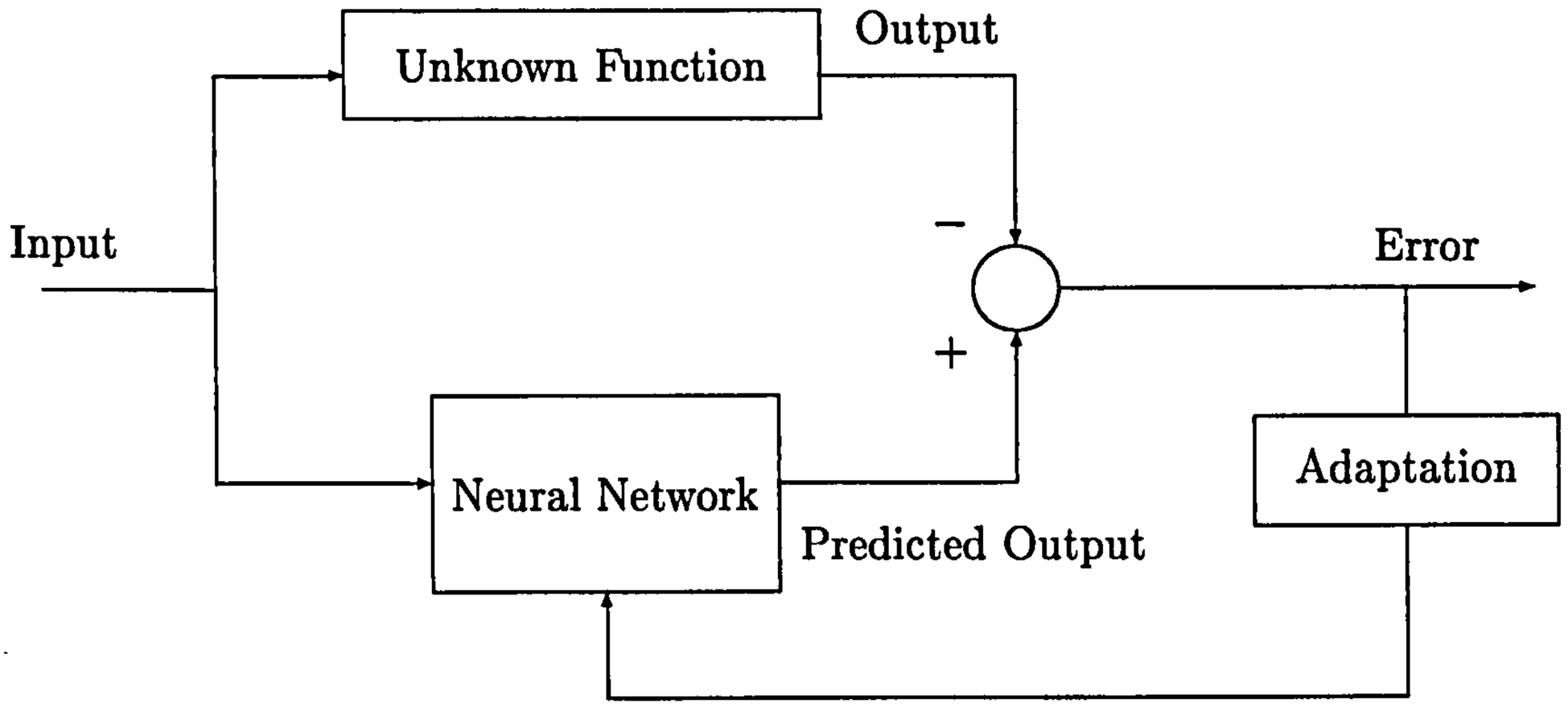

Figure 7.7: Neural network as function approximator

This section describes applications of artificial neural networks (ANN) for the inverse dynamic modelling of Diesel engines and presents a technique for the design of input estimators using feedback and ANN feedforward. The method is applied to the problem of estimating indicated torque from a measurement of crankshaft angular velocity and displacement in internal combustion engines.

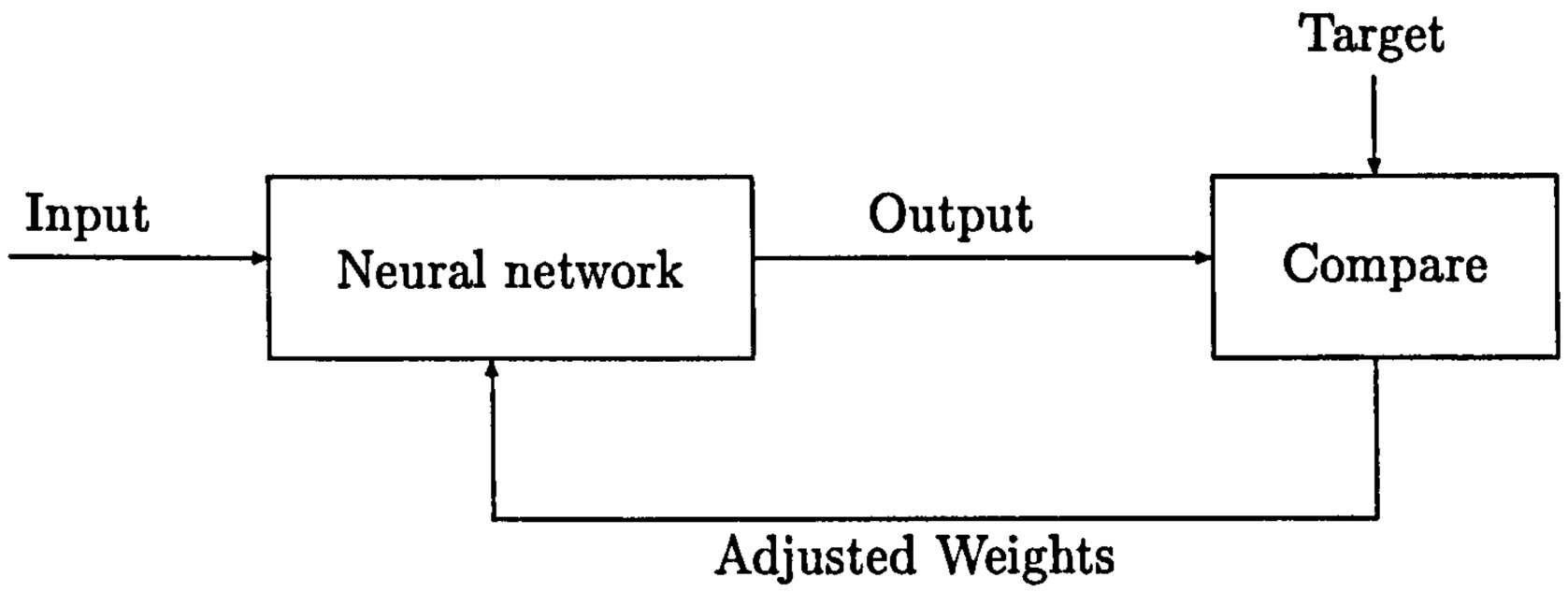

Figure 7.8: Supervised neural network

In this application, an ANN is used as a function approximator. As shown in Figure 7.7, there is an unknown function that is needed to be approximated.

The parameters of the network are adjusted so that it produces the same response as the unknown function, if the same input is applied to both systems. Also, the ANN can be trained to perform a particular function by adjusting the values of the connections (weights) between elements. Usually neural networks are trained, so that a particular input leads to a specific output (supervised training), as shown in Figure 7.8.

An alternative to the approach proposed in Chapter 6 to the problem of estimating engine indicated torque from crankshaft speed and position measurements, is to formulate a closed loop structure to perform the estimation. The approach is to design indicated torque estimators using feedback and ANN model as feedforward. Such an approach can offer the advantage of being amenable to real-time implementation. The approach encompasses the dynamic model, the neural network model as a feedforward block and a proportional corrector; the block diagram of such an estimator is illustrated in Figure 7.9. In Figure 7.9, $\dot{\theta}_1$ and $\hat{\dot{\theta}}_1$ are the measured and estimated crankshaft speed respectively. The Dynamic Model block is a forward engine dynamic model relating engine indicated torque to the crankshaft speed, i.e., the two degree of freedom single cylinder Diesel engine dynamic model, developed in Sections 2.2.1-2.2.2, coupled with a transformation into the crank angle domain as shown in Section 4.2. The Corrector block is an estimator gain chosen to ensure adequate estimation accuracy over the range of interest. The Neural Network block represents a feedforward ANN inverse engine dynamic model and $\hat{T}_i$ is the estimated indicted torque.

For an accurate estimation of a time-varying speed signal usually a higher gain of the corrector is required. The requirement of accuracy and high speed of response of the estimator therefore dictates a high value of the gain of the corrector. Stability considerations impose a limit on how high the corrector gain can become. Estimator design involves a favorable solution of these conflicting requirements. The indicated torque estimator in this chapter, employing both feedforward and feedback, as shown in Figure 7.9, can solve the conflict between response speed and stability of the estimator. The advantage of employing an

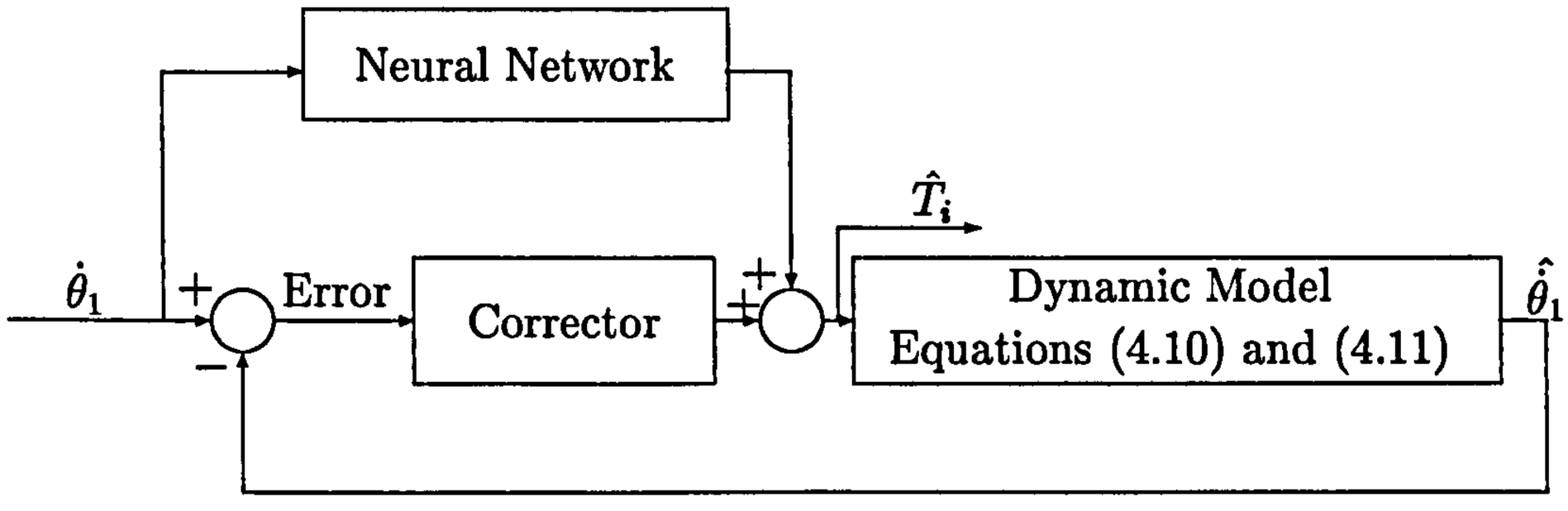

Figure 7.9: ANN based engine indicated torque estimator

approximate feedforward path in the estimator is to decrease requirement for high value of the corrector gain, therefore solving the contradiction between stability and response speed.

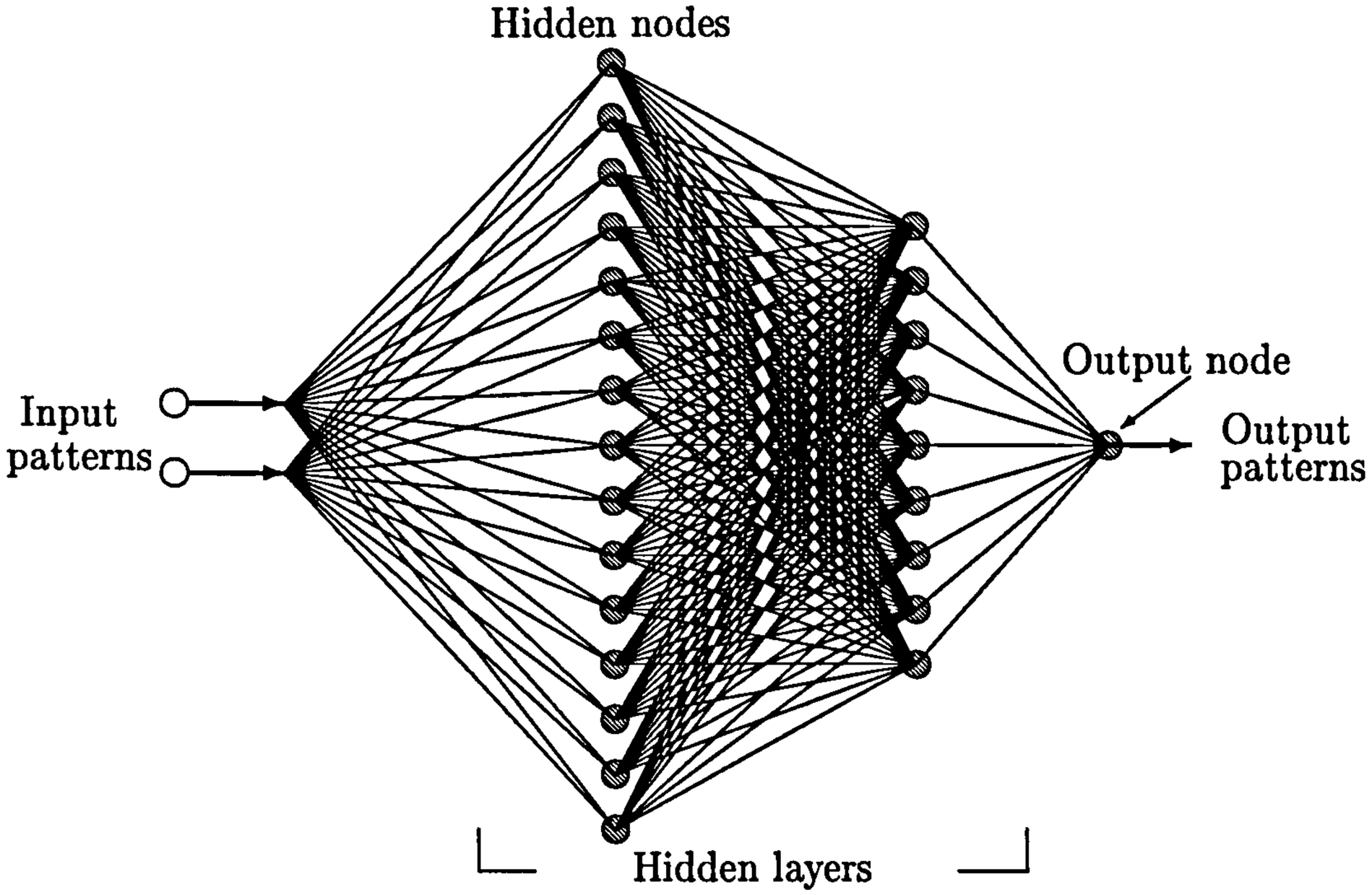

Figure 7.10: Structure of the neural network

The main aim is to train the neural network to obtain indicated torque (input of the dynamic model) from speed and position measurements (output of the

dynamic model). The task is to train the network using the proposed new three-term backpropagation algorithm, and finally to find the optimum variables that would lead to the required results.

7.3.1 Testing and validation

This section demonstrates the behaviour of the estimation scheme and the validation against experimental data. The geometrical specifications for the engine are shown in Table G.1, in Appendix G. The measured data are speed, position and indicated torque data and taken from [FA97] and [Fil99]. The data of 850 sets are chosen representing about one third of the engine data, i.e., from 10 to 55 rad, and used for training purposes. Each input data set is associated with a particular output data set. A network with two hidden layers containing 15, 9, nodes respectively is implemented. A typical neural network structure as shown in Figure 7.10 is used. The network is trained to formulate the relationship between engine speed and position on the one hand, and the indicated torque on the other hand (feedforward model). In Figure 7.10, the input patterns contain the measured crankshaft speed and position data sets. The hidden layers which connect the input patterns to the output node are composed of weight space (connections), biases and hidden nodes. Each hidden node and output node is activated by the logistic activation function $\sigma(x) = 1/(1 + \exp^{-x})$.

Input data (speed and position of the crankshaft) is normalized between 0 and 0.7 (instead of 0 and 1) and the output data is normalized between -0.3 and 0.7 (instead of -1 and 1), which proved to immensely speed up the learning procedure as well as improve its generalization capability outside the training limits, i.e., to avoid saturation. After only 550 training iterations, the network has converged to a very small error, 10^{-6}. Using Matlab on a Pentium IV-1.5 GHZ processor, it takes less than 30 seconds to train the network. Using the new three-term backpropagation algorithm provided a single functional relationship between the engine speed and position, and the indicated torque. The convergence of the learning process is measured by observing the sum-of-squared error objective

function.

After finishing the training, the bias and weight values were acquired. These values combined with the logistic activation functions in order to form the formula for obtaining indicated torque from speed and position measurements. The measured speed training set that was used to train network is shown in Figure 7.11. This model is created in order to check that the weight and bias values were correctly calculated. By applying the measured speed and position training set, the results obtained are shown in Figure 7.12, proving that the ANN model predicted indicted torque is almost the same as the measured. The proposed algorithm helps the system to learn successfully within 550 epochs, with an error of 10^{-6}, as shown in Figure 7.13.

To check the behaviour of the neural network model in a wide operating range, the measured speed shown in Figure 7.14 is used as an input to the neural network model. The comparison between the predicted from the neural network model and the measured indicated torque is shown in Figure 7.15. These results indicate that the neural network model works properly when operating under the conditions covered by the training set.

The aim is to test the proposed technique which is shown in Figure 7.9, if the proportional corrector could produce a correction term that could improve the estimation of indicated torque, and to see how well the network works with all three models blocks included. After testing the model many times, it seen from Figures 7.16 and 7.17 the estimated torque closely track the measured torque when the gain of the corrector is equal to 1000. For this model, the indicated torque was not used at all. However, within the model, two sets of signals were produced. The first signal is the output of the neural network model (feedforward) and the second signal is the output of the corrector and the summation of these signals gives the estimated indicated torque.

In order to validate the behaviour of proposed estimator with experimental results, the feedforward ANN model and the two degree of freedom single cylinder Diesel engine dynamic model; transformed into the crank angle; Section 4.2 and

instantaneous friction model; Section 3.2, along with corrector are implemented in the proposed estimation scheme. The measured data are taken from [FA97] and [Fil99]. The validation of the estimator is carried out during transient engine response, and the engine speed is used to estimate the indicated torque is shown in Figure 7.14. Figure 7.16 shows that the estimator has converged to the correct indicated torque.

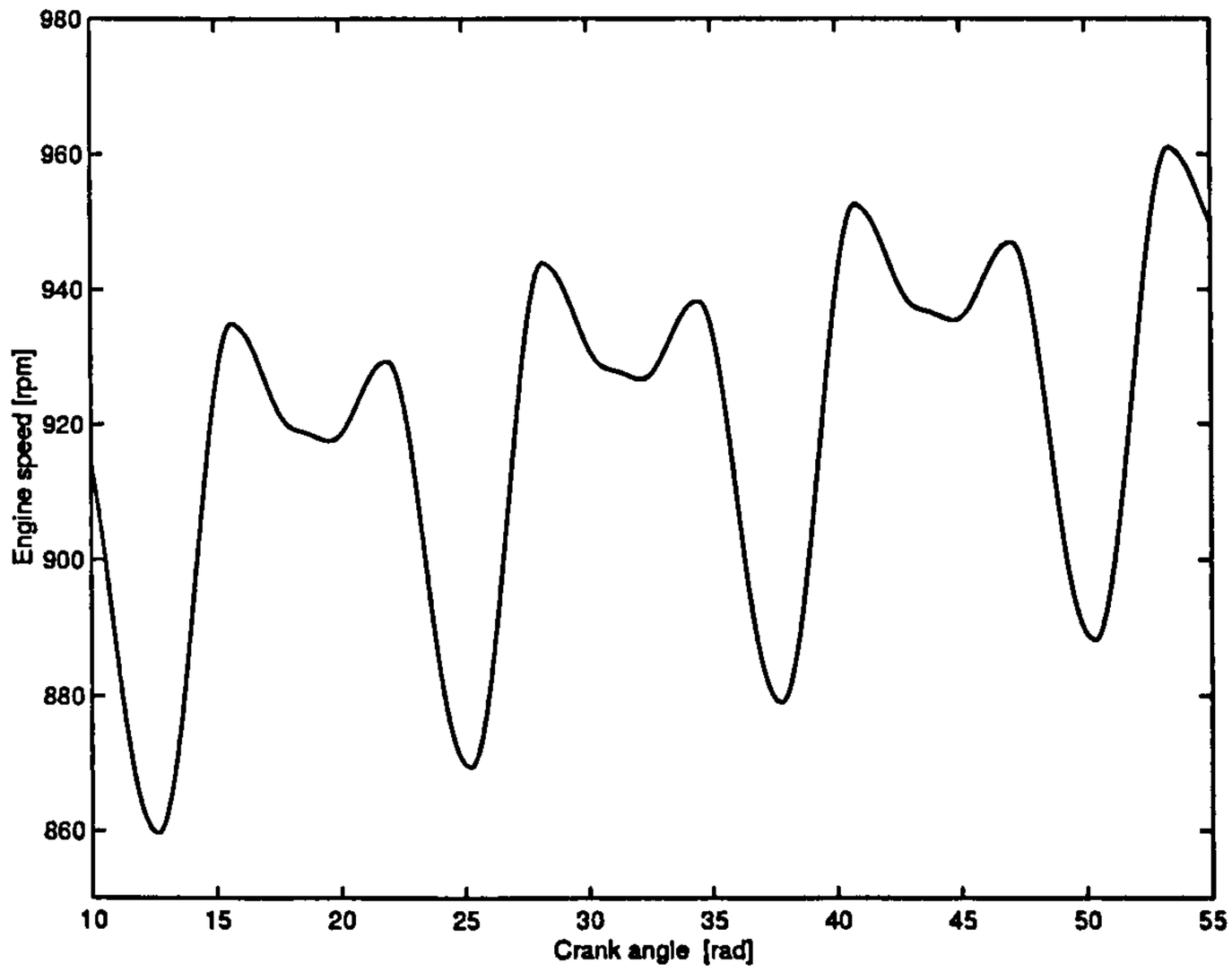

Figure 7.11: Measured engine speed [FA97]

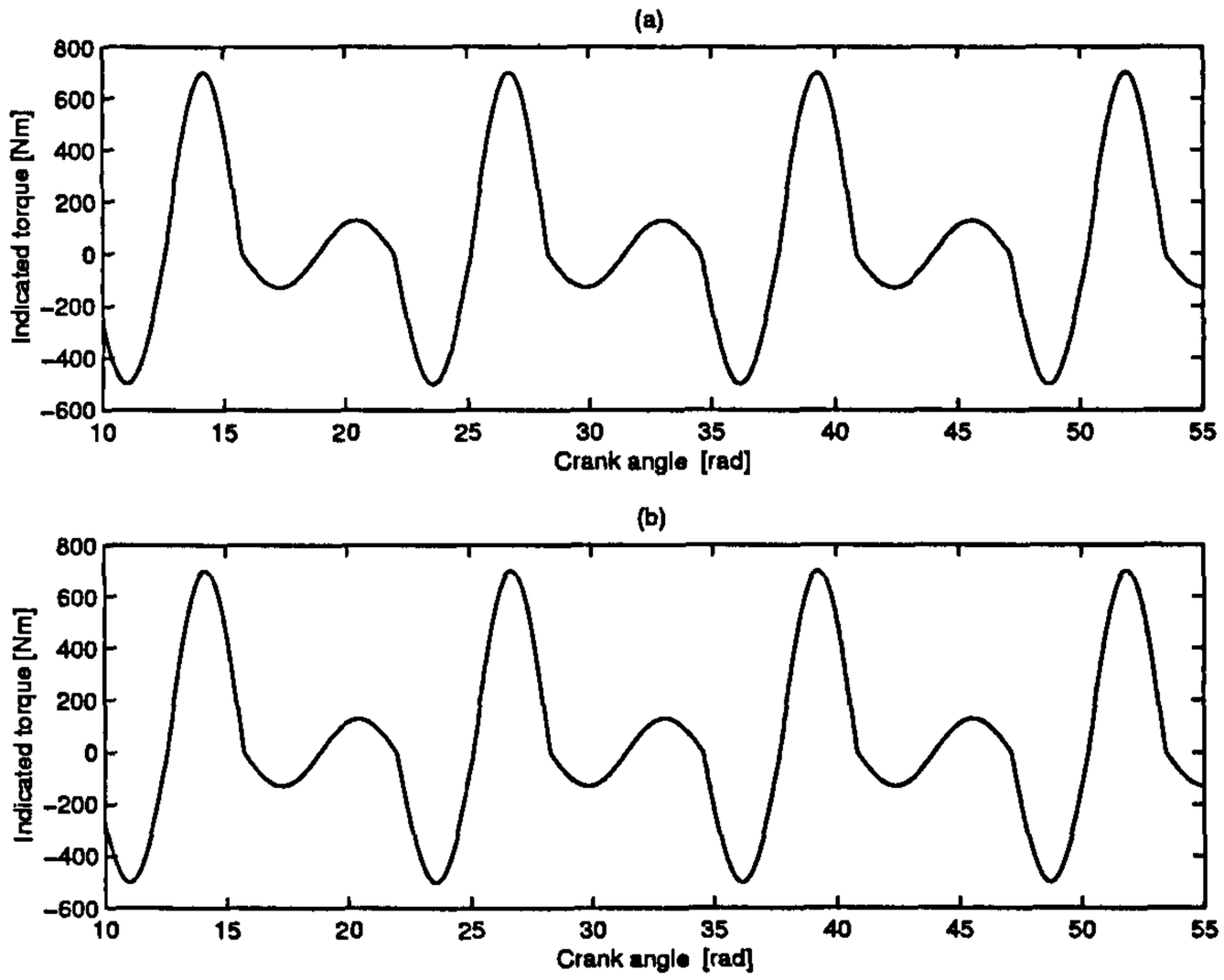

Figure 7.12: Indicated torque: (a) measured [FA97] and (b) obtained from the trained network

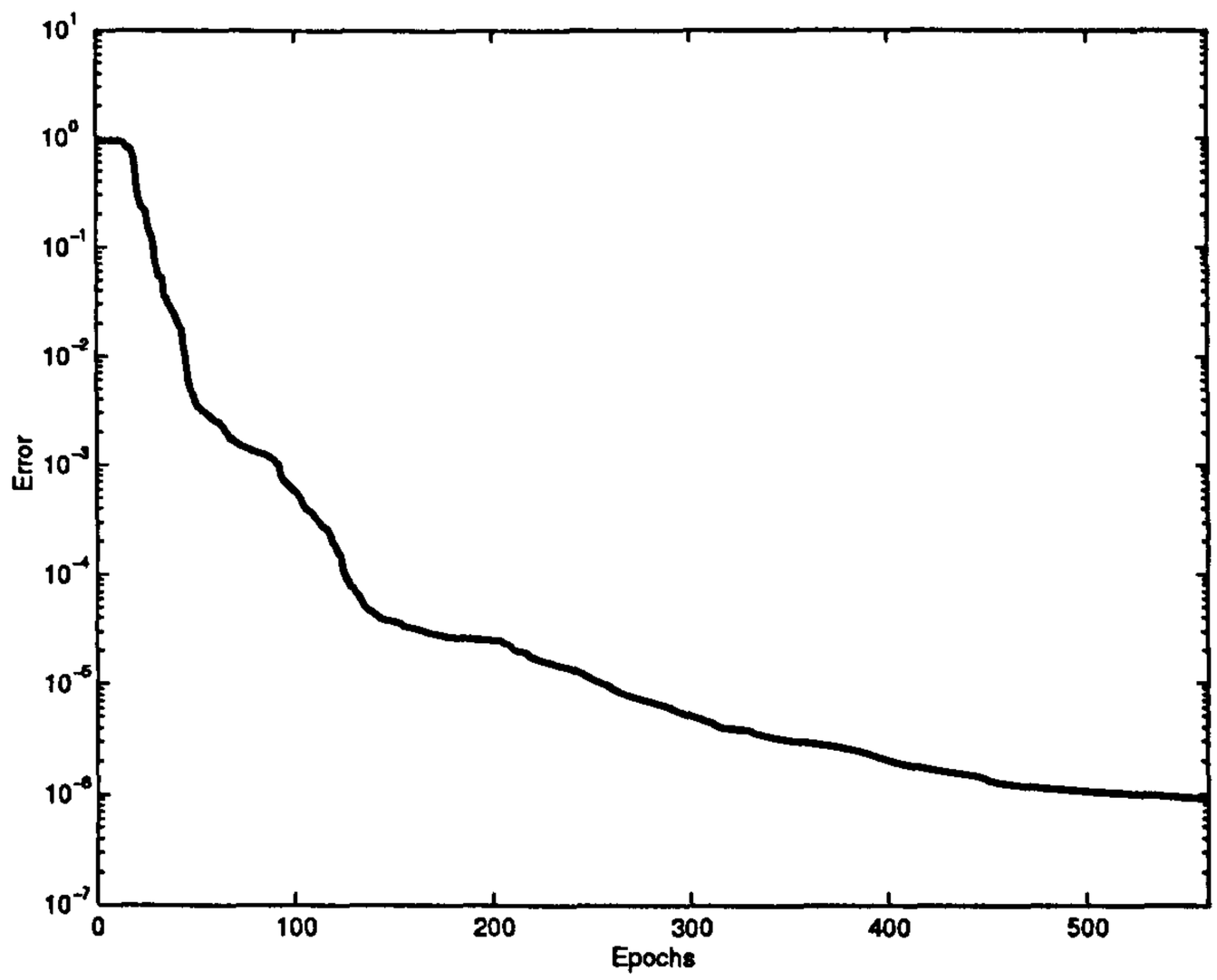

Figure 7.13: Evolution of error ($\alpha = 1.1 \;\; \beta = .3 \;\; \gamma = .7$).

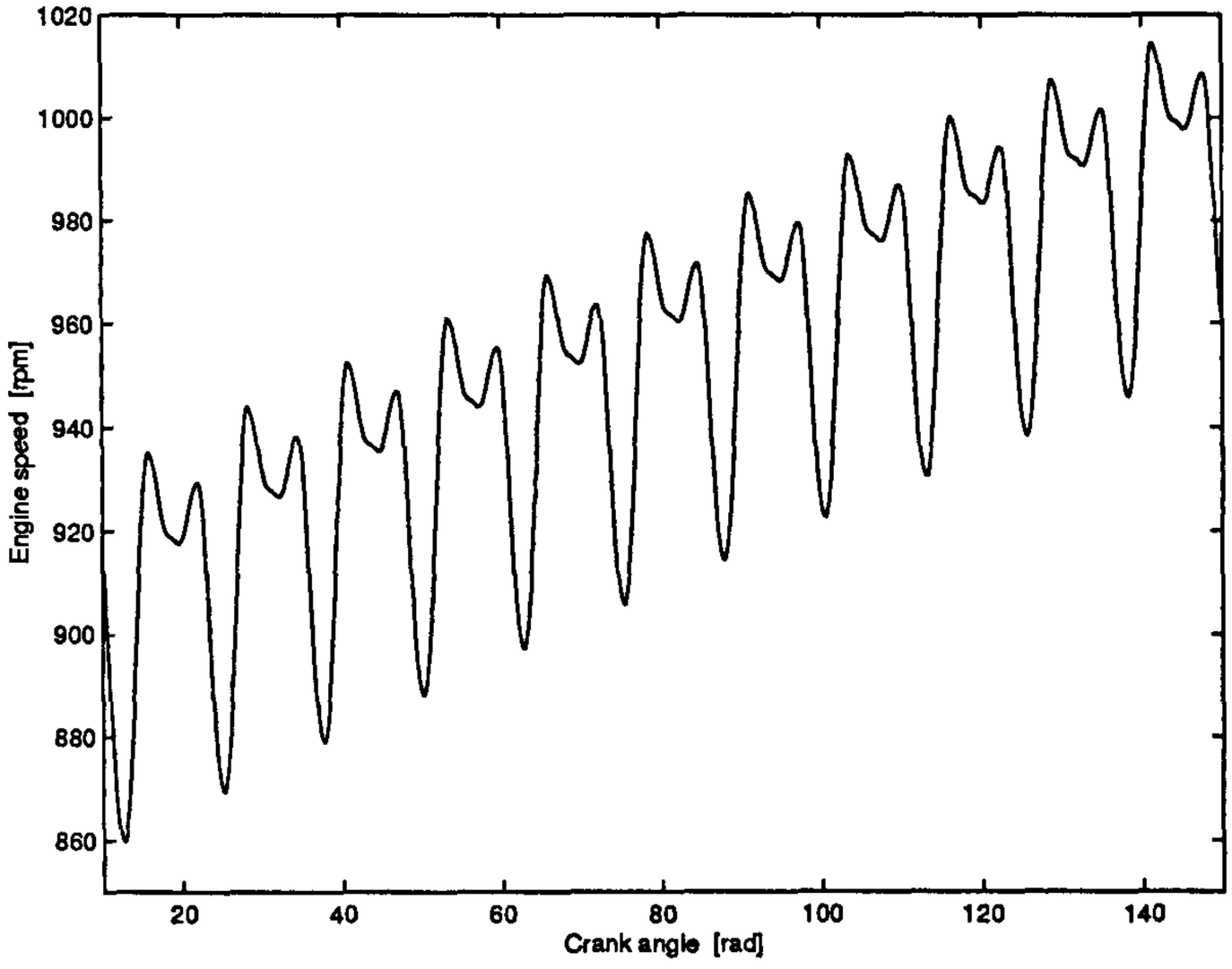

Figure 7.14: Measured engine speed [FA97]

Figure 7.15: Indicated torque: (a) measured [FA97] and (b) obtained from the trained network

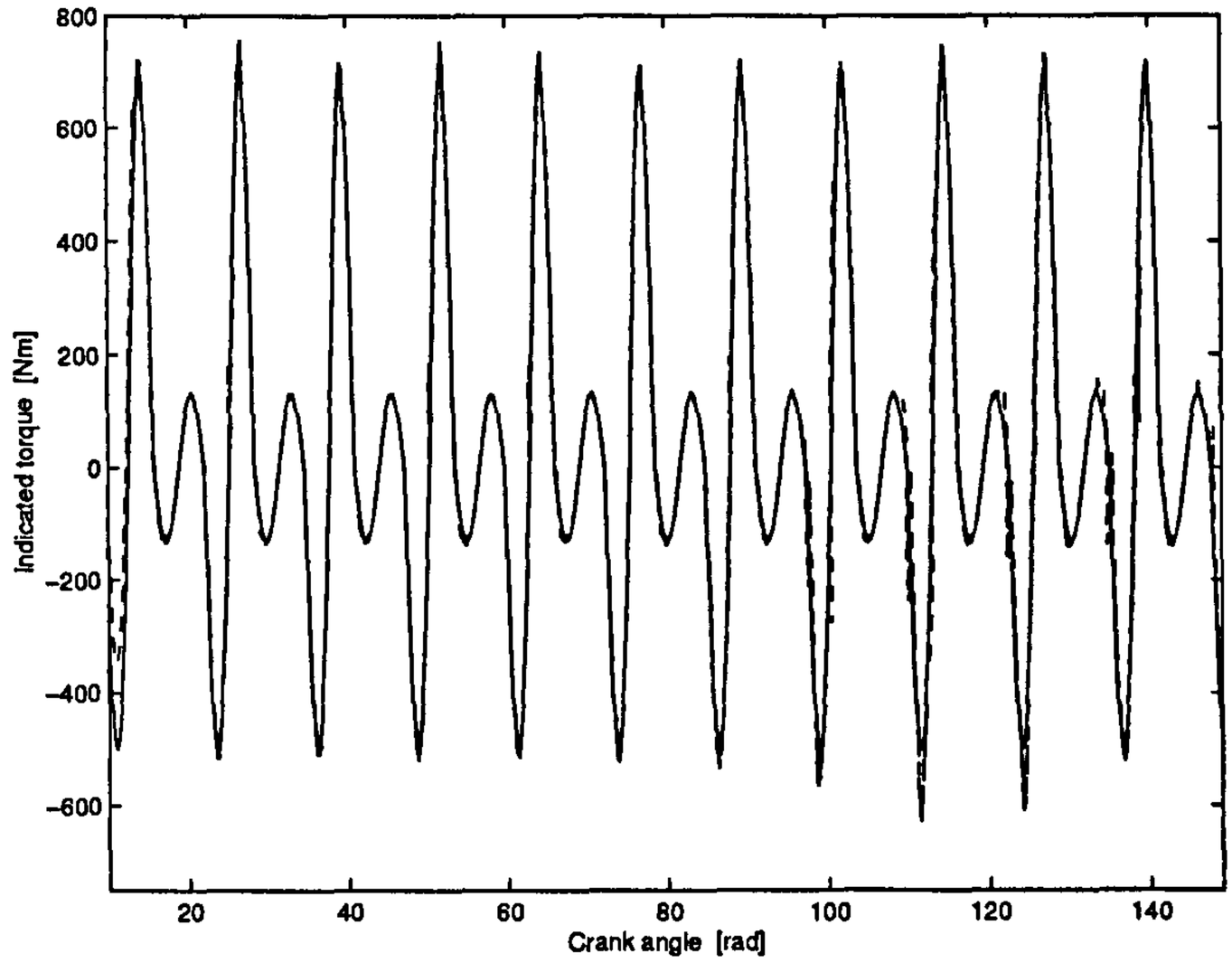

Figure 7.16: Comparison between measured (——) [FA97] and estimated (- - -) engine indicated torque

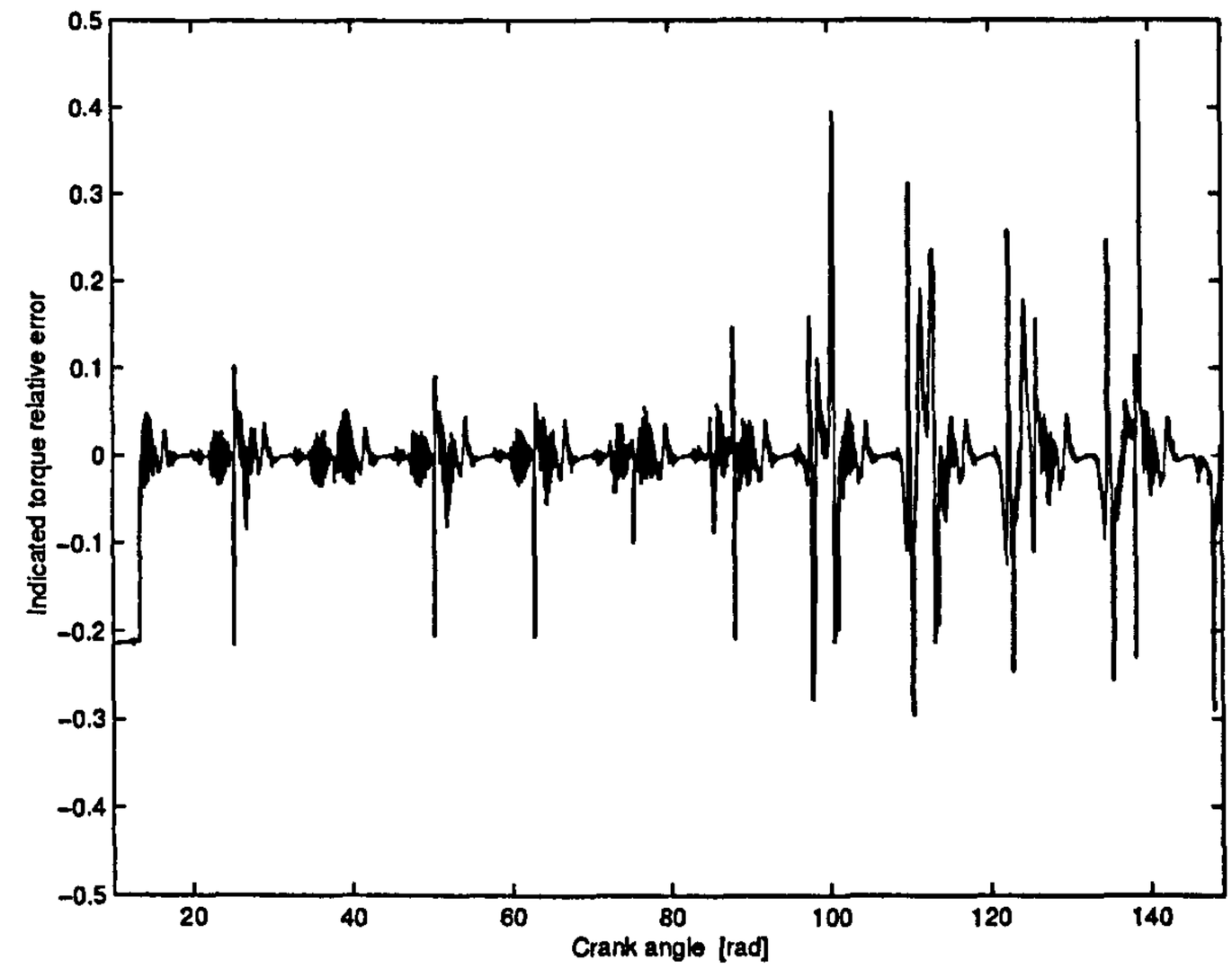

Figure 7.17: Indicated torque relative error

7.4 Discussion and conclusions

Figure 7.16 shows that the estimated torque converges to the correct indicated torque. Also, the figure depicts a good agreement between the estimated and measured indicated engine torque. The relative error between measured and estimated indicated torque is shown in Figure 7.17, and although the maximum errors are quite large, the average error is not excessive. This indicates that the ANN based estimation scheme has further potential.

Comparing the results of the ANN based estimator, (Figure 7.16), and the sliding mode observer results, (Figure 6.5), shows that the proposed estimator performs nearly as well as to the sliding mode estimation method. Also, the comparison between the relative errors of indicated torque shown in Figures 7.17 and 6.3(a), shows that the ANN based estimator gives a reasonable accuracy. The accuracy of the ANN estimator could improved by additional training. Investigation of the robustness of the estimator remains for further work.

The ANN based estimator has been designed to estimate only the indicated torque without loading. Thus the scheme needs to be extended to include estimation of the load torque. Furthermore, rigorous stability analysis is needed for the estimator. The work on this ANN based estimator is essentially of a preliminary nature, and although further research is required, it appears that the scheme has potential to provide an alternative practical approach to on-board diagnostics.

Chapter 8

Conclusions and Future Research

8.1 Conclusions

A detailed analytical model for a generic four-stroke direct injection single-cylinder Diesel engine is developed to predict the instantaneous engine speed and indicated torque from fuelling. The main features of this model are:

(a) A novel combination of equations for the friction of ring assembly, bearing mixed lubrication and valve train are presented.

(b) The instantaneous friction model can simulate instantaneous engine friction behaviour under transient and cold-start operating conditions by including the temperature-viscosity changes.

(c) The inertia variations of the crank shaft assembly with piston pin offset are included.

The model also includes the inertia of the dynamometer, and the stiffness and damping of the coupling. The Diesel engine model is implemented in Matlab/SIMULINK.

Profiles of the cylinder gas pressure and the instantaneous crankshaft angular velocities predicted by the model, through the transient and steady-state cycles during warm-up and cold start conditions, are in good agreement with measurements,

and it is shown that for the result tested, the model has a prediction accuracy of 97%.

A novel numerical inversion technique for the dynamic equations of a single cylinder Diesel engine is developed. The technique can estimate the dynamic model parameters at transient and steady state conditions. The numerical inversion technique uses the Newton-Raphson method. The input data, crankshaft velocity, indicated torque, dynamometer velocity and applied load are used to estimate the engine parameters. The estimated engine parameters have been compared with experimentally measured values and are in agreement. In the comparison study the technique predicted engines parameters with a maximum error of less than 2.5%.

It is noted that during transient response, the initial estimates for the parameters need to be within about 60% of their actual values for the technique to guarantee convergence.

A sliding mode observer is developed to estimate the engine indicated and load torques from crank shaft and coupling angular velocities, and angular displacements measurements. The main features of this observer are:

(a) New nonlinear observers for the engine indicated and load torques are developed.

(b) A new sliding gain for the indicated torque observer is designed as a nonlinear function of the engine crank angle to reduce the chattering effect.

(c) The stability of the observers are proved to guarantee convergence using Lyapunov stability theory.

It is shown that the estimated torque has a good accuracy when compared to experimental data.

A new artificial neural network based technique for Diesel engine indicated torque estimation is presented. The network is trained using a new three-term backpropagation algorithm. The technique is applied to the problem of estimating

indicated torque from measurements of crankshaft angular velocity and displacement. It is shown that the estimated torque has a good accuracy when compared to experimental data. The preliminary results are encouraging indicating promise for real-time applications and for use as an on-board diagnostic tool.

The standard two-term backpropagation algorithm is commonly used to train ANNs. However, this algorithm can have relatively slow rate of convergence, and may become unstable at high learning parameter values. To overcome these problems a new three-term BP algorithm to reduce the number of training epochs and provide escape from learning stalls whilst maintaining the simplicity of the standard BP algorithm is presented.

The main features of this algorithm are:

(a) A new additional term to speed-up the training is proposed; this being a proportional factor (PF).

(b) A new stability analysis is presented. The stability analysis creates necessary and sufficient conditions for the convergence of the three-term backpropagation algorithm.

(c) Novel optimization procedures for the learning parameter values selection of the new backpropagation algorithm are presented.

Comparative test results indicate that the new algorithm offers much higher speeds of convergence than the standard BP algorithm. The three-term algorithm is applicable to any network with any kind of activation functions. Such an algorithm is useful for Diesel engines modelling, estimation and control. The new algorithm is computationally simple, and is a simple extension of the standard BP algorithm. The three-term BP algorithm is more robust to the choice of initial weights, especially when relatively high values for the learning parameters are selected.

8.2 Suggestions for future research

Future research based on this thesis includes the following:

- The models should be extended to multi-cylinder Diesel engines. The models have been constructed using the SIMULINK hierarchical sub-model approach, and hence this task, although not trivial, should not be onerous.

- Further investigation of numerical inversion technique for the dynamics of Diesel engines is required, especially during transient response in order to make the approach less sensitive to initial guess and to cover a wide spectrum of the engine data. This could be based on advanced generalized Newton methods for systems of m equations in n variables [LBI01]. Such a method can be implemented in an adaptive way allowing a controlled increase of the ranks of the *outer inverse*. Also the method can be used if the Jacobian cannot be assumed nonsingular.

- Future work could use the same sliding mode observer to estimate cylinder by cylinder engine indicated torque for each cylinder of multi-cylinder Diesel engines, utilizing repeat speed sampling at each cylinder duration of the crank angle, which may be useful since the engine cylinders are working in a sequential fashion.

- Immediate research in order for feedback/ANN feedforward estimator to work robustly and to achieve accurate estimation, by including the load effects as disturbance inputs. Rigorous research is needed to analyze the stability for the closed loop of the estimator. Such an estimation scheme could allow the use a model-based estimator to maintain controller operation in the face of sensor failure.

- Diagnostics tools can be developed based on the proposed estimation strategies. Misfire of engine cylinders during operation could be diagnosed based on the difference between the firing indicated torque and the motoring (without

firing) indicated torque. Also, the indicated torque centroid could be used to diagnose problems with fuel injection timing and its duration.

- The thermodynamic model could be included in the estimator to provide a correction term. This would also enable estimation of the air fuel ratio. Air fuel ratio is an important aspect for fuelling control to reduce emissions.

- The testing of the estimation schemes have been performed only in simulation. It is essential that the schemes be tested experimentally before they can be seriously considered for possible implementation in production engines.

Appendix A

List of Publications Based on the Thesis

A.1 Journals

(1). Y.H. Zweiri, J.F. Whidborne and L.D. Seneviratne: Stability of Three-Term Backpropagation Algorithm. **Neural Network Journal.** Pending.

(2). Y.H. Zweiri, J.F. Whidborne and L.D. Seneviratne: Three-Term Backpropagation Algorithm. **Neurocomputing Journal,** 50:305-318. 2003.

(3). Y.H. Zweiri, J.F. Whidborne, L.D. Seneviratne, and K.A. Althoefer: A comparison of dynamic models of various complexity for diesel engines. **Math. & Comp. Modelling of Dyn. Syst. Journal,** 8(3):273-289. 2002.

(4). Y.H. Zweiri, J.F. Whidborne and L.D. Seneviratne: Detailed analytical model of a single-cylinder Diesel engine in the crank-angle domain. **Proc. IMechE, Part D: J of Automobile Eng,** 215(11):1197-1216. 2001.

(5). Y.H. Zweiri, J.F Whidborne, and L.D. Seneviratne. Instantaneous friction components model for transient engine operation. **Proc. IMechE, Part D: J of Automobile Eng**, 214(7):809-824. 2000.

(6). Y.H. Zweiri, J.F. Whidborne, and L.D. Seneviratne. Numerical inversion of the dynamic model of a single-cylinder Diesel engine. **Commun. Numer. Meth. Engng**, 16(7):505-517 . 2000.

(7). Y.H. Zweiri, J.F Whidborne, and L.D. Seneviratne. Dynamic simulation of a single-cylinder diesel engine including dynamometer modelling and friction. **Proc. IMechE, Part D: J of Automobile Eng**, 213:391-402. 1999.

(8). Y.H. Zweiri, J.F. Whidborne and L.D. Seneviratne: Diesel engine indicated and load torque estimation using sliding mode observer. To be submitted.

(9). Y.H. Zweiri, J.F. Whidborne and L.D. Seneviratne: Optimisation of Three-Term Backpropagation Algorithm. To be submitted.

A.2 Conferences

(1). Y.H. Zweiri, J.F. Whidborne, L.D. Seneviratne, and K.A. Althoefer: Dynamic modelling of diesel engines for design applications. *Engineering Design Conf.* 2002, pages 701-709, London, July 2002.

(2). Y.H. Zweiri, J.F Whidborne, K.A. Althoefer and L.D. Seneviratne. A new three-term backpropagation algorithm with convergence analysis. *Proc. 2002 IEEE Int. Conf. on Robotics and Automation* (ICRA'2002), pp. 3882-3887, Washington, D.C., 11-15 May, 2002.

(3). Y.H. Zweiri, J.F. Whidborne, and L.D. Seneviratne: Stability of a three-term backpropagation algorithm. *Int. Symp. Computational Intelligence* (CI'2000), Woolongong, Australia, December 2000. CD-ROM paper No. 1514-040.

(4). Y.H. Zweiri, J.F. Whidborne, and L.D. Seneviratne: Three-term backpropagation algorithm. *Int. Conf. Artificial Intelligence in Science and Technology* (AISAT 2000), Hobart, Australia, December 2000.

(5). Y.H. Zweiri, J.F. Whidborne, and L.D. Seneviratne: Diesel engine indicated and load torque estimation using sliding mode observer. *Proc. ASME-ICE Fall Engine Tech. Conf.* vol. 3, pp 95-103, Peoria, IL. September 2000.

(6). Y.H. Zweiri, J.F. Whidborne, and L.D. Seneviratne: Optimisation of a three-term backpropagation algorithm. *Proc. CONTROL 2000*, Cambridge, UK, September 2000. CD-ROM paper No. 196.

(7). Y.H. Zweiri, J.F. Whidborne, and L.D. Seneviratne: Efficient modelling for instantaneous friction components of Diesel Engines. *Proc. CONTROL 2000*, Cambridge, UK, September 2000. CD-ROM paper No. 194.

(8). Y.H. Zweiri, J.F. Whidborne, and L.D. Seneviratne: Diesel engine analytical model for non-linear control and estimation. *Proc. CONTROL 2000*, Cambridge, UK, September 2000. CD-ROM paper No. 195.

(9). Y.H. Zweiri, J.F. Whidborne and L.D. Seneviratne: Numerical inversion of the dynamic model of a single-cylinder diesel engine. *1999 ASME Spring Engine Tech. Conf.*, vol. 3, pp 139-149. Columbus, Indiana. April, 1999.

(10). Y.H. Zweiri, J.F. Whidborne and L.D. Seneviratne: A mathematical transient model for the dynamics of a single cylinder diesel engine, *Simulation '98*, pp 145-151, York, UK, September 1998.

Appendix B

Derivation of Equations for the Friction Components

Detail of the derivation of friction components due to ring assembly, bearing and valve train are given in this Appendix.

B.1 Ring assembly friction torque

The force components acting on the ring assembly include static ring tension (which depends on ring design and materials), the gas pressure force (which depends on the gas pressure beneath the rings (keystone effect)) and the crank-connecting rod force (which is related to the lateral force) [FTT81, UP83, CRD96].

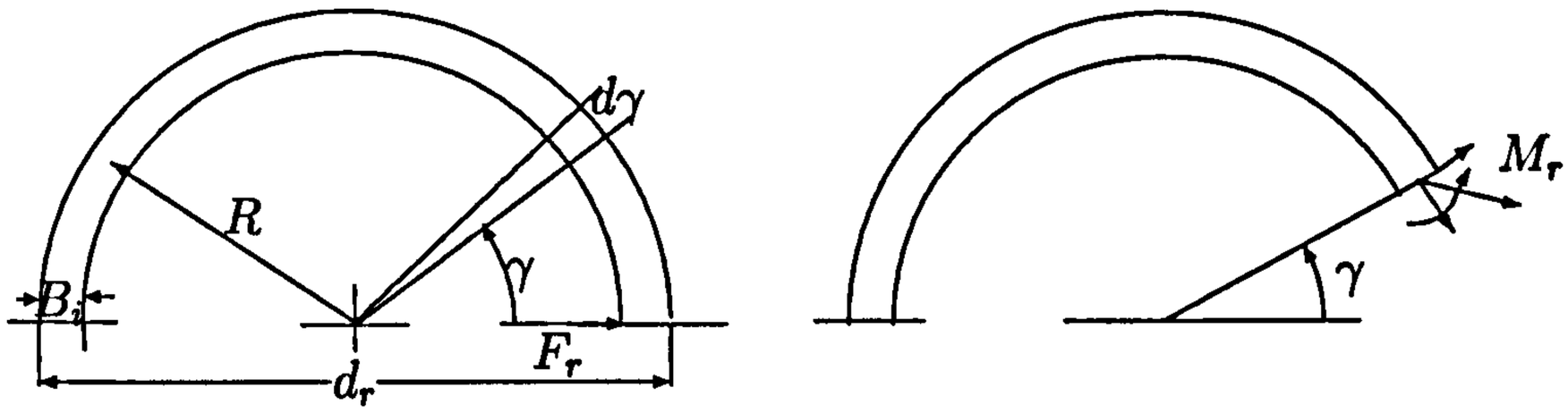

Figure B.1: Diagram showing forces acting on section of a ring

B.1.1 Ring assembly friction torque from the static tension (pressure)

The static ring tension is easily obtained using Castigliano's theorem. Castigliano's theorem [SM89], states that when forces act on an elastic system subject to small displacement, the displacement corresponding to any force, co-linear with the force, is equal to the partial derivative of the total strain energy with respect to that force. Three terms contribute to the total strain energy SE_r, a term due to bending moment, another due to normal force and the shear energy. Both the strain energy due to shear and normal force have a minor effect, so in this work only the bending moment is considered. Hence

$$SE_r = \int \frac{M_r R d\gamma}{2E_i I}. \tag{B.1}$$

Using Castigliano's theorem, the gap closure of the piston ring is derived as:

$$g_c = \frac{\partial SE_r}{\partial F_r} = \int_0^{\pi} \frac{M_r R}{E_i I} \left(\frac{\partial M_r}{\partial F_r} \right) d\gamma. \tag{B.2}$$

Now, from Figure B.1,

$$M_r = F_r R \sin\gamma, \tag{B.3}$$

so, substituting M_r into Equation (B.2) yields

$$F_r = \frac{2CE_i I g_c}{\pi R^3}, \tag{B.4}$$

where $R = (\frac{d_r}{2} - \frac{B_i}{2})$ is the mean radius of the ring, $I = \frac{\pi}{64} B_i^4$ is the moment of inertia of the ring and $C = 1.778$ is a correction factor [SM89]. The ratio between the static tension (pressure) and the ring force F_r is $\pi d_r B_i$, so by substituting into Equation (B.4), the static tension (pressure) can be expressed as

$$\frac{F_r}{\pi d_r B_i} = \frac{E_i g_c}{7.07 d_r \left(\frac{d_r}{B_i} - 1\right)^3}, \tag{B.5}$$

since $\frac{C}{4\pi} = \frac{1}{7.07}$. Thus the ring assembly friction force, F_{f1_1}, from the static tension is expressed as:

$$F_{f1_1} = \eta \sum_{i=1}^{N} \left(\frac{E_i g_c}{7.07 d_r (\frac{d_r}{B_i} - 1)^3} \right) \pi d_r B_i, \tag{B.6}$$

and the ring assembly friction torque, T_{f1_1}, from the static tension is given as:

$$T_{f1_1} = \eta r \left| G(\theta_1) \right| \sum_{i=1}^{N} \left(\frac{E_i g_c}{7.07 d_r (\frac{d_r}{B_i} - 1)^3} \right) \pi d_r B_i. \tag{B.7}$$

B.1.2 Ring assembly friction torque from the gas pressure

The effect of the gas pressure on each ring friction is included by taking into consideration the reduction in pressure at each successive ring. The reduction factors a_i for piston rings have been taken as 1 for the first compression ring, 0.5 for the second compression ring and for the oil ring is equal to the percent of the blowby pressure with respect to the indicated pressure, and it is equal 4%–12% [DER+79]. The ring assembly friction force, F_{f1_2}, from the gas pressure is expressed as:

$$F_{f1_2} = \eta \sum_{i=1}^{N} a_i \left| p_I - p_{atm} \right| \pi d_r B_i, \tag{B.8}$$

and the ring assembly friction torque, T_{f1_2}, from the gas pressure is given as:

$$T_{f1_2} = \eta r \left| G(\theta_1) \right| \sum_{i=1}^{N} a_i \left| p_I - p_{atm} \right| \pi d_r B_i. \tag{B.9}$$

B.1.3 Ring assembly friction torque from the crank-connecting rod lateral force

In this section, the friction resulting from the lateral component of the crank-connecting rod force is calculated. It is assumed that this acts linearly in addition to the friction forces previously determined. From Figure 2.2, the effects of the inertia force on the ring assembly friction component are derived as:

$$\sum F_y = M\frac{d\dot{y}}{dt} = -F_{cr}\cos\beta + |p_I - p_{atm}|\,\frac{\pi}{4}d^2 - F_f, \tag{B.10}$$

$$\sum F_x = 0 = F_{st} - F_{cr}\sin\beta, \tag{B.11}$$

$$F_{f1_3} = \eta F_{st}, \tag{B.12}$$

where F_f is the total friction, F_{f1_3} is the friction force resulting from the crank-connecting rod lateral effect, F_{cr} is the connecting rod force and F_{st} is the side thrust force. Now $F_f = F_{f1_3} + F_\epsilon$ where F_ϵ represents the friction forces due to piston skirt friction, static tension and keystone effects given by (3.6), (B.6) and (B.8) respectively. The acceleration is given by $\ddot{y} = G_1(\theta_1)\dot{\theta_1}^2 + G_2(\theta_1)\ddot{\theta_1}$, and it is assumed that $G_2(\theta_1)\ddot{\theta_1}$ is negligible compared to the Coriollis term, hence it is assumed that $\ddot{y} = G_1(\theta_1)\dot{\theta_1}^2$. Applying these assumptions to (B.10) and solving for F_{f1_3} with (B.11) and (B.12) gives

$$F_{f1_3} = \eta\frac{|p_I - p_{atm}|\,\frac{\pi}{4}d^2 - MG_1(\theta_1)\dot{\theta_1}^2 - F_\epsilon}{\eta + \cot\beta}. \tag{B.13}$$

Thus the friction torque of the ring assembly, T_{f1_1} resulting from the effect of the inertia forces is expressed as:

$$T_{f1_3} = \eta r\,|G(\theta_1)|\,\frac{|p_I - p_{atm}|\,\frac{\pi}{4}d^2 - MG_1(\theta_1)\dot{\theta_1}^2 - F_\epsilon}{\eta + \cot\beta}, \tag{B.14}$$

where from Equation (2.9)

$$\cot\beta = G_3(\theta_1) = \frac{L\sqrt{1 - \left(\frac{\delta + r\sin(\theta_1 - \phi)}{L}\right)^2}}{(\delta + r\,|\sin(\theta_1 - \phi)|)}. \tag{B.15}$$

Now, the summation of the three effects (F_{f1_1}, F_{f1_2} and F_{f1_3}) yields the total ring assembly friction torque as:

$$T_{f1} = r\,|G(\theta_1)| \left[F_{f1_1} + F_{f1_2} + \eta \left(\frac{|p_I - p_{atm}|\,\frac{\pi}{4}d^2 - MG_1(\theta_1)\dot{\theta_1}^2 - F_\epsilon}{\eta + G_3(\theta_1)} \right) \right]. \quad \text{(B.16)}$$

Substituting for $F_\epsilon = F_{f2} + \mathrm{sgn}(\dot{y})(F_{f1_1} + F_{f1_2})$ gives

$$T_{f1} = r\,|G(\theta_1)| \left\{ \left(1 - \frac{\mathrm{sgn}(\dot{y})\eta}{\eta + G_3(\theta_1)} \right) (F_{f1_1} + F_{f1_2}) \right.$$
$$\left. + \eta \left(\frac{|p_I - p_{atm}|\,\frac{\pi}{4}d^2 - MG_1(\theta_1)\dot{\theta_1}^2}{\eta + G_3(\theta_1)} \right) - \left(\frac{\eta}{\eta + G_3(\theta_1)} \right) F_{f2} \right\}, \quad \text{(B.17)}$$

where sgn is the signum function, which is given in Equation (2.15). From (3.6), (B.6) and (B.8), the total ring assembly friction torque is given by

$$T_{f1} = r\,|G(\theta_1)| \left\{ \eta \left[\left(1 - \frac{\mathrm{sgn}(\dot{y})\eta}{\eta + G_3(\theta_1)} \right) \left(\sum_{i=1}^{N} \left(\frac{E_i g_c}{7.07 d_r (\frac{d_r}{B_i} - 1)^3} \right) \pi d_r B_i \right. \right. \right.$$
$$\left. \left. + \sum_{i=1}^{N} a_i\,|p_I - p_{atm}|\,\pi d_r B_i \right) + \left(\frac{|p_I - p_{atm}|\,\frac{\pi}{4}d^2 - MG_1(\theta_1)\dot{\theta_1}^2}{\eta + G_3(\theta_1)} \right) \right]$$
$$\left. - \left(\frac{\eta}{\eta + G_3(\theta_1)} \right) \left(\frac{\mu\dot{\theta}_1 r G(\theta_1)}{O_c} \right) dL_s \right\}. \quad \text{(B.18)}$$

B.2 Bearing friction torque

Bearing mixed friction torque

From Figure 2.2, the bearing reaction force F_{br} can be expressed as

$$F_{br} = \frac{F_r}{\cos\beta}, \quad \text{(B.19)}$$

where F_r is the resultant force which is given as

$$F_r = |p_I - p_{atm}|\,\frac{\pi}{4}d^2 + F_i, \quad \text{(B.20)}$$

where F_i is the inertia force acting at the wrist pin centre; which, from Figure 2.2, is

$$F_i = r\dot{\theta_1}^2 M \left(\cos\theta_1 + \frac{r}{L}\cos 2\theta_1 \right). \quad \text{(B.21)}$$

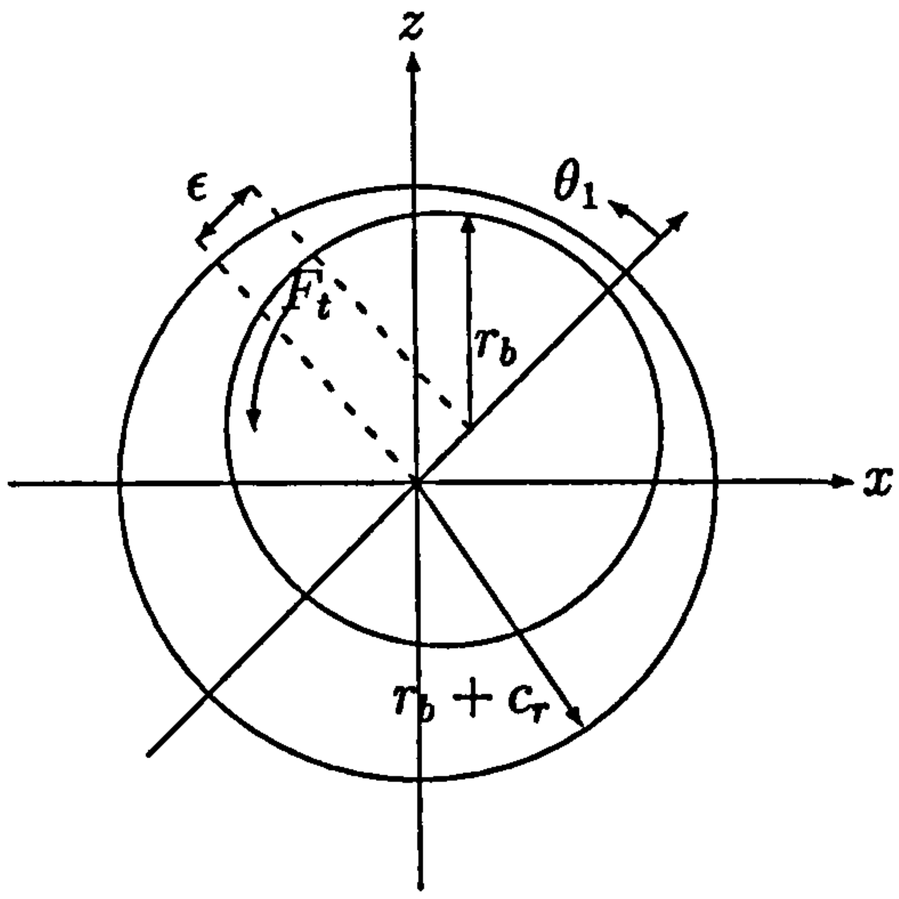

Figure B.2: Two-dimensional journal bearing geometry

Therefore

$$F_{br} = \frac{|p_I - p_{atm}| \frac{\pi}{4} d^2 - r\dot{\theta_1}^2 M \left(\cos\theta_1 + \frac{r}{L}\cos 2\theta_1\right)}{\cos\beta}, \tag{B.22}$$

By multiplying F_{br} by the friction coefficient for mixed lubrication, η_{bm}, and the bearing radius, r_b, the bearing mixed friction torque is

$$T_{f4} = \eta_{bm} r_b \left[\frac{|p_I - p_{atm}| \frac{\pi}{4} d^2 - r\dot{\theta_1}^2 M \left(\cos\theta_1 + \frac{r}{L}\cos 2\theta_1\right)}{\cos\beta}\right], \tag{B.23}$$

where from Equation (2.9),

$$\cos\beta = G_5(\theta_1) = \sqrt{1 - \left(\frac{\delta + r\sin(\theta_1 - \phi)}{L}\right)^2}. \tag{B.24}$$

B.2.1 Bearing hydrodynamic friction torque

In the Figure B.2, y is a distance across the bearing. The oil film pressure, p and the oil dynamic viscosity, μ, are taken as being independent of z. So

$$\frac{\partial p}{\partial x} = \mu \frac{\partial^2 u}{\partial z^2}, \tag{B.25}$$

can be integrated directly to

$$\frac{\partial u}{\partial z} = \frac{1}{\mu}\frac{\partial pz}{\partial x} + C_1, \tag{B.26}$$

and integrating again gives

$$u = \frac{1}{\mu}\frac{\partial p}{\partial x}\frac{z^2}{2} + C_1 z + C_2, \tag{B.27}$$

where C_1 and C_2 are two integration constants, which need two boundary conditions for their evaluation. The term u is the velocity of the fluid adjacent to the boundaries and it is the same as that of the boundaries themselves. The local oil film thickness is z, so at $z = c_r(1+\epsilon\cos\theta_1)$, $u = U_1$ and at $z = 0$, $u = U_2$. The terms U_1 and U_2 are the surface velocities. Evaluating C_1 and C_2 and substituting C_1 in Equation (B.26) gives

$$\frac{\partial u}{\partial z} = \frac{1}{\mu}\frac{\partial p}{\partial x}\left(z - \frac{c_r(1+\epsilon\cos\theta_1)}{2}\right) + \left(\frac{U_1 - U_2}{c_r(1+\epsilon\cos\theta_1)}\right). \tag{B.28}$$

Now the friction stress τ at the two surfaces is required at $z = 0$ and $z = c_r(1+\epsilon\cos\theta_1)$, so

$$\tau = \mu\frac{\partial u}{\partial z} = \pm\frac{\partial p}{\partial x}\left(\frac{c_r(1+\epsilon\cos\theta_1)}{2}\right) + \left(\frac{U_1 - U_2}{c_r(1+\epsilon\cos\theta_1)}\right)\mu. \tag{B.29}$$

The total drag F_b on whole bearing surface under consideration, of extent $2\pi r_b$ and L_b, in the x and y direction is

$$\begin{aligned} F_b &= \int_0^{L_b}\int_0^{2\pi r_b} \tau\, dx\, dy = \int_0^{L_b}\left(\int_0^{2\pi} \pm\frac{dp}{r_b d\theta_1}\frac{c_r(1+\epsilon\cos\theta_1)}{2} r_b d\theta_1 \right. \\ &\quad \left. + \int_0^{2\pi}\frac{\mu U_b}{c_r(1+\epsilon\cos\theta_1)} r_b d\theta_1\right) dy, \end{aligned} \tag{B.30}$$

Integrating the first term by parts gives

$$F_b = \int_0^{L_b}\left(\left|\frac{p c_r(1+\epsilon\cos\theta_1)}{2}\right|_0^{2\pi} \pm \int_0^{2\pi}\frac{p}{2} c_r \epsilon\sin\theta_1 d\theta_1 + \int_0^{2\pi}\frac{\mu U_b r_b d\theta_1}{c_r(1+\epsilon\cos\theta_1)}\right) dy, \tag{B.31}$$

The first of these terms is zero, as $p = 0$ at $\theta_1 = 0$ and $\theta_1 = 2\pi$. For the second term, the integral is solved using the relation

$$\int_0^{L_b}\int_0^{2\pi} p r_b \sin\theta_1 d\theta_1 dy = \frac{F_t}{2}, \tag{B.32}$$

where F_t is the tangential force on the journal bearing from the oil film. Using Sommerfeld's substitution [CE81], integration of the third term gives

$$\begin{aligned} \frac{\mu U_b r_b}{c_r}\int_0^{L_b}\int_0^{2\pi}\frac{d\theta_1 dy}{(1+\epsilon\cos\theta_1)} &= \frac{\mu U_b r_b L_b}{c_r}\int_0^{2\pi}\frac{(1-\epsilon\cos\theta_1)\sqrt{1-\epsilon^2}}{(1-\epsilon^2)(1-\epsilon\cos\theta_1)} d\theta_1 \\ &= \frac{2\pi\mu U_b r_b L_b}{\sqrt{(c_r^2 - \epsilon^2)}}. \end{aligned} \tag{B.33}$$

Thus, the total integral becomes

$$F_b = \frac{F_t}{2} + \frac{2\pi\mu U_b r_b L_b}{\sqrt{c_r^2 - \epsilon^2}}. \tag{B.34}$$

By substituting for $U_b = \dot{\theta}_1 r_b G_4(\theta_1)$ in the above and multiplying the first term by ϵ and the second term by r_b, the bearing friction torque is obtained as

$$T_{f3} = \left[\frac{F_t \epsilon}{2} + \frac{2\pi\mu\dot{\theta}_1 r_b^3 L_b G_4(\theta_1)}{\sqrt{c_r^2 - \epsilon^2}}\right], \tag{B.35}$$

where the geometrical function $G_4(\theta_1)$ is

$$G_4(\theta_1) = \left[1 + \frac{\cos\theta_1}{\sqrt{\left(\frac{L}{r}\right)^2 - \sin^2\theta_1}}\right]. \tag{B.36}$$

B.3 Valve train friction torque

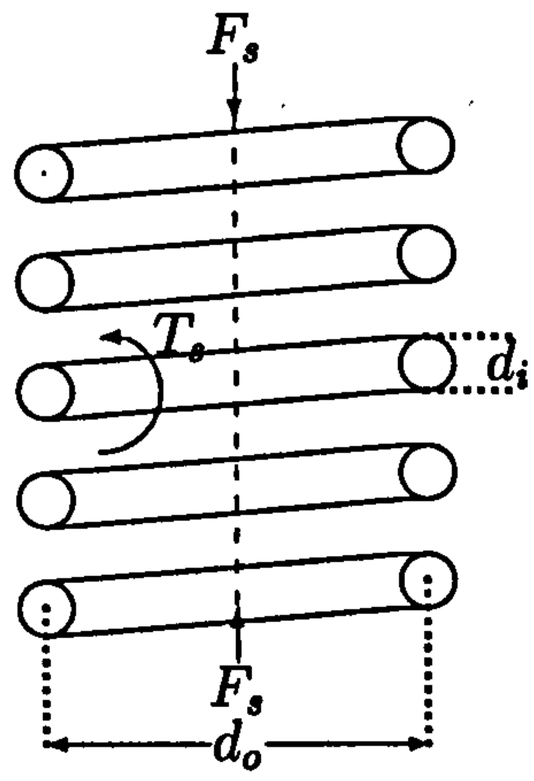

Figure B.3: The wire is subjected to a direct and a torsional shear

The spring rate is easily obtained using Castigliano's theorem. The total strain energy for a helical spring is composed of a torsional component and a shear component. The strain energy SE is

$$SE = \frac{T_s^2 \pi d_o N_t}{2 G_v J_s} + \frac{2 F_s^2 d_o N_t}{d_i^2 G_v}, \tag{B.37}$$

where from Figure B.3, $T_s = \frac{F_s d_o}{2}$ is the torsional torque, F_s is the axial force, d_o is the mean coil diameter and d_i is the wire diameter. The polar second moment of area is $J_s = \frac{\pi d_i^4}{32}$. Using Castigliano's theorem, the valve lift V_l is

$$V_l = \frac{\partial SE}{\partial F_S} = \frac{8F_s d_o^3 N_t}{d_i^4 G_v} + \frac{4F_s d_o N_t}{d_i^2 G_v} = \frac{8F_s d_o^3 N_t}{d_i^4 G_v}\left(1 + \frac{d_i^2}{2d_o^2}\right) \approx \frac{8F_s d_o^3 N_t}{d_i^4 G_v}. \quad \text{(B.38)}$$

The term $(\frac{d_i^2}{2d_o^2})$ is negligible because $(\frac{d_i}{d_o})$ is in the region of $(\frac{1}{10} - \frac{1}{14})$. The spring rate (stiffness) is equal to $F_s/V_l = \frac{d_i^4 G_v}{8d_o^3 N_t}$.

The predominant regime of lubrication in the valve train at lower speed is boundary lubrication, and at high speed it is mixed [Ciu92]. Thus the friction decreases slightly with speed. Here, the friction decrease is assumed to be linear with speed, hence the term $(1 - c_3\dot{\theta}_1)$ is introduced to represent the friction coefficient [Bis65]. Adding the spring forces and multiplying by the coefficient of friction, the friction force is obtained. By multiplying the friction force by $r\,|G(\theta_1)|$, the valve train friction torque can be expressed as

$$T_{f5} = \left(\frac{d_i^4 G_v}{8d_o^3 N_t}\right) \dot{V}_l N_v \left(1 - c_3\dot{\theta}_1\right) r\,|G(\theta_1)|\,. \quad \text{(B.39)}$$

where $G(\theta_1)$ is the geometric function given by Equation (2.6).

Appendix C

Numerical Analysis Method for the Friction Model

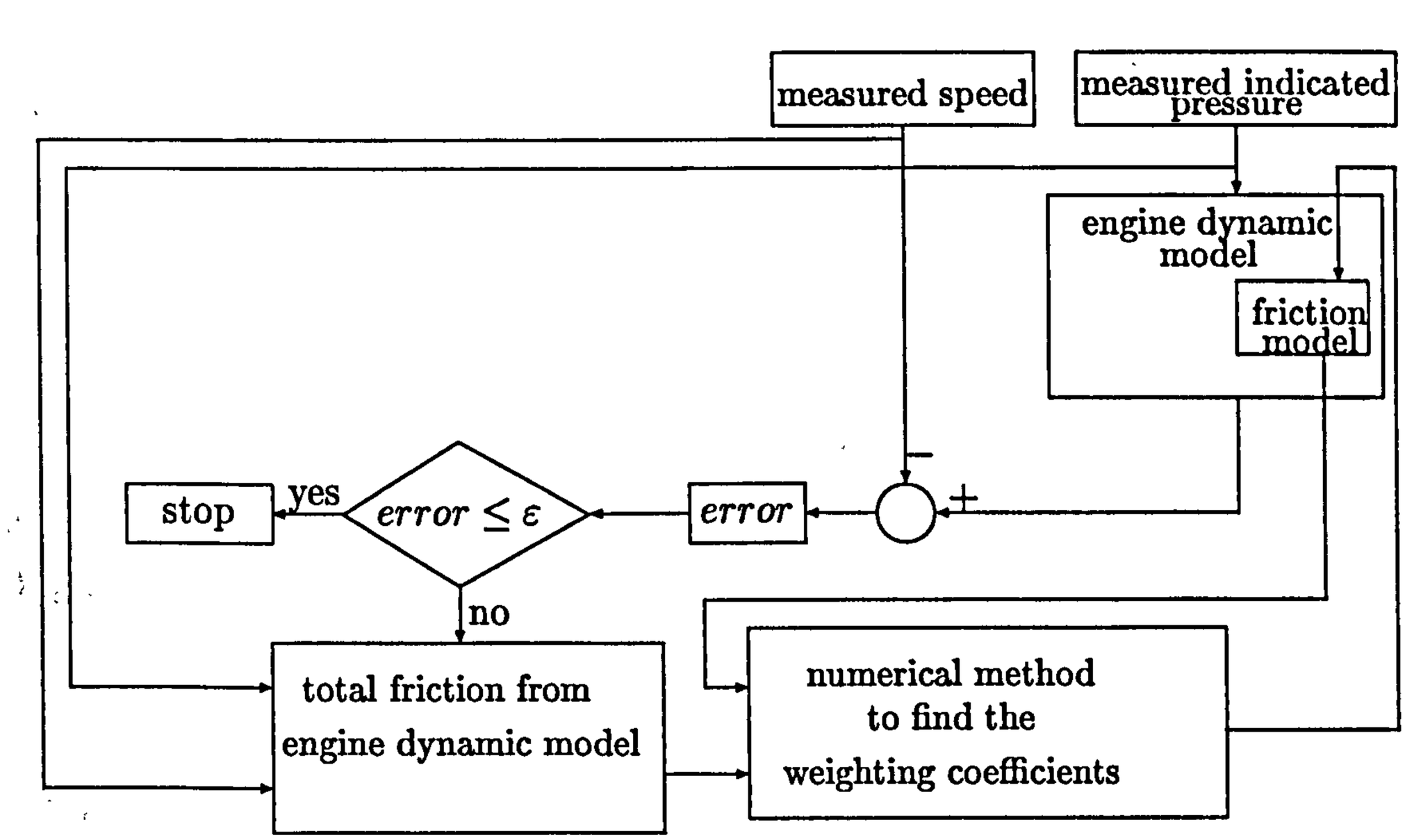

Figure C.1: Flow chart for numerical method

The modified friction model, Equation (3.18), contains six weighting coefficients, $\alpha_k, k = 1,\ldots,6$, to account for parameter and modelling uncertainties. These act in an affine manner on the 6 expressions $T_{fk}, k = 1,\ldots,6$, which describe the friction components, and are given by (3.1), (3.7), (3.8), (3.11), (3.13) and (3.14). Now, given $\alpha_k, k = 1,\ldots,6$, $p_I(t)$, and $T_L(t)$, $\dot{\theta}_{1(simu)}(t)$ can be calculated from the full engine model described by Equations (2.2)–(2.4) and (3.18). Since a measurement of speed, $\dot{\theta}_{1(meas)}(t)$ is available from experimental data, a numerical algorithm for estimating values of α_k for $k = 1,\ldots,6$ which minimizes the error between simulated and experimental speed profiles, $\dot{\theta}_{1(simu)}(t)$ and $\dot{\theta}_{1(meas)}(t)$ respectively, can be devised. This is done by calculating the total friction $\sum_{k=1}^{6} T_{fk}$ in Equation (2.1) using Equations (2.1)–(2.4) and the experimental data. From this, the weightings on the friction components α_k can be calculated by equating with the weighted sum of the simulated values of the friction components. In theory, the problem is infinite dimensional, because the minimization is performed over continuous time, t. Thus, in practice, a set of m discrete time points $t_j, j = 1,\ldots,m$ is chosen which cover the full range of engine operation.

Let $\Phi = [\alpha_1,\ldots,\alpha_6]^T$ be a vector of weighting coefficients, and let $\Pi_{(simu)}$ be an $6 \times m$ matrix of friction components at each time t_j obtained from the simulation,

$$\Pi_{(simu)} = \begin{bmatrix} T_{f1}(t_1) & T_{f2}(t_1) & \cdots & T_{f6}(t_1) \\ \vdots & \vdots & \ddots & \vdots \\ T_{f1}(t_m) & T_{f2}(t_m) & \cdots & T_{f6}(t_m) \end{bmatrix} \tag{C.1}$$

and let $T_{(meas)}$ be a corresponding m-dimensional column vector of total friction at each time t_j calculated from the measurements $\dot{\theta}_{1(meas)}$, $p_I(t)$, and $T_L(t)$ using Equations (2.1)–(2.4). Now,

$$\Pi_{(simu)}\Phi = T_{(meas)}. \tag{C.2}$$

Clearly, if $m > 6$, the problem is over parameterized, so, by taking the Moore-Penrose inverse of $\Pi_{(simu)}$, the least squares solution can be obtained [HJ85, p. 421]. Thus, $\Phi = \Pi^{\dagger}_{(simu)} T_{(meas)}$ is the least squares solution to Equation (C.2).

C.1 Algorithm

i) Set iteration number, $i = 0$. Define (obtained from experimental data) $p_I(t)$, $T_L(t)$ and $\dot{\theta}_{1(meas)}(t)$ and set initial values of $\Phi^{(0)}$. From Equations (2.1)–(2.4), calculate $T_{(meas)}$.

ii) From Equations (2.2)–(2.4) and (3.18), calculate $\dot{\theta}_{1(simu)}^{(i)}(t)$.

iii) If $\left\| \dot{\theta}_{1(simu)}^{(i)} - \dot{\theta}_{1(meas)} \right\| < \epsilon$, then $\alpha_k = \alpha_k^{(i)}$ and stop.

iv) From Equations (3.1), (3.7), (3.8), (3.11), (3.13) and (3.14), calculate $\Pi_{(simu)}^{(i)}$.

v) Obtain the least squares solution by $\Phi^{(i+1)} = [\Pi^{(i)}]_{(simu)}^{\dagger} T_{(meas)}$.

vi) Set $i = i + 1$ and go to Step (ii).

There is no guarantee of convergence of the algorithm, but for the example presented in this paper, it always converged. The algorithm method is implemented during firing conditions with $m = 20$ from low idle speed. There was some difficulty in the simulation due to the cyclic periodicity, and due to singularities when evaluating the geometric function $G(\theta_1)$ at these points. This was resolved by choosing a different set of $t_j, i = 1, \ldots, m$.

Appendix D

Derivation of Equations for Inertia Variations, and Conservation of Mass and Energy

Detail of the derivation of inertia variation is given in this Appendix. From the piston-crank mechanism, Figure 2.2, the connecting rod angle can be calculated as:

$$\sin\beta = \frac{\delta + r\sin(\theta_1 - \phi)}{L} \tag{D.1}$$

Equations (2.7) and (D.1) yield:

$$\cos\beta = \sqrt{\lambda(\theta_1)} \tag{D.2}$$

D.1 Kinetic analysis

Considering the force equilibrium for the piston, shown in Figure D.1 (a detail of Figure 4.1),

$$\sum f_x = 0$$

$$f_{Ax} = f_{st} \tag{D.3}$$

and

$$\sum f_y = m_p a_{Ay}$$

$$-f_{Ay} + f_i = m_p a_{Ay} \tag{D.4}$$

where f_A is the reaction force from the connecting rod on the piston pin, f_{st} is the side thrust force and f_i is the force, coming from the indicated pressure and the piston weight.

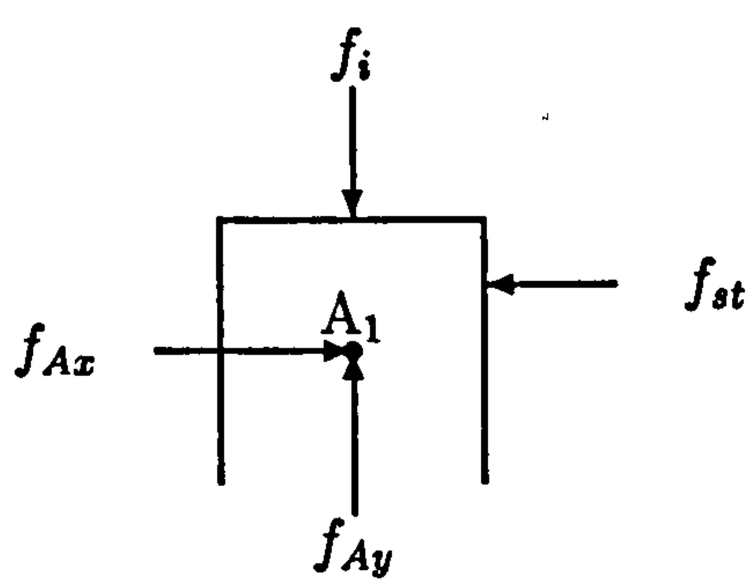

Figure D.1: Forces diagram for the piston

Considering the force and torque equilibrium for the connecting rod, shown in Figure D.2 (a detail of Figure 4.1),

$$\sum f_x = m_R a_{Bx}$$

$$-f_{Cx} + f_{Ax} = m_R a_{Bx} \tag{D.5}$$

$$\sum f_y = m_R a_{By}$$

$$-f_{Cy} + f_{Ay} + m_R g = m_R a_{By} \tag{D.6}$$

where f_C is the reaction force from the crank on the connecting rod, and

$$\sum M_B = J_R\ddot{\beta}$$

$$f_{Ax}(1-\hbar)L\cos\beta - f_{Ay}(1-\hbar)L\sin\beta + f_{Cx}\hbar L\cos\beta - f_{Cy}\hbar L\sin\beta = J_R\ddot{\beta} \quad \text{(D.7)}$$

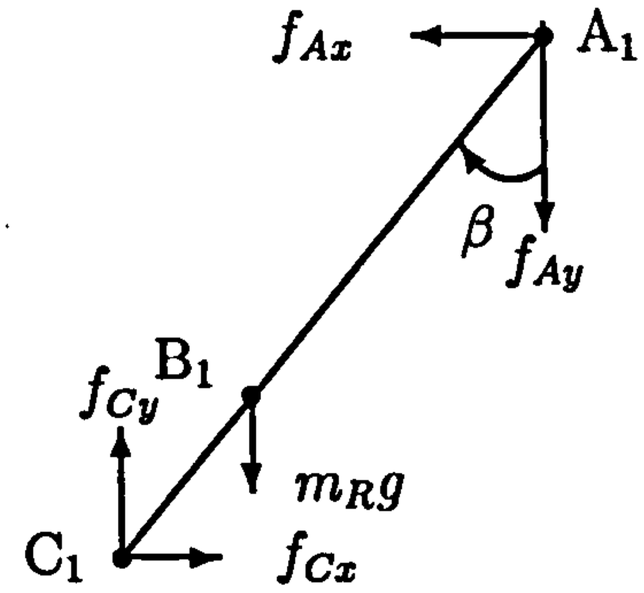

Figure D.2: Force diagram for the connecting rod

Considering the force and torque equilibrium for the crankshaft, shown in Figure D.3 (a detail of Figure 4.1),

$$\sum f_x = m_c a_{cx}$$

$$-f_{Dx} + f_{Cx} = m_c a_{cx} \quad \text{(D.8)}$$

$$\sum f_y = m_c a_{cy}$$

$$-f_{Dy} + m_c g + f_{Cy} = m_c a_{cy} \quad \text{(D.9)}$$

where f_D is the reaction from force of the bearing on the crank and T is an applied torque, and

$$\sum M_c = J_c\ddot{\theta}_1$$

$$\begin{aligned} T \;+\; & f_{Cx}(1+F)r\cos(\theta_1-\phi) + f_{Cy}(1+F)r\sin(\theta_1-\phi) \\ & -f_{Dx}Fr\cos(\theta_1-\phi) - f_{Dy}Fr\sin(\theta_1-\phi) = J_c\ddot{\theta}_1 \end{aligned} \quad \text{(D.10)}$$

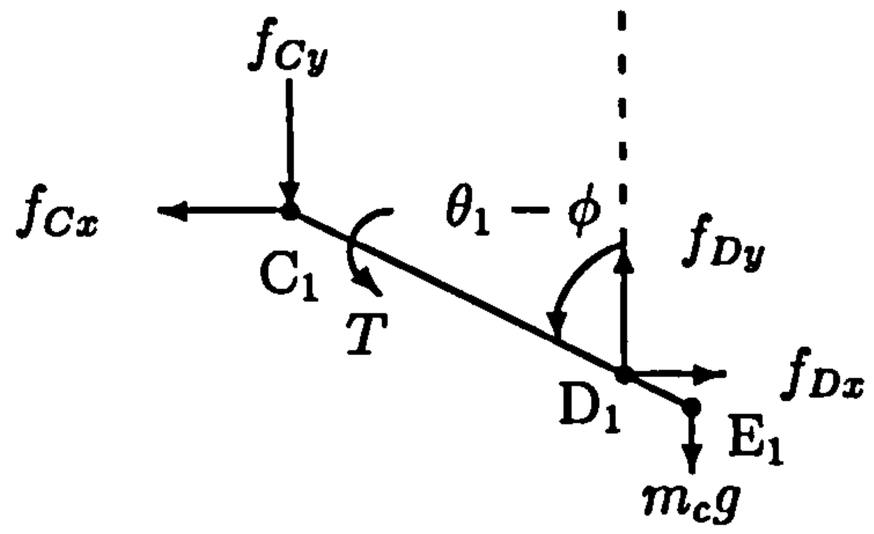

Figure D.3: Force diagram for the crankshaft

By substituting Equations (D.3) to (D.6) into Equation (D.7) gives f_{st}. Then substituting Equations (D.8) and (D.9) into Equation (D.10) yields:

$$\begin{aligned} T &= J_c\ddot{\theta}_1 - \frac{J_R\ddot{\beta}r\cos(\theta_1-\phi)}{L\cos\beta} - m_p a_{py}(r\cos(\theta_1-\phi)\tan\beta + r\sin(\theta_1-\phi)) \\ &\quad -m_R a_{Rx}(1-\hbar)r\cos(\theta_1-\phi) - m_R a_{Ry}(\hbar r\cos(\theta_1-\phi)\tan\beta + r\sin(\theta_1-\phi)) \\ &\quad +m_c a_{cx}\hbar r\cos(\theta_1-\phi) + m_c a_{cy}\hbar r\sin(\theta_1-\phi) - m_p g(r\cos(\theta_1-\phi)\tan\beta \\ &\quad +r\sin(\theta_1-\phi)) - m_R g(\hbar r\cos(\theta_1-\phi)\tan\beta + r\sin(\theta_1-\phi)) \\ &\quad -+ m_c g\hbar r\sin(\theta_1-\phi) f_i(r\cos(\theta_1-\phi)\tan\beta - r\sin(\theta_1-\phi)). \end{aligned} \tag{D.11}$$

D.2 Kinematic analysis

From Figure D.4, A_1 is connected to the piston, and in this analysis the piston is constrained to move in the y direction only. The velocity of the connecting rod can be calculated from Figure D.4 as:

$$\dot{\beta} = -\frac{\dot{\theta}_1 r\cos(\theta_1-\phi)}{L\cos\beta} \tag{D.12}$$

For the motion of the piston,

$$a_{px} = a_{Ax} = 0$$

$$a_{py} = a_{Ay} = a_{Cr}\cos(\theta_1-\phi) - a_{C\theta_1}\sin(\theta_1-\phi) + a_{A/Cr_1}\cos\beta + a_{A/C\vartheta}\sin\beta$$

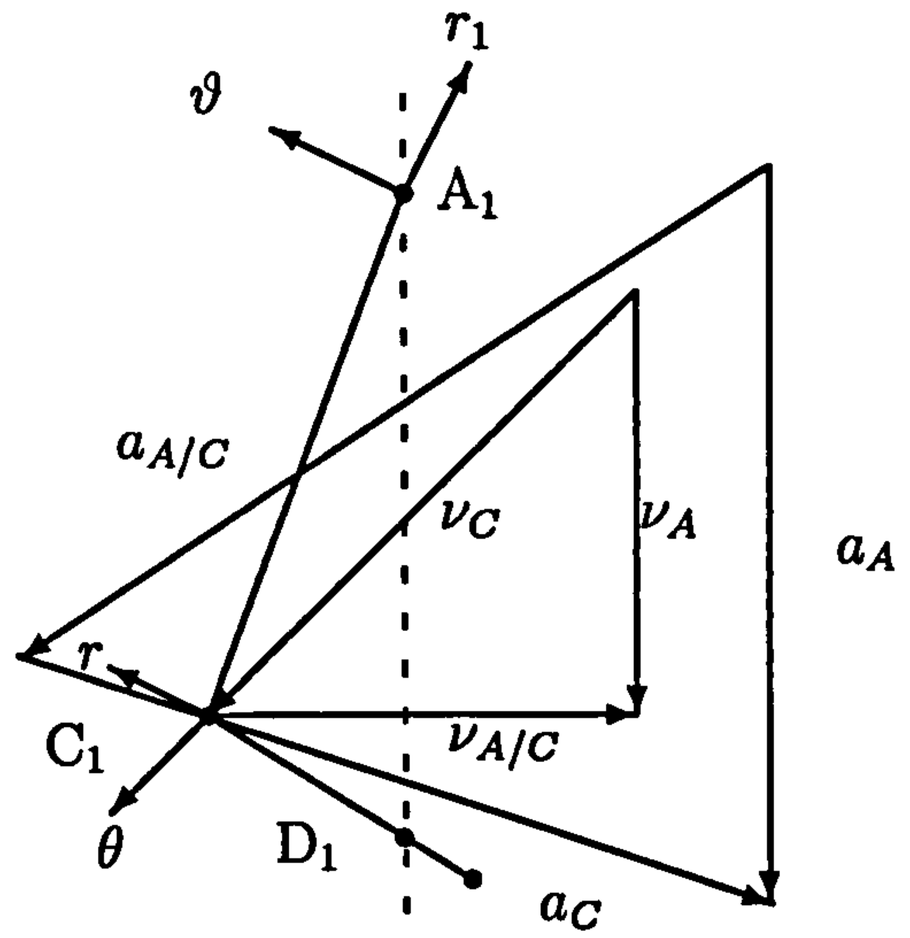

Figure D.4: Velocity and acceleration of the piston-crank mechanism

$$= \dot{\theta_1}^2 \left[-\frac{(r\cos(\theta_1-\phi))^2}{L\cos^3\beta} - r\cos(\theta_1-\phi) + r\sin(\theta_1-\phi)\tan\beta \right]$$
$$-\ddot{\theta}_1(r\cos(\theta_1-\phi)\tan\beta + r\sin(\theta_1-\phi)) \quad \text{(D.13)}$$

For the motion of the connecting rod,

$$a_{Rx} = \dot{\theta_1}^2(1-\hbar)r\sin(\theta_1-\phi) - \ddot{\theta}_1(1-\hbar)r\cos(\theta_1-\phi) \quad \text{(D.14)}$$

and

$$a_{Ry} = \dot{\theta_1}^2 \left[-\frac{(r\cos(\theta_1-\phi))^2}{L\cos^3\beta} - r\cos(\theta_1-\phi) + \hbar r\sin(\theta_1-\phi)\tan\beta \right]$$
$$-\ddot{\theta}_1(\hbar r\cos(\theta_1-\phi)\tan\beta + r\sin(\theta_1-\phi)) \quad \text{(D.15)}$$

For the motion of the crankshaft,

$$a_{cx} = -\dot{\theta_1}^2 F r\sin(\theta_1-\phi) + \ddot{\theta}_1 F r\cos(\theta_1-\phi) \quad \text{(D.16)}$$

$$a_{cy} = -\dot{\theta_1}^2 F r\cos(\theta_1-\phi) + \ddot{\theta}_1 F r\sin(\theta_1-\phi) \quad \text{(D.17)}$$

After substituting kinematic Equations (D.12)-(D.17) into Equation (D.11), rearranging yields:

$$\sum T = J_c + m_c(Fr)^2 + J_R\left[\left(\frac{r}{L}\right)^2 \frac{1}{\lambda(\theta_1)}\cos^2(\theta_1-\phi)\right]$$

$$+m_p r^2\left(\sqrt{\frac{1-\lambda(\theta_1)}{\lambda(\theta_1)}}\cos(\theta_1-\phi)+\sin(\theta_1-\phi)\right)^2+m_R r^2(1-\hbar)^2$$
$$\times\cos^2(\theta_1-\phi)+m_R r^2\left(\hbar\sqrt{\frac{1-\lambda(\theta_1)}{\lambda(\theta_1)}}\cos(\theta_1-\phi)+\sin(\theta_1-\phi)\right)^2\left[\ddot{\theta}_1\right]$$
$$+\left[\frac{1}{2}\dot{\theta_1}^2\right]2J_R\left[\left(\frac{r}{L}\right)^3\frac{\sqrt{1-\lambda(\theta_1)}}{\lambda(\theta_1)^2}\cos^3(\theta_1-\phi)-\left(\frac{r}{L}\right)^2\frac{1}{\lambda(\theta_1)}\cos(\theta_1-\phi)\right.$$
$$\left.\times\sin(\theta_1-\phi)\right]-2m_R(1-\hbar)^2r^2\cos(\theta_1-\phi)\times\sin(\theta_1-\phi)-m_R r^2$$
$$\times\left(\hbar\sqrt{\frac{1-\lambda(\theta_1)}{\lambda(\theta_1)}}\cos(\theta_1-\phi)-\sin(\theta_1-\phi)\right)\left[-\left(\frac{r\hbar}{L\sqrt{\lambda(\theta_1)^3}}\right)\right.$$
$$\left.\cos^2(\theta_1-\phi)-\cos(\theta_1-\phi)+\hbar\sqrt{\frac{1-\lambda(\theta_1)}{\lambda(\theta_1)}}\sin(\theta_1-\phi)\right]-m_p r^2$$
$$\left(\sqrt{\frac{1-\lambda(\theta_1)}{\lambda(\theta_1)}}\cos(\theta_1-\phi)+\sin(\theta_1-\phi)\right)\left[\left(\frac{r}{L\sqrt{\lambda(\theta_1)^3}}\right)\cos^2(\theta_1-\phi)\right.$$
$$\left.-\cos(\theta_1-\phi)+\sqrt{\frac{1-\lambda(\theta_1)}{\lambda(\theta_1)}}\sin(\theta_1-\phi)\right] \tag{D.18}$$

By comparing Equation (4.3) with Equation (D.18), Equations (4.1) and (4.2) are obtained.

D.3 Equations for conservation of mass and energy

The filling and emptying method treats the cylinder and each manifold as a thermodynamic control volume. The first law of thermodynamic for an open system can be written as:

$$\acute{U}=\acute{Q}-\acute{W}+\sum_{ii}\acute{H}_{0ii}, \tag{D.19}$$

where subscript ii denotes different entries to the control volume. Equation (D.19) can be written as:

$$(\acute{m}u)=\sum_{j}\acute{Q}_j-P\acute{V}+\sum_{ii}h_{0ii}\acute{m}_{ii}, \tag{D.20}$$

where j denotes surfaces with different rates of heat transfer, Q includes heat released by combustion, h_0 is the stagnation enthalpy, u is the specific internal energy, P and T are control volume pressure and temperature respectively and m is the mass.

Differentiating the left-hand side of Equation (D.20) gives

$$m\acute{u} + u\acute{m} = \sum_j \acute{Q}_j - P\acute{V} + \sum_{ii} h_{0ii}\acute{m}_{ii}, \tag{D.21}$$

The specific internal energy u is assumed to be a function of temperature T and the equivalence ratio F only. Thus $u = u(T, F)$, the first term in Equation (D.21) becomes:

$$m\acute{u} = m\left[\frac{\partial T}{\partial T}\acute{T} + \frac{\partial u}{\partial F}\acute{F}\right] \tag{D.22}$$

A curve fit of combustion product data, as a continuous function is used [WJ82], based on absolute zero temperature of the elements:

$$u = \frac{K_1(T) - K_2(T)F}{1 + f_s F} \tag{D.23}$$

where

$$K_1(T) = .692T + 39.17\times10^{-6}T^2 + 52.9\times10^{-9}T^3 - 228.62\times10^{-13}T^4 + 277.58\times10^{-17}T^5$$

and

$$K_2(T) = 3049.39 - 5.7\times10^{-2}T - 9.5\times10^{-5}T^2 + 21.53\times10^{-9}T^3 - 200.26\times10^{-14}T^4$$

This technique has the advantage that it automatically predicts a reduction of specific heat release by combustion at the richer than stoichiometric fuel air ratios, that occur during transient operation. Thus

$$\acute{Q} = \acute{Q}_{ht} + \acute{m}_f h_{for} \tag{D.24}$$

where $\acute{Q}_{ht}$ is the heat transfer rate, m_f is the mass of fuel burnt, and h_{for} is the enthalpy of formation of the hydrocarbons (fuel), given by [Ram89]:

$$h_{for} = 2.326[\psi - 19183 + .5(T_{fuel} - 537)] \tag{D.25}$$

ψ is the low heating value of the fuel.

Using Equations (D.21), (D.22) and (D.24), Equation (4.15) is obtained.

Assuming that the gases involved behave as perfect gases, i.e., $PV = mRT$, a control volume pressure P can be calculated.

D.4 Application of conservation equations

The solution of Equations (4.15), (4.18) and (4.21) are considered for each control volume, i.e., cylinder, inlet and exhaust manifolds in turn. In all cases it is assumed that T, m, F, and P are known at the beginning of each step. For the first step, estimated values are used as initial conditions, for the remaining steps, values are known from the previous step.

D.4.1 Cylinder

The basic processes occurring in the four-stroke cylinder can be divided into following: intake stroke, compression stroke, combustion and expansion stroke, and exhaust stroke. These are be considered separately, and are sub-divided according to flow direction and whether combustion is occurring.

i) Intake stroke: During this period, $\acute{m}_{out} = 0$, $\acute{m}_f = 0$, $\acute{m}_{fb} = 0$ and $\acute{m} = \acute{m}_{in}$. Equations (4.15) and (4.21) become

$$\acute{T} = \left[\left(\sum_j \acute{Q}_{htj} + \sum_{in} h_{oin}\acute{m}_{in} - u\acute{m}\right)\frac{1}{m} - \frac{RT}{V}\acute{V} - \frac{\partial u}{\partial F}\acute{F}\right] \Big/ \frac{\partial u}{\partial T}. \quad \text{(D.26)}$$

$$\acute{F} = -\left[\frac{1 + f_s F}{m}\right][F\acute{m}_{in}] \quad \text{(D.27)}$$

ii) Compression stroke: During this period $\acute{F} = 0$; $\acute{m} = 0$; $\acute{h}_{inorout} = 0$; $\acute{m}_{fb} = 0$

Equation (4.15) becomes

$$\acute{T} = \left[\sum_j \acute{Q}_{htj}\frac{1}{m} - \frac{RT}{V}\acute{V}\right] \Big/ \frac{\partial u}{\partial T}. \quad \text{(D.28)}$$

iii) Combustion and expansion: During this period $\acute{m} = \acute{m}_f$; $\acute{h}_{inorout} = 0$

Equations (4.15) and (4.21) become

$$\acute{T} = \left[\left(\sum_j \acute{Q}_{htj} + \acute{m}_f h_{for} - u\acute{m}\right)\frac{1}{m} - \frac{RT}{V}\acute{V} - \frac{\partial u}{\partial F}\acute{F}\right] \Big/ \frac{\partial u}{\partial T}. \quad \text{(D.29)}$$

$$\acute{F} = \left[\frac{1+f_s F}{m}\right]\left[\frac{1+f_s F}{f_s}\acute{m}_{bf} - F\acute{m}_f\right] \quad \text{(D.30)}$$

iv) Exhaust stroke: During this period, combustion is assumed to be completed and the equivalence ratio is constant. i.e $\acute{F} = 0$, $\acute{m}_{in} = 0$, $\acute{h}_{0in} = 0$, $\acute{m}_f = 0$ and $\acute{m} = \acute{m}_{out}$. Equations (4.15) becomes

$$\acute{T} = \left[\left(\sum_j \acute{Q}_{htj} + \sum_{out} h_{0out}\acute{m}_{out} - u\acute{m}\right)\frac{1}{m} - \frac{RT}{V}\acute{V}\right] \Big/ \frac{\partial u}{\partial T}. \quad \text{(D.31)}$$

D.4.2 Manifolds

Inlet Manifold

The air flow is supplied, hence the equivalence ratio is zero, so $\acute{F} = 0$. In addition $\acute{m}_{fb} = 0$, $\acute{Q}_{ht} = 0$, $\acute{V} = 0$ and $\acute{m} = \acute{m}_{in} - \acute{m}_{out}$. Equation (4.15) becomes

$$\acute{T} = \left[\left(\sum_{in} h_{oin}\acute{m}_{in} - \sum_{iout} h_{0out}\acute{m}_{out} - u\acute{m}\right)\frac{1}{m}\right] \Big/ \frac{\partial u}{\partial T}. \quad \text{(D.32)}$$

Exhaust manifold

Here, $\acute{m}_{fb} = 0$, $\acute{V} = 0$ and $\acute{m} = \acute{m}_{in} - \acute{m}_{out}$. Equations (4.15) and (4.21) become

$$\acute{T} = \left[\left(\sum_j \acute{Q}_{htj} + \sum_{in} h_{oin}\acute{m}_{in} - \sum_{out} h_{0out}\acute{m}_{out} - u\acute{m}\right)\frac{1}{m} - \frac{\partial u}{\partial F}\acute{F}\right] \Big/ \frac{\partial u}{\partial T}. \quad \text{(D.33)}$$

$$\acute{F} = -\left[\frac{1+f_s F}{m}\right][F\acute{m}] \quad \text{(D.34)}$$

Appendix E

Stability Analysis

In this appendix, the modified three-term BP algorithm is analyzed, and it is shown that all local minima of the least square error function are the only locally asymptotically stable points of the algorithm.

Equation (7.5) can be written as,

$$W(k+1) = W(k) - \alpha\nabla E(W(k)) + \beta\Delta W(k-1) + \gamma e(W(k)), \quad \text{(E.1)}$$

Let $\varrho_1(k) = W(k)$ and $\varrho_2(k) = W(k) - W(k-1)$. Then a state variable representation for Equation (E.1) is

$$\varrho_1(k+1) = \varrho_1(k) - \alpha\nabla E(\varrho_1(k)) + \beta\varrho_2(k) + \gamma e(\varrho_1(k)) \quad \text{(E.2)}$$

and

$$\varrho_2(k+1) = -\alpha\nabla E(\varrho_1(k)) + \beta\varrho_2(k) + \gamma e(\varrho_1(k)) \quad \text{(E.3)}$$

Lemma 2 *$c = (c_1, c_2)$ is an equilibrium point of the system given by Equations (E.2) and (E.3) if $c_2 = 0$ and $\alpha\nabla E(\varrho_1(k)) = \gamma e(\varrho_1(k))$.*

Proof: If $c = (c_1, c_2)$ is an equilibrium point, then $\varrho_1(k) = c_1$ and $\varrho_2(k) = c_2$ and

$$\varrho_1(k+1) - \varrho_1(k) = 0 \quad \text{(E.4)}$$

and

$$\varrho_2(k+1) - \varrho_2(k) = 0 \tag{E.5}$$

Then substituting in Equations (E.2) and (E.3) gives:

$$(1-\beta)\varrho_2(k) = -\alpha\nabla E(\varrho_1(k)) + \gamma e(\varrho_1(k)) \tag{E.6}$$

and

$$-\beta\varrho_2(k) = -\alpha\nabla E(\varrho_1(k)) + \gamma e(\varrho_1(k)) \tag{E.7}$$

Subtracting Equation (E.6) from Equation (E.7), yields $\varrho_2(k) = 0 \Longrightarrow c_2 = 0$. Substituting $\varrho_2(k) = 0$ into Equation (E.6) or (E.7), gives

$$\alpha\nabla E(\varrho_1(k)) = \gamma e(\varrho_1(k)). \tag{E.8}$$

■■

Remark 1 *Since* $c = (c_1, c_2)$ *is an equilibrium point of Equations (E.2) and (E.3) and* $e(\varrho_1(k)) = 0$, *then* $\nabla E(\varrho_1(k)) = 0$

Local stability properties around an equilibrium point (c_1, c_2) can be examined by using small signal analysis. Let the perturbed signals be defined as $\varphi_1 = \varrho_1 - c_1$ and $\varphi_2 = \varrho_2 - c_2$. Then the state equation becomes:

$$\varphi_1(k+1) = \varphi_1(k) - \alpha\nabla E(c_1 + \varphi_1(k)) + \beta\varphi_2(k) + \gamma e(c_1 + \varphi_1(k)), \tag{E.9}$$

$$\varphi_2(k+1) = -\alpha\nabla E(c_1 + \varphi_1(k)) + \beta\varphi_2(k) + \gamma e(c_1 + \varphi_1(k)). \tag{E.10}$$

By linearization around the equilibrium point c, Equations (E.9) and (E.10) become:

$$\varphi_1(k+1) \approx \varphi_1(k) - \alpha\nabla^2 E(c_1)(\varphi_1(k)) + \beta\varphi_2(k) + \gamma\nabla e(c_1)(\varphi_1(k)), \tag{E.11}$$

and

$$\varphi_2(k+1) \approx -\alpha\nabla^2 E(c_1)(\varphi_1(k)) + \beta\varphi_2(k) + \gamma\nabla e(c_1)(\varphi_1(k)). \tag{E.12}$$

Let the Hessian be defined as $A \in \mathbb{R}^{Q \times Q}$ and $\nabla e(c_1)$ be defined as $D \in \mathbb{R}^{Q \times Q}$, where Q is the size of the weight vector. Then

$$\begin{bmatrix} \varphi_1(k+1) \\ \varphi_2(k+1) \end{bmatrix} = \begin{bmatrix} I - \alpha A + \gamma D & \beta I \\ -\alpha A + \gamma D & \beta I \end{bmatrix} \begin{bmatrix} \varphi_1(k) \\ \varphi_2(k) \end{bmatrix} \tag{E.13}$$

This can be written in more compact form as

$$\phi(k+1) = \Theta\phi(k). \tag{E.14}$$

It is well-known that the discrete-time system in Equation (E.14) is asymptotically stable if (Θ) has distinct eigenvalues (Ψ_i) and each of the eigenvalues (Ψ_i) of (Θ) satisfy [Lei85]

$$|\Psi_i| < 1. \tag{E.15}$$

Lemma 3 *If λ is an eigenvalue of F, where $F = \left(\frac{A}{\gamma} - \frac{D}{\alpha}\right)$, then the corresponding eigenvalues of Θ are given by the solution of the quadratic equation*

$$\Psi^2 - (1 + \beta - \alpha\lambda\gamma)\Psi + \beta = 0 \tag{E.16}$$

where Ψ is any eigenvalue of Θ.

Proof: Θ is invertible for any A and D, as long as $\beta \neq 0$. All Ψ are non-zero since Θ is non-singular. Let $z = (\mathbf{x}, \mathbf{y})$ be a non-zero eigenvector corresponding to Ψ. Then

$$\Theta z = \Psi z, \tag{E.17}$$

which leads to

$$\mathbf{x} - \alpha A\mathbf{x} + \gamma D\mathbf{x} + \beta\mathbf{y} = \Psi\mathbf{x}, \tag{E.18}$$

and

$$-\alpha A\mathbf{x} + \gamma D\mathbf{x} + \beta\mathbf{y} = \Psi\mathbf{y}. \tag{E.19}$$

By substituting Equation (E.19) in Equation (E.18) and solving for $\mathbf{y}$ ($\Psi \neq 0$) gives

$$\mathbf{y} = \frac{(\Psi - 1)}{\Psi}\mathbf{x}. \tag{E.20}$$

Substituting Equation (E.20) into Equation (E.19) gives

$$(-\alpha A + \gamma D)\mathbf{x} = \left((\Psi - 1) - \frac{\beta(\Psi - 1)}{\Psi}\right)\mathbf{x}. \tag{E.21}$$

Since $\left(\frac{A}{\gamma} - \frac{D}{\alpha}\right) = F$; substituting into Equation (E.21) gives

$$F\mathbf{x} = \left(\frac{(\Psi - 1)(\frac{\beta}{\Psi} - 1)}{\alpha\gamma}\right)\mathbf{x}. \tag{E.22}$$

As $\left(\frac{(\Psi-1)(\frac{\beta}{\Psi}-1)}{\alpha\gamma}\right)$ is scalar and non-zero, if vector $\mathbf{x}$ satisfies this equation, then $\mathbf{x}$ is an eigenvector of F [HJ85]. Now λ is an eigenvalue of F and since $F\mathbf{x} = \lambda$, then clearly

$$\lambda = \left(\frac{(\Psi - 1)(\frac{\beta}{\Psi} - 1)}{\alpha\gamma}\right) \tag{E.23}$$

with corresponding eigenvector, $\mathbf{x}$. Rearranging Equation (E.23) yields

$$\Psi^2 - (1 + \beta - \alpha\lambda\gamma)\Psi + \beta = 0. \tag{E.24}$$

■■

Remark 2 *Vector $\boldsymbol{x}$ is non-zero. Otherwise, it is deduced from Equations (E.18) and (E.19) that $\boldsymbol{y}$ will be zero and therefore z is zero.*

Theorem 1 *The roots Ψ of Equation (E.24) satisfy $|\Psi| < 1$, and hence the system described by Equations (E.11) and (E.12) is stable if and only if the following conditions are satisfied:*

$$0 < \beta < 1, \tag{E.25}$$

and

$$0 < \alpha\gamma\lambda < 4. \tag{E.26}$$

Proof: The polynomial in Equation (E.24) is second-order and can be written as $f(z) = a_2 z^2 + a_1 z + a_0 = 0$. From the Jury test (see Section E.2), the roots of $f(z)$ are in the unit circle if and only if

$$|a_0| < a_2 \tag{E.27}$$

$$f(1) > 0 \tag{E.28}$$

and

$$(-1)^2 f(-1) > 0. \tag{E.29}$$

Applying the Jury test to Equations (E.24) yields roots within the unit circle if

$$|\beta| < 1, \tag{E.30}$$

$$(1+\beta) > ((1+\beta) - \alpha\gamma\lambda), \tag{E.31}$$

and

$$(1+\beta) > (-(1+\beta) + \alpha\gamma\lambda). \tag{E.32}$$

Hence inequality (E.31) leads to

$$\alpha\gamma\lambda > 0, \tag{E.33}$$

and inequality (E.32) leads to

$$\beta > \frac{\alpha\gamma\lambda}{2} - 1. \tag{E.34}$$

Since the momentum factor, β, is positive,

$$0 < \beta < 1. \tag{E.35}$$

Using inequality (E.35) on (E.34) yields

$$0 < \alpha\gamma\lambda < 4. \tag{E.36}$$

■■

The values of α and γ should be positive, to allow the system to learn. Thus it is sufficient that all eigenvalues of F be positive to conclude that c is a local minimum. So all the local minima of $E(\cdot)$ are locally asymptotically stable. Also, since $E(\cdot)$ has a local minimum then the Hessian A is a positive definite matrix.

E.1 Condition of D-matrix

Inequality (E.26) bounds the values of the learning rate α, the proportional factor γ and the eigenvalue of F. The aim of this sub-section is to investigate sufficient stability conditions such that relationships between the learning parameters α and γ can be found. An investigation is carried out to evaluate the conditions on matrix D such that matrix F is positive definite, where

$$F = \left(\frac{A}{\gamma} - \frac{D}{\alpha}\right). \tag{E.37}$$

The following theorem from [Gol91] is employed:

Theorem 2 *F is positive definite if and only if there exists a real nonsingular upper triangular matrix H such that $F = H^T H$.*

Two cases are considered:

Case I: Assume D is negative semidefinite, then $-D$ is positive semidefinite, and let $B = -D$.

Theorem 3 *Suppose B is positive semidefinite and A is positive definite. Then $F = \left(\frac{A}{\gamma} + \frac{B}{\alpha}\right)$ is positive definite and $\gamma \geq \det(A)/\det(F)$*

Proof: Since $A \geq 0$, from Theorem 2,

$$A = H^T H. \tag{E.38}$$

Let

$$S = H^{-1}, \tag{E.39}$$

then $A = S^{-T} S^{-1}$, so that $F = \left(\frac{A}{\gamma} + \frac{B}{\alpha}\right)$. This

$$S^T F S = \frac{I}{\gamma} + \frac{S^T B S}{\alpha}. \tag{E.40}$$

Since B is positive semidefinite, so is $S^T B S$; hence the eigenvalues of $S^T B S$ are positive. Therefore the eigenvalues of Equation (E.40) are no less than $\frac{1}{\gamma}$, which implies that

$$\det(S^T F S) \geq \frac{1}{\gamma}, \tag{E.41}$$

and hence, that $S^T FS$ is positive definite. Now

$$\det(A) = \det(S^{-T} S^{-1}) = (\det(S))^{-2}, \tag{E.42}$$

and therefore

$$\frac{1}{\gamma} \leq \det(S^T FS) = (\det(S))^2 \det(F) = \frac{\det(F)}{\det(A)}, \tag{E.43}$$

by rearranging Equation (E.43) yields to

$$\gamma \geq \frac{\det(A)}{\det(F)}. \tag{E.44}$$

■■

Since D is negative semidefinite then F is positive definite.

Case II: Assume D is positive semidefinite.

Theorem 4 *Suppose D is positive semidefinite and A is positive definite. Then $F = \left(\frac{A}{\gamma} - \frac{D}{\alpha}\right)$ is positive definite and $\frac{\alpha}{\gamma} I > S^T DS$.*

Proof: According to the previous proof

$$S^T FS = \frac{I}{\gamma} - \frac{S^T DS}{\alpha}, \tag{E.45}$$

In order for F to be positive definite, the right hand side of Equation (E.45) has to be positive $\frac{I}{\gamma} - \frac{S^T DS}{\alpha} > 0$, which implies that

$$\frac{\alpha}{\gamma} I > S^T DS. \tag{E.46}$$

■■

E.2 Stability analysis by using Jury test

The Jury test [PH96] is a stability criterion for sampled-data systems in the z-plane. It provides necessary and sufficient conditions for any polynomial to have no roots outside or on the unit circle. It can be applied to equations of any

order. Let the characteristic equation of a sampled-data system be expressed as the polynomial

$$f(z) = a_n z^n + a_{n-1} z^{n-1} + \ldots + a_1 z + a_0 = 0, \qquad a_n > 0.$$

To apply the Jury test, the stability test array should be obtained. The elements of the first two rows are obtained from the coefficients of the polynomial equation, and the elements of the remaining rows are calculated from the determinants

$$b_k = \begin{vmatrix} a_0 & a_{n-k} \\ a_n & a_k \end{vmatrix} \qquad c_k = \begin{vmatrix} b_0 & b_{n-1-k} \\ b_{n-1} & b_k \end{vmatrix}$$

$$d_k = \begin{vmatrix} c_0 & c_{n-2-k} \\ c_{n-2} & c_k \end{vmatrix} \qquad \vdots$$

The necessary and sufficient conditions for the polynomial $f(z)$ to have no roots outside or on the unit circle are:

$$f(1) > 0 \qquad (-1)^n f(-1) > 0$$

$$|a_0| < a_n \qquad |b_0| > |b_{n-1}| \quad \cdots$$

Appendix F

Optimization Procedures

In this appendix, the optimization of the new back-propagation algorithm is considered by using derivative information. A family of approaches exploiting the derivatives with respect to the learning rate, momentum factor and proportional factor is presented. These autonomously compute the derivatives in the weight space, by using information gathered from the forward and backward procedures.

The optimization of α, β, and γ, such that $W(k+1)$ minimizes E is required. The objective function E can be treated as a function with three independent variables $E(\alpha, \beta, \gamma)$. From (7.5)

$$W(k+1) = W(k) + \alpha P(k) + \beta \Delta W(k-1) + \gamma e(k), \tag{F.1}$$

where $P(k) = -\nabla E(k)$ is a descent directional vector. Substituting (F.1) into (7.3) gives

$$o_{s,i}^m = f([W_i^m(k) + \alpha P_i^m(k) + \beta \Delta W_i^m(k-1) + \gamma e_i^m(k)]^T O_s^{m-1}). \tag{F.2}$$

Computation of the first and the second derivative of E with respect to α, β and

γ yields:

$$g(\alpha,\beta,\gamma) = \begin{bmatrix} \frac{\partial E(\alpha,\beta,\gamma)}{\partial \alpha} \\ \frac{\partial E(\alpha,\beta,\gamma)}{\partial \beta} \\ \frac{\partial E(\alpha,\beta,\gamma)}{\partial \gamma} \end{bmatrix} \tag{F.3}$$

where

$$\frac{\partial E(\alpha,\beta,\gamma)}{\partial \alpha} = \frac{-2}{nZ_M} \sum_{s=1}^{n} \left[T_s - O_s^M\right]^T \frac{\partial O_s^M}{\partial \alpha} \tag{F.4}$$

$$\frac{\partial E(\alpha,\beta,\gamma)}{\partial \beta} = \frac{-2}{nZ_M} \sum_{s=1}^{n} \left[T_s - O_s^M\right]^T \frac{\partial O_s^M}{\partial \beta} \tag{F.5}$$

$$\frac{\partial E(\alpha,\beta,\gamma)}{\partial \gamma} = \frac{-2}{nZ_M} \sum_{s=1}^{n} \left[T_s - O_s^M\right]^T \frac{\partial O_s^M}{\partial \gamma} \tag{F.6}$$

The Hessian matrix of E is given by

$$H(\alpha,\beta,\gamma) = \begin{bmatrix} \frac{\partial^2 E(\alpha,\beta,\gamma)}{\partial \alpha^2} & \frac{\partial^2 E(\alpha,\beta,\gamma)}{\partial \alpha \partial \beta} & \frac{\partial^2 E(\alpha,\beta,\gamma)}{\partial \alpha \partial \gamma} \\ \frac{\partial^2 E(\alpha,\beta,\gamma)}{\partial \beta \partial \alpha} & \frac{\partial^2 E(\alpha,\beta,\gamma)}{\partial \beta^2} & \frac{\partial^2 E(\alpha,\beta,\gamma)}{\partial \beta \partial \gamma} \\ \frac{\partial^2 E(\alpha,\beta,\gamma)}{\partial \gamma \partial \alpha} & \frac{\partial^2 E(\alpha,\beta,\gamma)}{\partial \gamma \partial \beta} & \frac{\partial^2 E(\alpha,\beta,\gamma)}{\partial \gamma^2} \end{bmatrix} \tag{F.7}$$

where

$$\frac{\partial^2 E(\alpha,\beta,\gamma)}{\partial \alpha^2} = \frac{-2}{nZ_M} \sum_{s=1}^{n} \left(\left[T_s - O_s^M\right]^T \frac{\partial^2 O_s^M}{\partial \alpha^2} - \left[\frac{\partial O_s^M}{\partial \alpha}\right]^T \frac{\partial O_s^M}{\partial \alpha} \right) \tag{F.8}$$

$$\frac{\partial^2 E(\alpha,\beta,\gamma)}{\partial \beta^2} = \frac{-2}{nZ_M} \sum_{s=1}^{n} \left(\left[T_s - O_s^M\right]^T \frac{\partial^2 O_s^M}{\partial \beta^2} - \left[\frac{\partial O_s^M}{\partial \beta}\right]^T \frac{\partial O_s^M}{\partial \beta} \right) \tag{F.9}$$

$$\frac{\partial^2 E(\alpha,\beta,\gamma)}{\partial \gamma^2} = \frac{-2}{nZ_M} \sum_{s=1}^{n} \left(\left[T_s - O_s^M\right]^T \frac{\partial^2 O_s^M}{\partial \gamma^2} - \left[\frac{\partial O_s^M}{\partial \gamma}\right]^T \frac{\partial O_s^M}{\partial \gamma} \right) \tag{F.10}$$

$$\frac{\partial^2 E(\alpha,\beta,\gamma)}{\partial \alpha \partial \beta} = \frac{-2}{nZ_M} \sum_{s=1}^{n} \left(\left[T_s - O_s^M\right]^T \frac{\partial^2 O_s^M}{\partial \alpha \partial \beta} - \left[\frac{\partial O_s^M}{\partial \alpha}\right]^T \frac{\partial O_s^M}{\partial \beta} \right) \tag{F.11}$$

$$\frac{\partial^2 E(\alpha,\beta,\gamma)}{\partial \beta \partial \gamma} = \frac{-2}{nZ_M} \sum_{s=1}^{n} \left(\left[T_s - O_s^M\right]^T \frac{\partial^2 O_s^M}{\partial \beta \partial \gamma} - \left[\frac{\partial O_s^M}{\partial \beta}\right]^T \frac{\partial O_s^M}{\partial \gamma} \right) \tag{F.12}$$

$$\frac{\partial^2 E(\alpha,\beta,\gamma)}{\partial \gamma \partial \alpha} = \frac{-2}{nZ_M} \sum_{s=1}^{n} \left(\left[T_s - O_s^M\right]^T \frac{\partial^2 O_s^M}{\partial \gamma \partial \alpha} - \left[\frac{\partial O_s^M}{\partial \gamma}\right]^T \frac{\partial O_s^M}{\partial \alpha} \right) \tag{F.13}$$

To complete the computation of the gradient (F.3) and the Hessian matrix (F.7), the derivatives of O_s^M at $(\alpha_0, \beta_0, \gamma_0)$ can be computed from (F.2). Details

can be found in Section F.2. Thus the derivatives of the objective function $E(\mathbf{X})$ can be found, where

$$\mathbf{X} = [\alpha \quad \beta \quad \gamma]^{\mathcal{T}}. \tag{F.14}$$

F.1 Estimation of optimal LR, MF and PF terms

F.1.1 Error quadratic approximation approach

A second order Taylor polynomial of degree 2 can be used to approximate $E(\mathbf{X})$ for $\mathbf{X}$ near $(\alpha_0, \beta_0, \gamma_0)$. Since $E(\mathbf{X})$ has continuous second-order partial derivative, this gives

$$\begin{aligned} E(\mathbf{X}) \approx\ & E(\alpha_0,\beta_0,\gamma_0) + (\alpha-\alpha_0)\frac{\partial E}{\partial \alpha} + (\beta-\beta_0)\frac{\partial E}{\partial \beta} + (\gamma-\gamma_0)\frac{\partial E}{\partial \gamma} + \frac{1}{2}(\alpha-\alpha_0)^2 \\ & \times\frac{\partial^2 E}{\partial \alpha^2} + \frac{1}{2}(\beta-\beta_0)^2\frac{\partial^2 E}{\partial \beta^2} + \frac{1}{2}(\gamma-\gamma_0)^2\frac{\partial^2 E}{\partial \gamma^2} + (\alpha-\alpha_0)(\beta-\beta_0)\frac{\partial^2 E}{\partial \alpha \partial \beta} \\ & +(\beta-\beta_0)(\gamma-\gamma_0)\frac{\partial^2 E}{\partial \beta \partial \gamma} + (\gamma-\gamma_0)(\alpha-\alpha_0)\frac{\partial^2 E}{\partial \gamma \partial \alpha} \\ =\ & \frac{1}{2}\Gamma^{\mathcal{T}} H_e \Gamma + \Gamma^{\mathcal{T}} g_e + a_e \end{aligned} \tag{F.15}$$

where $\Gamma = [\alpha-\alpha_0 \quad \beta-\beta_0 \quad \gamma-\gamma_0]^{\mathcal{T}}$, $a_e = E(\alpha_0,\beta_0,\gamma_0)$, and the gradient vector g is given by (F.3) and the Hessian matrix H by (F.7) .

Cases

Four separate cases are considered.

Case I: From [Wol78], $E(\mathbf{X})$ has continuous second partial derivatives in a convex set Υ and let the Hessian matrix $H(\mathbf{X})$ at $\mathbf{X}$ be positive definite for all $\mathbf{X}$ in Υ. Also let $\mathbf{y}$ be a critical point of $E(\mathbf{X})$ in Υ. Then $E(\mathbf{X})$ is strictly convex in Υ and so $\mathbf{y}$ is a strong global minimizer of $E(\mathbf{X})$ over Υ. Suppose that E is a function with $E(0,0,0) = 0$ and gradient $E(0,0,0) = 0$. From (F.15), the quadratic polynomial simplifies to

$$E(\mathbf{X}) \approx \frac{1}{2}\alpha^2 E_{\alpha\alpha} + \frac{1}{2}\beta^2 E_{\beta\beta} + \frac{1}{2}\gamma^2 E_{\gamma\gamma} + \alpha\beta E_{\alpha\beta} + \beta\gamma E_{\beta\gamma} + \gamma\alpha E_{\gamma\alpha}. \tag{F.16}$$

The discriminants are

$$D_1 = 4(\frac{1}{4}E_{\alpha\alpha})(\frac{1}{4}E_{\beta\beta}) - (E_{\alpha\beta})^2$$

$$D_2 = 4(\frac{1}{4}E_{\alpha\alpha})(\frac{1}{4}E_{\gamma\gamma}) - (E_{\alpha\gamma})^2$$

$$D_3 = 4(\frac{1}{4}E_{\beta\beta})(\frac{1}{4}E_{\gamma\gamma}) - (E_{\beta\gamma})^2$$

When H is a positive definite (i.e. $E_{\alpha\alpha} > 0$, $D_1 > 0$), symmetric, square matrix and ($D_2 > 0$, $D_3 > 0$), the optimal LR, MF and PF terms can be calculated as

$$\frac{dE}{d\Gamma} = H\Gamma + g = 0 \Rightarrow \Gamma = -H^{-1}g \tag{F.17}$$

It is noted that this procedure minimizes Equation (F.15).

Case II: When H is a positive definite matrix and at least one of D_2 or D_3 is negative. Then $E(\alpha, \beta, \gamma)$ cannot be characterized as convex, but $E(\alpha, \beta, 0)$ is convex and optimal LR and MF can be calculated as in Case I by setting $\gamma = 0$.

Case III: When H is a non-positive definite matrix and $E_{\alpha\alpha} > 0$, the second order expansion of $E(\alpha, 0, 0)$ is convex along the descent direction of $P(k)$. Then the optimal LR can be calculated as in Case I by setting $\beta = \gamma = 0$.

Case IV: When H is a non-positive definite matrix and $E_{\alpha\alpha} < 0$. In such a case, the optimization target behaves in an accelerated decreased manner along the descent direction $P(k)$ because both E_α and $E_{\alpha\alpha}$ take negative values. Then the optimal LR can be estimated by the line search method proposed by Yu et al. [YCC95], which has been shown to be capable of providing an effective descent to the optimization target.

F.1.2 Output quadratic approximation approach

In this approach, the convexity of $E(\alpha, \beta, \gamma)$ is established by substituting the quadratic approximation of the output with respect to α, β, and γ in the E term. The output approximation is given by:

$$O_s^M(\mathbf{X}) \approx O_s^M(\alpha_0, \beta_0, \gamma_0) + (\alpha - \alpha_0)\frac{\partial O_s^M}{\partial \alpha} + (\beta - \beta_0)\frac{\partial O_s^M}{\partial \beta} + (\gamma - \gamma_0)\frac{\partial O_s^M}{\partial \gamma} + \frac{1}{2}$$

$$\times(\alpha-\alpha_0)^2\frac{\partial^2 O_s^M}{\partial\alpha^2}+\frac{1}{2}(\beta-\beta_0)^2\frac{\partial^2 O_s^M}{\partial\beta^2}+\frac{1}{2}(\gamma-\gamma_0)^2\frac{\partial^2 O_s^M}{\partial\gamma^2}+(\alpha-\alpha_0)$$
$$\times(\beta-\beta_0)\frac{\partial^2 O_s^M}{\partial\alpha\partial\beta}+(\beta-\beta_0)(\gamma-\gamma_0)\frac{\partial^2 O_s^M}{\partial\beta\partial\gamma}+(\gamma-\gamma_0)(\alpha-\alpha_0)\frac{\partial^2 O_s^M}{\partial\gamma\partial\alpha}$$
$$=\frac{1}{2}\Gamma^T H_o\Gamma+\Gamma^T g_o+a_o \tag{F.18}$$

By substituting (F.18) into (F.4)-(F.6) and letting E_α, E_β and E_γ equal zero gives

$$\frac{1}{2}\sum_{s=1}^{n}\left[\frac{\partial O_s^M}{\partial\alpha}\right]^T(\Gamma^T H_o\Gamma)+\sum_{s=1}^{n}\left[\frac{\partial O_s^M}{\partial\alpha}\right]^T(g_o\Gamma^T)+\sum_{s=1}^{n}\left[\frac{\partial O_s^M}{\partial\alpha}\right]^T(a_o-T_s)=0 \tag{F.19}$$

$$\frac{1}{2}\sum_{s=1}^{n}\left[\frac{\partial O_s^M}{\partial\beta}\right]^T(\Gamma^T H_o\Gamma)+\sum_{s=1}^{n}\left[\frac{\partial O_s^M}{\partial\beta}\right]^T(g_o\Gamma^T)+\sum_{s=1}^{n}\left[\frac{\partial O_s^M}{\partial\beta}\right]^T(a_o-T_s)=0 \tag{F.20}$$

$$\frac{1}{2}\sum_{s=1}^{n}\left[\frac{\partial O_s^M}{\partial\gamma}\right]^T(\Gamma^T H_o\Gamma)+\sum_{s=1}^{n}\left[\frac{\partial O_s^M}{\partial\gamma}\right]^T(g_o\Gamma^T)+\sum_{s=1}^{n}\left[\frac{\partial O_s^M}{\partial\gamma}\right]^T(a_o-T_s)=0 \tag{F.21}$$

These equations can be solved simultaneously by the Newton-Raphson method to find the optimal Γ which satisfies $E(\Gamma(k+1))<E(\Gamma(k))$ at each iteration. The Newton-Raphson method gives rapid convergence, the accuracy approximately doubling with each iteration.

There are 3 unknown system parameters in the vector $\mathbf{X}\in\mathbb{R}^{3\times1}$. Equations (F.19)-(F.21), can be expressed by 3 non-linear equations:

$$\begin{aligned} f_1(\alpha,\beta,\gamma) &= 0,\\ f_2(\alpha,\beta,\gamma) &= 0,\\ f_3(\alpha,\beta,\gamma) &= 0. \end{aligned}$$

Let $\tilde{\mathbf{X}}_0$ be an initial estimate of $\mathbf{X}$ known to be in the vicinity of the actual solution of $\mathbf{F}(\mathbf{X})$. $\mathbf{F}(\mathbf{X})$ can be expanded by a first-order Taylor series as

$$f_1(\alpha,\beta,\gamma)=f_{01}+\left.\frac{\partial f_1}{\partial\alpha}\right|_0(\alpha-\tilde{\alpha}_0)+\left.\frac{\partial f_1}{\partial\beta}\right|_0(\beta-\tilde{\beta}_0)+\left.\frac{\partial f_1}{\partial\gamma}\right|_0(\gamma-\tilde{\gamma}_0) \tag{F.22}$$

$$f_2(\alpha,\beta,\gamma)=f_{02}+\left.\frac{\partial f_2}{\partial\alpha}\right|_0(\alpha-\tilde{\alpha}_0)+\left.\frac{\partial f_2}{\partial\beta}\right|_0(\beta-\tilde{\beta}_0)+\left.\frac{\partial f_2}{\partial\gamma}\right|_0(\gamma-\tilde{\gamma}_0) \tag{F.23}$$

$$f_3(\alpha,\beta,\gamma)=f_{03}+\left.\frac{\partial f_3}{\partial\alpha}\right|_0(\alpha-\tilde{\alpha}_0)+\left.\frac{\partial f_3}{\partial\beta}\right|_0(\beta-\tilde{\beta}_0)+\left.\frac{\partial f_3}{\partial\gamma}\right|_0(\gamma-\tilde{\gamma}_0) \tag{F.24}$$

Setting $\mathbf{F(X)} = 0$, gives 3 equations in the 3 unknowns α, β and γ. These equations can be solved using a generalized Newton-Raphson method:

$$\mathbf{X} \approx \tilde{\mathbf{X}}_0 - \mathbf{J}^{-1}\mathbf{F}_0 \tag{F.25}$$

where J is the system Jacobian given by

$$\mathbf{J} = \left[\begin{array}{ccc} \frac{\partial f_1}{\partial \alpha} & \frac{\partial f_1}{\partial \beta} & \frac{\partial f_1}{\partial \gamma} \\ \frac{\partial f_2}{\partial \alpha} & \frac{\partial f_2}{\partial \beta} & \frac{\partial f_2}{\partial \gamma} \\ \frac{\partial f_3}{\partial \alpha} & \frac{\partial f_3}{\partial \beta} & \frac{\partial f_3}{\partial \gamma} \end{array} \right]\Bigg|_0 \tag{F.26}$$

and

$$\mathbf{F}_0 = \left[\begin{array}{c} f_{01} \\ f_{02} \\ f_{03} \end{array} \right]. \tag{F.27}$$

The zero subscript indicates that the functions and all the partial derivatives are evaluated at $\tilde{\mathbf{X}}_0$.

F.1.3 First-order approximation approach

In this approach, the convexity of $E(\alpha, \beta, \gamma)$ is obtained by substituting the first-order Taylor expansion of the output with respect to α, β, and γ in the objective function E. The first-order Taylor series approximation of the output is given by

$$O_s^M(\mathbf{X}) \approx O_s^M(\alpha_0, \beta_0, \gamma_0) + (\alpha - \alpha_0)\frac{\partial O_s^M}{\partial \alpha} + (\beta - \beta_0)\frac{\partial O_s^M}{\partial \beta} + (\gamma - \gamma_0)\frac{\partial O_s^M}{\partial \gamma} \tag{F.28}$$

Substituting (F.28) into (7.1), the objective function becomes

$$\begin{aligned} E \approx \frac{1}{nZ_M}\sum_{s=1}^{n}\Bigg(T_s - O_s^M(\alpha_0, \beta_0, \gamma_0) - (\alpha - \alpha_0)\frac{\partial O_s^M}{\partial \alpha} - (\beta - \beta_0)\frac{\partial O_s^M}{\partial \beta} \\ -(\gamma - \gamma_0)\frac{\partial O_s^M}{\partial \gamma}\Bigg)^2, \end{aligned} \tag{F.29}$$

From (F.29), setting the partial derivatives of E with respect to α, β and γ equal to zero, yields three equations in the three unknowns:

$$\begin{aligned} &(\alpha - \alpha_0)\sum_{s=1}^{n}\left\|\frac{\partial O_s^M}{\partial \alpha}\right\|^2 + (\beta - \beta_0)\sum_{s=1}^{n}\left[\frac{\partial O_s^M}{\partial \alpha}\right]^T\frac{\partial O_s^M}{\partial \beta} \\ &+(\gamma - \gamma_0)\sum_{s=1}^{n}\left[\frac{\partial O_s^M}{\partial \alpha}\right]^T\frac{\partial O_s^M}{\partial \gamma} = \sum_{s=1}^{n}\left[\frac{\partial O_s^M}{\partial \alpha}\right]^T(T_s - O_s^M(\alpha_0, \beta_0, \gamma_0)) \end{aligned} \tag{F.30}$$

$$(\alpha-\alpha_0)\sum_{s=1}^{n}\left[\frac{\partial O_s^M}{\partial\beta}\right]^T\frac{\partial O_s^M}{\partial\alpha}+(\beta-\beta_0)\sum_{s=1}^{n}\left\|\frac{\partial O_s^M}{\partial\beta}\right\|^2$$
$$+(\gamma-\gamma_0)\sum_{s=1}^{n}\left[\frac{\partial O_s^M}{\partial\beta}\right]^T\frac{\partial O_s^M}{\partial\gamma}=\sum_{s=1}^{n}\left[\frac{\partial O_s^M}{\partial\beta}\right]^T(T_s-O_s^M(\alpha_0,\beta_0,\gamma_0)) \quad \text{(F.31)}$$

$$(\alpha-\alpha_0)\sum_{s=1}^{n}\left[\frac{\partial O_s^M}{\partial\gamma}\right]^T\frac{\partial O_s^M}{\partial\alpha}+(\beta-\beta_0)\sum_{s=1}^{n}\left[\frac{\partial O_s^M}{\partial\gamma}\right]^T\frac{\partial O_s^M}{\partial\beta}$$
$$+(\gamma-\gamma_0)\sum_{s=1}^{n}\left\|\frac{\partial O_s^M}{\partial\gamma}\right\|^2=\sum_{s=1}^{n}\left[\frac{\partial O_s^M}{\partial\gamma}\right]^T(T_s-O_s^M(\alpha_0,\beta_0,\gamma_0)) \quad \text{(F.32)}$$

The optimal α, β and γ values can be calculated by solving (F.30)–(F.32) simultaneously.

$$\Gamma=A_1^{-1}R_1 \quad \text{(F.33)}$$

where

$$A_1=\begin{bmatrix}\sum_{s=1}^{n}\left\|\frac{\partial O_s^M}{\partial\alpha}\right\|^2 & \sum_{s=1}^{n}\left[\frac{\partial O_s^M}{\partial\alpha}\right]^T\frac{\partial O_s^M}{\partial\beta} & \sum_{s=1}^{n}\left[\frac{\partial O_s^M}{\partial\alpha}\right]^T\frac{\partial O_s^M}{\partial\gamma}\\ \sum_{s=1}^{n}\left[\frac{\partial O_s^M}{\partial\beta}\right]^T\frac{\partial O_s^M}{\partial\alpha} & \sum_{s=1}^{n}\left\|\frac{\partial O_s^M}{\partial\beta}\right\|^2 & \sum_{s=1}^{n}\left[\frac{\partial O_s^M}{\partial\beta}\right]^T\frac{\partial O_s^M}{\partial\gamma}\\ \sum_{s=1}^{n}\left[\frac{\partial O_s^M}{\partial\gamma}\right]^T\frac{\partial O_s^M}{\partial\alpha} & \sum_{s=1}^{n}\left[\frac{\partial O_s^M}{\partial\gamma}\right]^T\frac{\partial O_s^M}{\partial\beta} & \sum_{s=1}^{n}\left\|\frac{\partial O_s^M}{\partial\gamma}\right\|^2\end{bmatrix} \quad \text{(F.34)}$$

and

$$R_1=\begin{bmatrix}\sum_{s=1}^{n}\left[\frac{\partial O_s^M}{\partial\alpha}\right]^T(T_s-O_s^M(\alpha_0,\beta_0,\gamma_0))\\ \sum_{s=1}^{n}\left[\frac{\partial O_s^M}{\partial\beta}\right]^T(T_s-O_s^M(\alpha_0,\beta_0,\gamma_0))\\ \sum_{s=1}^{n}\left[\frac{\partial O_s^M}{\partial\gamma}\right]^T(T_s-O_s^M(\alpha_0,\beta_0,\gamma_0))\end{bmatrix} \quad \text{(F.35)}$$

F.1.4 Approximation of the Sigmoidal nonlinearity function

Let $([W_i^M(k)+\alpha P_i^M(k)+\beta\Delta W_i^M(k-1)+\gamma e_i^M(k)]^T O_s^{M-1})=x$. Then the sigmoidal nonlinear function of the output layer can be approximated by a set of linear functions:

$$f(x)=\begin{cases}m_1x+b_1 & \text{for } x_1\le x\le x_2,\\ m_2x+b_2 & \text{for } x_1\ge x,\\ m_2x+(2b_1-b_2) & \text{for } x_2\le x\end{cases} \quad \text{(F.36)}$$

$$O_s^M = f([W_i^M(k) + \alpha P_i^M(k) + \beta \Delta W_i^M(k-1) + \gamma e_i^M(k)]^T O_s^{M-1}) \tag{F.37}$$

By substituting Equation (F.37) into Equations (F.4)-(F.6) and equating e_α, e_β, and e_γ to zero yields:

$$\alpha m_j P_i^M \sum_{s=1}^{n} \left[\frac{\partial O_s^M}{\partial \alpha}\right]^T O_s^{M-1} + \beta m_j \Delta W_i^M(k-1) \sum_{s=1}^{n} \left[\frac{\partial O_s^M}{\partial \alpha}\right]^T O_s^{M-1} + \gamma m_j e_i^M$$
$$\times \sum_{s=1}^{n} \left[\frac{\partial O_s^M}{\partial \alpha}\right]^T O_s^{M-1} = \sum_{s=1}^{n} \left[\frac{\partial O_s^M}{\partial \alpha}\right]^T (T_s - m_j W_i^M(k) O_s^{M-1} - b_j) \tag{F.38}$$

$$\alpha m_j P_i^M \sum_{s=1}^{n} \left[\frac{\partial O_s^M}{\partial \beta}\right]^T O_s^{M-1} + \beta m_j \Delta W_i^M(k-1) \sum_{s=1}^{n} \left[\frac{\partial O_s^M}{\partial \beta}\right]^T O_s^{M-1} + \gamma m_j e_i^M$$
$$\times \sum_{s=1}^{n} \left[\frac{\partial O_s^M}{\partial \beta}\right]^T O_s^{M-1} = \sum_{s=1}^{n} \left[\frac{\partial O_s^M}{\partial \beta}\right]^T (T_s - m_j W_i^M(k) O_s^{M-1} - b_j) \tag{F.39}$$

$$\alpha m_j P_i^M \sum_{s=1}^{n} \left[\frac{\partial O_s^M}{\partial \gamma}\right]^T O_s^{M-1} + \beta m_j \Delta W_i^M(k-1) \sum_{s=1}^{n} \left[\frac{\partial O_s^M}{\partial \gamma}\right]^T O_s^{M-1} + \gamma m_j e_i^M$$
$$\times \sum_{s=1}^{n} \left[\frac{\partial O_s^M}{\partial \gamma}\right]^T O_s^{M-1} = \sum_{s=1}^{n} \left[\frac{\partial O_s^M}{\partial \gamma}\right]^T (T_s - m_j W_i^M(k) O_s^{M-1} - b_j) \tag{F.40}$$

Since the matrix A_2 is a nonsingular, the optimal α, β and γ can be calculated by solving Equations (F.38)-(F.40) simultaneously:

$$\Gamma = A_2^{-1} R_2 \tag{F.41}$$

$$A_2 = \begin{bmatrix} A_{11} & A_{12} & A_{13} \\ A_{21} & A_{22} & A_{23} \\ A_{31} & A_{32} & A_{33} \end{bmatrix} \tag{F.42}$$

where

$$A_{11} = m_j P_i^M \sum_{s=1}^{n} \left[\frac{\partial O_s^M}{\partial \alpha}\right]^T O_s^{M-1}, \quad A_{12} = m_j \Delta W_i^M(k-1) \sum_{s=1}^{n} \left[\frac{\partial O_s^M}{\partial \alpha}\right]^T O_s^{M-1}$$

$$A_{13} = m_j e_i^M \sum_{s=1}^{n} \left[\frac{\partial O_s^M}{\partial \alpha}\right]^T O_s^{M-1}, \quad A_{21} = m_j P_i^M \sum_{s=1}^{n} \left[\frac{\partial O_s^M}{\partial \beta}\right]^T O_s^{M-1}$$

$$A_{22} = m_j \Delta W_i^M(k-1) \sum_{s=1}^{n} \left[\frac{\partial O_s^M}{\partial \beta}\right]^T O_s^{M-1}, \quad A_{23} = m_j e_i^M \sum_{s=1}^{n} \left[\frac{\partial O_s^M}{\partial \beta}\right]^T O_s^{M-1}$$

$$A_{31} = m_j P_i^M \sum_{s=1}^{n} \left[\frac{\partial O_s^M}{\partial \gamma}\right]^T O_s^{M-1}, \quad A_{32} = m_j \Delta W_i^M(k-1) \sum_{s=1}^{n} \left[\frac{\partial O_s^M}{\partial \gamma}\right]^T O_s^{M-1}$$

$$A_{33} = m_j e_i^M \sum_{s=1}^{n} \left[\frac{\partial O_s^M}{\partial \gamma}\right]^T O_s^{M-1}$$

and

$$R_2 = \begin{bmatrix} \sum_{s=1}^{n} \left[\frac{\partial O_s^M}{\partial \alpha}\right]^T (T_s - m_j W_i^M(k) O_s^{M-1} - b_j) \\ \sum_{s=1}^{n} \left[\frac{\partial O_s^M}{\partial \beta}\right]^T (T_s - m_j W_i^M(k) O_s^{M-1} - b_j) \\ \sum_{s=1}^{n} \left[\frac{\partial O_s^M}{\partial \gamma}\right]^T (T_s - m_j W_i^M(k) O_s^{M-1} - b_j) \end{bmatrix} \tag{F.43}$$

$$\begin{aligned} \frac{\partial o_{s,i}^m}{\partial \alpha} &= f_\alpha \left([W_i^m(k) + \alpha_0 P_i^m(k) + \beta_0 \Delta W_i^m(k-1) + \gamma_0 e_i^m(k)]^T O_s^{m-1}\right) \Big([P_i^m(k)]^T \\ & O_s^{m-1} + [W_i^m(k) + \alpha_0 P_i^m(k) + \beta_0 \Delta W_i^m(k-1) \\ & + \gamma_0 e_i^m(k)]^T \frac{\partial O_s^{m-1}}{\partial \alpha} \Big) \end{aligned} \tag{F.44}$$

$$\begin{aligned} \frac{\partial o_{s,i}^m}{\partial \beta} &= f_\beta \left([W_i^m(k) + \alpha_0 P_i^m(k) + \beta_0 \Delta W_i^m(k-1) + \gamma_0 e_i^m(k)]^T O_s^{m-1}\right) \\ & \Big([\Delta W_i^m(k-1)]^T O_s^{m-1} + [W_i^m(k) + \alpha_0 P_i^m(k) + \beta_0 \Delta W_i^m(k-1) \\ & + \gamma_0 e_i^m(k)]^T \frac{\partial O_s^{m-1}}{\partial \beta} \Big) \end{aligned} \tag{F.45}$$

$$\begin{aligned} \frac{\partial o_{s,i}^m}{\partial \gamma} &= f_\gamma \left([W_i^m(k) + \alpha_0 P_i^m(k) + \beta_0 \Delta W_i^m(k-1) + \gamma_0 e_i^m(k)]^T O_s^{m-1}\right) \Big([e_i^m(k)]^T \\ & O_s^{m-1} + [W_i^m(k) + \alpha_0 P_i^m(k) + \beta_0 \Delta W_i^m(k-1) \\ & + \gamma_0 e_i^m(k)]^T \frac{\partial O_s^{m-1}}{\partial \gamma} \Big) \end{aligned} \tag{F.46}$$

F.2 Derivative of output equations

$$\begin{aligned}\frac{\partial^2 o_{s,i}^m}{\partial \alpha^2} &= f_{\alpha\alpha}\left([W_i^m(k)+\alpha_0 P_i^m(k)+\beta_0 \Delta W_i^m(k-1)+\gamma_0 e_i^m(k)]^T O_s^{m-1}\right)\\ &\left([P_i^m(k)]^T O_s^{m-1}+[W_i^m(k)+\alpha_0 P_i^m(k)+\beta_0 \Delta W_i^m(k-1)+\gamma_0 e_i^m(k)]^T\right.\\ &\left.\frac{\partial O_s^{m-1}}{\partial \alpha}\right)^2+f_\alpha([W_i^m(k)+\alpha_0 P_i^m(k)+\beta_0 \Delta W_i^m(k-1)\\ &+\gamma_0 e_i^m(k)]^T O_s^{m-1})\left(2[P_i^m(k)]^T \frac{\partial O_s^{m-1}}{\partial \alpha}+[W_i^m(k)+\alpha_0 P_i^m(k)\right.\\ &\left.+\beta_0 \Delta W_i^m(k-1)+\gamma_0 e_i^m(k)]^T \frac{\partial^2 O_s^{m-1}}{\partial \alpha^2}\right) \qquad \text{(F.47)}\end{aligned}$$

$$\begin{aligned}\frac{\partial^2 o_{s,i}^m}{\partial \beta^2} &= f_{\beta\beta}\left([W_i^m(k)+\alpha_0 P_i^m(k)+\beta_0 \Delta W_i^m(k-1)+\gamma_0 e_i^m(k)]^T O_s^{m-1}\right)\\ &\times\left([\Delta W_i^m(k-1)]^T O_s^{m-1}+[W_i^m(k)+\alpha_0 P_i^m(k)+\beta_0 \Delta W_i^m(k-1)\right.\\ &\left.+\gamma_0 e_i^m(k)]^T \frac{\partial O_s^{m-1}}{\partial \beta}\right)^2+f_\beta\left([W_i^m(k)+\alpha_0 P_i^m(k)+\beta_0 \Delta W_i^m(k-1)\right.\\ &\left.+\gamma_0 e_i^m(k)]^T O_s^{m-1}\right)\times\left([2\Delta W_i^m(k-1)]^T \frac{\partial O_s^{m-1}}{\partial \beta}+[W_i^m(k)\right.\\ &\left.+\alpha_0 P_i^m(k)+\beta_0 \Delta W_i^m(k-1)+\gamma_0 e_i^m(k)]^T \frac{\partial^2 O_s^{m-1}}{\partial \beta^2}\right) \qquad \text{(F.48)}\end{aligned}$$

$$\begin{aligned}\frac{\partial^2 o_{s,i}^m}{\partial \gamma^2} &= f_{\gamma\gamma}\left([W_i^m(k)+\alpha_0 P_i^m(k)+\beta_0 \Delta W_i^m(k-1)+\gamma_0 e_i^m(k)]^T O_s^{m-1}\right)\\ &\left([e_i^m(k)]^T O_s^{m-1}+[W_i^m(k)+\alpha_0 P_i^m(k)+\beta_0 \Delta W_i^m(k-1)+\gamma_0 e_i^m(k)]^T\right.\\ &\left.\frac{\partial O_s^{m-1}}{\partial \gamma}\right)^2+f_\gamma\left([W_i^m(k)+\alpha_0 P_i^m(k)+\beta_0 \Delta W_i^m(k-1)+\gamma_0 e_i^m(k)]^T\right.\\ &\left.O_s^{m-1}\right)\times\left([2e_i^m(k)]^T \frac{\partial O_s^{m-1}}{\partial \beta}+[W_i^m(k)+\alpha_0 P_i^m(k)\right.\\ &\left.+\beta_0 \Delta W_i^m(k-1)+\gamma_0 e_i^m(k)]^T \frac{\partial^2 O_s^{m-1}}{\partial \beta^2}\right) \qquad \text{(F.49)}\end{aligned}$$

$$\begin{aligned}\frac{\partial^2 o_{s,i}^m}{\partial\alpha\partial\beta} &= f_{\alpha\beta}\Big([W_i^m(k)+\alpha_0 P_i^m(k)+\beta_0\Delta W_i^m(k-1)+\gamma_0 e_i^m(k)]^T O_s^{m-1}\Big)\\ &\Big([P_i^m(k)]^T O_s^{m-1}+[W_i^m(k)+\alpha_0 P_i^m(k)+\beta_0\Delta W_i^m(k-1)\\ &+\gamma_0 e_i^m(k)]^T\frac{\partial O_s^{m-1}}{\partial\alpha}\Big)\Big([\Delta W_i^m(k-1)]^T O_s^{m-1}+[W_i^m(k)+\alpha_0 P_i^m(k)\\ &+\beta_0\Delta W_i^m(k-1)+\gamma_0 e_i^m(k)]^T\frac{\partial O_s^{m-1}}{\partial\beta}\Big)+f_\alpha\Big([W_i^m(k)+\alpha_0 P_i^m(k)\\ &+\beta_0\Delta W_i^m(k-1)+\gamma_0 e_i^m(k)]^T O_s^{m-1}\Big)\times\Big([P_i^m(k)]^T\frac{\partial O_s^{m-1}}{\partial\beta}\\ &+[\Delta W_i^m(k-1)]^T\frac{\partial O_s^{m-1}}{\partial\alpha}+[W_i^m(k)+\alpha_0 P_i^m(k)+\beta_0\Delta W_i^m(k-1)\\ &+\gamma_0 e_i^m(k)]^T\frac{\partial^2 O_s^{m-1}}{\partial\alpha\partial\beta}\Big)\end{aligned}\tag{F.50}$$

$$\begin{aligned}\frac{\partial^2 o_{s,i}^m}{\partial\beta\partial\gamma} &= f_{\beta\gamma}\left([W_i^m(k)+\alpha_0 P_i^m(k)+\beta_0\Delta W_i^m(k-1)+\gamma_0 e_i^m(k)]^T O_s^{m-1}\right)\\ &\times\Big([\Delta W_i^m(k-1)]^T O_s^{m-1}+[W_i^m(k)+\alpha_0 P_i^m(k)+\beta_0\Delta W_i^m(k-1)\\ &+\gamma_0 e_i^m(k)]^T\frac{\partial O_s^{m-1}}{\partial\beta}\Big)\times\Big([e_i^m(k)]^T O_s^{m-1}+[W_i^m(k)+\alpha_0 P_i^m(k)\\ &+\beta_0\Delta W_i^m(k-1)+\gamma_0 e_i^m(k)]^T\frac{\partial O_s^{m-1}}{\partial\gamma}\Big)+f_\beta\Big([W_i^m(k)+\alpha_0 P_i^m(k)\\ &+\beta_0\Delta W_i^m(k-1)+\gamma_0 e_i^m(k)]^T O_s^{m-1}\Big)\times\Big([\Delta W_i^m(k-1)]^T\frac{\partial O_s^{m-1}}{\partial\gamma}\\ &+[e_i^m(k)]^T\frac{\partial O_s^{m-1}}{\partial\beta}+[W_i^m(k)+\alpha_0 P_i^m(k)+\beta_0\Delta W_i^m(k-1)\\ &+\gamma_0 e_i^m(k)]^T\frac{\partial^2 O_s^{m-1}}{\partial\beta\partial\gamma}\Big)\end{aligned}\tag{F.51}$$

$$\begin{aligned}\frac{\partial^2 o_{s,i}^m}{\partial\gamma\partial\alpha} &= f_{\gamma\alpha}\left([W_i^m(k)+\alpha_0 P_i^m(k)+\beta_0\Delta W_i^m(k-1)+\gamma_0 e_i^m(k)]^T O_s^{m-1}\right)\\ &\Big([e_i^m(k)]^T O_s^{m-1}+[W_i^m(k)+\alpha_0 P_i^m(k)+\beta_0\Delta W_i^m(k-1)+\gamma_0 e_i^m(k)]^T\\ &\frac{\partial O_s^{m-1}}{\partial\gamma}\Big)\Big([P_i^m(k)]^T O_s^{m-1}+[W_i^m(k)+\alpha_0 P_i^m(k)+\beta_0\Delta W_i^m(k-1)\\ &+\gamma_0 e_i^m(k)]^T\frac{\partial O_s^{m-1}}{\partial\alpha}\Big)+f_\gamma\Big([W_i^m(k)+\alpha_0 P_i^m(k)+\beta_0\Delta W_i^m(k-1)\\ &+\gamma_0 e_i^m(k)]^T O_s^{m-1}\Big)\Big([e_i^m(k)]^T\frac{\partial O_s^{m-1}}{\partial\alpha}+[P_i^m(k)]^T\frac{\partial O_s^{m-1}}{\partial\gamma}+[W_i^m(k)\\ &+\alpha_0 P_i^m(k)+\beta_0\Delta W_i^m(k-1)+\gamma_0 e_i^m(k)]^T\frac{\partial^2 O_s^{m-1}}{\partial\gamma\partial\alpha}\Big)\end{aligned}\tag{F.52}$$

Appendix G

Engines Specifications

The following three tables for engines specifications are used to validate the work presented in this thesis.

Bore (d)	130 [mm]
Crank radius (r)	80 [mm]
Connecting rod length (L)	269.3 [mm]
Compression ratio (c)	15
Piston pin offset (δ)	1.69 [mm]
Equivalent mass (M)	1.08 [kg]
Mass of piston (m_p)	.8 [kg]
Mass of crankshaft (m_c)	3 [kg]
Mass of connecting rod (m_R)	.6 [kg]
Crankshaft moment of inertia (J_c)	1.4 [kgm^2]
Width of the rings ($B_{1,2,3,4}$)	3.4, 3.4, 3, 2.6 [mm]
Moment of inertia of connecting rod (J_R)	.008 [kgm^2]
Dynamometer moment of inertia (J_2)	.37 [kgm^2]
Coupling stiffness (S)	19200 [Nm/(rad)]
Damping coefficient (D)	125 [Nm/(rad/s)]
Journal bearing radius (r_b)	40 [mm]
Wire diameter ($d_{1,2}$)	2.2, 3.5 [mm]
Spring diameter ($d_{1,2}$)	22, 25 [mm]
Journal bearing length (L_b)	30 [mm]
Journal bearing radial clearance (C_r)	4×10^{-3} [mm]
Skirt length (L_s)	80 [mm]
Skirt oil film thickness (O_c)	2×10^{-2} [mm]
Qap closure of the piston ring (g_c)	1.16 [mm]
Valve lift (V_l)	8 [mm]
Inclination angle of the ring profile (ξ)	32 [deg]
Intake valve diameter (D_{iv})	30 [mm]
Number of intake or exhaust valve (n_{iv})	2
Number of coils (N_t)	7, 8
modulus of rigidity of valve (G_v)	5671.2

Table G.1: Engine A geometrical specifications, DDC DI four-stroke Diesel engine

Bore (d)	100 [mm]
Journal bearing radius (r_b)	45.5 [mm]
Crank radius (r)	62.5 [mm]
Connecting rod length (L)	218.8 [mm]
Width of compression rings ($B_{1,2,3}$)	3.2, 3.2, 2.35 [mm]
Width of oil rings ($B_{1,2}$)	4.7 [mm]
Compression ratio (c)	18
Piston offset (δ)	1.75 [mm]
Inclination angle of the ring profile (ξ)	25 [deg]
Engine moment of inertia (J_1)	1.7 [kgm^2]
Dynamometer moment of inertia (J_2)	.37 [kgm^2]
Coupling stiffness (S)	19200 [Nm/(rad)]
Damping coefficient (D)	125 [Nm/(rad/s)]
Equivalent mass (M)	1.7 [kg]
Intake valve diameter (D_{iv})	28 [mm]
Number of intake or exhaust valve (n_{iv})	2

Table G.2: Engine B geometrical specifications, Caterpillar 8201 DI four-stroke Diesel engine

Bore (d)	95 [mm]
Wire diameter ($d_{1,2}$)	2, 3 [mm]
Stroke	95 [mm]
Spring diameter ($d_{1,2}$)	18, 21 [mm]
Inner exhaust diameter (D_i)	60 [mm]
Outer exhaust diameter (D_0)	65 [mm]
Crank radius (r)	47.5 [mm]
Connecting rod length (L)	160 [mm]
Width of the rings ($B_{1,2,3,4}$)	2.9, 2.9, 2.3, 3.6 [mm]
Displacement (V_d)	673 [cm^3]
Compression ratio (c)	17
Piston pin offset (δ)	1.65 [mm]
Mass of piston and rings (M)	1.18 [kg]
Mass of piston (m_p)	.98 [kg]
Mass of connecting rod (m_R)	.65 [kg]
Injection timing ($BTDC$)	23 [deg]
Intake valve opens ($BTDC$)	21 [deg]
Intake valve close ($ABDC$)	62 [deg]
Exhaust valve opens ($BBDC$)	62 [deg]
Exhaust valve close ($ATDC$)	21 [deg]
Crankshaft moment of inertia (J_c)	.3825 [kgm^2]
Journal bearing radius (r_b)	35 [mm]
Journal bearing length (L_b)	27 [mm]
Journal bearing radial clearance (C_r)	25×10^{-4} [mm]
Skirt length (L_s)	66.5 [mm]
Skirt oil film thickness (O_c)	15×10^{-3} [mm]
Qap closure of the piston ring (g_c)	1.10 [mm]
Valve lift (V_l)	6.7 [mm]
Number of coils (N_t)	6, 7
modulus of rigidity of valve (G_v)	4661.4

Table G.3: Engine C geometrical specifications, F1L 210 DEUTZ MAG DI four-stroke Diesel engine

References

[AAB+97] D. Assanis, A. Atreya, C. Borgnakke, D. Dowling, Z. Filipi, S. Hoffman, S. Homsy, F. Kanafani, K. Morrison, D. Patterson, M. Syrimis, D. Winton, G. Zhang, and W. Bryzik. Development of a modular, transient, multi-cylinder diesel engine simulation for system performance and vibration studies. In *Proc. Tech. Conf. ASME ICE*, volume 1, pages 87–101, Colorado, 1997.

[AH86] D.N. Assanis and J.B. Heywood. Development and use of a computer simulation of the turbocompounded diesel system for engine system for engine performance component heat transfer studies. *SAE paper No. 860329*, 1986.

[APT99] N. Ampazis, S.J. Perantonis, and J.G. Taylor. Dynamics of multilayer networks in the vicinity of temporary minima. *Neural Networks*, 12:43–58, *1999.*

[BCHW73] D.E. Bowns, P.R. Cave, M.R.O. Hargreaves, *and F.J. Wallace.* Transient characteristics of turbochargediesel engines. *Proceedings of the Institution of Mechanical Engineers*, CP15, 1973.

[BDV+94] C.J. Brace, M. Deacon, N.D. Vaughan, R.W. Horrock, and C.R. Burrows. Prediction of emissions from a turbocharged passenger car dieselengine using a neural-network. In *Turbocharging and Turbochargers - International Conference Proceedings of the IMechE series*, pages 83–91, 1994.

[BDV+99] C.J. Brace, M. Deacon, N.D. Vaughan, R.W. Horrock, and C.R. Burrows. An operating point optimizer for the design and calibration of an

integrated diesel/continuously variable transmission powertrain. *Proceedings of the Institution of Mechanical Engineers part D*, 213:215–226, 1999.

[BF97] R.L. Burden and J.D. Faires. *Numerical Analysis.* Brooks/Cole, Pacific Grove, Calif., 1997.

[Bis65] I.N. Bishop. Effect of design variables on friction and economy. *SAE Trans.*, 73:334–358, 1965.

[Bla99] G.P. Blair. *Design and Simulation of Four-Stroke Engines.* SAE International, Warrendale, PA, 1999.

[BN87] G. Borman and K. Nishiwaki. A review of internal combustion engine heat transfer. *Prog. Energy Combust. Sci.*, 13:1–46, 1987.

[Bor97] G.J. Borse. *Numerical Methods with MATLAB: a Resource for Scientists and Engineers.* PWS, Boston, 1997.

[Bra94] C.J. Brace. Prediction of diesel engine exhaust emissions using artificial neural networks. In *IMechE Seminar S591, Lucas Electrical and Electronic Systems*, 1994.

[CC93] S.K. Chen and S.X. Chen. Engine diagnostics by dynamic shaft measurement. *SAE paper No. 932412*, 1993.

[CC99] S.W. Cho and T.W.S. Chow. Training multilayer neural networks using fast global learning algorithm - least-squares and penalized optimization methods. *Neurocomputing*, 25:115–131, 1999.

[CE81] A. Cameron and C.M. Ettles. *Basic Lubrication Theory.* Ellis Horwood, Chichester, UK, 1981.

[Ciu92] E. Ciulli. A review of internal combustion engine losses - part 1: Specific studies on the motion of pistons, valves and bearing. *Proceedings of the Institution of Mechanical Engineers part D*, 206:223–236, 1992.

[Ciu93] E. Ciulli. A review of internal combustion engine losses - part 2: Studies for global evaluations. *Proceedings of the Institution of Mechanical Engineers part D*, 207:229–240, 1993.

[CM97] S.X. Chen and J.J. Moskwa. Application of nonlinear sliding mode observer for cylinder pressure reconstruction. *Control Eng. Practice*, 5:1115–1121, 1997.

[COC89] S. Citron, J. O'Higgins, and L. Chen. Cylinder by cylinder engine pressure torque waveform determination utilizing crankshaft speed fluctuation. *SAE paper No. 890486*, 1989.

[CRD96] E. Ciulli, G. Rizzoni, and J. Dawson. Numerical and experimental study of friction on a single cylinder CFR engine. *SAE Paper No. 960357*, 1996.

[DBV+99] M. Deacon, C.J. Brace, N.D. Vaughan, C.R. Burrows, and R.W. Horrock. Impact of alternative controller strategies on exhaust emissions from an integrated diesel continuously variable transmission powertrain. *Proceedings of the Institution of Mechanical Engineers part D*, 213:95–107, 1999.

[DER+79] D. Dowson, P.N. Economou, B.L. Ruddy, P.J. Strachan, and A.J. Backer. Piston ring lubriction - part II: Theoretical analysis of a single ring and complete ring pack. *In Energy Conservation Through Film Lubrication Technology: Frontiers in Research and Design, the Winter Annual Meeting of the ASME*, pages 23–52, 1979.

[DHS99] S.J. Drew, D.C. Hesterman, and B.J. Stone. The torsional excitation of variable inertia effects in a reciprocating engine. *Mechanical Systems and Signal Processing*, 13(1):125–144, 1999.

[ES98] C. Edwards and S.K. Spurgeon. *Sliding Mode Control Theory and Applications*. Taylor & Francis, London, 1998.

[FA97] Z.S. Filipi and D.N. Assanis. A non-linear, transient, single-cylinder diesel engine simulation for predictions of instantaneous engine speed and torque. In *Proc. Tech. Conf. ASME ICE*, volume 1, pages 61–70, Colorado, 1997.

[Fer86] C. R. Ferguson. *Internal combustion engines applied thermosciences.* John Wiley, New York, 1986.

[FG74] J.O. Flower and R.K. Gupta. Optimal control consideration of diesel engine discrete models. *Int. J. Control*, 19:1057–1068, 1974.

[FHP96] L.M. Fu, H.H. Hsu, and C.J. Principe. Incremental backpropagation learning networks. *IEEE Transactions on Neural Networks*, 7(3):757–761, 1996.

[Fil98] Z.S. Filipi. Personal communication. *University of Michigan, Deptartment of Mechanical Engn, Ann Arbor, MI 48109 USA*, March 1998.

[Fil99] Z.S. Filipi. Personal communication. *University of Michigan, Deptartment of Mechanical Engn, Ann Arbor, MI 48109 USA*, June 1999.

[FTT81] S. Furuhama, M. Takiguchi, and K. Tomizawa. Effect of piston and piston ring designs on the piston friction forces in diesel engines. *SAE paper No. 810977*, 1981.

[FW76] J.O. Flower and G.P. Windett. Dynamic measurements of a large diesel engine using P.R.B.S. techniques - part I development of theory for closed loop sampled systems, - part II instrumentation, experimental techniques and results. *Int. J. Control*, 24:379–404, 1976.

[GA98] L. Guzzella and A. Amstutz. Control of diesel engines. *IEEE Control Systems Magazine*, 18(5):53–71, 1998.

[GH88] T.P. Gardner and N.A. Henein. Diesel starting: A mathematical model. *SAE paper No. 880426*, 1988.

[GM96] M. Gori and M. Maggini. Optimal convergence of on-line backpropagation. *IEEE Transactions on Neural Networks*, 7:251–254, 1996.

[GMM+99] H.T. Grimmelius, P.P. Meiler, H.L. Maas, B. Bonnier, J.S. Grevink, and R.F. van Kuilenburg. Three state-of-the-art methods for condition monitoring. *IEEE Transactions on Industrial Electronics*, 46:407–416, 1999.

[Gol91] J.L. Goldberg. *Matrix Theory with Application.* McGraw-Hill, New York, 1991.

[GRH89] G.L. Gissinger, R. Renard, and M. Hassenforder. Model based design and control of diesel engines. *SAE paper No. 890568*, 1989.

[Hey88] J. B. Heywood. *Internal combustion engine fundamentals.* McGraw-Hill, New York, 1988.

[HF71] P.A. Hazell and J.O. Flower. Sampled-data theory applied to the modelling and control analysis of compression-ignition engines. *Int. J. Control*, 13:549–562, 1971.

[HGH93] J.Y. Hung, W. Gao, and J.C. Hung. Variable structure control: A survey. *IEEE Trans. Industrial Electronics*, 40(1):2–21, 1993.

[HJ85] R.A. Horn and C.R. Johnson. *Matrix Analysis.* Cambridge University Press, Cambridge, U.K., 1985.

[HK99] D.T. Hountalas and A.D. Kouremenos. Development and application of a fully automatic troubleshooting method for large marine diesel engines. *Applied Thermal Engineering*, 19:299–324, 1999.

[HS94] D.C. Hesterman and B.J. Stone. A system approach to the torsional vibration of multi-cylinder reciprocating engines and pumps. *Proceedings of the Institution of Mechanical Engineers part C*, 208:395–408, 1994.

[HSNI00] M. Hafner, M. Schuler, O. Nelles, and R. Isermann. Fast neural networks for diesel engine control design. *Control Engineering Practice*, 8:1211–1221, 2000.

[IH01] R. Isermann and M. Hafner. Mechatronic combustion engines - from modeling to optimal control. *European Journal of Control*, 7:220–247, 2001.

[Jac88] R.A. Jacobs. Increasing rate of convergence through learning rate adaptation. *Neural Networks*, 1(4):295–307, 1988.

[JJK00] M. Jankovic, M. Jankovic, and I. Kolmanovsky. Constructive Lyapunov control design for turbocharged diesel engines. *IEEE Trans. on Control Systems Technology*, 8(2):288–299, 2000.

[JKS+91] J.-P. Jensen, A.F. Kristensen, S.C. Serenson, N. Houbak, and E. Hendricks. Mean value modeling of a small turbocharged diesel engine. *SAE paper No. 910070*, 1991.

[JS00] J. Jerrelind and A. Stensson. Nonlinear dynamics of parts in engineering systems. *Chaos Solitons and Fractals*, 11:2413–2428, 2000.

[Kah98] O. Kahldy. Personal communication. *King Abdullah Design and Development Bureau, Jordan*, February 1998.

[KH91] C.M. Kuan and K. Hornik. Convergence of learning algorithm with constant learning rates. *IEEE Transactions on Neural Networks*, 2(5):484–489, 1991.

[KM94] M. Kao and J.J. Moskwa. Model based engine fault detection using cylinder pressure estimates from nonlinear observers. In *IEEE Conf. on Decision and Control*, pages 2742–2747, 1994.

[KM95] M. Kao and J.J. Moskwa. Turbocharged diesel engine modelling for nonlinear engine control and state estimation. *Transactions of*

the ASME Journal of Dynamic Systems, Measurement, and Control, 117:20–30, 1995.

[KP88] Y. Ku and D.J. Patterson. Piston and ring friction by the fixed sleeve method. *SAE paper No. 880571*, 1988.

[KP95] D.A. Karras and S.J. Perantonis. An efficient constrained training algorithm for feedforward networks. *IEEE Transactions on Neural Networks*, 6:1420–1434, 1995.

[KP99] S.V. Kamarthi and S. Pittner. Accelerating neural network training using weight extrapolations. *Neural Networks*, 12:1285–1299, 1999.

[KRW99] Y.W. Kim, G. Rizzoni, and Y-Y. Wang. Design of an IC engine torque estimator using unknown input observer. *ASME J. of Dynamic Systems, Measurement, and Control*, 121:487–495, 1999.

[LAK90] K. Lida, K. Akatsuo, and K. Kido. IMEP estimation from instantaneous crankshaft torque variation. *SAE Technical paper No. 900617*, 1990.

[LBI01] Y. Levin and A. Ben-Israel. A Newton method for systems of m equations in n variables. *Nonlinear Analysis*, 47:1961–1971, 2001.

[LCH97] H. Liu, N.G. Chalhoub, and N. Henein. Simulation of a single cylinder diesel engine under cold start conditions using SIMULINK. In *Proc. Tech. Conf. ASME ICE*, number 97-ICE-2, pages 9–18, Colorado, 1997.

[LDCL01] A. De Lucas, A. Duran, M. Carmona, and M. Lapuerta. Modeling diesel particulate emissions with neural networks. *FUEL*, 80:539–548, 2001.

[Lei85] J.R. Leigh. *Applied Digital Control.* Prentice-Hall, Englewood-Cliffs, NJ, 1985.

[LFLY00] S. Lixiang, E.H. Francis, Q. Liangsheng, and S. Yudi. Fault diagnosis using rough sets theory. *Computer in Industry*, 43:61–72, 2000.

[LPCG02] W. Li, R.M. Parkin, J. Coy, and F. Gu. Acoustic based condition monitoring of a diesel engine using self-organising map networks. *Applied Acoustics Journal*, 63:699–711, 2002.

[LS99] H. Li and B.J. Stone. Time domain modelling of a reciprocating engine. *Mechanical Systems and Signal Processing*, 13(1):169–178, 1999.

[LW71] J.D. Ledger and S. Walmsley. Computer simulation of a turbocharged diesel engine operating under transient load conditions. *SAE paper No. 710177*, 1971.

[Mat92] J.H. Mathews. *Numerical Methods for Mathematics, Science, and Engineering*. Prentice-Hall, Englewood Cliffs, NJ., 1992.

[Mat97] The MathWorks, Inc., MA, USA. *MATLAB: Reference Guide*, 1997.

[Mcg78] J.A. *Mcgeehan. A literature* review of the effect of piston and ring friction and lubricating oil vicosity *on fuel economy. SAE paper No. 780673*, 1978.

[Mes01] E. Mesbahi. An intelligent sensor validation and fault diagnostic technique for diesel engines. *Journal of Dynamic Systems Measurement and Control-Transactions of the ASME*, 123:141–144, 2001.

[MF89] J.D.C. Mcivor and D.N. Fenner. Finite-element analysis of dynamically loaded flexible journal bearings - a fast newton-raphson method. *Transactions of the ASME Journal of Tribology*, 111:597–604, 1989.

[Mil87] G.K. Miltsios. *Lubrication and friction of piston and piston ring in internal combustion engines.* PhD thesis, University of Michigan, Ann Arbor, MI, 1987.

[MP97] G.K. Miltsios and D.J. Patterson. A simplified model for piston ring friction calculation in internal combustion engines. In *Proc. Tech. Conf. ASME ICE*, volume 1, pages 1–8, Colorado, 1997.

[NKM+00] M.J. Van Nieuwstadt, I.V. Kolmanovsky, P.E. Moraal, A. Stefanopoulou, and M. Jankovic. EGR-VGT control schemes: experimental comparison for a high-speed diesel engine. *IEEE Control Systems Magazine*, 20(3):64–79, 2000.

[ON92] A.O. Ooyen and B. Neinhuis. Improving the convergence of the back-propagation algorithm. *Neural Networks*, 5:465–471, 1992.

[Ozi85] M.N. Ozisik. *Heat Transfer: a Basic Approach.* McGraw-Hill, New York, 1985.

[PF86] R.J. Primus and P.F. Flynn. The assessment of losses in diesel engines using second law analysis. In *Computer-Aided Engineering and Energy Systems, ASME, New York*, volume 3, pages 61–68, 1986.

[PH96] C.L. Phillips and R.D. Harbor. *Feedback Control Systems.* Prentice-Hall, Englewood-Cliffs, NJ, 1996.

[PKG00] N.G. Pantelelis, A.E. Kanarachos, and N. Gotzias. Neural networks and simple models for the fault diagnosis of naval turbochargers. *Mathematics and Computers in Simulation*, 51:387–397, 2000.

[Ram89] J.I. Ramos. *Internal Combustion Engine Modeling.* Hemisphere Publishing, New York, 1989.

[Rao90] S.S. Rao. *Mechanical Vibration.* Addison-Wesley, Reading, Mass, Wokingham, 1990.

[RDW95] G. Rizzoni, S. Drakunov, and Y-Y. Wang. On line estimation of indicated torque in IC engines via sliding mode observer. In *Amer. Contr. Conf.*, pages 2123–2127, 1995.

[RG97] C.G. Rakopoulos and E.G. Giakoumis. Simulation and exergy analysis of transient diesel-engine operation. *Energy*, 22(9):875–885, 1997.

[RH84] S.F. Rezeka and N.A. Henein. A new approach to evaluate instantaneous friction and its components in internal combustion engines. *SAE Technical paper No. 840179*, 1984.

[Ric00] D.E. Richardson. Review of power cylinder friction for diesel engines. *Transactions of the ASME Journal of Engineering for Gas Turbines and Power*, 122:506–519, 2000.

[RIV91] A. Rigler, J. Irvine, and T. Vodel. Rescaling of the variables in backpropagation learning. *Neural Networks*, 4:225–229, 1991.

[Riz89] G. Rizzoni. Estimate of indicated torque from crankshaft speed fluctuations: a model for the dynamic of the IC engine. *IEEE Trans. Vehicular Technology*, 38(3):168–179, 1989.

[RM86] D.E. Rumelhart and J.L. McClelland. *Parallel Distributed Proccessing: Explorations in the Microstructure of Cognition*, volume I. MIT Press, MA, 1986.

[Ros82] R.C. Rosenberg. General friction consideration for engine design. *SAE paper No. 821756*, 1982.

[RZ94] G. Rizzoni and Y. Zhang. Identification of a non-linear internal combustion engine model for on-line indicated torque estimation. *Mechanical Systems and Signal Processing*, 8(3):275–287, 1994.

[SBTM01] P.J. Shayler, J.A. Burrows, C.R. Tindle, and M. Murphy. Engine friction characteristics under cold start conditions. In *Proc. Tech. Conf. ASME ICE*, volume 37-3, pages 67–76, 2001.

[SH96] R. Salomon and J.L. Hemmen. Accelerating backpropagation through dynamic self-adaptation. *Neural Networks*, 9(4):589–601, 1996.

[SI02] A. Schwarte and R. Isermann. Neural network applications for model based fault detection with parity equations. *15th Triennial World Congress*, CD-ROM paper no. 2846, Barcelona, Spain 2002.

[SIM97] The MathWorks, Inc., MA, USA. *SIMULINK: A Program for Simulating Dynamic Systems*, 1997.

[SM89] J.E. Shigley and C.R. Mischke. *Mechanical Engineering Design.* McGraw-Hill, New York, 1989.

[SM95] Y. Shiao and J.J. Moskwa. Cylinder pressure and combustion heat release estimation for SI engine diagnostics using nonlinear sliding observer. *IEEE Trans. Control Systems Tech.*, 3:70–77, 1995.

[SRTL92] K. Srinivasan, G. Rizzoni, M. Trigui, and G-C. Luh. On-line estimation of net engine torque from crankshaft angular velocity measurement using repetitive estimators. In *Amer. Contr. Conf.*, pages 516–520, 1992.

[TC99] R.I. Taylor and R.C. Coy. Improved fuel efficiency by lubrication design: a review. *Proceedings of the Institution of Mechanical Engineers part J*, 214:1–15, 1999.

[UGS99] V. Utkin, J. Guldner, and J. Shi. *Sliding Mode Control in Electromechanical Systems.* Taylor & Francis, London, 1999.

[UP83] M.H. Uras and D.J. Patterson. Measurement of piston and ring assembly friction instantaneous IMEP method. *SAE Technical paper No. 830416*, 1983.

[Utk78] V.I. Utkin. Variable structure systems with sliding modes. *IEEE Trans. Automatic Control.*, AC-22(2):212–222, 1978.

[Wat84] N. Watson. Dynamic turbocharged diesel engine simulator for electronic control system development. *Transactions of the ASME Journal of Dynamic Systems, Measurement, and Control*, 106:27–45, 1984.

[WJ82] N. Watson and M.S. Janota. *Turbocharging the Internal Combustion Engine.* Macmillan, London, 1982.

[WKR97] Y-Y.W Wang, V. Krishnaswami, and G. Rizzoni. Event based estimation of indicated torque for IC engines using sliding mode observers. *Control Eng. Practice*, 5(8):1123–1129, 1997.

[WM95] R.W. Weeks and J.J. Moskwa. Automotive engine modeling for real-time control using Matlab/SIMULINK. *SAE paper No. 950417*, 1995.

[Wol78] M.A. Wolfe. *Numerical Methods for Unconstrained Optimization.* VNR, Wokingham, U.K., 1978.

[WT81] D.E. Winterbone and D.W.H. Tennant. The variation of friction and combustion rates during diesel engine transients. *SAE Technical paper No. 810339*, 1981.

[WTW77] D.E. Winterbone, C. Thiruarooran, and P.E. Wellstead. A wholly dynamic model of turbocharged diesel engine for transfer function evaluation. *SAE Paper No. 770124*, 1977.

[YC97] X.H. Yu and G.A. Chen. Efficient backpropagation learning using optimal learning rate and momentum. *Neural Networks*, 10(3):517–527, 1997.

[YC00] J.Y.F. Yam and T.W.S. Chow. A weight initialization method for improving training speed in feedforward neural network. *Neurocomputing*, 30:219–232, 2000.

[YCC95] X.H. Yu, G.A. Chen, and S.X. Cheng. Dynamic learning rate optimization of the backpropagation algorithm. *IEEE Transactions on Neural Networks*, 6(4):669–677, 1995.

[ZPHS92] Y. Zhang, K. Phaneuf, R. Hanson, and N. Showalter. Computer modeling on exhaust system heat transfer. *SAE paper No. 920262*, 1992.

[ZR93] Y. Zhang and G. Rizzoni. An on-line indicated torque estimator for IC engine diagnosis and control. *ASME J. Advanced Automotive Tech.*, 52:147–162, 1993.